Measurement of the top quark decay branching fraction ratio $R_b = \mathcal{B}(t \to Wb)/\mathcal{B}(t \to Wq)$ and of the inclusive production cross section $pp \to t\bar{t}$ in the dilepton channel at ATLAS

Dissertation
zur
Erlangung des Doktorgrades (Dr. rer. nat.)
der
Mathematisch-Naturwissenschaftlichen Fakultät
der
Rheinischen Friedrich-Wilhelms-Universität Bonn

vorgelegt von
Agnieszka Leyko
aus
Lodz, Polen

Bonn, December 2020

Angefertigt mit Genehmigung der Mathematisch-Naturwissenschaftlichen Fakultät der Rheinischen Friedrich-Wilhelms-Universität Bonn

1. Gutachter:	Prof. Dr. Markus Cristinziani
2. Gutachter:	Prof. Dr. Norbert Wermes
Tag der Promotion:	21. Januar 2021
Erscheinungsjahr:	2022

Abstract

The top quark branching fraction ratio R_b and the inclusive production cross section $\sigma_{t\bar{t}}$ are measured in the dilepton channel using 4.6 fb^{-1} of proton-proton collisions at the centre-of-mass energy $\sqrt{s}$ = 7 TeV collected with the ATLAS detector at the Large Hadron Collider at CERN. Template fits to the distribution of the number of b-tagged jets find $R_b = 1.02 \pm 0.01\,(\text{stat.}) \pm 0.07\,(\text{syst.})$ and $\sigma_{t\bar{t}} = 178 \pm 3\,(\text{stat.}) \pm 19\,(\text{syst.})$ pb. Lower limits on R_b and on the CKM matrix element $|V_{tb}|$ are set with the measured value of R_b to $R_b > 0.88$ and $|V_{tb}| > 0.94$ at 95% confidence level.

Contents

Introduction

The standard model of particle physics describes the building blocks of matter and the fundamental interactions among them. It introduces structure and symmetry, which led to discoveries of new particles and allowed physicists to make a significant progress in understanding the universe. However, the standard model leaves a number of key questions unanswered. Why do particles have different masses? Why is there such an imbalance of matter and antimatter in the universe? What does the dark matter consist of?

This thesis describes the measurement of the top quark branching fraction to the bottom quark[1], using data collected by the ATLAS[2] detector at the Large Hadron Collider at CERN[3] in 2011. The top quark is the heaviest elementary particle known to date. Its mass is comparable to the mass of an atom of gold. It is over 40 times greater than the mass of the second heaviest elementary particle, the bottom quark[4]. Such an exceptionally large mass made the top quark a very interesting object of research since it was discovered at Fermilab[5] in 1995. Though predicted by the standard model, many hope it could be a gateway to physics "beyond the standard model".

A number of theories predict that the "new physics" would unveil itself in small distortions of top quark properties from the values predicted by the standard model. This thesis searches for anomalous effects in the value of the branching fraction of the top quark. In the standard model, the top quark branching fraction, R_b, is equal to $|V_{tb}|^2$, the CKM matrix[6] element. The standard model orders the quarks into generations, organising them by their properties. The higher the generation, the larger the mass of the particles. Top and bottom quarks belong to the third generation. Although the standard model does not limit the number of generations, there are currently only three known. Under the assumption that only three generations of quarks exist and that CKM is a unitary matrix, $|V_{tb}| \approx 1$. Thus, a top quark is expected to decay almost exclusively to a bottom quark. If more than three generations of quarks existed, or the top quark decayed to light quarks at a higher rate than predicted by the standard model, R_b and $|V_{tb}|$ would take values significantly lower than 1.

Because of its high top quark events production rates the Large Hadron Collider was nicknamed the "top quark factory". These high production rates are achieved through an unprecedented high collision energy. The Large Hadron Collider was designed to collide protons at centre-of-mass energy of $\sqrt{s} = 14$ TeV, but due to an accident in 2008, it started operating at half of the design energy and was increasing its collision energy with time. In 2010 and 2011 it was operated at 7 TeV, which is approx.

[1] Often referred to as just b quark
[2] A Toroidal LHC ApparatuS
[3] European Organization for Nuclear Research (French: Organisation européenne pour la recherche nucléaire), Geneva, Switzerland
[4] The mass of the top quark is approx. 173 GeV, mass of the bottom quark is approx. 4.18 GeV
[5] Fermi National Lab located in Batavia, IL in USA
[6] Cabibbo-Kobayashi-Maskawa matrix describes mixing between quarks

3.5 higher than the highest energy achieved by the Tevatron[7]. The Large Hadron Collider consists of two beam pipes, in which the particles travel in opposite directions. There are four intersection points at which collisions are possible and detectors are built around them. Apart from protons, the Large Hadron Collider can also collide heavy ions, for example lead.

The ATLAS detector is designed to precisely reconstruct trajectories of charged particles, measure energy of charged and neutral particles, as well as estimate the energy of particles that weakly interact with matter and escape the detector without leaving any signal. When high energy particles pass through the detector they produce cascades and showers of particles called "jets". Understanding the performance of the identification and reconstruction of jets originating from the b quarks is the centrepiece of this R_b measurement. The identification of b-jets, often referred to as b-tagging, utilizes information from all sub-detectors of ATLAS as well as advanced analysis methods such as neural networks.

In this analysis, R_b is measured in the top quark pair dilepton channel with a template fit using the distribution of the number of b-tagged jets. Additionally, this method allows for a measurement of the cross section of the top quark pairs production $\sigma_{t\bar{t}}$.

The measured values of $R_b = 1.02 \pm 0.01\,(\text{stat.}) \pm 0.07\,(\text{syst.})$ and $|V_{tb}| = 1.01 \pm 0.01\,(\text{stat.}) \pm 0.03\,(\text{syst.})$, though not having statistical significance to report any effects in disagreement with the standard model, leave room for such measurement in the future, once methods with higher precision are available. The measured value of the top quark pair production cross section, $\sigma_{t\bar{t}} = 178 \pm 3\,(\text{stat.}) \pm 19\,(\text{syst.})$ pb is in agreement with the standard model.

This thesis is organized across five chapters: Chapter One gives an overview of the standard model and recent searches for new physics involving the top quark. Chapter Two describes the infrastructure: the Large Hadron Collider, the ATLAS detector, Monte Carlo simulations, the Worldwide LHC Computing Grid and the ROOT scientific software framework. Chapter Three discusses the reconstruction and identification of top quark events in the ATLAS detector. Chapter Four is devoted to the principles and the performance of b-tagging. Experience gained by the author while working on b-tagging calibration with the kinematic selection in the single lepton channel proved itself invaluable during the later analysis. Chapter Five presents the measurement of the top quark branching fraction and the cross section of top quark pair production.

[7] The collision energy of run II at Tevatron was 1.96 TeV.

CHAPTER 1

Top quark physics at hadron colliders

1.1 The standard model of particle physics

The standard model [1, 2] is a theory which explains the fundamental structure of matter by describing the elementary particles and the interactions among them. The elementary particles are presented in figure 1.1.

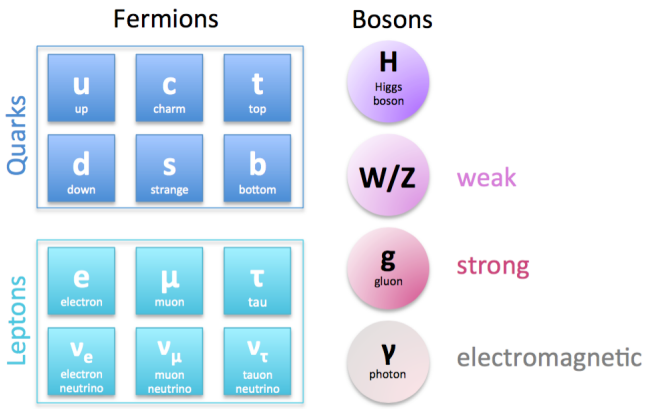

Figure 1.1: Elementary particles of the standard model.

They can be divided into the following groups based on their properties:

- Fermions are elementary constituents of matter. They have half-integer spin.
  - Leptons have integer electric charge and are organised in isospin doublets of an electrically charged particle and its electrically neutral partner, e.g. electron e and electron neutrino ν_e, $\binom{\nu_e}{e}$. All leptons take part in the weak interaction. Charged leptons additionally take part in the electromagnetic interaction.
  - Quarks have fractional electric charge and are organised in isospin doublets of charge $+2/3$ (up-type) and $-1/3$ (down-type) quarks, $\binom{u}{d}$. Quarks take part in the electromagnetic, weak and strong interactions.

- Bosons are particles with integer spin.
  - Gauge bosons mediate interactions. The photon γ is the mediator of the electromagnetic interaction, the $W^{\pm}$ and Z bosons of the weak interaction and gluons g of the strong interaction.
  - The Higgs boson is the excitation of the Higgs field, which gives masses to the other particles.

Leptons and quarks are arranged in three generations. Corresponding particles in different generations have the same quantum numbers, like electric charge, but the higher the generation, the larger the masses. Table 1.1 provides an overview of the known quarks and their masses.

Generation	1	2	3
up-type, $Q = +2/3$	up (u) $2.2^{+0.5}_{-0.4}$ MeV	charm (c) $1.275 \pm^{+0.025}_{-0.035}$ GeV	top (t) 173.0 ± 0.4 GeV
down-type, $Q = -1/3$	down (d) $4.7^{+0.5}_{-0.3}$ MeV	strange (s) 93^{+11}_{-5} MeV	bottom (b) $4.18^{+0.04}_{-0.03}$ GeV

Table 1.1: Masses of quarks of the three known generations [3].

Leptons of the first generation are the electron e ($m_e \approx 0.5$ MeV) and the electron neutrino ν_e, followed by the muon μ ($m_\mu \approx 106$ MeV) and the muon neutrino ν_μ and the tau lepton τ ($m_\tau \approx 1.8$ GeV) and the tau neutrino ν_τ in the second and third generation. The masses of neutrinos are not precisely known yet, but a limit has been set to $m_\nu < 2$ eV [3].

A particle needs to carry a specific charge to undergo a particular interaction. The charge of the electromagnetic interaction is the electric charge Q, the charge of the weak interaction, the weak isospin T, and that of the strong interaction, the colour charge C. Each of the fermions has its antiparticle with an opposite charge[1]. Another property that determines the particle's interactions is the chirality P. Left-handed particles form the doublets described above, e.g. $\binom{u}{d}_L$, while right-handed particles form singlets, e.g. u_R, d_R. The weak interaction breaks the P-symmetry and acts only on the left-handed particles and right-handed antiparticles. An overview of the quantum numbers of the fermions is presented in table 1.2. Right-handed neutrinos do not carry any charge, therefore do not interact with other particles.

The standard model engages the mathematical framework of quantum field theory and is based on a $\mathrm{SU}(3)_C \times \mathrm{SU}(2)_L \times \mathrm{U}(1)_Y$ gauge symmetry [4]. In this convention fermions are expressed as fields (vectors) and interactions as operators (tensors). The general Lagrangian for the standard model consists of the following terms

$$\mathcal{L}_{\mathrm{SM}} = \mathcal{L}_{\mathrm{Gauge}} + \mathcal{L}_{\mathrm{Matter}} + \mathcal{L}_{\mathrm{Yukawa}} + \mathcal{L}_{\mathrm{Higgs}}. \tag{1.1}$$

$\mathcal{L}_{\mathrm{Gauge}}$ contains the kinetic energy of the gauge fields (bosons) and describes their self interactions, $\mathcal{L}_{\mathrm{Matter}}$ contains the kinetic energy of the matter particles (fermions) and describes their interactions with the gauge bosons, $\mathcal{L}_{\mathrm{Yukawa}}$ describes the interaction of the Higgs boson with fermions and $\mathcal{L}_{\mathrm{Higgs}}$ describes the kinetic energy of the Higgs field, its gauge interactions and the Higgs potential.

Each of the interactions defined in the standard model is represented by a separate term in the $\mathcal{L}_{\mathrm{Matter}}$ Lagrangian. The theory describing strong interactions is called quantum chromodynamics (QCD) and

[1] For charges different than zero.

		P	Q	T	T_3	Y_W	C
Quarks	$Q_L^i = \begin{pmatrix} u^i \\ d^i \end{pmatrix}_L$	L	$+2/3$ $-1/3$	$1/2$	$+1/2$ $-1/2$	$1/3$	$b/g/r$
	u_R^i d_R^i	R	$+2/3$ $-1/3$	0	0	$4/3$ $-2/3$	
Leptons	$L_L^i = \begin{pmatrix} \nu^i \\ e^i \end{pmatrix}_L$	L	0 -1	$1/2$	$+1/2$ $-1/2$	-1	-
	ν_R^i e_R^i	R	0 -1	0	0	0 -2	

Table 1.2: Quantum numbers of fermions: P - chirality, Q - electric charge, T - weak isospin, T_3 - third component of weak isospin, $Y_W = 2(Q - T_3)$ - weak hypercharge, C - colour charge [4]. The index $i = 1, 2, 3$ denotes fermion generations, e.g. u_L^i denotes left-handed up-type quarks: $u_L^1 = u_L$, $u_L^2 = c_L$ and $u_L^3 = t_L$.

is based on the $\mathrm{SU}(3)_C$ symmetry. Its term in the $\mathcal{L}_{\mathrm{Matter}}$ Lagrangian can be written as

$$\mathcal{L}_{\mathrm{QCD}} = -\sum_{\psi} \bar{\psi}\gamma^{\mu} g_s T_a G_{\mu}^a \psi, \tag{1.2}$$

where ψ represents quark fields $\psi = Q_L^i, u_R^i, d_R^i$ (compare with table 1.2), γ^{μ} are Dirac matrices, G_{μ}^a are the SU(3) gauge fields containing gluons, T_a are the SU(3) generators and g_s is the strong coupling constant.

The unified theory of electroweak (EW) interactions is based on the $\mathrm{SU}(2)_L \times \mathrm{U}(1)_Y$ symmetry and its term in $\mathcal{L}_{\mathrm{Matter}}$ is described in the following way:

$$\mathcal{L}_{\mathrm{EW}} = \sum_{\psi} \bar{\psi}\gamma^{\mu} \left(-g' \frac{1}{2} Y_W B_{\mu} - g \frac{1}{2} \sigma_j W_{\mu}^j \right) \psi, \tag{1.3}$$

where ψ represents fermion fields $\psi = L_L^i, e_R^i, Q_L^i, u_R^i, d_R^i$ (compare with table 1.2), Y_W is the weak hypercharge, B_{μ} is the U(1) gauge field, σ_j are Pauli matrices, which are SU(2) generators and act only on left-handed particles, W_{μ}^j represents the three SU(2) gauge fields: $W^{\pm}$ and Z, and g and g' are coupling constants.

The $\mathcal{L}_{\mathrm{Matter}}$ Lagrangian, after including the kinetic energy component, takes the following form:

$$\mathcal{L}_{\mathrm{Matter}} = \sum_{\psi} \bar{\psi}\gamma^{\mu} \left(i\partial_{\mu} - g_s T_a G_{\mu}^a - \frac{1}{2} g' Y_{\mathrm{W}} B_{\mu} - \frac{1}{2} g \sigma_j W_{\mu}^j \right) \psi, \tag{1.4}$$

where ψ denotes particles that undergo respective interaction as specified in discussion of equations 1.2 and 1.3, $\psi = L_L^i, e_R^i, Q_L^i, u_R^i, d_R^i$.

The self interactions of gauge bosons are described with the gauge field strength tensors

$$\mathcal{L}_{\mathrm{Gauge}} = \frac{1}{2g_s^2} \mathrm{Tr}\, G^{\mu\nu} G_{\mu\nu} + \frac{1}{2g^2} \mathrm{Tr}\, W^{\mu\nu} W_{\mu\nu} - \frac{1}{4g'^2} \mathrm{Tr}\, B^{\mu\nu} B_{\mu\nu}. \tag{1.5}$$

The coupling constants are the only parameters of the first two terms of $\mathcal{L}_{\mathrm{SM}}$. At M_Z energy scale their

values are

$$\begin{aligned} g_s &\approx 1, \\ g &\approx \frac{2}{3}, \\ g' &\approx \frac{2}{3\sqrt{3}}. \end{aligned} \tag{1.6}$$

The gauge symmetries, as presented in the equations above, assume that all particles are massless. The mass terms appear due to a spontaneous breaking of the electroweak field symmetry. This requires the introduction of an additional field: particles[2] acquire their mass by interacting with the Higgs field. The Higgs field $\phi = \binom{\phi^+}{\phi^0}$ (the upper index denotes the electric charge) is a complex scalar field. The $\mathcal{L}_{\text{Higgs}}$ Lagrangian describes the kinetic energy of the Higgs field, its interactions with the gauge bosons and the Higgs potential

$$\mathcal{L}_{\text{Higgs}} = \left|\left(i\partial_\mu - \frac{1}{2}g\sigma_j W_\mu^j - \frac{1}{2}g' Y_{\text{W}} B_\mu\right)\phi\right|^2 - \mu^2\phi^\dagger\phi - \frac{\lambda^2}{2}(\phi^\dagger\phi)^2. \tag{1.7}$$

Spontaneous symmetry breaking happens when the potential does not have a minimum at 0, but at $\phi_0 \neq 0$. The Higgs potential $V(\phi) = \mu^2\phi^\dagger\phi + \frac{\lambda}{2}(\phi^\dagger\phi)^2$ reaches a minimum at $\langle\phi_0\rangle = \mu/\lambda = v/\sqrt{2}$. The parameter v is called the vacuum expectation value and its value is $v \approx 246$ GeV, while λ is the quartic coupling and describes the Higgs boson interaction with itself.

The interaction of the Higgs field with massless fermions ψ is described by the Yukawa interaction and the Yukawa Lagrangian can be written as

$$\mathcal{L}_{\text{Yukawa}} = -\Gamma_u^{ij}\bar{Q}_L^i\epsilon\phi^* u_R^j - \Gamma_d^{ij}\bar{Q}_L^i\phi d_R^j - \Gamma_l^{ij}\bar{L}_L^i\epsilon\phi e_R^j + h.c. \tag{1.8}$$

where Q_L^i/L_L^i denote the quark/lepton left-handed doublets and $u_R^j/d_R^j/e_R^j$ the right-handed singlets, the indices $i,j = 1,2,3$ represent three generations of fermions. Γ are Yukawa couplings represented by 3×3 complex arbitrary matrices in the fermion generations space. They are not diagonal and provide mixing between generations. ϵ is the total antisymmetric tensor related to the σ_2 Pauli matrix. The difference in the quarks and leptons terms can be explained by the fact that the Yukawa mechanism gives mass only to one partner of lepton doublets (neutrinos are considered massless). In order to give mass to both particles of the quark doublet [5], they have to couple with the Higgs doublet "charge conjugate" $\tilde{\phi} = \epsilon\binom{\phi^{0*}}{-\phi^{+*}}$. This also explains why there are different Yukawa couplings for up- and down-type quarks Γ_u and Γ_d.

The masses of fermions and bosons can be expressed as a function of the vacuum expectation value v

$$\begin{aligned} M_W &= \frac{1}{2}gv, \\ M_Z &= \frac{1}{2}\sqrt{g^2 + g'^2}v, \\ M_f^{ij} &= \Gamma_f^{ij}\frac{v}{\sqrt{2}}, \end{aligned} \tag{1.9}$$

where f stands for quarks and leptons.

[2] Charged fermions and weak gauge bosons are massive particles; neutrinos are considered massless.

As already mentioned, Γ_f are not diagonal and the physical states can be obtained by diagonalising them and introducing new matrices V, such that for leptons

$$V_L^l M_l V_L^{l\,\dagger} = \begin{pmatrix} m_e & 0 & 0 \\ 0 & m_\mu & 0 \\ 0 & 0 & m_\tau \end{pmatrix}$$

and similarly for quarks

$$V_L^d M_d V_L^{d\dagger} = \begin{pmatrix} m_d & 0 & 0 \\ 0 & m_s & 0 \\ 0 & 0 & m_b \end{pmatrix}, \quad V_L^u M_u V_L^{u\dagger} = \begin{pmatrix} m_u & 0 & 0 \\ 0 & m_c & 0 \\ 0 & 0 & m_t \end{pmatrix}. \tag{1.10}$$

From this it follows that mixing between different quark mass eigenstates is described by

$$V_{CKM} = V_L^u V_L^{d\dagger} = \begin{pmatrix} V_{ud} & V_{us} & V_{ub} \\ V_{cd} & V_{cs} & V_{cb} \\ V_{td} & V_{ts} & V_{tb} \end{pmatrix}, \tag{1.11}$$

which is called the Cabibbo-Kobayashi-Maskawa matrix. It is a 3×3 complex unitary matrix, which implies that the square sum for each row and column is equal 1. The CKM matrix can be parametrised by three mixing angles θ_{12}, θ_{13}, θ_{23} and the CP-violating Kobayashi-Maskawa phase δ [3]. Using $s_{ij} = \sin\theta_{ij}$ and $c_{ij} = \cos\theta_{ij}$ the CKM matrix can be written as

$$V_{CKM} = \begin{pmatrix} c_{12}c_{13} & s_{12}c_{13} & s_{13}e^{-i\delta} \\ -s_{12}c_{23} - c_{12}s_{23}s_{13}e^{i\delta} & c_{12}c_{23} - s_{12}s_{23}s_{13}e^{i\delta} & s_{23}c_{13} \\ s_{12}s_{23} - c_{12}c_{23}s_{13}e^{i\delta} & -c_{12}s_{23} - s_{12}c_{23}s_{13}e^{i\delta} & c_{23}c_{13} \end{pmatrix}. \tag{1.12}$$

The values of the CKM matrix elements are not specified by the theory. Taking into account the relations between the parameters of the standard model and their measured values, as well as direct measurements of the CKM matrix elements, the CKM matrix elements can be determined with a high precision [3]

$$V_{CKM} = \begin{pmatrix} 0.97446 \pm 0.00010 & 0.22452 \pm 0.00044 & 0.00365 \pm 0.00012 \\ 0.22438 \pm 0.00044 & 0.97359^{+0.00010}_{-0.00011} & 0.04214 \pm 0.00076 \\ 0.00896^{+0.00024}_{-0.00023} & 0.04133 \pm 0.00074 & 0.999105 \pm 0.000032 \end{pmatrix}. \tag{1.13}$$

The meaning of the CKM matrix in the context of quark's decays will be discussed in section 1.2.2.

Although the standard model is very successful in describing the interaction of elementary particles with force fields and allowed to predict the existence of not yet discovered particles (e.g. the top quark or the Higgs boson), its large number of arbitrary parameters might be an indication that it is not the final theory [3]. There are 19 arbitrary parameters

- 3 gauge couplings g_s, g and g',
- 9 fermion masses,
- 3 CKM matrix mixing angles and 1 phase,
- 2 Higgs parameters v and λ,
- 1 mixing angle θ associated with the QCD ground state.

Their values are known from experiments, but there is no explanation why these parameters should take these exact values. Furthermore, with the confirmation of neutrino oscillations (e.g. [6, 7]), which is an indirect proof of neutrino masses, there are at least 7 more parameters: 3 masses, 3 mixing angles, 1 Dirac CP-phase and possibly 2 Majorana phases.

In spite of describing observed phenomena, the standard model does not provide answers to some fundamental questions, such as why there are three generations of fermions (in principle more generations are allowed), what is the origin of fermion masses and mixing angles, or why there is such an imbalance between matter and antimatter in the universe. Some possible extensions to the standard model that could be confirmed or disproved using top quark measurements will be described in section 1.2.3.

1.2 Top quark physics and searches for "new physics"

The top quark is the heaviest and therefore last observed quark. It was discovered in 1995 by the D0 [8] and CDF [9] collaborations at Fermilab. Both experiments analysed proton-antiproton collisions from the Tevatron collider at the centre-of-mass energy of $\sqrt{s} = 1.8$ TeV. Later, it was observed and studied in proton-proton collisions at the Large Hadron Collider at CERN at the centre-of-mass energy starting from 7 TeV [10, 11]. The principles of operation and performance of the LHC will be described in section 2.2.

At hadron colliders top quarks can be produced either as single particles (referred to as *single top*) or as quark-antiquark pairs (referred to as *top quark pairs* or $t\bar{t}$). Because of different colliding particles and collision energy at the Tevatron and the LHC, the dominating top quark production mechanisms are different.

1.2.1 Top quark production at hadron colliders

Hadrons are made of quarks and gluons, collectively called *partons*. The quarks inside a hadron are divided into *valence quarks* and a sea of virtual quark-antiquark pairs. According to QCD, the only stable particles built from quarks are colour-neutral (i.e. have colour charge equal to 0). When a free quark is produced, it will immediately bond with other quarks in order to create a hadron. This process is called *hadronisation* and requires about 10^{-24} s.

The most common hadrons are *mesons* and *baryons*. Mesons consist of a combination of colour-anticolour pair of (valence) quark-antiquark. Baryons are a combination of three quarks with different colours ($b + g + r = 0$). *Tetraquarks* and *pentaquarks* consist of 4 and 5 quarks, respectively. Protons p (and antiprotons $\bar{p}$) used to produce top quarks at the LHC and Tevatron consist of uud valence quarks ($\bar{u}\bar{u}\bar{d}$ for antiprotons).

A single hadron in a hadron beam can be pictured as a beam of partons, each carrying a fraction x of the hadron's momentum. The interactions between hadrons during a collision can be described as interactions of partons from colliding particles. Parton interactions can be divided into short distance (hard scattering) and long distance interactions (soft scattering, often called *underlying event*).

The hard scattering of particles i and j is defined as a process with a high momentum transfer and is described by a partonic cross section $\hat{\sigma}_{ij}$. The *parton distribution function* (PDF) $f_i(x_i, \mu_F^2)$ describes the parton longitudinal momentum distribution in the hadron. The separation into short and long distance interaction is set by the factorisation momentum scale μ_F^2. The cross section $\hat{\sigma}_{ij}$ does not depend on the type of involved hadrons and is calculable in perturbative QCD, the PDFs are extracted in global QCD fits, e.g. from deep-inelastic scattering. To remove divergences appearing in the higher-order QCD calculations, a renormalisation procedure is applied. The renormalisation is defined at an arbitrary scale

μ_R [12]. Often, μ_R is chosen such that $\mu_R^2 = \mu_F^2 = \mu^2$. The top quark pair production cross section in a pp collision is given by the following formula [12]:

$$\sigma_{pp\to t\bar{t}}(\sqrt{s}, m_t) = \sum_{i,j=q,\bar{q},g} \int \mathrm{d}x_i \mathrm{d}x_j f_i(x_i,\mu^2) f_j(x_j,\mu^2) \times \hat{\sigma}_{ij\to t\bar{t}}(\rho, m_t^2, x_i, x_j, \alpha_S(\mu^2), \mu^2), \tag{1.14}$$

where $f_i(x_i,\mu^2)$ and $f_j(x_j,\mu^2)$ are the proton PDFs, $\rho = 4m_t^2/\sqrt{\hat{s}}$ and $\alpha_S(\mu^2)$ is the strong coupling constant at the μ^2 scale. The effective parton interaction energy can be expressed in terms of the beam's centre-of-mass energy $\sqrt{s}$, as $\sqrt{\hat{s}} = \sqrt{x_i x_j}\sqrt{s}$. To produce a particular final state, $\sqrt{\hat{s}}$ has to be equal to at least the sum of masses of the final state particles at rest. In order to produce a top quark pair, this implies $\sqrt{\hat{s}} \geq 2m_t$. Assuming that both partons would carry the same fraction of hadron's momentum, a parton must carry approximately $x_{\text{Tevatron}} = 0.2$ or $x_{\text{LHC}} = 0.025$ of the collision's energy at the Tevatron and LHC, respectively, in order to produce a top quark pair. Figure 1.2 shows the PDFs for protons. The PDFs for antiprotons look very similar, if one substitutes quarks with antiquarks. For $x = 0.2$ PDFs of valence quarks (antiquarks for antiproton) dominate over PDF of gluons, while for $x = 0.025$ the PDF of gluons dominates.

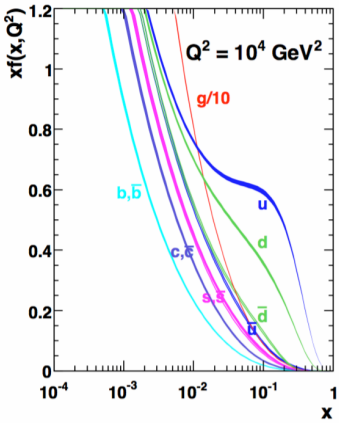

Figure 1.2: MSTW 2008 NLO PDFs at $Q^2 = 10^4$ GeV^2 [13] which corresponds to the order of magnitude of m_t^2.

Top quark production channels

Hadron colliders can produce top quark pairs either through gluon-gluon fusion or quark-antiquark annihilation, both presented in figure 1.3. At the Tevatron, which collided protons and antiprotons, top quark pairs were produced mainly through quark-antiquark annihilation (approx. 90% in Run 1 at $\sqrt{s} = 1.8$ TeV and 85% in Run 2 at $\sqrt{s} = 1.96$ TeV), gluon-gluon fusion contributed respectively in 10-15% [12]. At the LHC, which collides protons (no valence antiquarks), top quark pairs are produced through gluon-gluon fusion rather than quark-antiquark annihilation: 80% at the beginning of Run 1 with $\sqrt{s} = 7$ TeV and 90% at the design energy of $\sqrt{s} = 14$ TeV [3].

At the Tevatron single top quarks were produced mostly through s- and t-channels. The Wt channel was suppressed at the Tevatron, but can be observed at the LHC. All three production channels are shown in figure 1.4. The t- to s-channel ratio at the Tevatron was around 2, while at the LHC it is 15 at $\sqrt{s} = 8$ TeV [14].

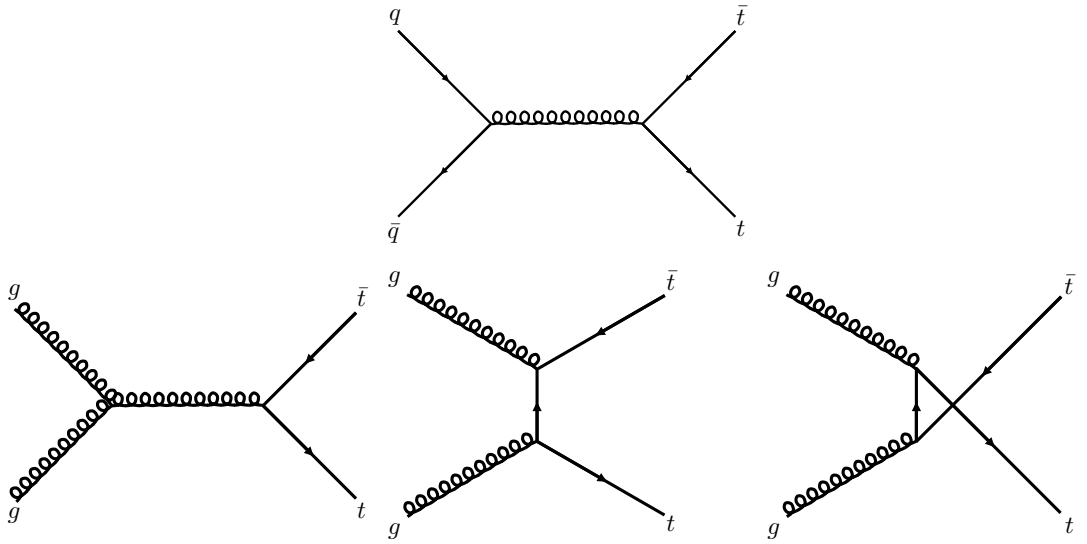

Figure 1.3: Leading order Feynman diagrams of top quark pair production: Quark-antiquark annihilation (upper row) and gluon-gluon fusion (lower row).

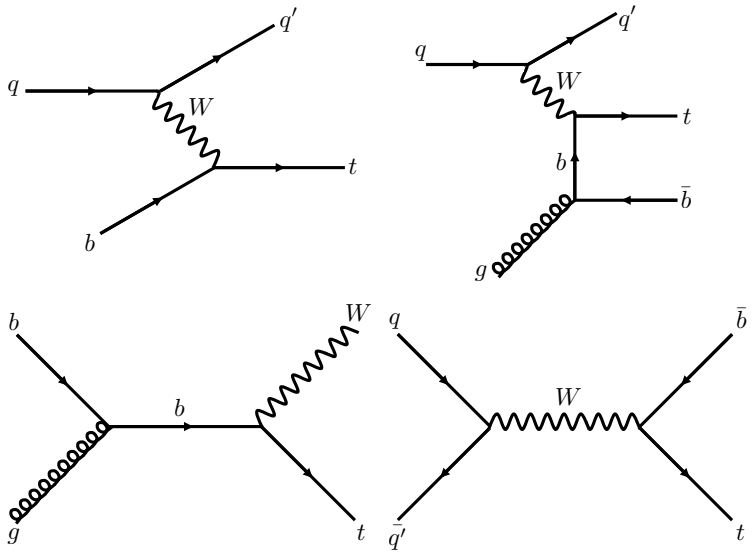

Figure 1.4: Feynman diagrams of electroweak single top production: t-channel or W-gluon fusion (upper row), Wt production (lower row left) and s-channel (lower row right).

Cross section calculation

QCD is a perturbation theory and cannot be calculated with exact solutions. This means that every calculation is only an approximation and experimental data is used to fine-tune some of its parameters. Depending on the number of terms considered, we distinguish following fixed order QCD calculations: leading order (LO), next-to-leading (NLO), next-to-next-to-leading order (NNLO), etc.

The leading-order (*Born level*) contributions to the $t\bar{t}$ production cross section are presented in figure 1.3. These are the simplest level calculations and they include only the phase-space integral over the tree-level matrix element $\mathcal{M}(\{p\}_m)$ and the jet measurement function $F_J(\{p\}_m)$, which defines the physical observables [12]

$$\sigma[F_J] = \int_m d\Gamma^{(m)}(\{p\}_m)|\mathcal{M}(\{p\}_m)|^2 F_J(\{p\}_m), \tag{1.15}$$

where $d\Gamma^{(m)}(\{p\}_m)$ is the phase-space measure and m denotes the number of produced partons. In the leading-order calculations hadronisation processes are not taken into account and every jet is reduced to just one parton, so there is no information about the jet structure available. Additionally, LO calculations have to bear with the following limitations: the result depends on the chosen renormalisation and factorisation scales, predictions for exclusive processes encounter large logarithms and in the phase-space regions where those logarithms dominate, the results are unreliable.

The NLO calculations provide a better precision by including *virtual* and *real* corrections. Examples for top quark pair production in quark-antiquark annihilation are presented in figure 1.5: a) is a virtual correction, b) and c) are real corrections. At the price of computational complexity, they provide more precise results and reduce the dependency on the renormalisation and factorisation scales.

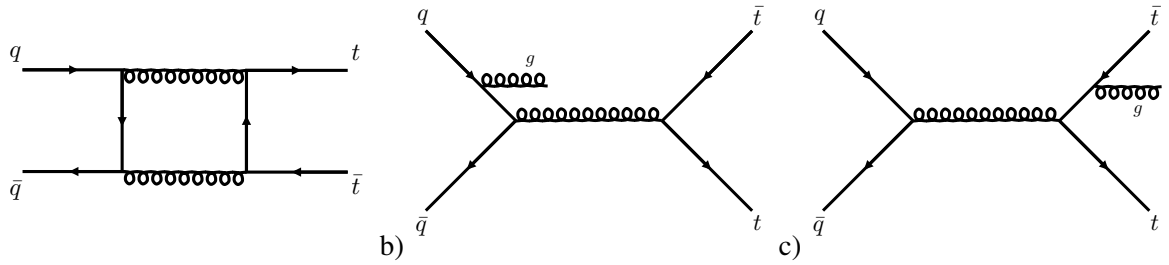

Figure 1.5: Examples of second order diagrams for $t\bar{t}$ production in quark-antiquark annihilation: a) box diagram, b) initial state radiation, c) final state radiation.

Even though the NNLO calculations allow to further improve precision, they still have to deal with large logarithms and do not describe hadronisation. Therefore, another approach is used. *Parton shower* calculations deal with the phase-space regions dominated by soft p_T. Parton showers are based on approximations of all orders calculations. The parton showers are then matched with the fixed order approximation, which enables covering a larger phase space.

The $t\bar{t}$ production cross section in hadron colliders depends on the centre-of-mass energy of the collisions, which is illustrated in figure 1.6 showing an overview of selected cross section measurement results.

The top quark pair production cross section also depends linearly on the top quark mass, which will be discussed in more detail in section 5.4.4. To enable easier comparison, all cross section values cited in this work were measured or calculated assuming $m_t = 172.5$ GeV, if not stated differently. Cross sections are expressed in barns where 1b = 10^{-24} cm^2 and for the $t\bar{t}$ production it ranges from 7 pb at

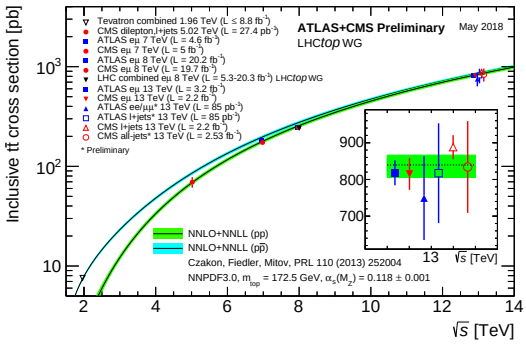

Figure 1.6: Summary of LHC and Tevatron measurements of the $t\bar{t}$ production cross section for various centre-of-mass energies compared to the NNLO QCD calculation with NNLL resummation (using the top++2.0 program). The uncertainty band represents uncertainties due to renormalisation and factorisation scale, parton density functions and the strong coupling [15].

$\sqrt{s} = 1.96$ TeV for the Tevatron, through 177 pb for the LHC at its initial energy at $\sqrt{s} = 7$ TeV to almost 900 pb for the LHC at $\sqrt{s} = 14$ TeV. The calculations for $\sqrt{s} = 7$ TeV used for the R_b measurement will be discussed in more detail in section 3.4.

1.2.2 Top quark decay

The lifetime of the top quark is an order of magnitude shorter than the time required for hadronisation [3]. This means that the top quark decays before hadronisation can happen and in this way offers a unique opportunity to measure the properties of a free, unbound quark. Of course, due to its extremely short lifetime, the top quark can not be measured directly. Its presence can be recognised only after reconstruction of its decay products.

According to the standard model, an up-type quark can only decay to a down-type quark and the branching fractions are equal to the corresponding CKM matrix elements squared. It is an electroweak decay, in which a W boson is produced. A decay of a top quark is schematically presented in figure 1.7. Using values from equation 1.13, this gives approximately: $\mathcal{B}(t \to Wb) \approx 99.8\%$, $\mathcal{B}(t \to Ws) \approx 0.2\%$ and $\mathcal{B}(t \to Wd) < 0.01\%$.

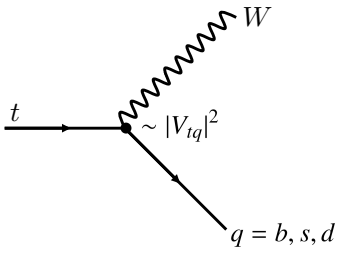

Figure 1.7: Top quarks decay to a down-type quark and a W boson.

The top quark pair decay channels are defined by the decay products of the W boson as presented in figure 1.8:

- *all-jets* – both W bosons decay hadronically into quarks, which then form jets (45.7%[3]),

[3] The reported fractions are from reference [3].

- *lepton+jets (single lepton)* – one W boson decays hadronically, one into a charged lepton and a neutrino (43.8%),
- *dilepton* – both W bosons decay into a charged lepton and a neutrino (10.5%).

Each of the decay channels presents a different experimental challenge. The all-jets, although it has the highest branching fraction, has the lowest signal-to-background ratio. The background is irreducible and originates mainly from QCD multijet processes, which are extremely difficult to model. On the other hand, the dilepton channel has a very high signal-to-background ratio, but it is impossible to unambiguously measure the energy of each of the neutrinos separately. The lepton+jets channel places itself between those two extremities and provides a moderate branching fraction and signal-to-background ratio. Reliable identification of b-jets and measurement of their properties allows for better identification of top quark events and enhances the signal-to-background ratio; therefore it often plays a key role in top quark measurements.

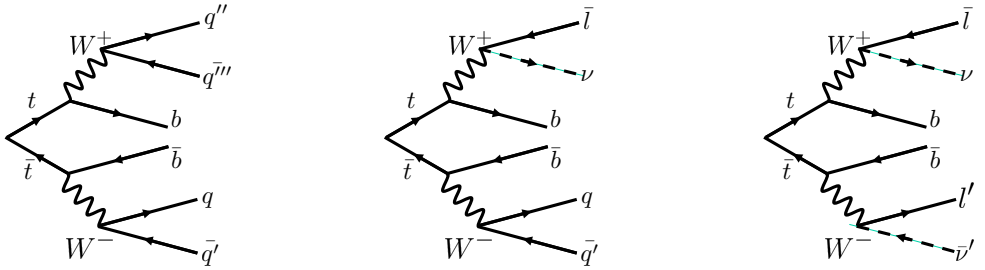

Figure 1.8: Top quark pair decay channels: All-jets (left), lepton+jets (middle) and dilepton (right) final states.

The τ lepton has a lifetime of less than 10^{-14} s and decays before reaching the first layer of the detector. Like the top quark, τ leptons decay through a W boson either hadronically or into an e/μ and e/μ neutrino. Additionally, in both cases, a τ neutrino is present. Therefore, in the $t\bar{t}$ final states often only stable charged leptons (e and μ) are considered, including those coming from τ lepton decay. Taking that into account, the branching fraction of dilepton[4] $t\bar{t}$ decays can be expressed as

$$\begin{aligned}\mathcal{B}(t\bar{t} \to \text{dilepton}) = \mathcal{B}^2(W \to e/\mu\ \nu) + 2 \cdot \mathcal{B}(W \to e/\mu\ \nu)\mathcal{B}(W \to \tau\nu)\mathcal{B}(\tau \to e/\mu\ \nu\nu) \\ + \mathcal{B}^2(W \to \tau\nu)\mathcal{B}^2(\tau \to e/\mu\ \nu\nu).\end{aligned} \tag{1.16}$$

The branching fractions used in equation 1.16 are described in table 1.3 and the resulting value of the dilepton branching fraction is $\mathcal{B}(t\bar{t} \to \text{dilepton}) = 0.0639 \pm 0.0011$.

process	comment	branching fraction
$W \to e/\mu\ \nu$	W decays to e/μ	0.2132 ± 0.0020
$W \to \tau\nu$	inclusive W decays to τ	0.1125 ± 0.0020
$\tau \to e/\mu\ \nu\nu$	leptonic τ decays	0.3524 ± 0.0001

Table 1.3: Values of branching fractions necessary to calculate $\mathcal{B}(t\bar{t} \to \text{dilepton})$ from reference [16].

Since the three $t\bar{t}$ decay channels have different signatures, requiring different analysis techniques, they are usually measured separately. One can define a cross section for each of the decay final states

[4] The dilepton channel is the main focus of this thesis, as the main measurement was performed in the dilepton channel.

using the branching fractions. For example, the $t\bar{t}$ dilepton cross section σ_{dilepton} is calculated from the inclusive $t\bar{t}$ cross section in the following way

$$\sigma_{\text{dilepton}} = \sigma_{t\bar{t}} \cdot \mathcal{B}(t\bar{t} \to \text{dilepton}). \tag{1.17}$$

Using the theoretical value of $t\bar{t}$ cross section for a centre-of-mass energy of $\sqrt{s} = 7$ TeV, $\sigma_{t\bar{t}} = 177^{+10}_{-11}$ pb[5], the dilepton cross section can be calculated as

$$\sigma_{\text{dilepton}} = 11.33^{+0.67}_{-0.72} \text{ pb}. \tag{1.18}$$

1.2.3 Searches for "new physics"

Because of its extraordinary high mass, the top quark is considered to be a gateway to yet undiscovered physics models referred to as *new physics* (NP) or *beyond standard model* (BSM) physics. Hints for new phenomena are searched for both in the top quark production measurements and in its decay studies. The top quark is also considered an important background in searches for new heavy particles, therefore it is crucial to measure its properties and production rates with high precision.

The top quark plays a key role in many BSM models, for example:

- **Supersymmetry (SUSY)** is a theory that assumes that each standard model particle has a "super-partner", whose spin differs by $^1/_2$. *Stop*, the scalar partner of the top quark, would be the lightest of all *squarks* and would decay to a top quark with a large branching fraction.
- **Little Higgs** is a theory in which the Higgs boson is a pseudo-Goldstone boson arising from global symmetry breaking. It predicts the existence of a t' particle with the same spin and colour as the top quark, but with a different electroweak coupling. Similarly to stops, t' would also decay to top quarks.
- **Top-colour** predicts the existence of a new strong gauge force coupling only to third generation quarks.
- **Technicolour** assumes the existence of a new heavy boson, Z', with a strong coupling to the top quark.
- **Top compositeness** assumes that the right-handed top quark t_R is a composite particle and introduces a new force. Predictions of this theory lead to an excess in $t\bar{t}t\bar{t}$ events.

Cross section

An excess of the cross section above the standard model expectation would be an obvious sign of new $t\bar{t}$ production modes. The ATLAS collaboration reported a measurement of $\sigma_{t\bar{t}} = 182.9 \pm 3.1\,(\text{stat.}) \pm 4.2\,(\text{syst.}) \pm 3.6\,(\text{lumi.}) \pm 3.3\,(\text{beam})$ pb at a centre-of-mass energy of 7 TeV, where the uncertainties are respectively: statistical, systematic, luminosity and beam energy [17]. At the same centre-of-mass energy CMS measured $\sigma_{t\bar{t}} = 161.9 \pm 2.5\,(\text{stat.})\,^{+5.1}_{-5.0}\,(\text{syst.}) \pm 3.6\,(\text{lumi.})$ pb [18]. For $\sqrt{s} = 8$ TeV ATLAS and CMS provide a combined result of $\sigma_{t\bar{t}} = 241.4 \pm 1.4\,(\text{stat.}) \pm 5.7\,(\text{syst.}) \pm 6.2\,(\text{lumi.})$ pb, corresponding to a total uncertainty of 3.5% [19]. Finally, the measurements from the LHC Run 2 with $\sqrt{s} = 13$ TeV are available, where the ATLAS collaboration found $\sigma_{t\bar{t}} = 818 \pm 8\,(\text{stat.}) \pm 27\,(\text{syst.}) \pm 19\,(\text{lumi.}) \pm 12\,(\text{beam})$ pb [20] and CMS $\sigma_{t\bar{t}} = 815 \pm 9\,(\text{stat.}) \pm 38\,(\text{syst.}) \pm 19\,(\text{lumi.})$ pb [21].

[5] The cross section calculations for $\sqrt{s} = 7$ TeV will be discussed in detail in section 3.4.

As presented in figure 1.6, all cross section measurements to date agree with the standard model expectations. Cross section measurements, and even more so, differential cross section measurements, are a valuable input for calibration of QCD calculation models.

The principle of differential cross section measurements is to measure the cross section as a function of properties of the final state particles, such as the mass or momentum. Some recent measurements for $t\bar{t}$ production can be found in reference [14].

CKM matrix element $|V_{tb}|$

The element $|V_{tb}|$ can be directly measured in single top events, because its production cross section is proportional to $|V_{tb}|^2$. In the top quark pair production it is possible to measure the ratio of top branching fractions defined as

$$R_b = \frac{\mathcal{B}(t \to Wb)}{\mathcal{B}(t \to Wq)} = \frac{|V_{tb}|^2}{|V_{tb}|^2 + |V_{ts}|^2 + |V_{td}|^2}, \tag{1.19}$$

which, under the assumption of three generations of quarks, is equal to $0.99830^{+0.00006}_{-0.00009}$ [22]. If, however, more than three generations of quarks exist, or the top quark decays to light quarks at a higher rate than predicted by the standard model, $|V_{tb}|$ and R_b could take lower values.

The combination of D0 and CDF measurements with single top data yields $|V_{tb}| = 1.02^{+0.06}_{-0.05}$ [14], while LHC experiments report $|V_{tb}| = 1.020 \pm 0.040\,(\text{meas.}) \pm 0.020\,(\text{theo.})$ [15]. An overview of results of direct $|V_{tb}|$ measurements by ATLAS and CMS is presented in figure 1.9.

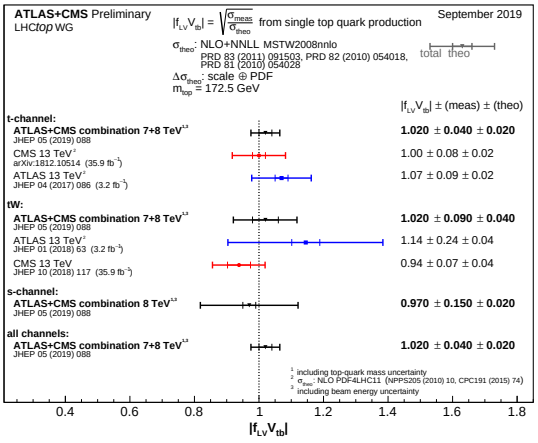

Figure 1.9: Summary of the ATLAS and CMS direct $|V_{tb}|$ measurements [23].

Also R_b was measured by collaborations at both the Tevatron and the LHC. The D0 collaboration reported a measurement of $R_b = 0.90 \pm 0.04$ [22] with 5.4 fb^{-1} and using both the dilepton and single lepton channels, which is barely compatible with the expectation of $R_b \approx 1$. The latest measurement by the CDF collaboration was performed in the single lepton channel, obtaining $R_b = 0.94 \pm 0.09$ (stat. + syst.) and $|V_{tb}| = 0.97 \pm 0.05$ (stat. + syst.); setting a limit of $|V_{tb}| > 0.89$ at 95% C.L. [24]. The first measurement at the LHC was performed by CMS in the dilepton channel at $\sqrt{s} = 7$ TeV [25]. A new measurement at 8 TeV, using 16.7 fb^{-1} of data in the dilepton channel, was released [26], with $R_b = 1.023^{+0.036}_{-0.034}$ (stat. + syst.) and a limit on $|V_{tb}| > 0.972$ at 95% C.L.

Mass

The mass is currently the most precisely measured property of the top quark, but given this high precision some discussion is needed. Since QCD does not predict quarks to exists as free particles, the definition of their masses is not precise and depends on the approach used. The *pole mass*, which is defined as the pole of the normalised top quark propagator, is an intuitive definition of mass of a point-like particle. The pole mass, however, can only be estimated with a precision of several hundred MeV due to so-called infrared renormalons [27]. The previously mentioned $m_t = 172.5$ GeV is interpreted as a pole mass. An alternative is the *on-shell mass* or $\overline{\text{MS}}$ *mass* which is defined by a perturbative approach (minimal subtraction scheme). It is more than 10 GeV lower than the pole mass [28] and can only be measured indirectly, for example extracted from a cross section measurement.

The best result reported by the Tevatron is a combination of CDF and D0 results: $m_t = 174.30 \pm 0.35(\text{stat.}) \pm 0.54(\text{sys.})$ GeV [29]. An overview of LHC results is presented in figure 1.10. The combination of the best results yields for ATLAS $m_t = 172.84 \pm 0.34(\text{stat.}) \pm 0.61(\text{sys.})$ GeV [30] and for CMS $m_t = 172.44 \pm 0.13(\text{stat.}) \pm 0.47(\text{sys.})$ GeV [31]. The majority of top quark mass measurements use the so called “template method", where templates with given theoretical assumption are fitted to data. Therefore, the mass that follows from the simulation used to create the templates is measured. There is some uncertainty between the mass generated in simulation and the pole mass, but the quantitative difference is about 1 GeV [32].

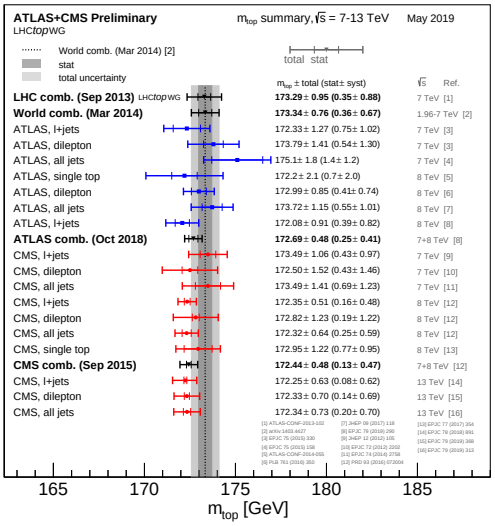

Figure 1.10: Summary of the ATLAS and CMS direct m_t measurements [33].

The top quark mass can also be used to verify the CPT-symmetry. For this purpose the difference between the mass of the top quark and antiquark $\Delta m_t = m_t - m_{\bar{t}}$ is measured. All measurements conducted by experiments at the Tevatron and the LHC do not show any deviation from the standard model predicted value of 0 [34, 35].

Spin correlation

The spin is another top quark property that can be measured indirectly thanks to its extremely short lifetime. Information about the top quark’s spin is accessible because it decays before creating a bound state with other quarks which could change its spin.

Although the top quarks from the top quark pairs production at hadron collisions are not polarised, the spins of top and antitop quarks in a $t\bar{t}$ pair are correlated. The strong interaction conserves parity: If $t\bar{t}$ is produced in quark-antiquark annihilation or gluon-gluon fusion with opposite helicity, t and $\bar{t}$ will have opposite helicities and their spins will be parallel as presented in the upper row of figure 1.11. While for those coming from gluon-gluon fusion with the same helicity, the spins will be antiparallel [36], see figure 1.11 bottom row.

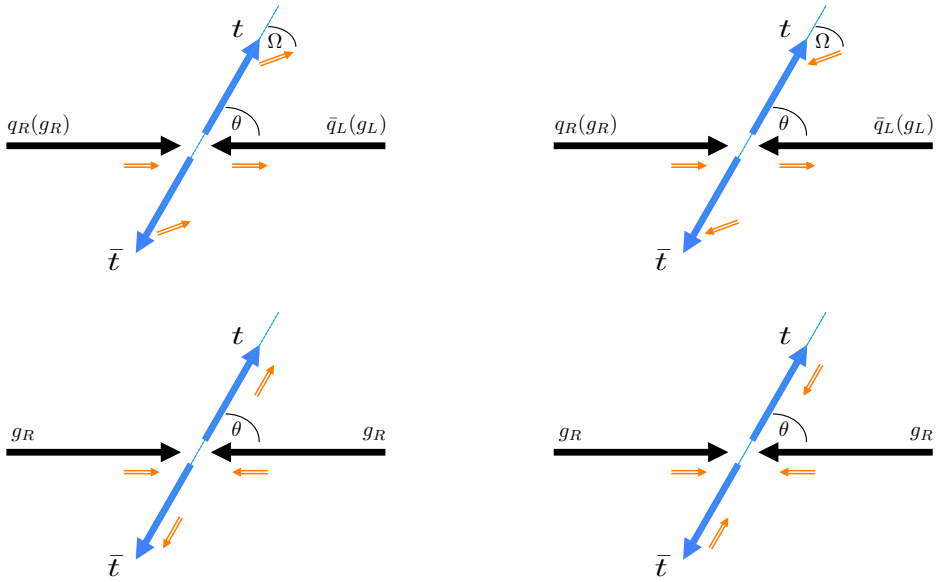

Figure 1.11: $t\bar{t}$ spin configuration in different production modes presented in the so-called off-diagonal basis. Upper row: top quarks are produced from opposite helicity quarks or gluons. The angle Ω depends on the energy of the top quark: $\tan\Omega = (1-\beta^2)\tan\theta$, where θ is the top quark's scattering angle and β it's velocity in the zero momentum frame. At threshold, $\beta \to 0$, $\Omega = \theta$ and the spin is parallel to the beam axis, while for relativistic top quarks $\Omega = 0$ and the spin is aligned with the top quark's momentum. Lower row: the top quark is produced from same helicity gluons. Although the illustration shows only right-handed gluons, the same spin final states will be produced for both right- and left-handed gluons [36].

The top quark spin information is passed to its decay products and there is a 100% correlation between the top quark spin and the angular distribution of the down-type fermion (d-type quark or charged lepton). The following double-differential distribution can be measured in the $t\bar{t}$ dilepton channel [12]

$$\frac{1}{\sigma}\frac{\mathrm{d}\sigma}{\cos\theta_l \cos\theta_{\bar{l}}} = \frac{1}{4}(1 + B_1 \cos\theta_l + B_2 \cos\theta_{\bar{l}} - C\cos\theta_l \cos\theta_{\bar{l}}), \tag{1.20}$$

where θ_l and $\theta_{\bar{l}}$ are the angles of the leptons origination from the t and $\bar{t}$ decay, with respect to the quantisation axis. The coefficients $B_{1,2}$ are related to the top quark polarisation, and since, according to the standard model, $t\bar{t}$ are produced unpolarised, are equal zero.

The hypothesis of no spin correlation between t and $\bar{t}$ was excluded by experiments both at the Tevatron [37] and the LHC [38, 39]. The latest results from ATLAS agree with the SM predictions within 3.2σ [40]. The spin correlation of $t\bar{t}$ could be modified by BSM contributions, such as decay of stop, Z', through Kaluza-Klein gluons or a Higgs boson.

Charge asymmetry

In the standard model the forward-backward asymmetry A_{FB} and charge asymmetry A_{C} are a result of the interference between the Born (figure 1.3 upper row) and box diagrams (figure 1.5 a) in $t\bar{t}$ production through quark-antiquark annihilation, as well as interference between initial and final state radiation diagrams shown in figure 1.5 b) and c).

A top quark created in $q\bar{q}$ annihilation tends to be emitted in the direction of the original quark q, while $\bar{t}$ follows the direction of $\bar{q}$. The asymmetry arises when the top quark flies in the direction of $\bar{q}$, while the top antiquark in the direction of q.

Since the forward-backward asymmetry is present only in the quark-antiquark annihilation production mode, it is only visible at the Tevatron and is predicted to be $(9.5 \pm 0.7)\%$ [41]. Apart from the much smaller expected effect, an additional challenge at the LHC is the identification of the forward and backward direction, as the collisions are symmetric: At the Tevatron the forward direction is simply the direction of the proton beam and the forward-background asymmetry is defined as the difference in the number of measured events with positive and events with negative rapidity difference

$$A_{\mathrm{FB}} = \frac{N(\Delta y > 0) - N(\Delta y < 0)}{N_{\mathrm{total}}}, \tag{1.21}$$

where $\Delta y = y_t - y_{\bar{t}}$. The rapidity y is a measure of the particle's boost and is defined as follows

$$y = \frac{1}{2}\left(\frac{E + p_z}{E - p_z}\right), \tag{1.22}$$

where E is the particle's total energy and p_z is the momentum component along the z-axis.

At the LHC, instead of A_{FB}, the charge asymmetry is used, which is defined as

$$A_{\mathrm{C}} = \frac{N(\Delta|y| > 0) - N(\Delta|y| < 0)}{N_{\mathrm{total}}}. \tag{1.23}$$

Here, $|y|$ is the top-antitop rapidity difference with respect to a specified, but arbitrarily chosen, direction. The A_{C} at the LHC is predicted to be $(1.23 \pm 0.05)\%$ at $\sqrt{s} = 7$ TeV and $(1.11 \pm 0.04)\%$ for 8 TeV [42].

Experimental results are in agreement with the SM predictions, but carry sizable uncertainties. The experiments at the Tevatron measured $A_{\mathrm{FB}} = (12.8 \pm 2.5)\%$ [43]. The experiments at the LHC measured $A_{\mathrm{C}} = 0.005 \pm 0.007(\mathrm{stat.}) \pm 0.006(\mathrm{sys.})$ for $\sqrt{s} = 7$ TeV, while for 8 TeV $A_{\mathrm{C}} = 0.0055 \pm 0.0023(\mathrm{stat.}) \pm 0.0025(\mathrm{sys.})$ [15].

$t\bar{t}$ resonances and $t\bar{t}$ associated production

Experiments at the Tevatron and the LHC are searching for $t\bar{t}$ resonances which would indicate the existence of new massive neutral particles decaying to a top quark pair, such as Z'. So far, however, none of the experiments measured any evidence of resonances in the $t\bar{t}$ spectrum [44].

New particles could also cause an excess of rare top decays or $t\bar{t}$ associated production, where top quark pairs are produced together with other standard model particles. Due to the top quark's coupling to heavy bosons, investigations of processes such as $t\bar{t}Z$, $t\bar{t}H$, $t\bar{t}W$, as well as $t\bar{t}\gamma$, are of highest interest. These processes have a relatively low production cross section and were not accessible at the Tevatron. The experiments at the LHC were able to confirm and observe them, but it's too early to precisely measure their cross sections and identify possible excesses due to the non-SM contributions.

The LO calculations rescaled to NLO predict the cross section of the $t\bar{t}\gamma$ associated production as

$\sigma^{\mathrm{SM}}_{t\bar{t}\gamma} = 48 \pm 10$ fb for $\sqrt{s} = 7$ TeV[6]. ATLAS observed the $t\bar{t}\gamma$ associated production in the 2011 dataset using a binned likelihood template fit [45]. The background-only hypothesis was rejected with a 5.3σ significance. The reported value of the cross section $\sigma_{t\bar{t}\gamma} = 63 \pm 8(\mathrm{stat.})^{+17}_{-13}(\mathrm{syst.}) \pm 1(\mathrm{lumi})$ fb carries a total uncertainty of approximately 30% and is in agreement with the SM prediction.

The $t\bar{t}W$ and $t\bar{t}Z$ production was first observed in the 8 TeV data. The NLO calculations for the standard model predict $\sigma^{\mathrm{SM}}_{t\bar{t}W} = 232 \pm 32$ fb and $\sigma^{\mathrm{SM}}_{t\bar{t}Z} = 215 \pm 30$ fb for this centre-of-mass energy. The cross sections of the $t\bar{t}W$ and $t\bar{t}Z$ processes can be measured together, from a sample consisting of the following signatures: opposite sign dilepton, same sign dilepton, trilepton and tetralepton. ATLAS used a simultaneous maximum likelihood fit and obtained 5.0σ and 4.2σ significance over the background-only hypothesis for $t\bar{t}W$ and $t\bar{t}Z$ respectively [46]. The corresponding measured cross sections are $\sigma_{t\bar{t}W} = 369^{+86}_{-79}(\mathrm{stat.}) \pm 44(\mathrm{syst.})$ fb and $\sigma_{t\bar{t}Z} = 176^{+52}_{-48}(\mathrm{stat.}) \pm 24(\mathrm{syst.})$ fb. CMS analysed the same final states with the help of boosted decision trees and obtained 6.4σ and 4.8σ significance over the background-only hypothesis for $t\bar{t}W$ and $t\bar{t}Z$, respectively [47]. The reported cross sections are $\sigma_{t\bar{t}W} = 382^{+117}_{-102}$ fb and $\sigma_{t\bar{t}Z} = 242^{+65}_{55}$ fb. Values measured by both experiments are in agreement with the SM prediction within the uncertainties.

Finally, both ATLAS and CMS measured the $t\bar{t}H$ associated production by combining results of $t\bar{t}$ associated by $H \to b\bar{b}$, $H \to \gamma\gamma$ $H \to$ leptons[7]. Both experiments used the dataset combining $\sqrt{s} = 7$ TeV, $\sqrt{s} = 8$ TeV and $\sqrt{s} = 13$ TeV data. CMS achieved signal significance of 5.2 standard deviations [48], while ATLAS 6.3σ. ATLAS additionally provided the first measurement of the $t\bar{t}H$ cross section at 13 TeV of $\sigma_{t\bar{t}H} = 670 \pm 90(\mathrm{stat.})^{+110}_{-100}(\mathrm{syst.})$ fb [49]. The measured $\sigma_{t\bar{t}H}$ is in agreement with the standard model next-to-leading-order prediction of 507^{+35}_{-50} fb [50–59].

Measurement of the top quark - Higgs boson coupling plays an important role in the studies of the standard model. It is described by the Yukawa coupling, $y_t = \sqrt{2}m_t/v$ (v is the vacuum expectation value), which for the top quark, because of its large mass, takes value close to the unity [3]. The value of y_t can now be directly measured in the $t\bar{t}H$ events.

Flavour changing neutral current

One of the phenomena that is often searched for in the top quark decays is flavour changing neutral current (FCNC), where a top quark would decay to another up-type quark without emitting an additional electrically charged particle, $t \to Z/H/\gamma/g\ q$, in the case of the standard model version, or to a new particle in the case of BSM models. There was no evidence found yet, but both ATLAS and CMS set limits on the FCNC processes [28]. The most interesting results were found for $t \to qH$, where ATLAS and CMS set upper limits on the branching fraction of 0.22% for $t \to cH$ and 0.24% for $t \to uH$ [60] and CMS set upper limits at 0.47% for both decays [61], while the SM prediction is of the order of $O(10^{-17} - 10^{-15})$. There are several BSM models that predict an excess of the $t \to qH$ events above the standard model predictions [62].

[6] Fiducial cross section within the acceptance of the ATLAS detector [45].
[7] combination of $H \to WW$, $H \to ZZ$ and $H \to \tau\tau$.

CHAPTER 2

Experimental setup

2.1 Large Hadron Collider

The Large Hadron Collider (LHC) is the largest accelerator in the CERN's accelerator complex and currently the most powerful accelerator in the world. It is situated in a 26.7 km long circular tunnel [63] approximately 100 m below the ground. The tunnel was previously occupied by the Large Electron-Positron (LEP) collider, which was decommissioned in 2000. The LHC is a proton-proton collider and its two proton beams travel in opposite directions in two separate beam pipes. The beam pipes cross in four interaction points, around which the detectors are built: ALICE, ATLAS, CMS and LHCb. The locations of interaction points are marked with yellow dots in figure 2.1.

The LHC's huge radius $\rho = 2804$ m [63] requires protons to be pre-accelerated before they can be injected into the LHC. After the protons are obtained from hydrogen gas, they are first accelerated by LINAC 2 to the energy of 5 MeV. From there they travel to the BOOSTER, where their energy is increased to 1.4 GeV. Next, they are passed to the Proton Synchrotron (PS), which they leave with 25 GeV to enter the Super Proton Synchrotron (SPS) and finally, with the energy of 450 GeV [65], they are injected to the LHC. In the LHC, the beam is further accelerated and focused. The LHC is a storage ring. The proton losses during collisions are very small and the same beam can keep colliding for several hours. Each experiment monitors the delivered luminosity, to include beam's changing conditions in the data analysis.

The proton beam at the LHC is not a homogeneous flux of particles. Instead, the protons are grouped in bunches, 1.15×10^{11} protons each [63]. In total, 2808 bunches can be circulating in each beampipe. To keep the high-energy beam in the ring, a very strong magnetic field is needed. The LHC uses superconducting electromagnets, which are kept at a temperature of 1.9 K with liquid helium. The LHC consists in total of 9593 magnets. 1232 of those are the main dipoles, which are responsible for bending the beam's trajectory and keeping it in the ring, and 392 are main quadrupoles – their task is to focus the beam [63]. The transverse RMS beam size varies from $200 - 300$ μm in the ring to 16 μm at the interaction points [12]. The remaining magnets include sextupoles, octupoles, decapoles and they help to optimize beam's trajectory. Additionally, the LHC has 8 radiofrequency cavities per beam, which provide longitudinal electric fields to accelerate the beam and control the longitudinal dimension of the particles bunches. The length of a bunch is approximately 30 cm [63].

The main dipoles can induce a magnetic field of up to 8.33 T, which requires a current of 12 kA [63]. Running at the design power, the LHC is able to accelerate each of the beams to 7 TeV, which results

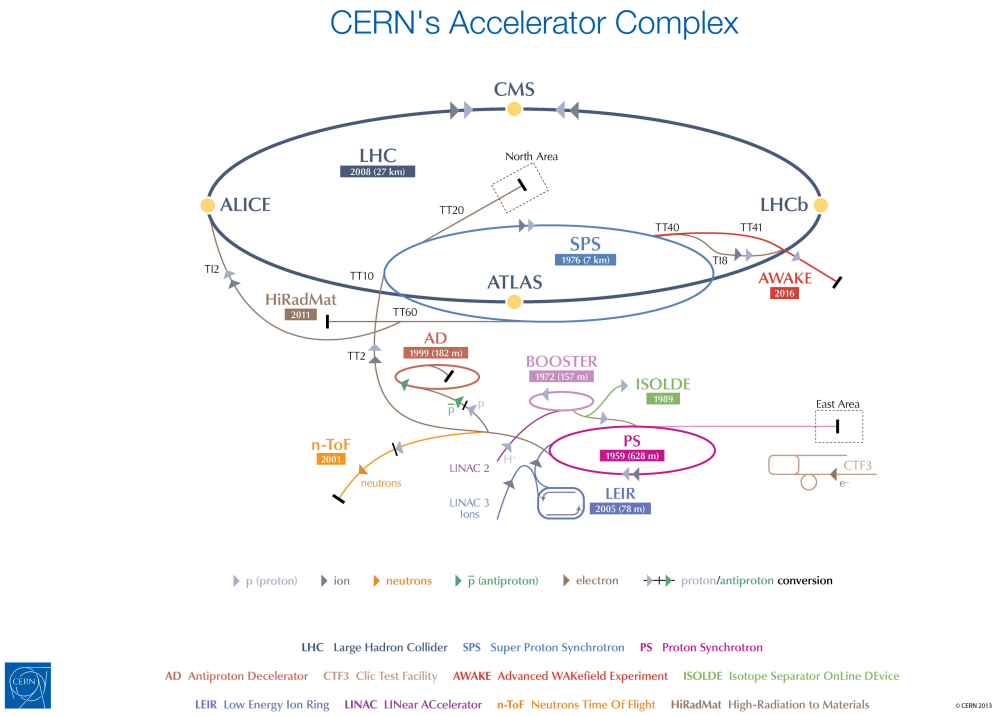

Figure 2.1: CERN's accelerator complex [64].

in collisions at a centre-of-mass energy of $\sqrt{s} = 14$ TeV. However, shortly after the start of the LHC in 2008, an accident occurred: Due to a faulty connection, one of the magnets lost superconductivity, leading to a huge heat release. As a result, helium was heated above its boiling temperature and caused an explosion [66]. After investigating the cause of the accident and repairing the damage, it was decided that the LHC would operate at a point lower than the design energy in its first years. The LHC was re-launched in late 2009 and the experiments began to take data at $\sqrt{s} = 7$ TeV in 2010 and at $\sqrt{s} = 8$ TeV in 2012. In early 2013 the Run 1 ended and the LHC was shut down for a technical upgrade to allow higher beam energies. The Run 2 started in 2015 and lasted until the end of 2018 with collisions at $\sqrt{s} = 13$ TeV.

The reason why the LHC uses protons instead of electrons and positrons, as its predecessor, is the synchrotron radiation U. It is proportional to the fourth power of particle's energy E and reversely proportional to the fourth power of particle's mass m and its trajectory radius ρ:

$$U \propto \frac{E^4}{\rho m^4}. \tag{2.1}$$

At LEP, already with a beam energy of 0.1 TeV, electrons were losing 3% of their energy per turn. In order to achieve higher collisions energy without increasing ρ, heavier particles are necessary. In the LHC at the nominal beam energy of 7 TeV protons lose only about 10^{-7}% of their energy per turn [12].

When colliding two particle beams, it is not possible to influence the type of collisions products, which follow some probability distribution. Additionally, using protons, which are not elementary particles, brings the disadvantage of not exactly knowing the energy of the partons that collided. Therefore, in order to ensure enough amount of data for physics measurements, the LHC was designed to

achieve a higher peak luminosity than LEP – 10^{34} cm^{-2}s^{-1} compared to 10^{32} cm^{-2}s^{-1}, as well as much higher frequency of collisions (LEP used only 4 bunches per beam) [12]. On the other hand, the hadron colliders offer the possibility to scan the entire mass spectrum of collision products and discover unexpected particles.

Apart from protons, the LHC can also collide other hadrons, such as lead ions. The ALICE detector was specially designed to study heavy ion collisions, but the general purpose detectors, ATLAS and CMS, also analyse heavy ion data. Also LHCb, which is equipped with a special forward spectrometer to investigate CP-symmetry violation in decays of the b quark hadrons, takes data during the heavy ion collisions.

2.2 ATLAS detector

ATLAS is a general purpose detector located at one of the interaction regions at the LHC and its name stands for "A Toroidal LHC ApparatuS". General purpose detectors are, as the name suggests, meant to conduct a broad spectrum of measurements. They are not designed to measure a specific type of particles or phenomena and their design should allow detection of all kinds of known and predicted particles, as well as enable broad scanning of mass and energy spectra.

It is of fundamental importance for general purpose detectors to precisely determine quantities such as the position of the interaction point (primary vertex), position of the decay of the primary products (secondary vertex), charge, mass, and energy (momentum) of the particles. It is also crucial to capture all produced particles and measure the total energy of the collision. Therefore, the detector should cover as large a solid angle as possible around the interaction point. In practice, this is achieved with a cylindrical design. As shown in figure 2.2, the cylinder, the so-called *barrel*, is aligned with the beamline with its centre in the beam crossing point and is closed with *end caps* perpendicular to the beamline, which are built with similar detector material as the barrel. Using end caps improves the precision of measurement of particles travelling at small angles with respect to the beamline, because it limits the amount of material they are traversing, which makes the detector more compact and cost effective.

In the right-handed ATLAS coordinate system the x axis points towards the centre of the LHC ring, the y axis points up and the z axis is aligned with the beamline as presented in figure 2.2. The azimuthal angle ϕ is measured with respect to the x axis and the polar angle θ is measured with respect to the LHC beamline. The pseudorapidity η is defined as $\eta = -\ln[\tan(\theta/2)]$.

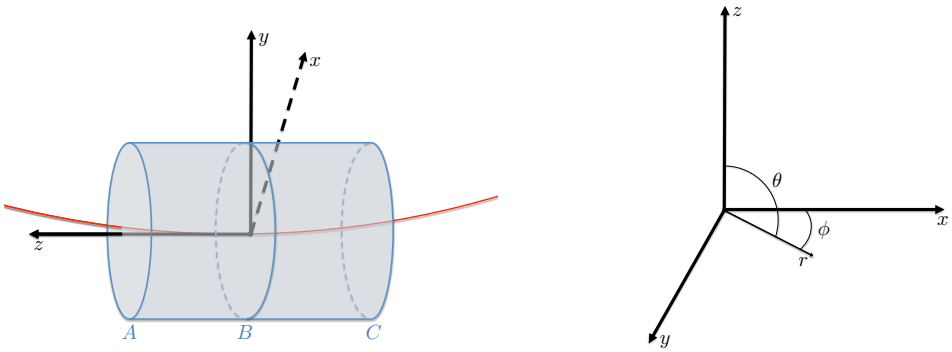

Figure 2.2: Coordinate frame of the ATLAS detector.

The ATLAS detector is 44 m long, 25 m high and weighs approximately 7000 t [67]. The measurement of each of the particle properties requires application of a different technology and thus a dedicated

subdetector. The main ATLAS detector components are:

- Inner detector – measures trajectories of charged particles, position of primary and secondary vertices and is used in the momentum and charge determination.
- Calorimeter – measures predominantly the energy, but also the direction of particles. It consists of two layers, the electromagnetic calorimeter measures energy deposited by particles interacting electromagnetically, the hadronic calorimeter measures energy deposited in hadronic interactions.
- Muon spectrometer – detects charged particles escaping other ATLAS detectors (mostly muons).
- Magnets – bend trajectories of charged particles which allows for their charge sign and momentum determination.
- Forward detectors – measure parameters of the beam around the ATLAS detector.

Magnets do not conduct any measurement, however, the magnetic field is crucial for the measurement performed by the inner detector and muon spectrometer. The subdetectors and principle of measurement of various types of particles are sketched in figure 2.3. The setup of the ATLAS components is presented in figure 2.4. Details of the subdetectors will be discussed in the next section.

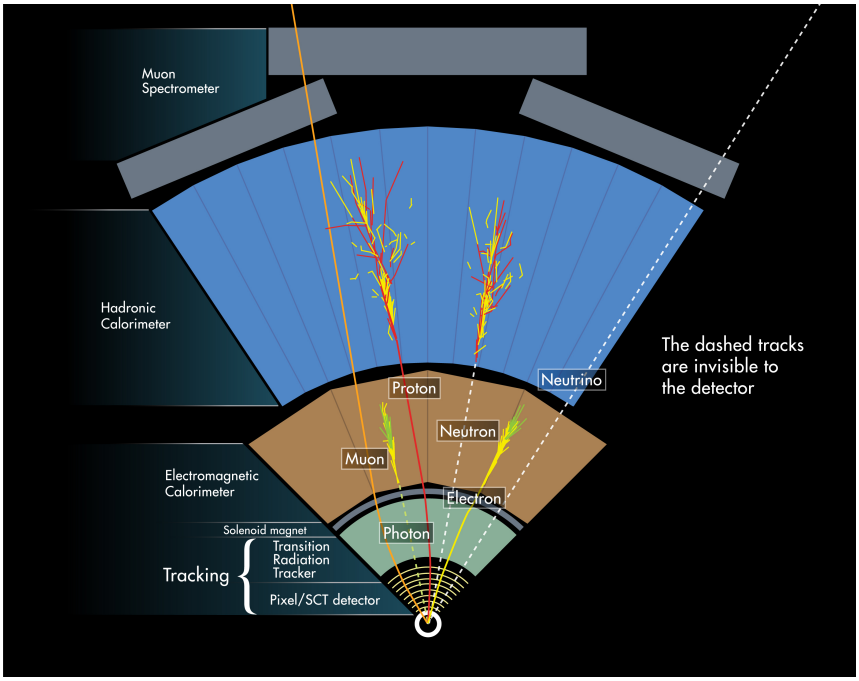

Figure 2.3: Principles of particles detection in the ATLAS detector [68].

The collision events are often analysed in the plane transverse to the beam axis. The transverse momentum and energy are defined as $p_T = p \sin\theta$ and $E_T = E \sin\theta$. The exact energy of the colliding particles in the hadron colliders is not known, but the momentum of the protons in the transverse plane is equal to 0. The conservation law implies that the vector sum of p_T of all product particles should be 0, too. Any deficit of p_T is interpreted as the energy carried away by invisible particles, like the neutrino marked in figure 2.3. Because of the way they are measured, transverse momentum and energy of

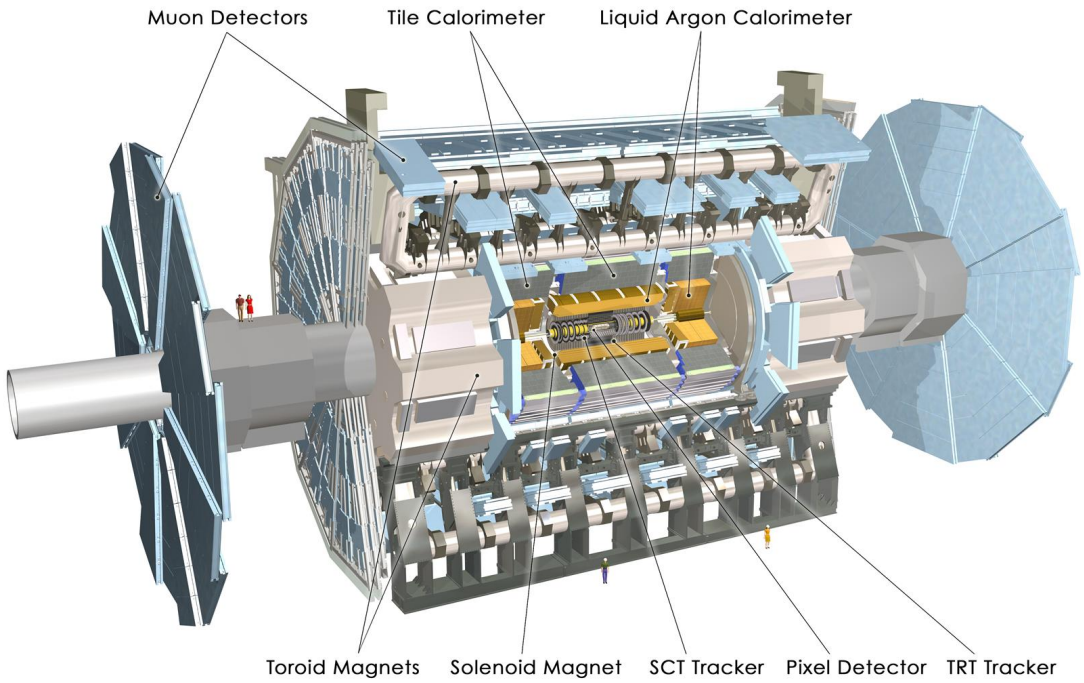

Figure 2.4: Main components of the ATLAS detector [69].

invisible particles are called *missing transverse momentum* and *missing transverse energy* and denoted as p_{T}^{miss} and $E_{\mathrm{T}}^{\mathrm{miss}}$.

When all of the 2808 bunches are filled in each beam, the bunches collide every 25 ns, which corresponds to a frequency of 40 MHz. On average, with nominal LHC performance there are 20 interaction per bunch collision, which leads to over 1000 high-energy particles crossing the detector [12]. This puts very stringent requirements on the read-out electronics and signal transmission outside of the detector. They should be fast, resistant to high radiation and use as little material as possible in order not to bias the measurements.

It is impossible and unnecessary to store data of each collision. The main limiting factors are the signal processing speed and available physical storage. However, interesting physics processes do not appear in every collision either. The trigger system, described in section 2.2.2, selects promising events in real time and allows reduction of the rate of stored events to 200 Hz [67]. Those events are then processed and reconstructed by offline algorithms and are made available for physics analysis. Considering that the detectors can record hundreds of hours of collisions every year, there is a very high demand on computing power to process, reconstruct, analyse and also generate a high number of simulated events for numerous physics processes (the simulation methods used for ATLAS are described in section 2.3). Therefore, CERN developed ROOT, a dedicated software framework addressing all the needs of high energy particle physics data analysis and created a new computing solution: Worldwide LHC computing grid – a complex distributed computing network. Their principles are described in section 2.4 and 2.5.

2.2.1 Subdetectors

This section provides an overview of the components of the ATLAS detector and a description of the principles of the measurements which they perform. Particular attention is paid to the intrinsic accuracy

of the detectors and aspects of their geometry and technology that introduce limitations to the top quark branching ratio measurement. The entire section 2.2.1 is based on the ATLAS design and performance report [67] and focuses on the design of the detector during the LHC Run 1 (2010-2012), unless stated otherwise.

Inner detector

The main role of the inner detector (ID) is to measure trajectories of charged particles. The trajectories are used to reconstruct primary and secondary vertices, as well as to measure charge and momentum of particles. The ID is able to measure tracks with $p_{\mathrm{T}} > 0.5\,\mathrm{GeV}$ and $|\eta| < 2.5$. The ID is also used for identification of electrons with $0.5\,\mathrm{GeV} < p_{\mathrm{T}} < 150\,\mathrm{GeV}$ and $|\eta| < 2$. The inner detector consists of three subdetectors. The first one counting from the beampipe is the Pixel Detector (Pixel), followed by the Semi-Conductor Tracker (SCT) and finally, the Transition Radiation Tracker (TRT). The alignment and space coverage of the subdetectors is presented in figure 2.5. Table 2.1 provides details of the measurement- relevant quantities: the η coverage of the subdetectors and the type and size of their sensors, as well as their intrinsic accuracy. The η coverage of the ID defines the area of the high resolution measurement and influences the distribution of resolution of other ATLAS components.

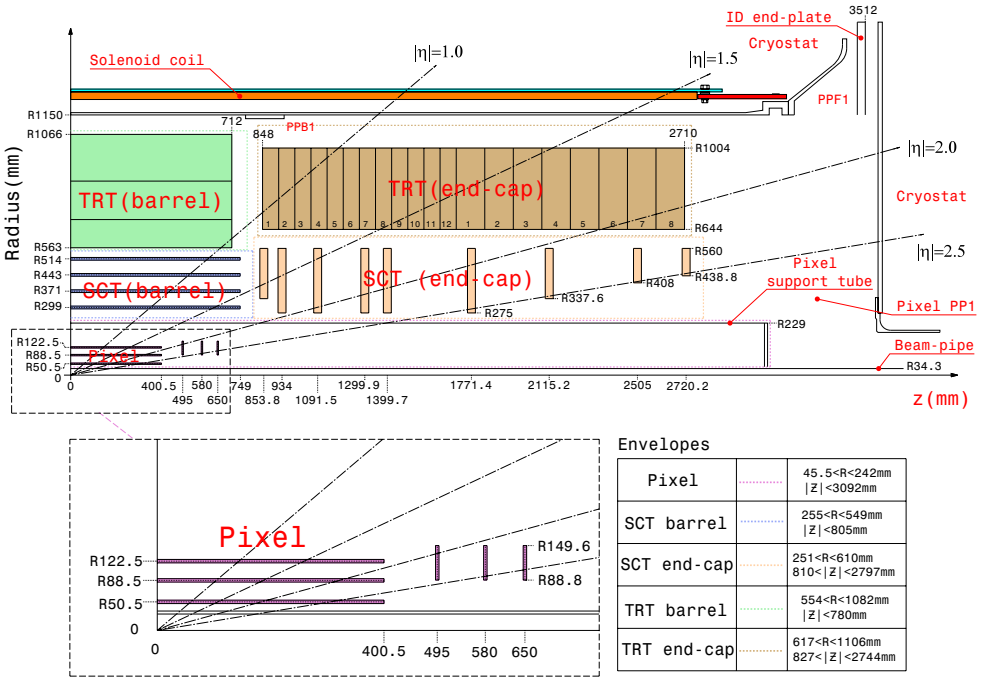

Figure 2.5: Alignment of the components of the inner detector [67].

The beampipe is integrated within the ID. It is sealed hermetically to maintain the ultra-high vacuum inside. In the LHC ring the beampipe is made of austenitic stainless steel. The section around the interaction point in the ATLAS detector is made of 0.8 mm thick beryllium foil. Beryllium was chosen as the building material, because it is stiff enough to withstand forces created by the vacuum and at the same time it has a very low density and is almost transparent for traversing high energy particles.

Pixel and the SCT use pn-junction semiconductor sensors operated in reverse bias mode. Semiconductor sensors ensure excellent resolution, high sensitivity to charged particles and fast signal transport and collection. However, semiconductors are sensitive to radiation. The sensor's leakage current, which

causes measurement noise, increases linearly with the absorbed integrated radiation dose. Therefore, to keep a significant depletion depth, the bias voltage is increased with time. Additionally, since the leakage current decreases in low temperature, both Pixel and SCT operate at a temperature between −5 and −10°C.

The exact layout and manufacturing technique of Pixel and the SCT differ due to their different distances from the interaction point and therefore different particle flux and expected hit rate. Pixel consists of three layers in the barrel area and three layers in end caps, placed in such a way that each particle traversing the detector volume, crosses at least three layers, which is illustrated in figure 2.5. Pixel sensors are built of n-type oxygenated silicon wafer with an n^+-type implant. As a result of the radiation, the n-type silicon becomes p-type in the course of separation. In comparison with a standard pn-junction layout, the oxygenated silicon is more resistant to damage caused by charged hadrons and the n^+-type material provides a better charge collection. The rectangular readout pixels define the size of the detector's segmentation. They are located on the implant side and are segmented in $(R-\phi)\times z$ ($(R-\phi)\times R$ in end caps). In total, Pixel has approximately 80.4 million readout channels.

	η coverage	Segmentation type and size	Detector intrinsic accuracy [μm]
Pixel	$0 < \lvert\eta\rvert < 2.5$	Pixel	
Barrel		$50 \times 400\ \mu\text{m}^2$	$10(R-\phi)$, $115(z)$
End cap			$10(R-\phi)$, $115(R)$
SCT	$0 < \lvert\eta\rvert < 2.5$	Microstrip	
Barrel		$O(10\ \mu\text{m}) \times O(\text{cm})$	$17(R-\phi)$, $580(z)$
End cap			$17(R-\phi)$, $580(R)$
TRT	$0 < \lvert\eta\rvert < 2.0$	Straw tube	
Barrel		$\varnothing 4$ mm × 144 cm(z)	$130(R-\phi)$
End cap		$\varnothing 4$ mm × 37 cm(z)	$130(R-\phi)$

Table 2.1: Coverage of sensitive layers of the components of the inner detector, their intrinsic accuracy and details of their segmentation [67].

Since the particle flux reaching the SCT detector is lower, the hit rate per unit area is smaller and the segmentation can be larger without risking to saturate the readout channels. The SCT segmentation in the barrel region is an extremely narrow strip of width in the order of several tens of μm and length of 6.4 cm. In end caps, the sensors have a trapezoidal shape and their size varies depending on the position. The distance between sensor strips (pitch) is equal $\approx 80\ \mu m$ both in barrel and end cap. The SCT sensors use a standard p-in-n technology. SCT consists of 4 layers in the barrel and 9 in the end caps. On average, each track crosses 4 SCT layers. Each layer consists of two stereo strips mounted back to back and rotated by an angle of 40 mrad with respect to each other in order to provide a measurement in two dimensions. The SCT has in total 6.3 million readout channels.

The TRT uses a different principle than Pixel and SCT. It is build of straw tubes filled with a $Xe/CO_2/O_2$ gas mixture. High energy particles traversing the TRT tubes ionise the gas inside. The generated current is measured by a wire-anode located in the centre of the straw tube. The tube's wall plays the role of the cathode. Unlike Pixel and SCT, TRT provides a measurement in only one dimension: $(R-\phi)$.

To avoid pollution of the gas inside the straw tubes, the TRT modules are placed in a CO_2 envelope. The constantly circulating gas also helps to transport heat outside of the detector – TRT requires room temperature for optimal operation. On average, each particle crosses 36 tubes, which gives an

almost continuous tracking. This feature of the TRT detector makes it a key component of the electron identification procedure which is discussed in section 3.1.

Calorimeters

Calorimeters measure the energy of particles by completely stopping them and absorbing their energy. The way how the particles lose the energy depends on their properties. Those interacting electromagnetically, i.e. photons and charged particles, lose energy through ionisation of the matter they are travelling in. In the case of high energy photons travelling through matter, a spontaneous electron-positron pair production can occur. Its probability is proportional to photon's energy and the square of atomic number of the involved atom [12]. Charged particles can additionally lose energy through bremsstrahlung (photon radiation caused by deceleration in the electric field of atoms). Bremsstrahlung is in fact significant only for light particles like electrons, because its cross section is proportional to $1/m^2$ [12]. It is a similar effect to the synchrotron radiation discussed in section 2.1. The photons originating from bremsstrahlung, can produce an electron-positron pair, if their energy is high enough. After the electron reaches a specific limit energy, the ionisation takes over until all particles are absorbed.

Bremsstrahlung together with e^-e^+ pair production from photons cause creation of electromagnetic showers. Their size is characterised by the radiation length X_0 – mean path after which the particles energy decreases by a factor of $1/e$ [12]. In a simple approximation, the number of particles in electromagnetic shower doubles and their energy decrease by a half every radiation length.

Partons, independently of their charge, lose energy mainly through inelastic interaction with the nucleus of the atoms. Charged hadrons lose energy through ionisation too, but these are not as significant losses as for the light particles. Also the effects of bremsstrahlung are negligible due to their large mass. Nuclear interaction causes creation of hadronic cascades. Due to a bigger variety of underlying physics processes, they are more complex and more diverse than electromagnetic showers. They tend to have a higher number of particles produced in a single interaction, but fewer "generations" and as a result, smaller total number of particles [12]. If electrons are produced in hadronic cascades, they can start electromagnetic showers. Hadronic cascades are characterised by nuclear interaction length λ which is the mean distance travelled by a hadronic particle between nuclear interactions. The hadronic particle showers created in the calorimeter by partons are reconstructed in so called *jets*.

Because of different mechanisms of energy loss for electromagnetically and hadronically interacting particles, they require the application of different technologies. The calorimeter system of the ATLAS detector is divided into an electromagnetic calorimeter and a hadronic calorimeter. Although made of different materials, they apply a similar measurement technique. Both electromagnetic and hadronic calorimeters are sampling calorimeters consisting of interleaved layers of absorber and active medium. The absorber is made of dense material that triggers the electromagnetic shower or hadronic cascades. Some of the products will reach the active layer and produce a signal: produce light if the active material is a scintillator or ionise the medium. This means that only a fraction of the original particle's energy is measured and the rest is lost in the absorber. The sampling fraction can be calculated from the fraction of energy loss of a so called *minimum ionising particle* [12], for example a muon.

The ATLAS calorimeter system consists of the following components: Liquid Argon Electromagnetic Calorimeter (EM Calo), Liquid Argon End Cap Hadronic Calorimeter (HEC), Liquid Argon Forward Calorimeter (FCalo) and Hadronic Scintillator Tile Calorimeter (Tile). The whole calorimeter system covers the space of $|\eta| < 4.9$, the alignment of calorimeters and the coverage of each individual component is sketched in figure 2.6.

Liquid argon (LAr) was chosen as the active medium for most of the ATLAS calorimeters, because it has an intrinsic linear behaviour, guarantees a stable response over time and is radiation resistant. All

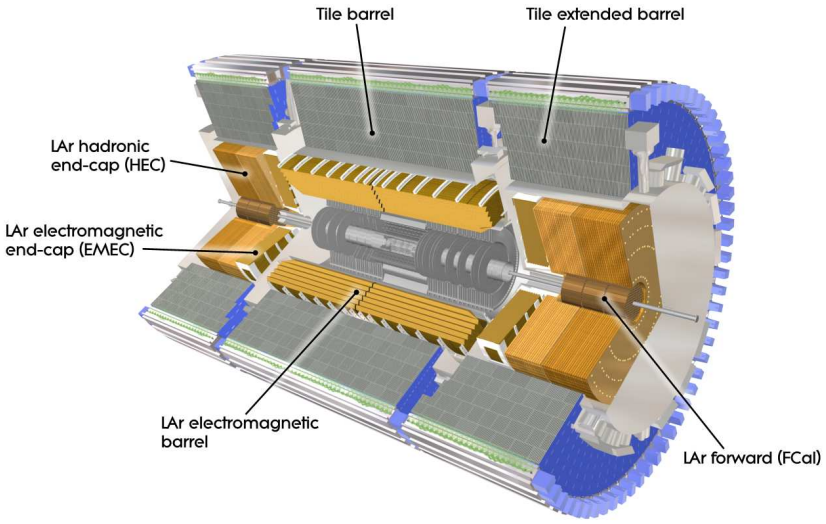

Figure 2.6: Alignment of the components of the calorimeters system [67].

liquid argon detectors require a cooling system to keep the argon liquid. To minimise the amount of non-active material in the measurement region, all end cap calorimeters share one cryostat (one per end cap). The EM Calo in the barrel region shares the cryostat and vacuum vessel only with the central solenoid magnet. The cryostats use liquid helium as coolant.

The EM Calo uses lead plates as absorber and liquid argon as active medium. Kapton electrodes are used to collect the signal. To maximise the active surface, the absorber plates and the electrodes have an accordion shape. Such a layout has a full symmetry with respect to ϕ without azimuthal cracks and allows for a hermetic coverage around the beampipe. The EM Calo is divided into barrel and two end caps modules, they have a depth of at least 22 X_0 and 24 X_0 respectively. The granularity of EM Calo and the number of layers and thickness of the absorber plates depend on $|\eta|$. It achieves the best resolution in the precision measurement region of $|\eta| < 2.5$ defined by the coverage of the inner detector to address the stringent requirements of photon and electron identification, which is discussed in detail in section 3.1. The calorimeter cells are bigger outside this region, but they still provide an excellent precision for jet energy and $E_{\mathrm{T}}^{\mathrm{miss}}$ estimation. In the barrel region, EM Calo consists of three layers of different cell size in the high precision area and two layers outside it or in the area overlapping with the end cap EM Calo discs. Similarly, the EM Calo end caps (EMEC) are built of two or three layers with varying granularity depending on $|\eta|$. The size of the calorimeter cells in all LAr calorimeters depend on the size of the readout electrodes and are listed in table 2.2.

To correct for the energy lost by the particles before reaching the calorimeter, EM Calo is equipped in an additional liquid argon layer called presampler both in the barrel region and in the end caps. It covers the region of $|\eta| < 1.8$ and allows to detect whether an electromagnetic shower started before reaching the first layer of the absorber.

The HEC calorimeter is placed directly behind the EMEC in the end cap region. HEC uses a flat-plate design. Its absorber plates are made of copper and the active medium is liquid argon. It consists of two wheels per end cap and each wheel has two layers. The size of the readout cells depends on the layer and $|\eta|$ and is described in table 2.2.

The FCal is designed to capture both electromagnetic showers and hadronic cascades. Its three modules in the front are optimised for electromagnetic interactions and use copper as absorber. The latter

		η coverage	Unit sensor type and size $[\Delta\eta \times \Delta\phi]$	
EM Calo presampler			Cell	
Barrel				
	1. layer	$0 < \lvert\eta\rvert < 1.52$	0.025×0.1	
End cap				
	1. layer	$1.5 < \lvert\eta\rvert < 1.8$	0.025×0.1	
EM Calo			Cell	
Barrel				
	1. layer	$0 < \lvert\eta\rvert < 1.475$	$0.025/8 \times 0.1$	$\lvert\eta\rvert < 1.40$
			0.025×0.025	$1.40 < \lvert\eta\rvert < 1.475$
	2. layer	$0 < \lvert\eta\rvert < 1.475$	0.025×0.025	$\lvert\eta\rvert < 1.40$
			0.075×0.025	$1.40 < \lvert\eta\rvert < 1.475$
	3. layer	$0 < \lvert\eta\rvert < 1.35$	0.050×0.025	
End cap				
	1. layer	$1.375 < \lvert\eta\rvert < 3.2$	$0.025/8 \times 0.1$ to 0.1×0.1 depending on $\lvert\eta\rvert$	
	2. layer	$1.375 < \lvert\eta\rvert < 3.2$	0.050×0.025	$1.375 < \lvert\eta\rvert < 1.425$
			0.025×0.025	$1.425 < \lvert\eta\rvert < 2.5$
			0.1×0.1	$2.5 < \lvert\eta\rvert < 3.2$
	3. layer	$1.5 < \lvert\eta\rvert < 2.5$	0.050×0.025	
HEC			Cell	
End cap				
	(4 layers)	$1.5 < \lvert\eta\rvert < 3.2$	0.1×0.1	$1.5 < \lvert\eta\rvert < 2.5$
			0.2×0.2	$2.5 < \lvert\eta\rvert < 3.2$
FCal			Cell	
End cap				
	FCal1	$3.10 < \lvert\eta\rvert < 4.83$	3.0×2.6	$3.15 < \lvert\eta\rvert < 4.30$
			and approx. 4× finer outside	
	FCal2	$3.2 < \lvert\eta\rvert < 4.81$	3.3×4.2	$3.24 < \lvert\eta\rvert < 4.50$
			and approx. 4× finer outside	
	FCal3	$3.29 < \lvert\eta\rvert < 4.75$	5.4×4.7	$3.32 < \lvert\eta\rvert < 4.60$
			and approx. 4× finer outside	
Tile			Scintillator tile	
Barrel				
	1. & 2. layer	$0 < \lvert\eta\rvert < 1.0$	0.1×0.1	
	3. layer	$0 < \lvert\eta\rvert < 1.0$	0.2×0.1	
Extended barrel				
	1. & 2. layer	$0.8 < \lvert\eta\rvert < 1.7$	0.1×0.1	
	3. layer	$0.8 < \lvert\eta\rvert < 1.7$	0.2×0.1	

Table 2.2: Coverage of sensitive layers of the components of the calorimeters system and details of their unit sensor [67].

two modules are devoted to hadronic interactions and use tungsten plates. Both parts use liquid argon as active medium. FCal is placed directly around the beampipe, just centimeters from the beam axis and is exposed to a high particle flux. To reduce the albedo effect in the inner detector region, FCal is moved away from the interaction point by 1.2 m with respect to the EMEC front surface. The thickness of FCal

is approx. 10λ.

The Tile calorimeter uses steel for absorber plates and scintillator tiles as active medium. Optic fibres are used to connect the scintillator cells with photomultipliers. The size of the cells depends on the position in the detector and is described in table 2.2. The Tile calorimeter is divided into a central barrel ($|\eta| < 1.0$) and two extended barrels ($0.8 < |\eta| < 1.7$). The thickness of the Tile calorimeter corresponds to approximately 7.4λ. The thickness of the entire calorimeter system, including the electromagnetic calorimeter, is approximately 10λ in both barrel and end caps regions. This is enough to absorb the hadronic cascades and prevent most of them from reaching the muon system.

There is a gap between the barrel and end cap calorimeters to route the readout cables, power supply and other services to the inner detector and the EM Calo. To improve energy measurement in this transition region, some additional scintillator tiles were installed in the gap: Plug Tile Calorimeter, Gap Scintillator and Cryostat Scintillator. They provide additional coverage of the calorimeter system and help to reduce the punch-through of particles into the muon system. They are also used to correct for energy lost in the non-active material in the transition region and cryostats.

The accuracy of the components of the calorimeters system was estimated experimentally with a test-beam. The results for electron beam are summarised in table 2.3.

	$\sigma(E)/E$	Energy range [GeV]
EM Calo	$\frac{(10.1\pm0.4)\%}{\sqrt{E}} \oplus (0.2 \pm 0.1)\%$	10-245
HEC	$\frac{(21.4\pm0.1)\%}{\sqrt{E}}$	10-200
FCal	$\frac{(28.5\pm1.0)\%}{\sqrt{E}} \oplus (3.5 \pm 0.1)\%$	10-200

Table 2.3: Measured electrons energy resolution [67].

The resolution of the Tile calorimeter was measured using a hadron beam with energies 20-180 GeV. The measured value yields $\sigma(E)/E = \frac{(56.4\pm0.4)\%}{\sqrt{E}} \oplus (5.5 \pm 0.1)\%$. The resolution of Tile calorimeter depends significantly on η, which is in detail discussed in [67].

Magnets

When charged particles move in the magnetic field, the Lorentz force plays the role of centripetal force. The following equation allows to obtain the particles charge and calculate the energy based on the measurement of the direction of bending of the trajectory and its radius

$$|\vec{F}| = |q\vec{v} \times \vec{B}| = \frac{m \cdot v^2}{r} \tag{2.2}$$

The magnetic field in the inner detector region is generated by the solenoid magnet placed right behind it, as marked in figure 2.3. Further three toroid magnets are placed behind the calorimeters around the muon systems. All ATLAS magnets use superconducting coils to produce strong magnetic field and therefore operate in low temperatures. They are placed in cryostats inside vacuum vessels and use liquid helium as coolant. Vacuum provides an isolation of the system. In the case of a quench, the energy is absorbed by the cold mass of the cryostats. The entire ATLAS magnet system defines the detector's huge size: the outer radius of the magnet system is 22 m and its length is 26 m.

The solenoid is aligned with the beam axis and produces a 2 T axial magnetic field in the inner detector. It has an inner diameter of 2.46 m, is 10 cm thick and almost 6 m long. As mentioned previously, it shares the vacuum vessel and cryostat with the EM Calo barrel.

Each of the toroid magnets consists of 8 coils. In the barrel region each of the coils has a separate vacuum vessel and cryostat. The coils of the end cap toroid are integrated into a single cold mass. The system of three toroids has an inner diameter of 9.4 m, outer diameter of 20.1 m and is over 25 m long. The toroid magnets produce a 0.5 T magnetic field in barrel region $|\eta| < 1.4$ and 1 T in the end caps $1.6 < |\eta| < 2.7$. The field is orthogonal to the expected muon tracks in most of the space. The end cap toroids are rotated by 22° with respect to the barrel toroid to optimise the magnetic field in the transition region. They are a key element in the muon measurements, bending their trajectories measured by the detectors of the muon spectrometer.

Since the magnetic field, especially in the muon spectrometer, is highly non-uniform, a precise field map can be determined only through a measurement. The magnetic field inside the inner detector was measured before the inner detector was mounted and is now monitored by permanently installed NMR probes. Similarly, there are also Hall sensors present in the muon system. Their measurements are used to correct the simulation.

The total magnetic field is calculated as a superposition of the Biot-Savart contributions from all magnets with contributions and perturbations caused by the detector components. The bending power of magnets is expressed as $\int B_n dl$, where B_n is the component normal (perpendicular) to the particle's trajectory. It reaches values of $1.5 - 5.5$ Tm in the barrel region and $1.0 - 7.5$ Tm in end caps, but it can go down to almost 0 in the transition region.

Muon spectrometer

Muons, being 200 times heavier than electrons, do not experience significant energy losses from bremsstrahlung and lose energy mainly through ionisation. Neither electromagnetic, nor hadronic calorimeter has enough material to stop them completely and they escape the detector carrying a portion of the energy from the collision. For the correct estimation of the missing energy, it is essential to precisely measure the energy of the escaping muons. Therefore, ATLAS is equipped with a complex spectrometer system designed to detect charged particles outside of the calorimeter. It consists of 4 subdetectors: Monitored Drift Tubes (MDT), Cathode Strip Chambers (CSC), Thin Gap Chambers (TGC) and Resistive-plate Chambers (RPC). The components of the muon spectrometer system are marked in figure 2.7 and details of their sensor sizes and accuracy are provided in table 2.4.

The main task of the MDT and CSC is precision tracking used for reconstruction of muons tracks deflected in the magnetic field of the toroid magnet. The MDT measures position only in η (variable in the bending plane), while CSC can also measure ϕ. TGC and RPC provide input to the trigger system to quickly identify events with high energy muons and they make a complementary measurement of η and ϕ. The TGC are also used for the bunch-crossing identification. The muon spectrometer can be used alone for tracking or combined with the inner detector. The muon spectrometer stand-alone momentum measurement has an uncertainty of about 10% for tracks of 1 TeV and it can reliably measure the p_{T} in the range down to few GeV. The measurements in the bending plane from the precision-tracking chambers are matched with those from trigger chambers to obtain the value of the second coordinate. In case there are more tracks crossing a given pair of tracking and trigger chambers, the matching is extended to tracks from the inner detector.

The MDT consists of three layers both in barrel region and end caps. Similarly to the components of the inner detector, it takes the form of a cylinder in the barrel and discs in end caps. Both in barrel and in end caps, each layer consist of partially overlaying chambers. This layout allows to maximise the

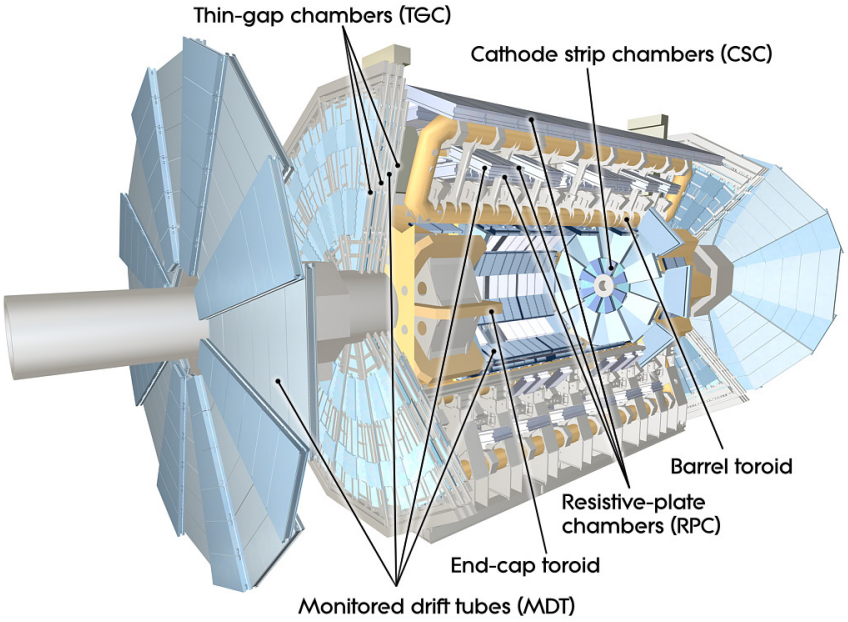

Figure 2.7: Alignment of the components of the muon spectrometer system and the coils of the toroid magnets [67].

	η coverage	Segmentation type and size	Detector intrinsic accuracy
MDT	$0 < \lvert\eta\rvert < 2.7$	Tube $\varnothing$ 29.970 mm × 1-6 m	35 μm(z)
CSC End cap	$2.0 < \lvert\eta\rvert < 2.7$	Strip 5.31 mm(η)× 21 mm(ϕ) or 5.56 mm(η)× 12.92 mm(ϕ)	40 μm(R), 5 mm(ϕ)
RPC Barrel	$0 < \lvert\eta\rvert < 1.05$	Strip 23-35 mm (η, ϕ)	10 mm(z), 10 mm(ϕ)
TGC End cap	$0 < \lvert\eta\rvert < 2.7$ (tracking) $0 < \lvert\eta\rvert < 2.4$ (trigger)	Strip 10.8-55.8 mm(η)× 2-3 mrad(ϕ)	2-6 mm(R), 3-7 mm(ϕ)

Table 2.4: Coverage of sensitive layers of the components of the muon spectrometer system and details of their segmentation [67]. The η and ϕ in the unit sensor size column denote the sizes in the bending and non-bending planes. In the case of strips, size refers to the size of pitch.

coverage and to control the relative alignment of the chambers by following tracks passing overlaying chambers.

In the barrel region, MDT chambers are placed in-between and on top of the toroid coils approximately 5 m, 7.5 m and 10 m from the beam axis. The cylinders have a $1 - 2$ m gap around $|\eta| = 0$ to allow for access to deeper layers of the detector. In the end caps, the MDT chambers are placed in front of and behind the toroid: 7.4 m, 14 m and 21.5 m from the interaction point. Additionally, there is an extra disc around the end caps toroid at $|z| = 10.8$ m.

Each chamber contains 3-8 layers of drift tubes. Their principle of operation is similar to TRT. The

tubes are filled with Ar/CO_2 gas mixture under pressure of 3 bars. In the centre of the tube there is tungsten-rhenium wire anode which collects electrons from the gas ionisation. On average, a particle traversing the muon spectrometer crosses 20 MDT tubes.

The MDT is replaced by the CSC in the first disc in the end caps for $2.0 < |\eta| < 2.7$, where the highest particle flux is expected. CSC is built of multiwire proportional chambers and is faster than MDT and therefore able to handle a higher hit rate. Similarly to MDT, CSC chambers are filled with Ar/CO_2 gas mixture. The CSC uses 2 sets of cathodes: Perpendicular to the wires for precision measurement and parallel to the wires for the second coordinate. The measurement is done by interpolating the charge collected by neighbouring cathode strips. CSC makes on average 4 measurements per track.

Trigger chambers deliver information within a fraction of a nanosecond after the passage of a particle. Their goal is to estimate the number and energy range of the detected particles. RPC is used in the barrel region and TGC in the end caps. RPC is a gaseous parallel electrode-plate detector. It is filled with $C_2H_2F_4/\text{Iso}{-}C_4H_{10}/SF_6$ gas mixture and its principle of measurement is similar to CSC, but it uses plates instead of wires. RPC has three layers and provides 6 measurements per track.

TGC consist of 4 discs: one in front of the toroid magnet and three behind it. The three latter layers are outside of the magnetic field of the toroid where tracks are less bent, which makes the momentum measurement more challenging and a higher granularity than in the case of RPC is necessary. Additionally, the particle flux in this region is expected to be higher than in barrel. Therefore, TGC uses the same multiwire proportional chambers technology as CSC, but with $CO_2/\text{n} - C_5H_{12}$ gas mixture. On average, TGC makes 9 measurements per track.

A very precise mechanical assembly and alignment monitoring of muon chambers is required to ensure the high precision of muon tracking. Muon chambers are equipped in sensors monitoring their position and deformation due to gravity and temperature. The MDT chambers in barrel region are equipped with sag-adjustment system, which allows to correct chambers geometry even after the assembly of the detector.

Forward detectors

ATLAS is equipped with three subdetectors to measure the parameters of the beam. LUCID (LUminosity measurement using Cerenkov Integrating Detector) is an online luminosity monitor placed ±17 m from the interaction point and measuring the inelastic pp scattering. Another luminosity detector is ALFA (Absolute Luminosity For ATLAS), placed ±240 m from the interaction point. ALFA uses scintillating fibre trackers which are placed in movable Roman pots which can be moved as close as 1 mm to the beam. ZDC (Zero-Degree Calorimeter), placed ±140 m from the interaction point, is used to measure the position of the heavy ion beam.

2.2.2 Trigger system

The trigger is a real-time decision system. Its task is to recognize and capture events with interesting signatures, which leads to the reduction of the recorded data volume. The ATLAS trigger is designed to select events with high-energy leptons, jets, high total transverse energy or significant missing energy.

Considering the unprecedented frequency of the LHC collisions and storage limitations, the trigger system has to be extremely fast. Therefore, it uses only partial data from the detector to make a decision. The trigger system consist of the following components, which are schematically presented in figure 2.8:

- Level 1 (L1) – is a hardware-based trigger implemented in electronics and firmware. It receives signal from the calorimeters and muon spectrometer and defines *Regions of Interest* (RoI). It reduces the event rate to below 75 kHz.

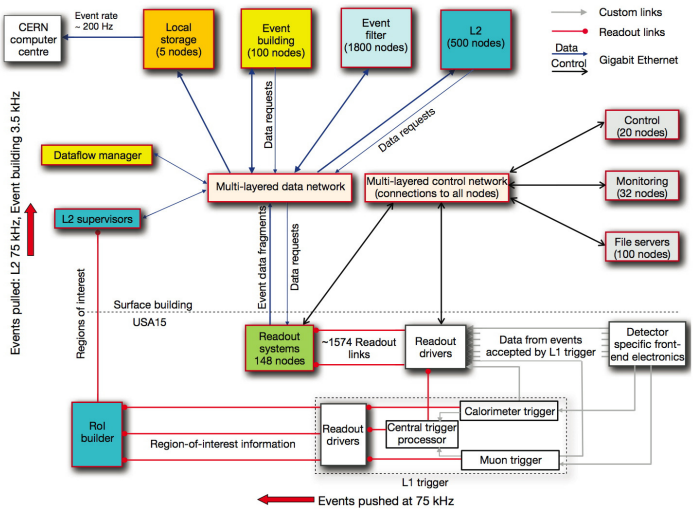

Figure 2.8: Components of the ATLAS trigger and data acquisition system [67].

- Level 2 (L2) – analyses the detailed data from RoIs (approx. 2% of whole event). It reduces the event rate to 3.5 kHz.
- Event filter (EF) – synchronises and combines signal from all subdetectors to make a final selection. It reduces the event rate to 200 Hz and sends a return signal to the detector components to send their data to the permanent storage [12].

The L1 trigger consists of the calorimeter trigger, the muon trigger and the L1 event-decision unit. The last one is a part of the Central Trigger Processor (CTP). The calorimeter trigger divides the calorimeter into approx. 7000 coarse regions called trigger towers. The calorimeter trigger searches for energetic electrons, photons, τ leptons and jets. The number of identified candidates, their type and energy as well as the total recorded energy are sent to the CTP. The muon trigger sends the information about the identified muon candidates.

The L1 trigger sends the data with full granularity from the RoIs for the selected events to the L2 trigger. The L2 trigger checks several conditions in parallel and directs the event to the Event Filter if any of them is fulfilled. The EF uses data from all detector components to reconstruct the event. Additional conditions, such as position of the primary vertex, can be investigated at this stage. If the event passes any of the trigger conditions, it is written to the long term storage. Due to a varying latency of the ATLAS subdetectors following from different response time and distance from the trigger unit, the signal from different parts of the detector would arrive to trigger at different time. In order to synchronise all pieces of data corresponding to one event and make it arrive to trigger at the same time, some signal propagation delays are introduced in the readout pipelines.

The ATLAS L1 trigger can be configured to trigger on up to 256 different conditions. However, filtering data online and looking only at a part of the initial data may introduce a bias to the measurement. Therefore, in the initial data taking phase with a low collision frequency a *minimum bias* trigger is used. It keeps information from each bunch crossing without any additional condition on the signature of the event and it helps to evaluate other triggers. The trigger information is added to the event data. During the analysis of data, it is possible to check which trigger conditions were initially fulfilled.

At the nominal collision frequency, the minimum bias trigger and other triggers with high event rate, such as lepton or jet triggers with low p_{T} threshold, are *prescaled*. For a trigger with a scale n, only every n-th event will be recorded [12]. Such events are kept as a reference and for some very specific studies. However, in precision measurements or searches for new particles no prescaled triggers are used.

2.3 Monte Carlo simulation

In order to interpret the results of an experiment, the measured values have to be compared to theory predictions. Because of the little information available about the course of the collision and a large number of possible scenarios due to probabilistic nature of quantum field theory, measurements in high energy particle physics rely on distributions of observables rather than single-point values. This requires simulation that follows a theoretical model under test and looks just like the data. Only then distributions of variables in simulation and data can be compared. High quality simulation has to face the following challenges:

- complexity of proton bunch collision – there are several hard interactions and countless soft interactions per bunch crossing;
- multiple scenarios for hard processes – one process can be realised in different ways, compare $t\bar{t}$ production in gluon-gluon fusion in figure 1.3;
- multiple scenarios for every step of the hadronisation.

Monte Carlo (MC) methods offer the possibility of simulating large number of events which follow a set of distribution functions. After event generation, all samples are processed with the GEANT4 [70, 71] simulation of the ATLAS detector [72], reconstructed and passed through the same analysis chain as the data.

The simulated samples usually focus on a certain process, like the production of top quark pairs or single top quark. To recreate the busy environment of the proton bunch collision, the Monte Carlo simulation samples include additional hard processes apart from the main process. This is achieved by adding simulated minimum bias events. The number of additional events added to each simulated event is chosen according to a Poisson distribution with an average number of interactions $\langle\mu\rangle$ between 0 and 18 to describe the various conditions of LHC luminosity[1]. The average number of interactions in the data is estimated for each luminosity block[2] to be

$$\langle\mu\rangle = \frac{L_{\mathrm{inst}} \times \sigma_{\mathrm{total}}}{N_{\mathrm{bunches}} \times f}, \tag{2.3}$$

where L_{inst} is the instantaneous luminosity measured in a given luminosity block, N_{bunches} is the number of colliding bunches, f is the machine revolution frequency and $\sigma_{\mathrm{total}} = 71.5$ mb is the total inelastic proton-proton cross section, estimated using simulation from the Pythia generator [73]. The Monte Carlo samples are re-weighted such that the $\langle\mu\rangle$ distribution in MC matches the distribution in data.

[1] Applies to data collected in 2011.
[2] Time interval during data recording, when the beam conditions are considered to be constant.

2.4 Worldwide LHC Computing Grid

The Worldwide LHC Computing GRID is a distributed computing system designed to store, process, analyse and simulate the LHC data serving over 10 thousand users [74]. It is a global collaboration of computing centres from 42 countries. It is organised in tiers which are used for different purposes:

- Tier 0 - comprises of two data centres connected with a special fast connection, one based locally at CERN and one in Budapest in Hungary. Its functions include safe-keeping of raw data, the first reconstruction cycle and further distribution of raw data and reconstruction outputs to Tier 1. Tier 0 resources are also used to re-process data during the LHC down times.
- Tier 1 - is built by 13 large computing centres. Its tasks are storing of the raw and reconstructed data from Tier 0, further reprocessing and storing the outputs and distribution of the data in analysis-ready format to Tier 2 as well as storage of outputs from Tier 2.
- Tier 2 - are smaller computing centres at the universities and research facilities. They are mainly used for data analysis, reconstruction and simulation.
- Tier 3 - local clusters or individual computers. They serve as front-end for the end users.

2.5 ROOT

ROOT is a modular scientific open source software framework [75]. It is an integral part of the LHC data analysis. It was developed at CERN and is used to process and manage the data, but it also has libraries containing advanced statistical and mathematical tools for data mining as well as a graphical module for all kinds of data visualisation. Moreover, it allows to simulate data following almost any arbitrary statistical or empirical model. Although written in C++, it is compatible with Python and R.

The LHC data is stored in a specially developed for this purpose file format *.root*. It is a compressed binary file allowing to organise the data in a *tree* structure. A tree consist of a collection of variables (*leaves*). It can extend over several files allowing for an easy division of a dataset into smaller batches and parallelisation of the analysis. The ROOT framework is optimised to work with root files.

CHAPTER 3

Reconstruction, simulation and background estimation

This chapter is dedicated to the description of the data sample used for the b-tagging calibration with $t\bar{t}$ events (section 4.3.2) and the measurement of the R_b and the $t\bar{t}$ production cross section (chapter 5). Both analyses exploit the $t\bar{t}$ events, however, the b-tagging calibration was performed in the single lepton, and the R_b and $\sigma_{t\bar{t}}$ measurement in the dilepton channel. Even though there are differences on the event selection level in the number of selected leptons and jets, they use the same object definitions.

As shown in figure 3.1, many processes at the LHC have cross section several orders of magnitude higher than the $t\bar{t}$ production. The goal of the object and event selection criteria described here is to find a phasespace with reduced contribution from the background processes and filter out a data sample with a high signal-to-background ratio.

Due to the different signatures of the final states, the single lepton and dilepton analyses are affected by different background processes. In the dilepton channel the significant background processes are the single top Wt channel, Drell-Yan events with associated jets [77], events with so called *fake leptons* and diboson production: WW, ZZ and WZ. In the Drell-Yan events, a virtual, electrically neutral boson, Z or γ, is produced through the quark-antiquark annihilation and decays into a pair of leptons. As the $t\bar{t}$ selection requires leptons to have a high transverse momentum, it is more likely that the boson in the Drell-Yan events passing the criteria is a Z boson. Therefore, this process is often referred to as Z+jets. Fake leptons is a collective name for events in which another object is falsely reconstructed as a prompt lepton, disregarding the underlying physics process. Contributions from both, Z+jets and events with fake leptons, are estimated with data-driven techniques in control regions. Contributions from other processes are derived from the Monte Carlo simulation.

In the single lepton channel the dominant background processes are the production of a W boson with associated jets and the QCD multijet events. In the W+jets events one prompt lepton from the decay of the W boson is present, the jets come from higher order QCD diagrams. Multijet events can contain fake leptons. Both processes are estimated with data-driven techniques. The remaining background processes are single top, Z+jets and diboson production. Many of these processes should have two prompt leptons in the final state, however due to limited detector coverage or lepton reconstruction errors, only one of them passes the selection criteria. Contributions of these processes are estimated with the Monte Carlo simulation.

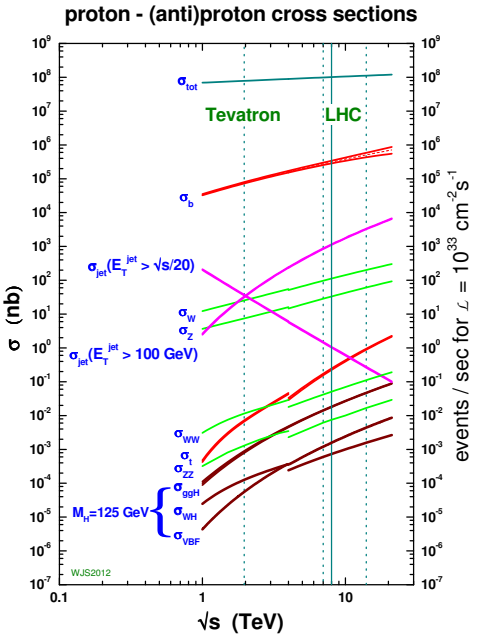

Figure 3.1: Cross section of chosen physics process at the Tevatron and the LHC. The cross section of the $t\bar{t}$ production is denoted σ_t [76].

3.1 Object reconstruction and selection

In order to lay down the event selection criteria, objects and their properties have to be defined. The definitions are dictated by the knowledge about the studied physics process and the technical constraints. For example, the requirements on the η of the leptons and jets are the result of the limited coverage of the detector. On the other hand, the criteria of high p_{T} or E_{T} and stringent isolation for leptons, help to select $t\bar{t}$ events over background events.

Primary vertex

The primary vertex is defined to be the vertex for which the associated tracks have the highest sum in squared transverse momenta. To ensure well reconstructed primary vertices, at least five tracks associated with the primary vertex are required.

Electrons

Electron candidates are reconstructed in the calorimeter using a cluster-based algorithm and are required to have $E_{\mathrm{T}} > 25$ GeV and $|\eta_{\mathrm{cl}}| < 2.47$, where η_{cl} denotes the pseudorapidity of the calorimeter cluster. Clusters falling in the calorimeter transition region, corresponding to $1.37 < |\eta_{\mathrm{cl}}| < 1.52$, are ignored.

High quality electron candidates are selected by matching inner detector tracks to electron cluster candidates and requiring stringent selection requirements on calorimeter, tracking and combined variables that provide a good discrimination between electrons and jets [78]. Electrons must also be isolated: the sum of the calorimeter transverse energy within a cone of radius $\Delta R = \sqrt{\Delta\eta^2 + \Delta\phi^2} = 0.2$, excluding the cells associated with the electron, is required to be below a certain threshold that depends on the

cluster energy, η, and the number of reconstructed vertices. The threshold is chosen such that the efficiency for electrons selected in $Z \to ee$ events to pass this isolation requirement is 90%. In addition, the p_{T} of any track within a cone of radius $\Delta R = 0.3$ around the electron direction, again excluding the track belonging to the electron, is restricted to be below a threshold that depends on the cluster energy and η. The efficiency for this track-based isolation requirement is also 90% for electrons selected in the $Z \to ee$ events. The combined track and calorimeter isolation efficiency is $(87 \pm 2)\%$.

Muons

Muon candidates are reconstructed by combining track segments found in the inner detector and in the muon spectrometer. Candidates with $p_{\mathrm{T}} > 20\,\mathrm{GeV}$ and $|\eta| < 2.5$ are selected. The selected muons must additionally satisfy a series of requirements on the number of track hits in the various tracking sub-detectors [79]. Muons are also required to be isolated: the sum of the calorimeter transverse energy within a cone of radius $\Delta R = 0.2$ is required to be below 4 GeV, and the p_{T} of all tracks within a cone of radius $\Delta R = 0.3$, excluding the track belonging to the muon, must be below 2.5 GeV. In addition, the impact parameter of electrons and muons with respect to the primary vertex, $|d_0|$, is required to be smaller than 2 mm.

Jets

Jets are reconstructed using the anti-k_t algorithm [80] with a radius parameter of 0.4, using topological clusters identified in the calorimeter as inputs to the jet clustering. Candidates with $p_{\mathrm{T}} > 25\,\mathrm{GeV}$ and $|\eta| < 2.5$ are selected. The response of the calorimeter is corrected through a p_{T}- and η-dependent scale that is derived from simulated events [81].

To reject jets from the pile-up interactions in the same bunch crossing, a quantity called *jet vertex fraction*, $\varepsilon_{\mathrm{jvf}}$, is defined for each jet using the tracks associated to that jet. It is defined as the ratio of the scalar p_{T} sum for the associated tracks that are used to reconstruct the primary vertex (considered to be associated with the hard-scattering collision) to the scalar p_{T} sum of all tracks associated to the jet:

$$\varepsilon_{\mathrm{jvf}}(\mathrm{jet}_i, \mathrm{vtx}_j) = \frac{\sum_k p_{\mathrm{T}}(\mathrm{trk}_k^{\mathrm{jet}_i}, \mathrm{vtx}_j)}{\sum_n \sum_l p_{\mathrm{T}}(\mathrm{trk}_l^{\mathrm{jet}_i}, \mathrm{vtx}_n)} \tag{3.1}$$

and is a measure for the probability of the jet to originate from that vertex. $\varepsilon_{\mathrm{jvf}}$ takes a value of -1 for jets with no tracks in them. Jets in the selected events are required to have $|\varepsilon_{\mathrm{jvf}}| > 0.75$.

Missing transverse momentum

The missing transverse momentum and its magnitude $E_{\mathrm{T}}^{\mathrm{miss}}$ are calculated using energy clusters in the calorimeters and corrected for the presence of electrons, muons, and jets [82].

In order to improve the agreement between data and Monte Carlo simulation, several corrections are applied to the reconstructed electrons, muons, and jets. They are further discussed together with their uncertainties in sections 4.3.2 and 5.4.

Overlap removal

After the object selections, the overlaps between different types of objects are considered to eliminate ambiguous and incorrectly reconstructed objects. First, muons within $\Delta R < 0.4$ of the selected jets

($p_{\mathrm{T}}^{\mathrm{jet}} > 25$ GeV) are removed, as they most likely originated from the jet. Then, any jets within $\Delta R < 0.2$ of the selected electron candidates are removed, as they could have been caused by the electron radiation. Finally, electrons within $\Delta R < 0.4$ of the remaining jets are removed, because the electron might have originated from the jet and not from the primary vertex.

3.2 Event selection

The event selection criteria, valid for both single lepton and dilepton channels, are:

- Data events must be recorded in a luminosity block from the "good run list". This means that the beams were in stable conditions, all ATLAS subsystems were operational and data passed the data acquisition quality control.
- Events are rejected if data integrity errors occurred in the liquid argon calorimeter.
- The appropriate single electron or single muon trigger has fired. The not pre-scaled triggers with the lowest object p_{T} threshold are employed. Due to changing beam conditions, and as a result, changing instantaneous luminosity, different triggers are used for data collected in different stages of the data taking. For electrons, first the `EF_e20_medium` trigger was used, then `EF_e22_medium` and finally the combination of `EF_e22vh_medium1` or `EF_e45_medium1`. For muons initially `EF_mu18` trigger was applied, but it was replaced later by `EF_mu18_medium`.

The data used in this analysis was recorded by the ATLAS detector during the 2011 data taking period with pp collisions at a centre-of-mass energy $\sqrt{s} = 7$ TeV. The b-tagging calibration with $t\bar{t}$ events described in section 4.3.2 used the initial estimate of the 2011 integrated luminosity of $\mathcal{L}_{\mathrm{int}} = 4.7$ fb^{-1} with a relative uncertainty of 3.9% [83]. The R_b and cross section measurement (chapter 5.1) used the more precise estimate released after the b-tagging calibration analysis was finalised: $\mathcal{L}_{\mathrm{int}} = 4.6$ fb^{-1} with a relative uncertainty of 1.8% [84].

3.2.1 Event selection for single lepton channel

In the single lepton channels (e+jets and μ+jets), the following event selection criteria are applied:

- The event contains exactly one reconstructed prompt lepton matching the corresponding high-level trigger object within $\Delta R < 0.15$.
- In the e+jets channel, the missing transverse momentum $E_{\mathrm{T}}^{\mathrm{miss}} > 30$ GeV and the transverse mass $m_{\mathrm{T}}(l\nu) > 30$ GeV, while, in the μ+jets channel, $E_{\mathrm{T}}^{\mathrm{miss}} > 20$ GeV and $E_{\mathrm{T}}^{\mathrm{miss}} + m_{\mathrm{T}}(l\nu) > 60$ GeV. Here, $m_{\mathrm{T}}(l\nu)$ is the transverse mass of the selected lepton l and the $E_{\mathrm{T}}^{\mathrm{miss}}$ vector. These requirements help to select events in which the missing transverse momentum can be identified with the neutrino ν originating from the W boson decay $W \to l\nu$ and significantly reduce the contribution from multijet background. Its impact on the $m_{\mathrm{T}}(l\nu)$ and $E_{\mathrm{T}}^{\mathrm{miss}}$ distributions is presented in figures 3.2 and 3.3.
- The event is required to have at least four jets. As can be seen in figure 3.4, bins with lower jet multiplicity are dominated by the background processes.
- At least one of the jets is tagged with the MV1 algorithm at the working point corresponding to the 70% b-tagging efficiency (see section 4.2).

The number of expected events passing these selection criteria are determined from Monte Carlo simulation (see section 3.4) and from data-driven methods (see section 3.3) and are shown in table 3.1.

Source	e+jets			μ+jets			Sum		
$t\bar{t}$ (MC@NLO)	17300	±	1700	28600	±	2800	45900	±	4600
W+jets	2800	±	400	5400	±	700	8200	±	1100
Multijet	2300	±	1100	1800	±	400	4100	±	1200
Single top	1430	±	110	2420	±	190	3850	±	310
Z+jets	510	±	310	558	±	330	1070	±	640
Diboson	55.9	±	2.8	86	±	4	142	±	7
$\sum$	24500	±	2100	38900	±	2900	63400	±	4900
Observed	21978			38188			60166		

Table 3.1: The number of events passing the single lepton selection requirements corresponding to a luminosity of 4.7 fb^{-1}, together with theoretical uncertainties on the cross sections ($t\bar{t}$, single top and Z+jets production) or uncertainties on the estimation directly from data (W+jets and multijet) [83].

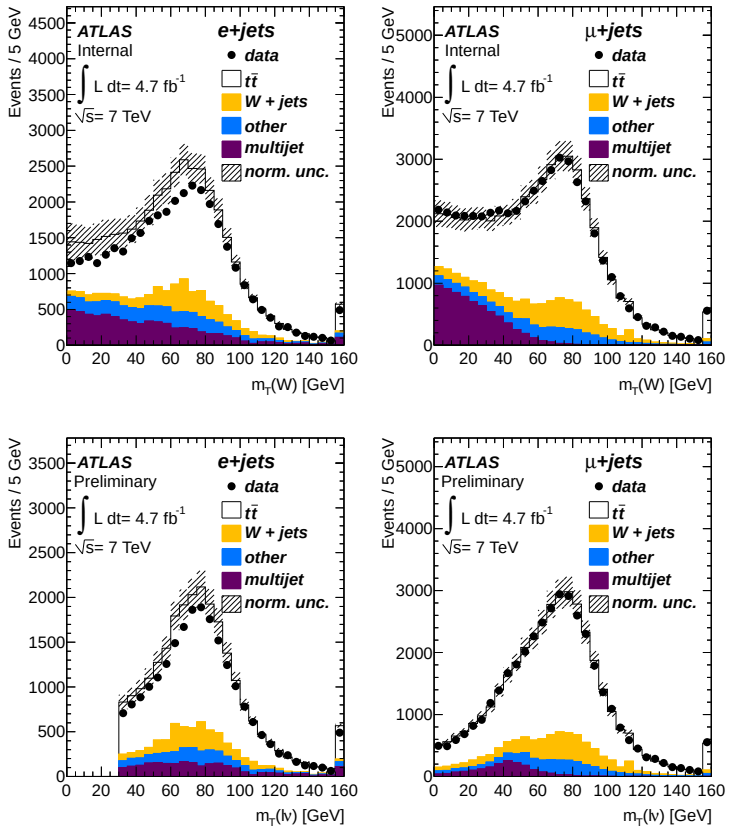

Figure 3.2: Transverse mass $m_{\mathrm{T}}(l\nu)$ ($m_{\mathrm{T}}(W)$) of the lepton and missing transverse momentum without [85] (upper row) and with [83] (lower row) the $E_{\mathrm{T}}^{\mathrm{miss}}$ and $m_{\mathrm{T}}(l\nu)$ requirements for the e+jets channel (left) and μ+jets channel (right). All other event selection criteria, including the requirement of at least one b-tagged jet, are applied. "Other" is a sum of contributions from Z+jets, single top and diboson production. The error band represents the sum of theoretical uncertainties on the cross sections ($t\bar{t}$, single top, diboson and Z+jets) and uncertainties on the estimation directly from data (W+jets and multijet). The last bin is inclusive.

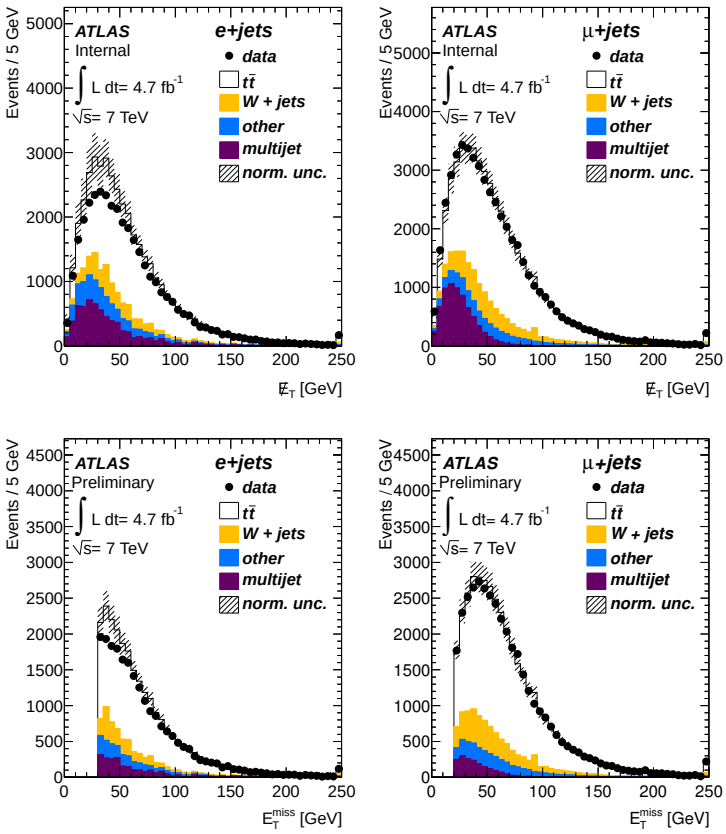

Figure 3.3: Missing transverse energy $E_{\mathrm{T}}^{\mathrm{miss}}$ without [85] (upper row) and with [83] (lower row) the $E_{\mathrm{T}}^{\mathrm{miss}}$ and $m_{\mathrm{T}}(l\nu)$ requirements for the e+jets channel (left) and μ+jets channel (right). All other event selection criteria, including the requirement of at least one b-tagged jet, are applied. "Other" is a sum of contributions from Z+jets, single top and diboson production. The error band represents the sum of theoretical uncertainties on the cross sections ($t\bar{t}$, single top, diboson and Z+jets) and uncertainties on the estimation directly from data (W+jets and multijet). The last bin is inclusive.

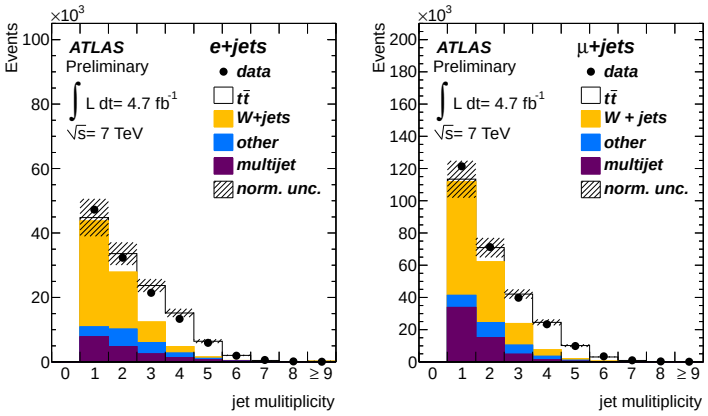

Figure 3.4: Jet multiplicity in the e+jets channel (left) and in the μ+jets channel (right) [83]. At least one jet is required in these distributions. All other event selection criteria, including the requirement of at least one b-tagged jet, are applied. "Other" is a sum of contributions from Z+jets, single top and diboson production. The error band represents the sum of theoretical uncertainties on the cross sections ($t\bar{t}$, single top, diboson and Z+jets) and uncertainties on the estimation directly from data (W+jets and multijet). The last bin is inclusive.

3.2.2 Event selection for dilepton channel

The analysis in the $t\bar{t}$ dilepton channel (ee, $\mu\mu$, $e\mu$) applied the following criteria:

- MC events must contain at least two prompt leptons. On the generator level, the presence of two leptons (e or μ), which are originating from W or Z bosons, is checked. Events with $W \rightarrow \tau\nu \rightarrow l\nu\nu\nu$ (similarly for Z) processes are considered as signal events as well.
- In simulated samples both selected leptons are required to match true leptons.
- Events must contain exactly two selected leptons with opposite electric charges. The distributions of the transverse momentum of the leptons in the selected events are shown in figure 3.5.
- To ensure that the event is triggered by the leptons used in the analysis, a matching between at least one selected, reconstructed lepton and the trigger object is required. The matching distance is $\Delta R < 0.15$.
- If a selected electron and a muon candidate share a track, the event is rejected.
- In order to accommodate requirements made on the Z+jets Monte Carlo samples, both the collisions and the simulation events in the ee and $\mu\mu$ channels with a small reconstructed dilepton mass, $m_{ll} < 15$ GeV, are rejected.
- In order to reject events compatible with the Z+jets production, events in the ee and $\mu\mu$ channels with dilepton mass close to the mass of the Z boson are discarded if $|m_{ll} - 91\ \text{GeV}| < 10$ GeV. Figure 3.6 shows that this region is dominated by the Z+jets contribution.
- In the ee and $\mu\mu$ channels, to suppress background processes such as Z+jets and fake lepton events, the missing transverse momentum must satisfy $E_{\text{T}}^{\text{miss}} > 60$ GeV. As can be seen in figure 3.7, the low $E_{\text{T}}^{\text{miss}}$ region is dominated by the Z+jets events.
- In the $e\mu$ channel, to suppress backgrounds such as events with fake leptons, the scalar sum of p_{T} of all selected jets and leptons in the event must satisfy $H_{\text{T}} > 130$ GeV.

- In order to obtain an accurate measurement of the $E_{\mathrm{T}}^{\mathrm{miss}}$, it is necessary to reject events that contain fake jets due to hardware problems, bad beam conditions, or cosmic ray showers. Jets that are poorly reconstructed according to the selection criteria are flagged. If after overlap removal a poorly reconstructed jet is identified as an electron, the event is not rejected. In contrast, if a pathological jet is treated as a jet rather than an electron, the event is rejected.

- Events must have at least two selected jets. The distributions of jet multiplicity are presented in figure 3.8. The distributions of the transverse momentum of the first and second jet in selected events are presented in figure 3.9.

The number of expected events passing these selection criteria are determined from Monte Carlo simulation and from data-driven methods (see section 3.3) and are shown in table 3.2. More kinematic distributions for the dilepton channel in the signal region, as well as in a background-rich control region, are presented in the appendix A. In all distributions of kinematic variables in the dilepton channel the shape from the Protos+Pythia sample (using only $tt \to WWbb$ events) is normalised to the corresponding number of selected events from Powheg+Pythia, for more details see section 3.4.

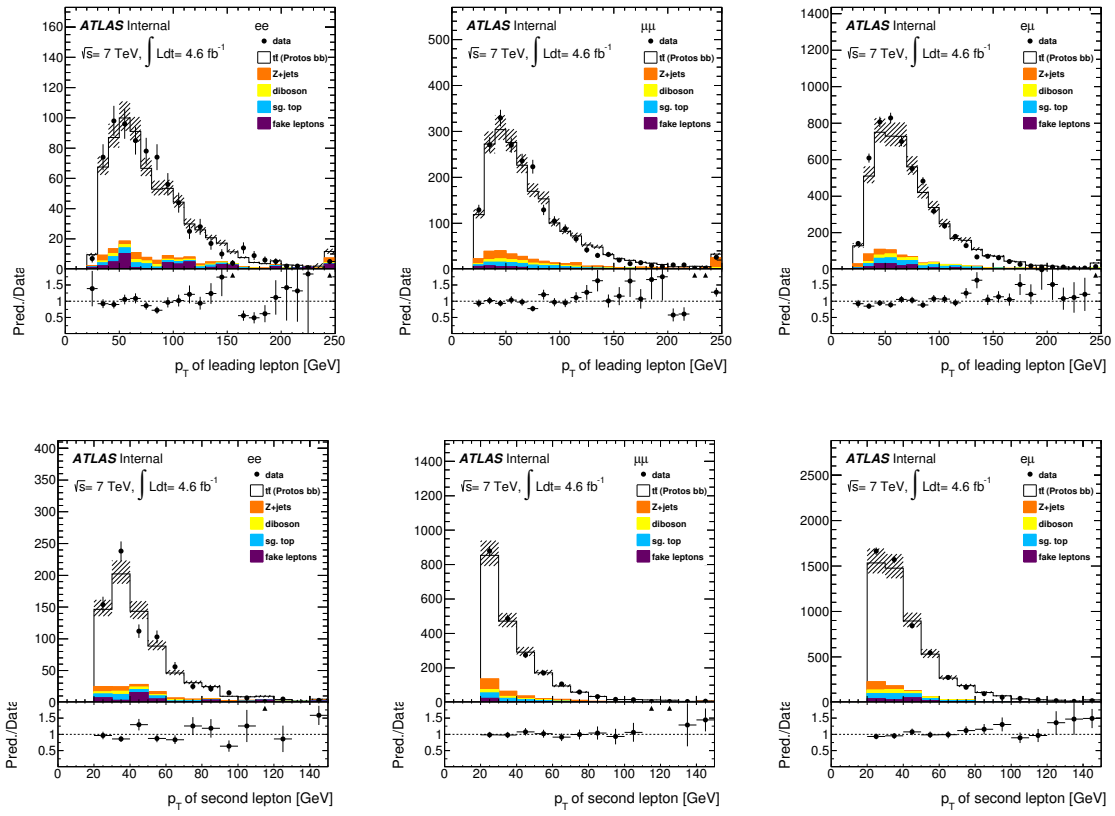

Figure 3.5: Distribution of the p_{T} of the leading (upper row) and second (lower row) lepton in the ee (left), $\mu\mu$ (middle) and $e\mu$ channel (right). All event selection criteria are applied. The error band represents the sum of theoretical uncertainties on the cross sections ($t\bar{t}$, single top, diboson and Z+jets production in $e\mu$ channel) and uncertainties on the estimation directly from data (fakes, $Z \to ee$ and $Z \to \mu\mu$). The last bin is inclusive.

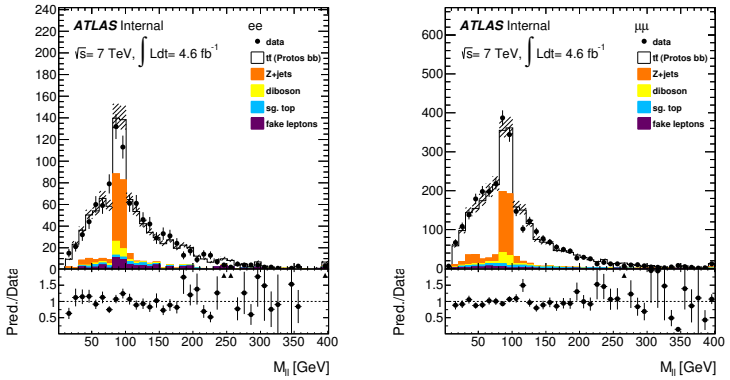

Figure 3.6: Distribution of the invariant mass of both selected leptons in the ee (left) and $\mu\mu$ channel (right). All event selection criteria, apart from the requirement on the m_{ll}, are applied. The error band represents the sum of theoretical uncertainties on the cross sections ($t\bar{t}$, single top, diboson) and uncertainties on the estimation directly from data (fakes, $Z \rightarrow ee$ and $Z \rightarrow \mu\mu$). The last bin is inclusive.

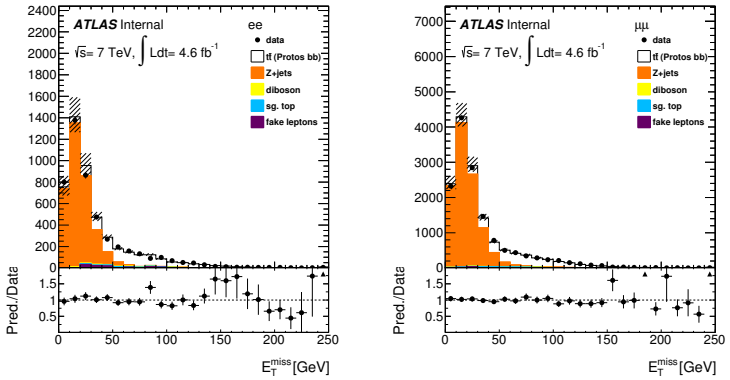

Figure 3.7: Distribution of the $E_{\mathrm{T}}^{\mathrm{miss}}$ in the ee (left) and $\mu\mu$ channel (right). All event selection criteria, apart from the requirement on the $E_{\mathrm{T}}^{\mathrm{miss}}$, are applied. The error band represents the sum of theoretical uncertainties on the cross sections ($t\bar{t}$, single top, diboson) and uncertainties on the estimation directly from data (fakes, $Z \rightarrow ee$ and $Z \rightarrow \mu\mu$). The last bin is inclusive.

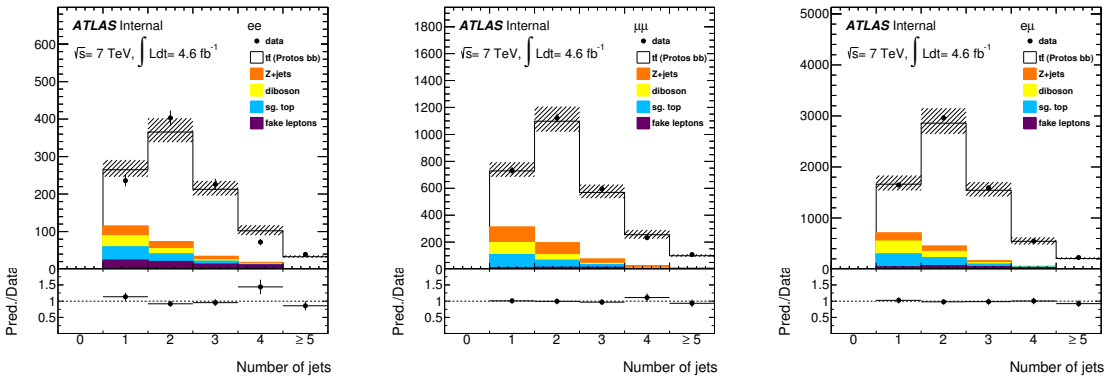

Figure 3.8: Distribution of the number of jets in the ee (left), $\mu\mu$ (right) and $e\mu$ channel (middle). At least one jet is required in these distributions. All other event selection criteria are applied. The error band represents the sum of theoretical uncertainties on the cross sections ($t\bar{t}$, single top, diboson and Z+jets production in $e\mu$ channel) and uncertainties on the estimation directly from data (fakes, $Z \to ee$ and $Z \to \mu\mu$). The last bin is inclusive.

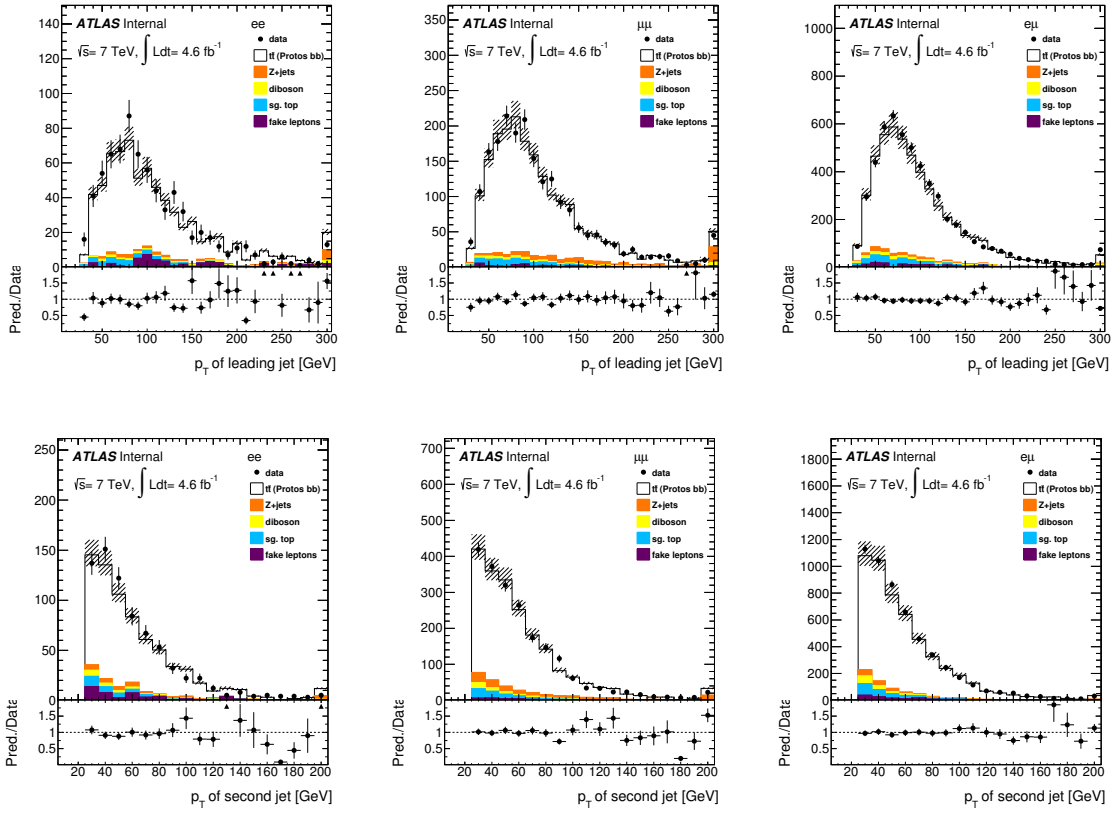

Figure 3.9: Distribution of the p_{T} of the leading (upper row) and second (lower row) jet in the ee (left), $\mu\mu$ (middle) and $e\mu$ channel (right). All event selection criteria are applied. The error band represents the sum of theoretical uncertainties on the cross sections ($t\bar{t}$, single top, diboson and Z+jets production in $e\mu$ channel) and uncertainties on the estimation directly from data (fakes, $Z \to ee$ and $Z \to \mu\mu$). The last bin is inclusive.

Source	ee			$\mu\mu$			$e\mu$			Sum		
$t\bar{t}$ Protos	647.5	±	64.8	1701.8	±	170.2	4522.3	±	452.2	6871.7	±	687.2
$t\bar{t}$ Powheg	571.5	±	57.1	1672.9	±	167.3	4343.8	±	434.4	6588.2	±	658.8
$Z \to ee, \mu\mu$	20.2	±	2.4	91.3	±	7.1	0.0	±	0.0	111.5	±	7.5
$Z \to \tau\tau$	14.2	±	5.0	58.9	±	20.6	150.9	±	52.8	224.0	±	78.4
Single top	30.2	±	2.6	78.0	±	6.6	231.6	±	19.7	339.8	±	28.9
Diboson	19.3	±	6.8	54.3	±	19.0	156.4	±	54.7	230.0	±	80.5
Fakes	43.8	±	21.9	32.4	±	13.0	139.6	±	41.9	215.8	±	49.0
$\sum$	699.2	±	61.8	1987.8	±	170.4	5022.3	±	443.4	7709.3	±	670.8
Observed	740			2058			5329			8127		

Table 3.2: The number of events passing ee, $\mu\mu$ and $e\mu$ selection requirements corresponding to a luminosity of 4.6 fb^{-1}, together with theoretical uncertainties on the cross sections ($t\bar{t}$, single top, diboson and Z+jets production in $e\mu$ channel) or uncertainties on the estimation directly from data (fakes and Z+jets production in ee and $\mu\mu$ channels). The Protos $t\bar{t}$ sample has a default value of $R_b = 0.5$, which is far from the theoretical expectations, thus in $\sum$, the sum of the simulation expectations, the result for the Powheg sample is considered.

3.3 Data-driven background estimation

In the studies of physics processes, the data is compared to the Monte Carlo simulation, which follows a chosen theoretical model. Before conducting a measurement of any physical quantity, the simulation has to be validated. The validation usually includes comparison of the shape of the distributions of e.g. kinematic variables and the overall number of selected events (normalisation of the distributions).

For some of the background processes, precise Monte Carlo simulation is not available. For processes such as W+jets and Z+jets, the physical quantities, i.e. the shape of their distributions, are considered to be modelled accurately. However, due to the high multiplicity of jets, the overall yields and flavour composition of the jets carry a high uncertainty. The production of associated jets is a result of high order QCD processes, which are difficult to model due the variety of possible scenarios, as discussed in section 1.2.1. There exist, however, data-driven techniques that allow to measure the yields with a lower uncertainty than that carried by the MC simulation. Therefore, for W/Z+jets processes, the shapes of the distributions are taken from the simulation, but they are normalised to the number obtained with the data-driven methods.

Backgrounds such as multijet production and events containing fake leptons, in fact consist of several physics processes and generating any simulation modelling these processes would be very time consuming and would still carry a very high uncertainty. Instead, contributions for multijet production and events containing fake leptons are estimated in data in control region, where the presence of signal events is minimal.

3.3.1 W boson production with associated jets (W+jets)

The dominant background in the single lepton channel arises from the W boson production with associated jets (W+jets). The $t\bar{t}$ signal signature is mimicked by a prompt lepton from the W boson decay and jets from the associated production. Its estimate is based on the prediction from the Monte Carlo simulation, corrected with scale factors derived from data. The correction of the overall normalisation is obtained with a *charge asymmetry* method [86]. It uses the fact that the probabilities for production of W^+ and W^- in a pp collision are not equal due to different production modes. The dominant production

modes for W^+ and W^- in pp collisions are:

$$u\bar{d} \to W^+$$
$$d\bar{u} \to W^-$$

The parton distribution functions in a proton are different for u and d quarks, as presented in figure 1.2, which leads to different production rates of W^+ and W^- boson. However, their ratio is predicted with a higher precision than production of W boson with four or more jets [87]. The flavour composition of the W+jets sample is measured with a *tag counting* method [88], which provides scale factors for $Wb\bar{b}/c\bar{c}$+jets, Wc+jets and W with light flavour jets events used to correct the Monte Carlo simulation predictions.

In the dilepton channel, the W+jets process contributes to events with fake leptons and its estimation is described in the next section.

3.3.2 Multijet production and events with fake leptons

The second most important contribution to the background comes from the QCD multijet production. In this case, there are no prompt leptons in the final state and another object fakes the signature of a *real* lepton. The contribution of the multijet background is measured directly in data using the *matrix method*, which relies on finding a relationship between events with real and *fake* leptons and events with *tight* and *loose* leptons [89–91]. The nature of fake leptons is different in the μ+jets and e+jets channels. The fake muons are muons that originate from semi-leptonic b quark decay within the b-jets. Most of them are rejected by the muon isolation criteria. Fake electrons are usually misreconstructed jets or electrons from photon conversion.

The matrix method studies events with tight, i.e. passing standard isolation criteria described in section 3.1, and loose leptons. The definition of loose muons requires no isolation, while for loose electrons, the isolation criteria is less strict than the standard selection [92]. In the single lepton channel, the number of events with loose and tight leptons can be written down as

$$\begin{aligned} N^{\text{loose}} &= N^{\text{loose}}_{\text{real}} + N^{\text{loose}}_{\text{fake}} \\ N^{\text{tight}} &= \varepsilon_{\text{real}} N^{\text{loose}}_{\text{real}} + \varepsilon_{\text{fake}} N^{\text{loose}}_{\text{fake}}, \end{aligned} \tag{3.2}$$

where N^{loose} and N^{tight} are the numbers of events measured with leptons passing loose and tight isolation criteria, $N^{\text{loose}}_{\text{real}}$ and $N^{\text{loose}}_{\text{fake}}$ are the events with real and fake leptons in the sample with loose isolation. $\varepsilon_{\text{real}}$ and $\varepsilon_{\text{fake}}$ are the efficiencies of real and fake loose leptons to pass the tight isolation criteria. They are estimated in control regions enriched in the leptons of the type of interest.

The $\varepsilon_{\text{real}}$ is estimated for both, muons and electrons in a sample of Z events ($Z \to \mu\mu$ and $Z \to ee$, respectively). The $\varepsilon_{\text{fake}}$ for muons is measured in two independent regions:

- Sample A: low $m_{\text{T}}(l\nu)$ region: $m_{\text{T}}(l\nu) < 20$ GeV and $E_{\text{T}}^{\text{miss}} + m_{\text{T}}(l\nu) < 60$ GeV,
- Sample B: muons are required to have a high impact parameter with respect to the primary vertex, which favours muons stemming from heavy flavour jets. This phenomenon is described in more details in section 4.1.

The average of the measurements in sample A and B is used as $\varepsilon_{\text{fake}}$ in the analysis. For electrons, $\varepsilon_{\text{fake}}$ is measured in a region with reverted $E_{\text{T}}^{\text{miss}}$ requirement: $E_{\text{T}}^{\text{miss}} < 20$ GeV.

Using the equation 3.2, the number of multijet events in the $t\bar{t}$ signal region can be expressed as

$$N_{\text{fake}}^{\text{tight}} = \frac{\varepsilon_{\text{fake}}}{\varepsilon_{\text{real}} - \varepsilon_{\text{fake}}} \left(\varepsilon_{\text{real}} N^{\text{loose}} - N^{\text{tight}} \right). \tag{3.3}$$

Figure 3.2 shows the transverse mass $m_{\text{T}}(l\nu)$ of the lepton and the $E_{\text{T}}^{\text{miss}}$ vector in the signal region before and after applying the $m_{\text{T}}(l\nu)$ and $E_{\text{T}}^{\text{miss}}$requirements. The $E_{\text{T}}^{\text{miss}}$ spectrum in the signal region before and after applying these requirements is presented in figure 3.3 and figure 3.4 presents the jet multiplicity (after applying the $m_{\text{T}}(l\nu)$ and $E_{\text{T}}^{\text{miss}}$requirements). Those distributions are sensitive to a correct description of the multijet and W+jets processes, and they all show a good agreement between the sum of multijet and W+jets data-driven predictions and simulated samples of other background and signal processes, and data.

The $t\bar{t}$ dilepton events contain two leptons from the two W bosons decays. The fake leptons background comes predominantly from single lepton $t\bar{t}$ decay and W+jets production with a real and a fake lepton, though there is a small contribution with two fake leptons coming from the QCD multijet production.

The estimate of the contribution of events with fake leptons in the dilepton channels uses the same principle as the matrix method described for the single lepton channel, but due to the presence of two leptons in the final state, the equation 3.2 takes a more complicated form:

$$\begin{pmatrix} N^{\text{tt}} \\ N^{\text{tl}} \\ N^{\text{lt}} \\ N^{\text{ll}} \end{pmatrix} = \mathbf{M} \begin{pmatrix} N_{\text{rr}}^{\text{ll}} \\ N_{\text{rf}}^{\text{ll}} \\ N_{\text{fr}}^{\text{ll}} \\ N_{\text{ff}}^{\text{ll}} \end{pmatrix}, \tag{3.4}$$

where the superscripts "l" and "t" refer to loose and tight and "r" and "f" refer to real and fake. The 4×4 matrix $\mathbf{M}$ contains the relative combinations of $\varepsilon_{\text{real}}$ and $\varepsilon_{\text{fake}}$.

The loose and tight definitions together with a more detailed explanation about the method and analysis are provided in reference [89].

3.3.3 $Z \to ee/\mu\mu$ with associated jets

The $t\bar{t}$ event selection includes requirements to reject Z+jets events. However, a small fraction of events in the $E_{\text{T}}^{\text{miss}}$ tails and dilepton invariant mass sidebands will be selected. These events are difficult to model properly in the simulation due to large uncertainties on the non-Gaussian nature of the missing energy tails, the Z boson cross section in higher jet multiplicity bins and the lepton energy resolution.

To estimate the $Z \to ee$ and $Z \to \mu\mu$ background, the number of these events is measured in a control region. The control region is defined by events with an invariant dilepton mass within ±10 GeV around the Z boson mass with at least two jets and with $E_{\text{T}}^{\text{miss}} > 30$ GeV. There are some other physics processes ($t\bar{t}$, $Z \to \tau\tau$, diboson, single top) contaminating this control region and their contribution is subtracted relying on their MC prediction. The number of $Z \to ee$ and $Z \to \mu\mu$ events in the signal region is then estimated using simulation to extrapolate from the control region:

$$Z \text{ boson background estimate in SR} = \frac{\text{MC}_Z(\text{SR})}{\text{MC}_Z(\text{CR})} \times (\text{Data(CR)} - \text{MC}_{\text{other}}(\text{CR})), \tag{3.5}$$

where $\text{MC}_Z(\text{SR/CR})$ represent the number of events in the signal and control region, respectively. MC_{other} is the number of events from physics backgrounds that contaminate the control region. Data(CR) represents the observed number of events in the control region in 4.6 fb^{-1} of data. The Monte Carlo

prediction is then scaled to match the estimate described by equation 3.5.

The robustness of the method is tested by varying the $E_{\mathrm{T}}^{\mathrm{miss}}$ requirement in the control region by ±10 GeV. The effect is included as method uncertainty. Uncertainties on the jet energy scale, resolution etc., described in section 5.4, are also considered. The estimate includes the uncertainty on the number of events in data as well. The resulting number of Z+jets background events from this data-driven method is shown in table 3.3 for the ee and $\mu\mu$ channel.

	ee	$\mu\mu$
Z+jets Monte Carlo	20.3 ± 7.1 (syst.)	84.5 ± 29.6 (syst.)
Data-driven	20.17 ± 2.38 (stat.) ± 0.45 (syst.)	91.25 ± 7.12 (stat.) ± 0.40 (syst.)
Scale factor	0.99 ± 0.12	1.08 ± 0.08

Table 3.3: Expected number of Z+jets events passing the ee and $\mu\mu$ selection requirements corresponding to a luminosity of 4.6 fb^{-1}. The result of the expectation from simulation and the data-driven method are shown.

The earlier discussed figures 3.6, 3.7 and 3.8, which present the invariant mass of two leptons in the ee and $\mu\mu$ channels without the requirement on the m_{ll}, the $E_{\mathrm{T}}^{\mathrm{miss}}$ without the $E_{\mathrm{T}}^{\mathrm{miss}}$requirement and jet multiplicity distributions, are sensitive to the correct description of the fake leptons and Z+jets background. Additionally, figures 3.10 and 3.11 present the jet multiplicity and jet transverse momentum in a control region containing the region used to estimate the Z+jets background: $E_{\mathrm{T}}^{\mathrm{miss}} < 60$ GeV or $|m_{ll} - 91\ \mathrm{GeV}| < 10$ GeV. All figures show a very good agreement between the data and the estimates from Monte Carlo and data-driven techniques.

In the single lepton channel, due to the low contribution of the Z+jets process, its estimation is based purely on the Monte Carlo simulation.

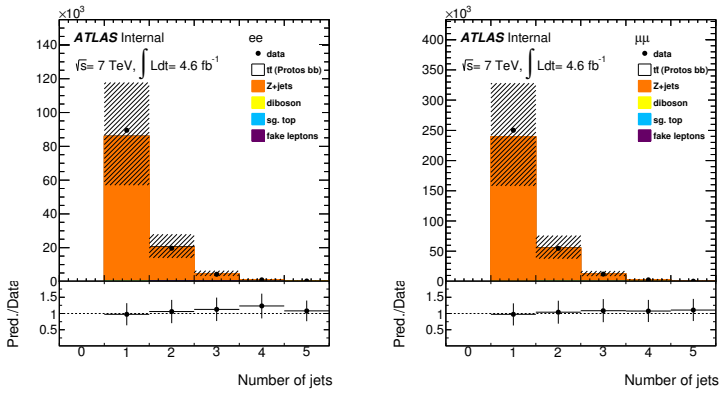

Figure 3.10: Distribution of the number of jets in ee (left) and $\mu\mu$ channel (right) in the control region with $E_{\mathrm{T}}^{\mathrm{miss}} < 60$ GeV or $|m_{ll} - 91\ \mathrm{GeV}| < 10$ GeV. At least one jet is required in these distributions. All other standard event selection criteria are applied. The error band represents the sum of theoretical uncertainties on the cross sections (Z+jets, $t\bar{t}$, single top, diboson) and uncertainties on the estimation directly from data (fake leptons). The last bin is inclusive.

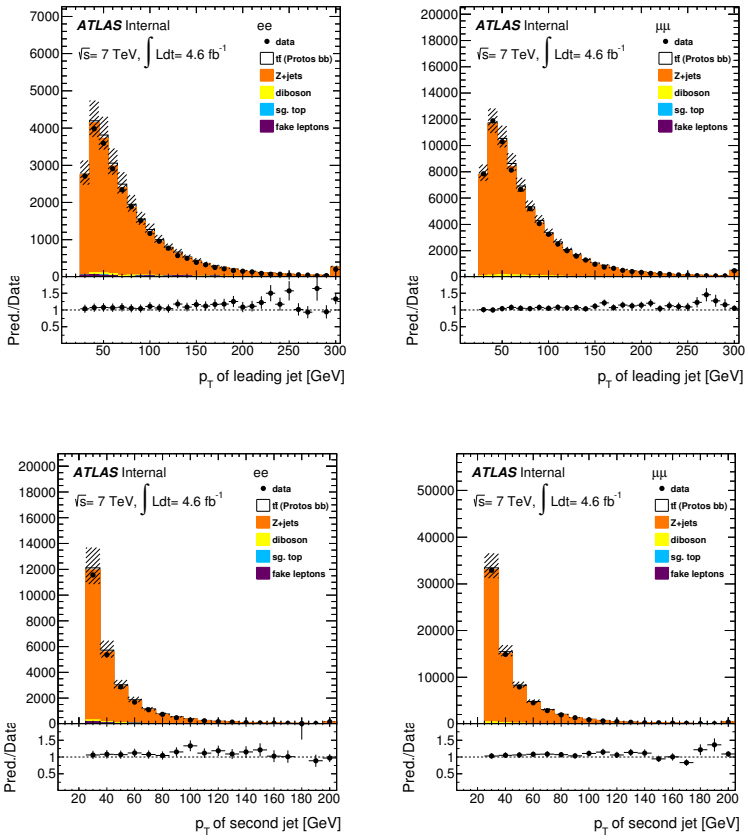

Figure 3.11: Distribution of the p_{T} of the leading (upper row) and second (lower row) jet for the ee (left) and $\mu\mu$ channel (right) in the control region with $E_{\mathrm{T}}^{\mathrm{miss}} < 60$ GeV or $|m_{ll} - 91\ \mathrm{GeV}| < 10$ GeV. All other standard event selection criteria are applied. The error band represents the sum of theoretical uncertainties on the cross sections (Z+jets, $t\bar{t}$, single top, diboson) and uncertainties on the estimation directly from data (fake leptons). The last bin is inclusive.

3.4 Simulation

Monte Carlo simulation samples have been used to develop and validate the analysis procedures, to calculate the selection and tagging efficiencies and to evaluate the contributions from the specific background processes.

3.4.1 $t\bar{t}$ samples

For the b-tagging calibration with the $t\bar{t}$ events in the single lepton channel, the inclusive $t\bar{t}$ sample generated with the MC@NLO generator [93–95] with the CT10 [96] PDF set is used. The hard scattering events are showered and hadronised with Herwig [97].

The dilepton $t\bar{t}$ signal events are generated using the Protos MC event generator [98,99] with modified CKM elements, $|V_{tb}|^2 = 0.5$ and $|V_{ts}|^2 = |V_{td}|^2 = 0.25$. The parton shower and the underlying event were added using the Pythia generator [73] with the AUET2B tunes [100] to the ATLAS data and the CTEQ6L1 PDF set [101]. At the truth level, the sample is filtered for dilepton decay final states, which means that both of the W bosons from top quark decay to a neutrino and an electron, a muon or a tau[1].

The $t\bar{t}$ normalisation cross section for pp collisions at a centre-of-mass energy of $\sqrt{s} = 7$ TeV is $\sigma_{t\bar{t}} = 177^{+10}_{-11}$ pb for a top quark mass of 172.5 GeV/c^2. It has been calculated at next-to-next-to-leading order (NNLO) in QCD including resummation of next-to-next-to-leading logarithmic (NNLL) soft gluon terms with top++2.0 [102–107]. The PDF and α_S uncertainties were calculated using the PDF4LHC prescription [108] with the MSTW2008 68% C.L. NNLO [13, 109], CT10 NNLO [96, 110] and NNPDF2.3 5f FFN [111] PDF sets, added in quadrature to the scale uncertainty. The NNLO+NNLL value is about 3% larger than the exact NNLO prediction, as implemented in Hathor 1.5 [112].

In the R_b and $\sigma_{t\bar{t}}$ analysis in the dilepton channel, the dependence on the Monte Carlo generator was studied in depth. A number of other $t\bar{t}$ samples generated with the assumption of $|V_{tb}| = 1$ are used to evaluate the impact of parameter choices on the R_b and $\sigma_{t\bar{t}}$ measurement. The systematic uncertainty of the measurement due to the choice of the matrix element generator is estimated with samples generated with MC@NLO, Powheg [113] and Alpgen [114]. The CTEQ6L1 PDF set is used in the generation of the Alpgen sample, which is produced with 0 to 5 (inclusive) additional partons in association to the $t\bar{t}$ event. The hard scattering events of Alpgen are showered and hadronised with Herwig [97].

The Powheg sample was generated using CT10 and the showering and hadronisation were obtained with Pythia as it was in the case of the generation of the Protos nominal sample. Powheg+Pythia is also used as a reference for the expected $tt \to WWbb$[2] events normalisation in the Protos nominal sample in the case of $|V_{tb}| = 1$. The Powheg+Pythia samples with varied top quark mass m_{top} were also produced with these settings. All these samples are further simulated using full simulation ("mc11c full" production).

Two additional Powheg samples are compared while determining the uncertainty due to the choice of the generator. They use different showering and hadronisation models (Pythia and Herwig). These samples are further simulated using fast simulation ("mc11b fast" production).

For the estimation of the systematic uncertainty due to modeling of the initial and final state radiation, ISR/FSR, two $t\bar{t}$ samples are generated with AcerMC [115] together with Pythia. They are produced with increased and decreased amount of radiation (see section 5.4.2). These samples are further simulated using fast simulation ("mc11c fast" production).

Two additional $t\bar{t}$ samples are generated using MC@NLO. These samples are produced with modified renormalisation and factorisation scales both simultaneously increased or decreased by a factor of two.

[1] Including hadronically decaying τ leptons.
[2] To improve legibility, the particle and antiparticle notation is omitted.

They are used to evaluate the systematic uncertainty in the final measurement due to the choice of scales. These samples are also a part of the "mc11c fast" production.

Three more $t\bar{t}$ samples, generated using POWHEG+PYTHIA, are used to evaluate systematic uncertainties due to the modeling of the underlying events and color reconnection. All these samples are generated using the CTEQ5L PDF set [116] with PYTHIA. The central sample is generated using the nominal settings of the P2011 tunes [117]. The sample used to estimate the systematic uncertainty due to modeling of the underlying event is generated with modified Λ_{QCD} in multi-parton interactions. The third sample is produced with the color reconnection switched off for the generation of events. Detector simulation is performed using "mc11c fast".

Two samples of $t\bar{t}$ production with associated heavy flavour quark pairs, $b\bar{b}$ and $c\bar{c}$, are produced with ALPGEN+HERWIG using CTEQ6L1. These samples contain events with no additional partons generated at the matrix element level by ALPGEN, as events with additional partons are expected to have negligible contribution due to the small cross section. These samples are complementary to the set of already mentioned ALPGEN+HERWIG $t\bar{t}$. The heavy flavour overlap removal tool [118] is used in order to remove the double counting of the heavy quark production. All these ALPGEN+HERWIG samples are used to evaluate the impact of the modeling of the heavy flavour quarks content in the $t\bar{t}$ production on the measurement of R_b and $\sigma_{\mathrm{dilepton}}$.

The $t\bar{t}$ samples used for the nominal analysis and for systematic uncertainty estimation are listed in table 3.4.

3.4.2 Background processes

Single top

In the analysis of the single lepton channel, single top samples generated with MC@NLO are used to match with the generator of the $t\bar{t}$ signal sample.

In the dilepton analysis only the Wt single top channel is included. An ACERMC+PYTHIA sample with the AUET2B tunes of PYTHIA parameters was chosen to match with the PROTOS+PYTHIA $t\bar{t}$ sample. Single top quark production in t- and s-channels are not directly considered since these samples do not contain final states with two prompt leptons (i.e. deriving from W bosons) and thus every event would fail the matching requirement between reconstructed and generated leptons in the event selection (see section 3.2.2). Like other standard top quark samples, the simulation of single top assumed $R_b = 1$.

Details of the ACERMC+PYTHIA sample are also shown in table 3.4. All single top samples are produced assuming a top quark mass of 172.5 GeV.

Z+jets

The generation of Z/γ^*+jets events uses ALPGEN v2.13 with CTEQ6L1 and the MLM scheme [119] for matching partons and jets. It implements the exact LO matrix elements for final states with up to 6 partons. The Z+jets samples are normalised with a k-factor of 1.25. For these samples the phase space has been restricted to the regions $10 < m_{ll} < 40$ GeV and $40 < m_{ll} < 2000$ GeV. The k-factor is used to scale the cross section from LO simulation to NNLO, because, even if higher order cross section calculation is available, the LO simulation is much faster. The k-factor is defined as a ratio of the cross sections calculated at different QCD order levels, in this case LO and NNLO:

$$k = \frac{\sigma_{\mathrm{NNLO}}}{\sigma_{\mathrm{LO}}}. \tag{3.6}$$

The additional partons produced in the matrix element part of the event generation can be either light partons (Z+jets) or heavy quarks ($Z+c\bar{c}$+jets and $Z+b\bar{b}$+jets). The inclusive Z+jets samples are obtained from the full set of the parton multiplicity sub-samples, including both the light partons with additional jets and the heavy quark with additional jets processes. As in the case of the $t\bar{t}$ ALPGEN +HERWIG samples, the heavy flavour overlap removal tool is used in order to remove the double counting of the heavy quark production. The Z+jets samples are listed in the appendix B.

W+jets

As for the Z+jets, for the W boson production in association with multiple jets ALPGEN v2.13 is also used. W+jets events with up to 5 partons are generated. In addition, separate samples containing $W+b\bar{b}$+jets, $W+c\bar{c}$+jets and $W+c$+jets events are produced and the heavy flavour overlap removal tool is used in order to remove the double counting of the heavy quark production.

Diboson

Diboson WW, WZ and ZZ events are modeled using the ALPGEN+HERWIG generators, normalised with appropriate k-factors of 1.26 (WW), 1.28 (WZ) and 1.30 (ZZ) to match the total cross section from NLO QCD predictions using calculations by the MCFM program [120]. Events are hadronised with HERWIG [121], using the JIMMY underlying event model [122, 123]. Both hadronisation programs are tuned to data using the ATLAS MC11c tune. The diboson samples are also listed in appendix B.

Generator	Description	$\sigma \cdot \mathcal{B}$ [pb]	k-factor	N_{events}	$\mathcal{L}$ [fb^{-1}]	Configuration tags
Protos+Pythia	Dilepton $R_b = 0.5$	18.65	n.a.	499797	26.79	e1423 s1372 s1370 r3108 r3109
MC@NLO+Herwig	No a.h.d.	79.01	1.22	14983835	120.28	e835 s1272 s1274 r3043 r2993
Powheg+Herwig	No a.h.d.	80.85	1.19	9984982	103.69	e1198 a131 s1353 a139 r2900
Powheg+Pythia	No a.h.d.	80.07	1.20	9994443	103.84	e1377 s1372 s1370 r3108 r3109
Powheg+Pythia	No a.h.d.	80.07	1.20	9992492	103.82	e1377 a131 s1353 a139 r2900
Powheg+Pythia	No a.h.d.	80.07	1.20	9994491	103.84	e1683 a131 s1353 a145 r2993
Powheg+Pythia	No a.h.d. mpiHi	80.06	1.20	9992985	103.76	e1683 a131 s1353 a145 r2993
Powheg+Pythia	No a.h.d. noCR	80.07	1.20	9995991	103.86	e1683 a131 s1353 a145 r2993
Powheg+Pythia	No a.h.d. ($m_{\text{top}} = 165$ GeV)	100.75	1.13	4999173	43.87	e1736 s1372 s1370 r3108 r3109
Powheg+Pythia	No a.h.d. ($m_{\text{top}} = 167.5$ GeV)	93.23	1.13	4992269	47.34	e1736 s1372 s1370 r3108 r3109
Powheg+Pythia	No a.h.d. ($m_{\text{top}} = 170$ GeV)	86.34	1.13	4988873	51.09	e1736 s1372 s1370 r3108 r3109
Powheg+Pythia	No a.h.d. ($m_{\text{top}} = 175$ GeV)	74.33	1.13	4997061	59.44	e1736 s1372 s1370 r3108 r3109
Powheg+Pythia	No a.h.d. ($m_{\text{top}} = 177.5$ GeV)	69.01	1.13	4999169	64.05	e1736 s1372 s1370 r3108 r3109
Powheg+Pythia	No a.h.d. ($m_{\text{top}} = 180$ GeV)	64.17	1.13	4994773	68.88	e1736 s1372 s1370 r3108 r3109
AcerMC+Pythia	No a.h.d. more PS	41.01	2.35	9993492	103.78	e1449 a131 s1353 a145 r2993
AcerMC+Pythia	No a.h.d. less PS	41.01	2.35	9994995	103.8	e1449 a131 s1353 a145 r2993
MC@NLO+Herwig	No a.h.d. ren/fac (down var.)	89.47	1.08	9989490	81.11	e1468 a131 s1353 a145 r2993
MC@NLO+Herwig	No a.h.d. ren/fac (up var.)	68.51	1.40	9982491	76.64	e1468 a131 s1353 a145 r2993
Alpgen+Herwig	Dilepton +0p	3.47	1.79	194499	31.26	e887 s1372 s1370 r3043 r2993
Alpgen+Herwig	Dilepton +1p	3.40	1.79	159999	26.24	e887 s1372 s1370 r3043 r2993
Alpgen+Herwig	Dilepton +2p	2.11	1.79	336897	89.05	e887 s1372 s1370 r3043 r2993
Alpgen+Herwig	Dilepton +3p	0.94	1.79	148000	87.81	e835 s1372 s1370 r3043 r2993
Alpgen+Herwig	Dilepton +4p	0.33	1.79	60000	101.40	e835 s1372 s1370 r3043 r2993
Alpgen+Herwig	Dilepton +5p	0.13	1.79	25000	107.25	e835 s1372 s1370 r3043 r2993
Alpgen+Herwig	Inc. $t\bar{t} + bb + 0$p	0.92	1.79	399298	242.06	e835 s1310 s1300 r3043 r2993
Alpgen+Herwig	Inc. $t\bar{t} + cc + 0$p	1.76	1.79	399998	126.75	e835 s1310 s1300 r3043 r2993
AcerMC+Pythia	$Wt \rightarrow$ incl.	14.79	1.06	974897	61.90	e835 s1310 s1300 r3043 r2993

Table 3.4: $t\bar{t}$ and single top simulation samples used in the dilepton analysis. The samples do not include all hadronic decays (No a.h.d.). The Protos+Pythia sample is used for the nominal analysis in the dilepton channel, the MC@NLO+Herwig sample is used for the nominal analysis in the single lepton channel. Other samples are used for the evaluation of systematic uncertainties.

CHAPTER 4

b-tagging calibration with $t\bar{t}$ events

Many physics studies at hadron colliders, such as Higgs boson (e.g. $H \to b\bar{b}$) analysis and searches for new physics phenomena, look for jets originating from b quarks in the final state. The b-tagging algorithms, which are designed to identify such jets, are thus of great importance and it is crucial to calibrate their performance directly with data by measuring the b-tagging efficiency and the mis-tag rates. Due to the close-to-unity branching fraction $\mathcal{B}(t \to Wb)$, $t\bar{t}$ events provide a sample rich in b-jets, which is ideal for studying the b-tagging performance.

In the initial phase of the data taking in LHC Run 1, ATLAS relied on the b-tagging calibration methods using jets containing muons created from large numbers of dijets events. As the ATLAS physics program advanced, the experiment collected enough top quark pair events to calibrate b-tagging algorithms with $t\bar{t}$ events. Calibration methods using the $t\bar{t}$ sample provide measurements of the b-tagging efficiency for jets with high transverse momentum which are beyond the reach of the muon-based methods.

This chapter focuses on the principles of the b-tagging techniques and presents results of the b-tagging calibration with the kinematic selection method in the $t\bar{t}$ single lepton channel. The kinematic selection method measures the b-tagging efficiency by exploiting the kinematics of the top quark pair decays and the flavour composition of the jets in the final states. The results of the calibration are p_{T}-dependent scale factors for jets in the p_{T} range of 25 to 300 GeV. The scale factors correct the b-tagging efficiency in simulation to the level measured in data. The analysis was performed on the full 2011 data sample of 4.7 fb^{-1} pp collisions collected by the ATLAS detector. The results presented in this chapter were made public in a conference note dedicated to the $t\bar{t}$ calibration methods [83] and a publication summarising the b-tagging performance with data collected by the ATLAS detector in 2011 [124]. They were also presented by the author at the ICHEP conference in Melbourne in 2012 [125].

4.1 Jets originating from b quarks

Jets originating from the decay of b quarks have several features that allow to distinguish them from other jets. A b quark undergoes hadronisation and creates a b hadron. The b hadrons have a lifetime of approximately 1.5 ps, which, for a particle with $p_{\mathrm{T}} = 50$ GeV, corresponds to a mean decay length of 5 mm. This is much more than the resolution of the primary vertex, which results in the ability to reconstruct the secondary vertex in the point of decay of the b hadron. This distinctive signature can be used to identify jets originating from b quarks. Due to the b quark's large mass, b-jets are also

characterised by a higher number of tracks (high multiplicity of the decay products). About 20% of the b-jets have a muon from the semileptonic decays of b and c hadrons. These muons usually have a low p_{T} and a large angle with respect to the jet axis. A sketch of a b-jet highlighting some of its unique features is presented in figure 4.1 a).

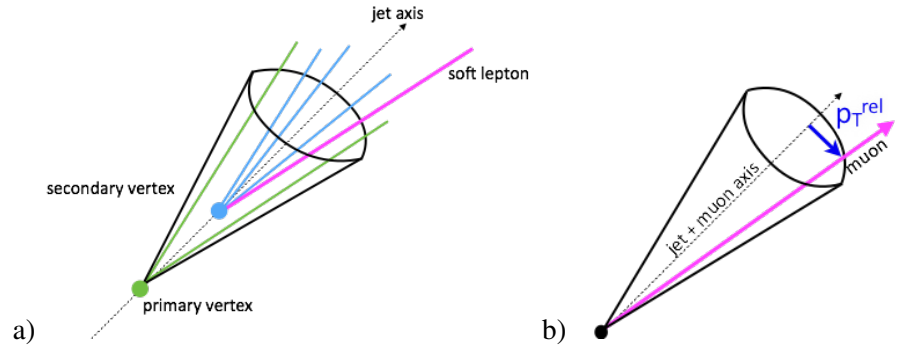

Figure 4.1: a) Tracks forming the primary and secondary vertex originating from the production and decay of a b quark. b) The $p_{\mathrm{T}}^{\mathrm{rel}}$ vector of a soft muon inside a jet.

The identification of these features requires an inner detector with a high resolution to measure trajectories of the particles within the jet and to identify the vertices. The precision of the reconstruction of the position of the vertex increases with the multiplicity of the associated tracks. In minimum bias events it is 300 μm in x and y (600 μm for z) for just 2 tracks and 20 μm (35 μm) for 70 tracks [124]. Due to the pile-up effect, there are multiple hadron interactions and thus multiple vertices along the beam axis. The selected primary vertex is the one with the highest square sum of p_{T} of associated tracks. The displacement of the secondary vertex can be measured with the transverse and longitudinal impact factors: d_0 and z_0, the distance between the primary and secondary vertices in the x-y plane and along the beam axis, respectively.

The b-tagging algorithm also requires a calorimeter detector with a high granularity to precisely measure the direction, energy and isolation of the jet and a muon detector with high efficiency and good resolution together with the inner detector to identify muon decays from the b hadrons. It is also crucial to match measurements from the subdetectors and correctly assign all particles belonging to a jet. b-jets are reconstructed using the same anti-k_t algorithm as described in section 3.1.

4.2 b-tagging algorithms

The aim of the b-tagging algorithms is to recognise jets originating from b quarks. To evaluate the b-tagging algorithm performance and the calibration, jets are divided in three categories: b-jets, c-jets originating from c quarks and light-flavour jets originating from u, d and s quarks, as well as gluons. The performance of a b-tagging algorithm can be assessed by studying the efficiency of correctly tagging b-jets and rejecting other jets. The rejection rate is defined as the ratio of all light-flavour jets to those tagged by the b-tagging algorithm. Figure 4.2 shows rejections rate as a function of b-tagging efficiency for various b-tagging algorithms.

The b-tagging algorithms apply the following additional track quality criteria to reject fake tracks (not all hits originate from the same charged particle), tracks from long-lived particles other than b hadrons (e.g. K_{S}, Λ) and tracks originating from material interactions (photon conversion, hadronic interactions) [124]:

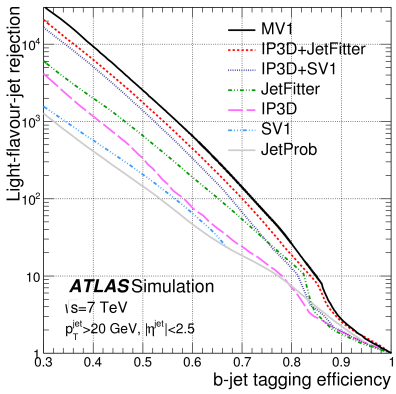

Figure 4.2: Expected rejection rate as a function of the b-jet tagging efficiency for various b-tagging algorithms [124].

- Track has at least 7 precision hits (pixel or SCT), from which at least 2 are pixel hits (1 in the first layer),
- p_{T} of the track: $p_{\mathrm{T}}^{\mathrm{track}} > 1$ GeV and
- Impact parameter with respect to the primary vertex: $|d_0| < 1$ mm and $|z_0| \sin\theta < 1.5$ mm.

Vertex-based algorithms use looser selection requirements, because they engage their own vertex reconstruction strategies. The algorithms used during LHC Run I are described in detail in reference [124], from which the information below was taken.

4.2.1 Impact parameter based algorithms

The impact parameter of a track is calculated with respect to the primary vertex. In the case of a b hadron decay, the secondary vertex is located "after" the primary vertex on the jet axis[1] and it is associated with a positive value of the impact parameter. When the secondary vertex is located "before" the primary vertex, it is assigned a negative sign.

An example of an impact parameter based b-tagging algorithm is IP3D. It engages a log-likelihood ratio of each track using probability density functions of 2-dimensional impact parameter significance $S = (d_0/\sigma_{d_0}, z_0/\sigma_{z_0})$ of the tracks in b-jets and light-flavour jets obtained from simulation. σ_{d_0} and σ_{z_0} are the reconstruction resolutions. The b-tagging weight of a jet is built by summing the log-likelihood ratios of the tracks associated to the jet.

4.2.2 Vertex based algorithms

Unlike the impact parameter based algorithms, which focus separately on each of the tracks associated with a jet, the vertex based algorithms aim at identifying the secondary vertex. The secondary vertex candidates are built from pairs of significantly displaced tracks from the primary vertex. Invariant mass requirements are applied to reject vertices originating from other long-lived particles and photon conversions. The position is ensured to be off the tracker layers to eliminate tracks stemming from material interactions. All remaining track pairs are then tested against the hypothesis of being generated

[1] The jet axis found with calorimeter information.

from a common secondary vertex [126]. Then, the flight length L_{3D}, the distance between the secondary and the primary vertex, is calculated.

The SV0 b-tagging algorithm uses the flight length significance $L_{3D}/\sigma_{L_{3D}}$ to separate b-jets from the light-flavour jets. It demonstrates a better rejection rate than the impact parameter based algorithms, but requires reconstruction of the inclusive secondary vertex, which succeeds only for approximately 70% of the b-jets.

The SV1 algorithm relies on the same procedure to identify the secondary vertex, but, similarly to the IP3D algorithm, engages the log-likelihood ratio method to identify the b-jet. The SV1 algorithm uses as discriminating variables the *vertex mass*, which is defined as the invariant mass of the tracks building the secondary vertex; the fraction of the energy carried by those tracks with respect to all tracks; the number of two-track vertices and ΔR between the calorimeter jet axis and the line connecting the primary and secondary vertices. The vertex mass and the energy fraction distributions for three flavours of jets are presented in figure 4.3 a) and b). The drawback of the SV1 algorithm is, that it heavily depends on the b hadron decay modelling in the simulation.

The JetFitter algorithm applies a different strategy than SV0 and SV1. It aims at reconstructing the full b quark decay chain inside the jet. JetFitter is an artificial neural network algorithm with 8 input nodes: number of vertices with at least two tracks, total number of tracks in each of those vertices, number of additional single-track vertices on the b hadron flight path, the vertex mass, the energy fraction, flight length significance L/σ_L, jet p_{T} and $|\eta|$. The network topology consists of two hidden layers with 12 and 7 nodes. The algorithm has three output nodes, corresponding to the b-jet, c-jet and light-flavour jet hypotheses.

4.2.3 Combined tagging algorithms

Combining the impact parameter based and the secondary vertex based algorithms allows to improve the performance of b-tagging by exploiting the advantages of a particular algorithm and diminishing its limitations. The simplest example is the IP3D+SV1 algorithm, which uses a sum of weights of the IP3D and SV1 taggers. The IP3D+JetFitter algorithm applies the same artificial neural network as the JetFitter with the IP3D weight as an additional input node and the number of nodes in the hidden layers is increased to 14 and 9, respectively.

The MV1 algorithm is another neural network algorithm. It uses the weights of the SV1, IP3D and IP3D+JetFitter algorithms as input. The network consists of two hidden layers with three and two nodes and a single output node. The distribution of the MV1 weight is presented in figure 4.3 c). Because of

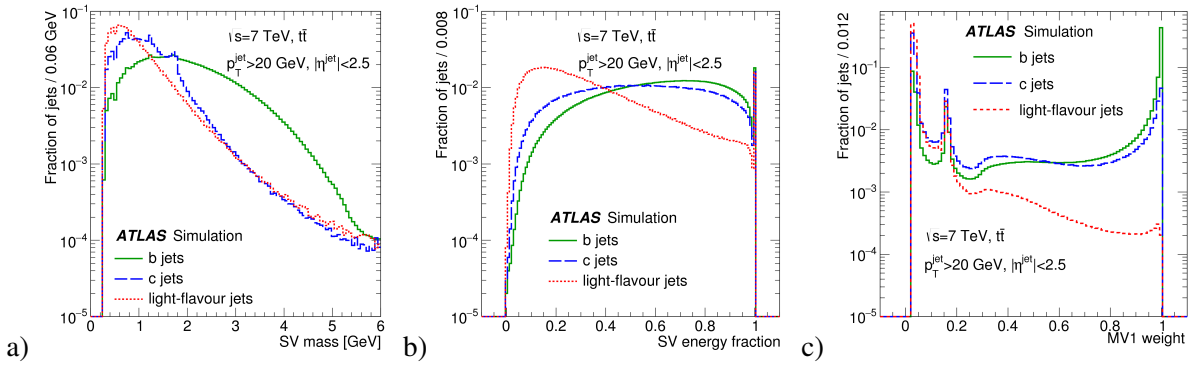

Figure 4.3: a) Vertex mass, b) energy fractions and c) MV1 weight for different flavours of jets. The spike of the MV1 weight distribution around 0.15 corresponds to the jets in which no secondary vertex was identified [124].

its excellent performance, MV1 is the most commonly used b-tagging algorithm in ATLAS in Run I.

4.3 Calibration of the b-tagging algorithms

The b-tagging algorithms use discriminants developed with simulation. Therefore, the performance of the b-tagging algorithms has to be verified using data, in order to correct for mismodellings in Monte Carlo simulation. The results of the calibration are presented in the form of p_{T}-dependent scale factors defined as

$$\kappa_{\varepsilon_b}^{\mathrm{data/sim}}(p_{\mathrm{T}}) = \frac{\varepsilon_b^{\mathrm{data}}(p_{\mathrm{T}})}{\varepsilon_b^{\mathrm{sim}}(p_{\mathrm{T}})}, \tag{4.1}$$

where $\varepsilon_b^{\mathrm{sim}}$ ($\varepsilon_b^{\mathrm{data}}$) is the fraction of b-jets which are tagged in simulation (data). In simulation, the flavour of the jet is determined by matching to the generator level partons. The $\varepsilon_b^{\mathrm{data}}$ is estimated with one of the methods described in the next section. In physics analyses, these p_{T} dependent scale factors are then applied as weights per jet to re-weight the Monte Carlo simulation, to correct the b-tagging efficiency to the values measured in data.

The mean b-tagging efficiencies $\langle\varepsilon_b^{\mathrm{sim}}\rangle$ of the individual operating points (tag weight w) of a tagger are derived from an inclusive simulated $t\bar{t}$ sample. A total of twelve operating points are calibrated, referred to as:

- **SV0**
  - SV0 50%: $\langle\varepsilon_b^{\mathrm{sim}}\rangle = 50\%$, $w > 5.65$
- **IP3D+SV1**
  - IP3D+SV1 60%: $\langle\varepsilon_b^{\mathrm{sim}}\rangle = 60\%$, $w > 4.55$
  - IP3D+SV1 70%: $\langle\varepsilon_b^{\mathrm{sim}}\rangle = 70\%$, $w > 1.70$
  - IP3D+SV1 80%: $\langle\varepsilon_b^{\mathrm{sim}}\rangle = 80\%$, $w > -0.80$
- **IP3D+JetFitter**
  - IP3D+JetFitter 57%: $\langle\varepsilon_b^{\mathrm{sim}}\rangle = 57\%$, $w > 2.20$
  - IP3D+JetFitter 60%: $\langle\varepsilon_b^{\mathrm{sim}}\rangle = 60\%$, $w > 1.80$
  - IP3D+JetFitter 70%: $\langle\varepsilon_b^{\mathrm{sim}}\rangle = 70\%$, $w > 0.35$
  - IP3D+JetFitter 80%: $\langle\varepsilon_b^{\mathrm{sim}}\rangle = 80\%$, $w > -1.25$
- **MV1**
  - MV1 60%: $\langle\varepsilon_b^{\mathrm{sim}}\rangle = 60\%$, $-\log(w) > 0.905363$
  - MV1 70%: $\langle\varepsilon_b^{\mathrm{sim}}\rangle = 70\%$, $-\log(w) > 0.601713$
  - MV1 75%: $\langle\varepsilon_b^{\mathrm{sim}}\rangle = 75\%$, $-\log(w) > 0.404219$
  - MV1 85%: $\langle\varepsilon_b^{\mathrm{sim}}\rangle = 85\%$, $-\log(w) > 0.0714225$

4.3.1 Measurement of b-tagging efficiency with jets containing muons

The baseline scale factors for the physics analyses with the dataset collected in 2011 were obtained with calibration methods using jets containing muons. These methods use dijet events, which have a high production cross section and ensured a big enough data sample even in the early stages of the data taking

in 2010. Jets containing muons are selected with the *soft muon tagger* (SMT) algorithm which identifies muons with low p_{T} in the ΔR proximity of the jet. The discussion in this section follows reference [124].

The first method, *pTrel*, exploits the difference in the distribution of $p_{\mathrm{T}}^{\mathrm{rel}}$, the component of muon's momentum transverse to the muon-jet axis, for different flavours of jets. The $p_{\mathrm{T}}^{\mathrm{rel}}$ vector is sketched in figure 4.1 b). Muons originating from b quarks have on average a higher $p_{\mathrm{T}}^{\mathrm{rel}}$ compared to muons from c and light-flavour jet, as shown in figure 4.4. The fractions of b-, c-, and light-flavour jets are extracted

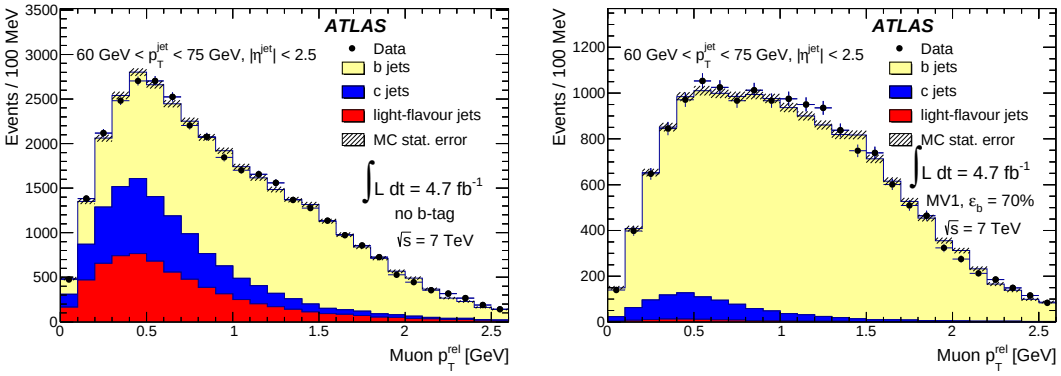

Figure 4.4: Example of a template fit to the $p_{\mathrm{T}}^{\mathrm{rel}}$ distribution in data before (left) and after (right) b-tagging.

by fitting the $p_{\mathrm{T}}^{\mathrm{rel}}$ distribution templates to data before and after tagging with the algorithm under test. The templates are obtained from the Monte Carlo simulation. The b-tagging efficiency measured by the pTrel method can be expressed as

$$\varepsilon_b^{\mathrm{data}} = \frac{f_b^{\mathrm{tag}} N^{\mathrm{tag}}}{f_b^{\mathrm{tag}} N^{\mathrm{tag}} + f_b^{\mathrm{untag}} N^{\mathrm{untag}}} \cdot C, \tag{4.2}$$

where f_b^{tag} and N^{tag} are the fraction of b-jets and the total number of jets in the tagged sample, and f_b^{untag} and N^{untag} in the sample with jets not tagged by the algorithm under study. The C component corrects for the differences in the b hadron direction modelling and the heavy-flavour contamination of the light-flavour jets template.

The *system8* method does not rely on the simulation as heavily as the pTrel method, as it does not use templates from simulation. Instead, it applies the following criteria to create subsamples with different content of b-jets:

- Presence of a muon in the jet tagged by the SMT has $p_{\mathrm{T}}^{\mathrm{rel}} > 700$ MeV (*muon tagging*, MT).
- Jet tagged by the SMT is also tagged with the b-tagging algorithm under test (*lifetime based*, LT).
- At least one more jet is present in the event, apart from the one tagged by SMT, which has a reconstructed secondary vertex and a signed decay length significance greater than 1. This requirement divides the dataset into two samples: the p sample that fulfils the requirement, and the n sample that does not fulfil it.

The following system of eight equations describes jets fulfilling combinations of any two of the above criteria and allows to extract the b-tagging efficiency of the algorithm under test, $\varepsilon_b^{\mathrm{LT}}$:

$$
\begin{aligned}
n &= n_b + n_{cl}, \\
p &= p_b + p_{cl}, \\
n^{\mathrm{LT}} &= \varepsilon_b^{\mathrm{LT}} n_b + \varepsilon_{cl}^{\mathrm{LT}} n_{cl}, \\
p^{\mathrm{LT}} &= \alpha_6 \varepsilon_b^{\mathrm{LT}} p_b + \alpha_4 \varepsilon_{cl}^{\mathrm{LT}} p_{cl}, \\
n^{\mathrm{MT}} &= \varepsilon_b^{\mathrm{MT}} n_b + \varepsilon_{cl}^{\mathrm{MT}} n_{cl}, \\
p^{\mathrm{MT}} &= \alpha_5 \varepsilon_b^{\mathrm{MT}} p_b + \alpha_3 \varepsilon_{cl}^{\mathrm{MT}} p_{cl}, \\
n^{\mathrm{LT,MT}} &= \alpha_1 \varepsilon_b^{\mathrm{LT}} \varepsilon_b^{\mathrm{MT}} n_b + \alpha_2 \varepsilon_{cl}^{\mathrm{LT}} \varepsilon_{cl}^{\mathrm{MT}} n_{cl}, \\
p^{\mathrm{LT,MT}} &= \alpha_5 \alpha_6 \alpha_7 \varepsilon_b^{\mathrm{LT}} \varepsilon_b^{\mathrm{MT}} p_b + \alpha_3 \alpha_4 \alpha_8 \varepsilon_{cl}^{\mathrm{LT}} \varepsilon_{cl}^{\mathrm{MT}} p_{cl}.
\end{aligned}
\tag{4.3}
$$

In this equation, ε_{cl} denotes the tagging efficiency for c-jets and light-flavour jets. The correction factors α_1,...,α_8 account for the correlations between the tagging efficiencies in the p and n samples.

The uncertainty associated with the scale factors determined by the pTrel and system8 methods originates mostly from the accuracy of the heavy-flavour production, decay and fragmentation modelling in the simulation. Other significant uncertainty sources are the jet energy scale and resolution, as well as pile-up. The combined results of both calibration methods in form of data-to-simulation scale factors are presented in figure 4.8 as grey blocks (the height of the block corresponds to the total uncertainty). Both approaches rely on low-p_{T} jet triggers to enable the measurement for the low-p_{T} jets, which has some statistical limitation. Moreover, the $p_{\mathrm{T}}^{\mathrm{rel}}$ variable is not anymore a good discriminant between b-, c- and light-jets for the high-p_{T} jets. Thus the methods using jets containing muons cannot be applied to jets with a very high p_{T}.

4.3.2 Measurement of b-tagging efficiency using $t\bar{t}$ events

At the LHC the large $t\bar{t}$ production cross section offers an alternative source of events enriched in b-jets. The distinctive topology with high-p_{T} leptons, multiple jets, and large missing transverse momentum is relatively easy to trigger on and to reconstruct. With the integrated luminosity of 4.7 fb^{-1} collected during 2011 with pp collisions at the centre-of-mass energy of $\sqrt{s} = 7$ GeV, the b-tagging calibration methods based on $t\bar{t}$ selections have become competitive for the first time. In addition to providing b-tagging calibration measurements in an inclusive b-jet sample rather than a sample of b-jets containing muons, these methods also allow to extend the calibrated jet p_{T} range. This section presents results of the kinematic selection method and an overview of other $t\bar{t}$ calibration methods applied to the 2011 dataset.

Kinematic selection method

The kinematic selection method in the single lepton channel is based on the standard $t\bar{t}$ selection criteria which require at least four jets, from which at least one jet has to be b-tagged with the MV1 tagger at a tagging efficiency of 70%, described in section 3.2.1. This requirement allows to increase the signal-to-background ratio, as well as the contribution of b-jets in the analysed jet sample. However, the information which jet was tagged in the event selection is not further used in this analysis. By decreasing the background contribution and increasing the b-purity, the impact of the uncertainties from the background normalisation and flavour composition were reduced.

In the measurement of the b-tagging efficiency, only the four jets with the highest p_{T} are considered and are assumed to come from the top quark pair decay. The b-tagging rate of the algorithm under test

is measured by a modified tag-and-probe method adapted to the events with four jets, among which two are expected to be b-jets:

- If the leading jet is b-tagged by the algorithm under test, the next three jets are used for the measurement (L234 sample).
- If the next-to-leading jet is b-tagged, the leading jet is used (L1 sample).

The L1 and L234 selections are schematically presented in figure 4.5. The jets in the $t\bar{t}$ event are sorted

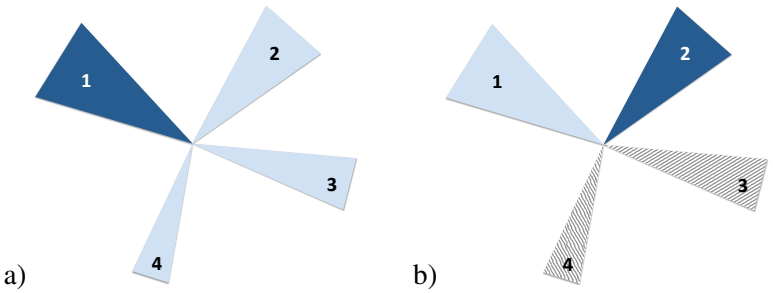

Figure 4.5: Jet samples used for the b-tagging efficiency measurement with the kinematic selection method. a) L234 sample: jet 1 is tagged, jets 2, 3 and 4 are used for the measurement, b) jet 2 is tagged, jet 1 is used for the measurement, jets 3 and 4 are not considered. Jets are ordered by p_{T}.

according to their p_{T} value to help divide them into L1 and L234 samples. However, after that initial step, the b-tagging efficiency is measured with individual jets, rather than events. The numbers of jets from both L1 and L234 selections are used to fill the bins in p_{T} and the b-tagging efficiency is measured in each p_{T} bin separately. The b-tagging efficiency in each p_{T} bin is derived from the following formula

$$\varepsilon_b = \frac{1}{f_{b\text{-jets}}} \cdot \left(f_{b\text{-tag}} - \varepsilon_c f_{c\text{-jets}} - \varepsilon_l f_{l\text{-jets}} - \varepsilon_{\text{multijet}} f_{\text{multijet}} \right). \tag{4.4}$$

Here, $f_{b\text{-tag}}$ is the fraction of jets b-tagged in data, $f_{b\text{-jets}}$, $f_{c\text{-jets}}$ and $f_{l\text{-jets}}$ are the expected fractions of b-, c- and light-flavour jets from simulated events and ε_c and ε_l are the mis-tag efficiencies. To estimate the multijet fraction f_{multijet}, the yields predicted by the matrix method described in section 3.3.2 are used. The fractions $f_{b\text{-jets}}$, $f_{c\text{-jets}}$, $f_{l\text{-jets}}$ and f_{multijet} are calculated with respect to the sum of jets from the lumi-weighted Monte Carlo simulation and jets from the matrix method estimation. The flavour fractions follow the relation $f_{b\text{-jets}} + f_{c\text{-jets}} + f_{l\text{-jets}} + f_{\text{multijet}} = 1$.

Separate parameters f_{multijet} and $\varepsilon_{\text{multijet}}$ for the multijet background were introduced, because the multijet background is estimated directly from the data and there is no information about the fractions of b-jets, c-jets and light jets in this jet sample. The b-tagging efficiency of the jets from the multijet events $\varepsilon_{\text{multijet}}$ is defined as a ratio of the b-tagged jets from the multijet events to the total number of jets from the multijet events and it is independent from the flavour of the jet. It is measured in a control region with a sample of events with leptons passing looser selection criteria, as the multijet events are rich in non-isolated leptons. Loose muons are not required to fulfil any isolation criteria, while the isolation for loose electron is less strict than for the tight used in the baseline event selection. For details see section 3.3.2. Moreover, in the selection of events with loose muons, muons overlapping with re-calibrated jets are removed, which is different from the default selection, where not re-calibrated jets are used. The purpose of the overlap removal is to suppress muons from heavy-flavour jets in multijet events. However, the mismatch between the jet p_{T} used for the overlap removal (not re-calibrated jets) and for the jet selection (re-calibrated jets) in the baseline selection [127] increases the efficiency of

finding such a muon and hence finding an event with a loose muon and a jet from a multijet event. In case the not re-calibrated jet p_{T} is below the jet p_{T} requirement, the muon appears isolated from jets for the overlap removal step, but it is not after the object and event selection. This leads to a higher b-tagging efficiency for multijet events for events with a leading jet p_{T} between 25 GeV and 30 GeV as compared to the other jet p_{T} bins. These jets were more likely to satisfy the p_{T} threshold after re-calibration. Tight muons are much less affected due to the more stringent isolation requirements. The problem is solved by using re-calibrated jets for the jet-muon overlap removal, as can be seen in figure 4.6 a). More

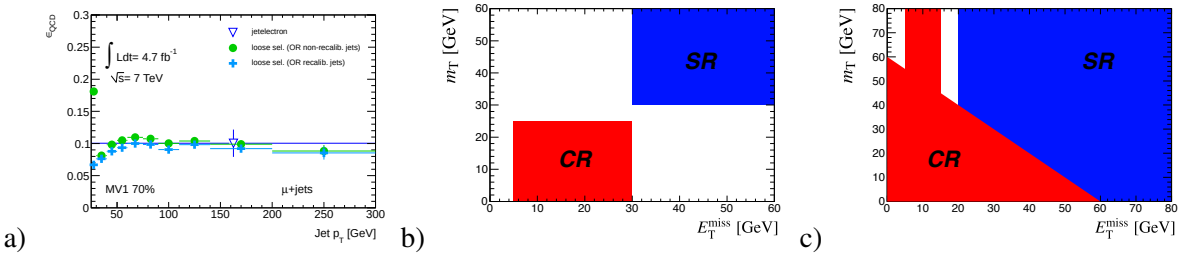

Figure 4.6: a) b-tagging efficiency of jets from multijet events in the muon channel. A large difference is observed if the jet-muon overlap removal is done with re-calibrated jets (blue crosses) or with not re-calibrated jets (green dots). The estimate from the so-called jetelectron model (dark blue triangle) [128] is used to evaluate the systematic uncertainty on the b-tagging efficiency of jets from multijet events. The control region in which the b-tagging efficiency of multijet events jets is measured for b) the electron channel and c) the muon channel [85].

information about the jet re-calibration is available in reference [127].

The control region is obtained by reverting the $E_{\mathrm{T}}^{\mathrm{miss}}$ and m_{T} criteria described in section 3.1 and leaving a 5 GeV band to ensure a better separation from the signal region and avoid events with $E_{\mathrm{T}}^{\mathrm{miss}}$ close to zero, as illustrated in figure 4.6 b) and c):

- electron channel: 5 GeV $< E_{\mathrm{T}}^{\mathrm{miss}} <$ 30 GeV and $m_{\mathrm{T}} <$ 25 GeV,
- muon channel: 5 GeV $< E_{\mathrm{T}}^{\mathrm{miss}} <$ 15 GeV or $E_{\mathrm{T}}^{\mathrm{miss}} + m_{\mathrm{T}} <$ 60 GeV.

The predicted $t\bar{t}$, single top, diboson, W+jets and Z+jets contributions obtained from Monte Carlo simulation are subtracted from the events measured in the control region in the data.

The mis-tagging efficiencies for c- and light-flavour jets that are tagged as b-jets, ε_c and ε_l, are taken from the Monte Carlo simulation, corrected for data-to-simulation scale factors [127], and are obtained from the sum of simulated events from all processes, assuming the expected jet kinematics and the expected signal and background contributions to the analysed sample.

Systematic uncertainties

The uncertainties in the b-tagging calibration with $t\bar{t}$ events with the kinematic selection method originate from the limited precision of the modelling of the $t\bar{t}$ processes, modelling and reconstruction of the heavy-flavour jets, as well as object recognition and reconstruction. Effects of the following sources were studied to asses the uncertainty on the measured scale factors:

- **Mis-tagging efficiencies** -The mis-tagging efficiencies for c- and light-flavour jets directly enter the expression used to obtain the b-tagging efficiency. The efficiencies in simulated events are adjusted by the data-to-simulation scale factors [124] and the efficiencies are then varied within the uncertainties of these correction factors, which range from approximately 12% to 50%.

- **$t\bar{t}$ cross section** - The $t\bar{t}$ cross section is used to normalise the expected $t\bar{t}$ signal. The $t\bar{t}$ cross section is varied by 10% [129] and the effect on the final result is taken as a systematic uncertainty.

- **Background normalisation** - The dominant background comes from W+jets production, and the normalisation of this background is varied by 13%.

  The multijet background measurement is varied by 50% in the e+jets channel, which is a conservative assumption, but allows to cover any differences in kinematic distributions arising from mismodelling of the multijet background. In the μ+jets channel by comparing estimates based on two different control regions, the uncertainty on the multijet sample normalisation can be reduced to 20%.

  The single top, diboson and Z+jets backgrounds are normalised to their theoretical cross sections. The single top Wt channel is varied by 10% [130], the t- and s-channels by 14% [131, 132], the diboson sample by 5% [133] and the Z+jets by 60%.

- **Background flavour composition** - The flavour composition of all background samples except W+jets is taken from simulation and not assigned a systematic uncertainty. For the W+jets background the scale factors for heavy-flavour (HF) events ($Wb\bar{b}$+jets, $Wc\bar{c}$+jets and Wc+jets) are varied within their uncertainties. Sources of systematic uncertainties that affect the HF scale factors in W+jets events often also affect the calibration method directly. Examples of such systematic uncertainties are uncertainties on the $t\bar{t}$ cross section and the W+jets normalisation. To account for such correlations, these uncertainties are evaluated by coherently evaluating their impact in all components of the analysis.

  The b-tagging rate $\varepsilon_{\text{multijet}}$ for jets from the multijet background is measured in a control region in data and its uncertainty is obtained by comparing baseline result with the b-tagging efficiencies measured in events from the jet electron model [128].

- **Jet reconstruction efficiency, energy scale and resolution** - Fluctuations in the jet energy scale (JES) [134], jet energy resolution (JER) and jet reconstruction efficiency (JRE) measurements may cause jets to migrate between p_{T} bins, which not only affects the numbers of jets in particular bins, but also influences the correction factors that are applied to simulation, such as corrections of the ε_l and ε_c, which depend on p_{T} and η of jet [124].

  The systematic uncertainty originating from the JES is evaluated by scaling the p_{T} of each jet in the simulation up and down by the estimated uncertainty on the jet energy scale. The nominal JER in Monte Carlo simulation and data are found to be compatible, but a systematic uncertainty is assigned to cover the effect of possible residual differences by smearing the jet energy in simulated events. The full difference with the nominal result is taken as the uncertainty. The JRE was derived using a tag-and-probe method in dijet events and found to be compatible to a measurement using simulated $t\bar{t}$ events. However, a systematic uncertainty is assigned to cover the effect of possible residual differences by randomly rejecting jets based on the measured JRE.

- **Trigger, lepton identification efficiency, energy scale and resolution** - The modelling in simulation of the lepton trigger, reconstruction and selection efficiencies as well as the energy resolution and scaling (e trig., μ trig., e recID, μ recID, e smear., μ smear, MC e-en.sc.) has been assessed using $Z \to ee$ and $Z \to \mu\mu$ events.

- **Generator and parton shower dependence** - The baseline generator MC@NLO+HERWIG may not correctly predict the kinematic distribution of the $t\bar{t}$ events, which may result in differences

in the acceptance and flavour composition of the selected events. A systematic uncertainty is assigned to the choice of Monte Carlo generator (Gen.) by comparing the results produced with the baseline $t\bar{t}$ generator with those produced with events simulated with POWHEG+HERWIG. Uncertainties in parton shower modelling (Fragm.) are estimated by comparing results between event generated with POWHEG+HERWIG and those generated using POWHEG+PYTHIA.

- **Initial and final state radiation** - Initial and final state radiation (IFSR) directly affects the flavour composition of the $t\bar{t}$ events. The associated systematic uncertainty due to IFSR is estimated by studies using samples generated with ACERMC [115] interfaced to PYTHIA, and by varying the parameters controlling ISR and FSR in a range consistent with experimental data [135].

- **Pile-up** - No explicit uncertainty is assigned to the effect of pile-up as the Monte Carlo simulation is reweighted on an event-by-event basis to reproduce the distribution of the average number of primary vertices measured in data. Uncertainties induced by pile-up indirectly enter the analysis through pile-up-related uncertainties in object modelling such as the jet energy scale and missing transverse momentum corrections ($E_{\mathrm{T}}^{\mathrm{miss}}$ pile-up).

- **Luminosity** - The uncertainty in the integrated luminosity affects the measurement of the b-tagging efficiency due to the change in the overall normalisation of the backgrounds estimated from simulation. The integrated luminosity has been measured with a precision of 3.9% and is taken as a systematic uncertainty.

Results

The kinematic selection method can measure the b-tagging efficiency separately in the e+jets and μ+jets channels, as well as in their combination. Since these samples are statistically uncorrelated, the combination is done by summing jets selected from both channels. No significant difference was observed between results from the e+jets and the μ+jets channels. This section presents only results from the combination of the two channels. Figure 4.7 shows a comparison of the b-tagging efficiency meas-

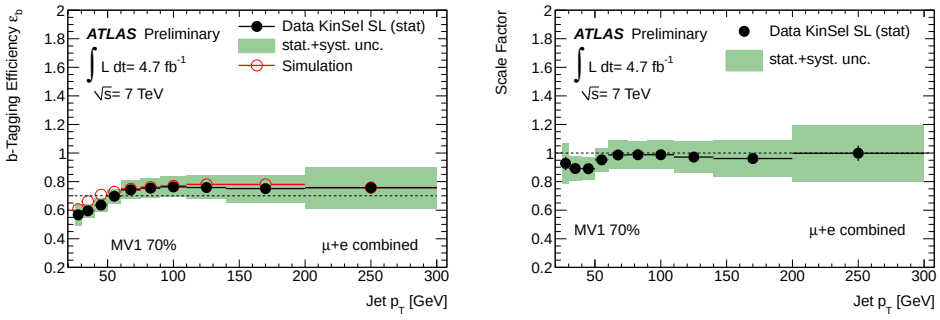

Figure 4.7: The b-tagging efficiency measured in data with the kinematic selection method compared to that in simulation (left) and the resulting scale factors (right) for the MV1 algorithm at 70% b-tagging efficiency. The dashed lines correspond to the $\langle \varepsilon_b^{\mathrm{sim}} \rangle$ for the b-tagging efficiency graph and to the value of 1 for the scale factors. The error bars show the statistical uncertainties while the green band indicates the total uncertainty [83].

ured in simulation and data, as well as the resulting scale factors as defined in equation 4.1 for the MV1 algorithm at the working point corresponding to the 70% efficiency. Table 4.1 summarises the values of the uncertainties on the scale factors. Separate results for each of the channels can be found in appendix C, together with the b-tagging efficiency measured for simulated events in different Monte Carlo samples. Moreover, figures for other working points of the MV1 algorithm, as well as for other algorithms listed in section 4.3, are also included in the appendix C.

p_{T}[GeV]	25-30	30-40	40-50	50-60	60-75	75-90	90-110	110-140	140-200	200-300
IFSR	±4.3	±3.2	±2.7	±3.1	±3.6	±4.0	±3.6	±4.0	±5.2	±8.0
Gen.	±0.5	±0.2	±0.0	±0.2	±0.3	±0.1	±0.6	±1.2	±1.9	±3.9
Fragm.	±0.1	±1.0	±1.9	±1.1	±2.0	±1.1	±0.8	±0.7	±0.3	±2.9
Diboson	±0.0	±0.0	±0.0	±0.0	±0.0	±0.0	±0.0	±0.0	±0.0	±0.0
Single top	±0.0	±0.0	±0.0	±0.0	±0.0	±0.1	±0.1	±0.1	±0.1	±0.2
Z+jets	±0.1	±0.1	±0.1	±0.1	±0.2	±0.2	±0.2	±0.3	±0.4	±0.5
W+jets	±1.8	±1.5	±1.0	±0.8	±0.8	±0.8	±0.7	±0.7	±1.0	±1.3
Mulitjet	±1.5	±1.3	±1.4	±1.7	±1.6	±1.4	±1.6	±1.6	±1.9	±1.9
$t\bar{t}$	±1.0	±0.9	±0.8	±0.9	±0.9	±0.9	±1.0	±1.1	±1.4	±1.5
$\varepsilon_{\mathrm{fake}}$	±1.7	±0.4	±0.2	±0.4	±0.4	±0.4	±0.4	±0.5	±0.5	±0.4
JES	±5.7	±3.2	±2.2	±1.1	±0.8	±0.4	±0.6	±1.2	±1.2	±2.8
JER	±5.0	±0.2	±0.5	±1.4	±0.3	±0.8	±0.6	±0.6	±0.6	±0.7
JRE	±0.0	±0.0	±0.0	±0.0	±0.0	±0.1	±0.0	±0.0	±0.1	±0.0
JVF	±0.2	±0.3	±0.0	±0.0	±0.2	±0.1	±0.0	±0.0	±0.0	±0.4
W+HF SF	±0.2	±0.2	±0.2	±0.2	±0.3	±0.3	±0.4	±0.5	±0.7	±0.9
ε_{c}	±0.6	±0.4	±0.3	±0.3	±0.3	±0.4	±0.4	±0.4	±0.5	±0.7
$\varepsilon_{\mathrm{light}}$	±0.3	±0.3	±0.4	±0.4	±0.6	±0.7	±0.9	±1.1	±1.4	±2.0
$E_{\mathrm{T}}^{\mathrm{miss}}$ cellout	±0.1	±0.0	±0.0	±0.0	±0.0	±0.1	±0.0	±0.1	±0.0	±0.1
$E_{\mathrm{T}}^{\mathrm{miss}}$ pile-up	±0.1	±0.0	±0.0	±0.0	±0.0	±0.0	±0.0	±0.0	±0.0	±0.1
e trig.	±0.0	±0.0	±0.0	±0.0	±0.0	±0.0	±0.0	±0.0	±0.0	±0.0
e smear.	±0.0	±0.0	±0.0	±0.0	±0.0	±0.0	±0.0	±0.0	±0.0	±0.0
e recID	±0.1	±0.0	±0.0	±0.0	±0.0	±0.0	±0.0	±0.0	±0.0	±0.0
MC e-en.sc.	±0.0	±0.0	±0.0	±0.0	±0.0	±0.0	±0.0	±0.0	±0.1	±0.0
μ trig.	±0.0	±0.0	±0.0	±0.0	±0.1	±0.1	±0.1	±0.0	±0.1	±0.1
μ smear.	±0.0	±0.0	±0.0	±0.0	±0.0	±0.0	±0.0	±0.0	±0.0	±0.0
μ recID	±0.0	±0.0	±0.0	±0.0	±0.0	±0.0	±0.0	±0.0	±0.0	±0.0
Lumi	±0.2	±0.2	±0.0	±0.0	±0.0	±0.0	±0.1	±0.1	±0.1	±0.1
Stat.	±5.0	±3.0	±2.6	±2.4	±1.9	±2.0	±1.9	±2.1	±2.6	±5.1
Total Syst.	±9.4	±5.2	±4.4	±4.3	±4.8	±4.8	±4.6	±5.2	±6.6	±10.6
Total	±10.6	±6.0	±5.2	±4.9	±5.1	±5.2	±5.0	±5.6	±7.1	±11.8

Table 4.1: Uncertainties for the kinematic selection method in the single lepton channel (e+jets and μ+jets channels combined). The table shows relative uncertainties (in %) on scale factors for the MV1 algorithm at an operating point corresponding to a 70% tagging efficiency [83].

The kinematic selection method can also be successfully applied to the dilepton $t\bar{t}$ channel. In that case, the tagging efficiency for the two jets with the highest p_{T} is measured and the division into two samples is not applied. Results for the kinematic selection method in the dilepton channel will be discussed together with results from other $t\bar{t}$-based b-tagging calibration methods below.

Other methods

Tag counting

The tag counting method makes use of the fact that each $t\bar{t}$ event is expected to contain exactly two b-jets. If there were no other sources of b-jets and if only b-jets were b-tagged, the expected number of events with two b-tagged jets would be $\varepsilon_b^2 N_{\mathrm{sig}}$, while the number of events with one b-tagged jet would be $2\varepsilon_b\,(1-\varepsilon_b) N_{\mathrm{sig}}$, where N_{sig} is the number of $t\bar{t}$ signal events.

In reality, the mean number of reconstructed (or tagged) b-jets in a $t\bar{t}$ event is not exactly two, since the b-jets from the top quark decays can be out of the detector acceptance, and additional b-jets can be produced through gluon splitting. Moreover, c-jets and light-flavour jets can be tagged as b-jets and consequently contribute to the number of b-tagged jets in the event. These effects are taken into account by evaluating the expected fractions, F_{ijk}, of events containing i b-jets, j c-jets and k light-flavour jets that pass the event selection. The F_{ijk} fractions are estimated from the Monte Carlo simulation and are derived separately for the $t\bar{t}$ signal and various background processes. The expected number of events with n b-jets, $\langle N_n \rangle$, is calculated as the sum of all contributions. The b-tagging efficiency can be extracted by fitting the expected event counts to the observed counts.

The expected number of $t\bar{t}$ signal events with n b-tagged jets is calculated as

$$\begin{aligned}\langle N_n \rangle \;=\; & \sum_{i,j,k} \Big\{ (\sigma_{t\bar{t}} \mathcal{B} A_{t\bar{t}} \mathcal{L} F_{ijk}^{t\bar{t}} + N_{\mathrm{bkg}} F_{ijk}^{\mathrm{bkg}}) \times \\ & \sum_{i'+j'+k'=n} \binom{i}{i'} {\varepsilon_b}^{i'} (1-\varepsilon_b)^{i-i'} \binom{j}{j'} {\varepsilon_c}^{j'} (1-\varepsilon_c)^{j-j'} \binom{k}{k'} {\varepsilon_l}^{k'} (1-\varepsilon_l)^{k-k'} \Big\}, \end{aligned} \tag{4.5}$$

where i, j and k (i', j' and k') represent the number of pre-tagged (tagged) b-, c- and light-flavour jets. $\mathcal{B}$ is the branching fraction to each final state, $A_{t\bar{t}}$ is the event selection efficiency for that particular final state and $\mathcal{L}$ is the integrated luminosity. The binomial coefficients account for the number of combinations in which the n-tags can be distributed. The efficiencies to mis-tag a c-jet or light-flavour jet as a b-jet, ε_c and ε_l respectively, are fixed to the values found in Monte Carlo simulation but with data-driven scale factors applied [136]. N_{bkg} is the number of background events.

To measure the b-tagging efficiency as a function of p_{T}, the n-tag distributions and F_{ijk} fractions are computed in p_{T} bins using only the jets in each event that fall in a given p_{T} bin. Independent fits are performed for each p_{T} bin. Since a single event can contribute to several p_{T} bins, this approach maximises the use of the available jets in the sample. The tag counting method can be used in both the single lepton and the dilepton $t\bar{t}$ channels.

Kinematic fit

The kinematic fit method is applied to events passing the $t\bar{t}$ single lepton channel selection criteria (see section 3.2.1). However, without applying the requirement of at least one jet to be b-tagged. The goal of this method is to provide a mapping between the reconstructed jets and the quarks in the $t\bar{t}$ decay event: b quarks from top quark decays and the quarks originating from the hadronic decay of the W boson. The fit, based on a χ^2 minimization, infers a best estimate for the measured observables. Obey-

ing constraints from the invariant masses of both top quarks and W bosons, and assuming the missing transverse momentum to be solely due to the neutrino, leaves its transverse component as the only unmeasured parameter. All permutations of four jets out of the six leading jets are fitted and the one with the lowest value of χ^2 is retained.

While the kinematic fit selects the correct jet association with a good efficiency, the permutation with the lowest χ^2 in the event is not always the correct one. In addition to the combinatorial background, the sample still contains physics background, such as single top and W+jets events. The single lepton sample can be further purified using an in-situ background estimate. Here, the sample is divided into two orthogonal subsamples based on the tag weights of the jets on the hadronic side of the event (where $W \rightarrow jj$): the first subsample (*signal sample*) is enriched in correct permutations, while the second subsample (*background sample*) is enriched in incorrect mappings. The MV1 b-tagging algorithm at 70% efficiency is used to split the data into the signal and background samples. In the signal sample, on the hadronic side of the event, the jet identified as b-jet is required to be b-tagged and the jets coming from the W are required to not be b-tagged. Additionally, only events with six or less jets passing the p_{T} threshold are selected. In the background sample, one of the jets from the hadronic decay of the W is required to be b-tagged.

The amount of background is estimated by normalising the χ^2 distributions of both samples and the shape is taken from the background sample. The b-tagging efficiency is measured from the background-subtracted tag weight distribution of the jet assigned to the b quark of the leptonic side of the event (where $W \rightarrow l\nu$).

Conclusion

Results of the methods discussed in this section, i.e. the scale factors including all systematic and statistical uncertainties, are summarised in table 4.2. The highest and lowest values of statistical and total systematic uncertainty are presented in table 4.3.

p_{T} [GeV]	TagCount SL	TagCount DL	KinSel SL	KinSel DL	KinFit SL
25-30	0.90±0.34	1.03±0.12	0.93 ± 0.10	1.04 ± 0.13	0.76 ± 0.15
30-40	0.98±0.16	1.01±0.09	0.89 ± 0.05	0.96 ± 0.07	1.03 ± 0.16
40-50	0.96±0.13	1.04±0.05	0.89 ± 0.05	1.01 ± 0.06	0.97 ± 0.10
50-60	0.96±0.06	0.98±0.05	0.95 ± 0.05	0.97 ± 0.06	0.89 ± 0.11
60-75	1.01±0.08	1.04±0.04	0.98 ± 0.05	1.01 ± 0.05	1.04 ± 0.08
75-90	0.93±0.07	0.99±0.04	0.98 ± 0.05	0.96 ± 0.06	0.93 ± 0.13
90-110	0.97±0.10	0.99±0.05	0.98 ± 0.05	0.98 ± 0.06	1.00 ± 0.08
110-140	1.04±0.10	0.98±0.10	0.97 ± 0.05	0.98 ± 0.06	0.97 ± 0.09
140-200	1.00±0.10	0.99±0.10	0.97 ± 0.07	0.99 ± 0.09	1.04 ± 0.09
200-300	1.04±0.20	0.79±0.24	1.00 ± 0.12	0.82 ± 0.15	

Table 4.2: Scale factors for the MV1 algorithm at 70% efficiency measured with 4.7 fb^{-1} of data with the tag counting (TagCount), kinematic selection (KinSel) and kinematic fit (KinFit) method in the single lepton (SL) and dilepton (DL) channels. The uncertainties are symmetrised and include the statistical uncertainty and all systematic uncertainties [125].

Figure 4.8 demonstrates the compatibility of all calibration methods. The individual $t\bar{t}$ based calibration methods, using different selections (single lepton and dilepton) are consistent with each other within uncertainties. Furthermore, all results are in good agreement with the earlier calibration methods

using jets containing muons and extend the range of the scale factors in p_T beyond 200 GeV, which was the limit for the muon based methods, to 300 GeV. The results of the combination of the system8 and p_T^{rel} methods [124], based on a dijet sample, are also shown in figure 4.8.

	TagCount SL	TagCount DL	KinSel SL	KinSel DL	KinFit SL
Stat. unc.	3.7% – 6.4%	2.9% – 9.4%	1.9% – 5.1%	2.1% – 10.7%	5.5% – 17.6%
Syst. unc.	6.5% – 27.2%	5.1% – 23.8%	4.3% – 10.6%	4.2% – 15.1%	6.1% – 12.5%

Table 4.3: The range of statistical and systematic uncertainties throughout the jet p_T bins for the tag counting (TagCount), kinematic selection (KinSel) and kinematic fit (KinFit) method in the single lepton (SL) and dilepton (DL) channels [125].

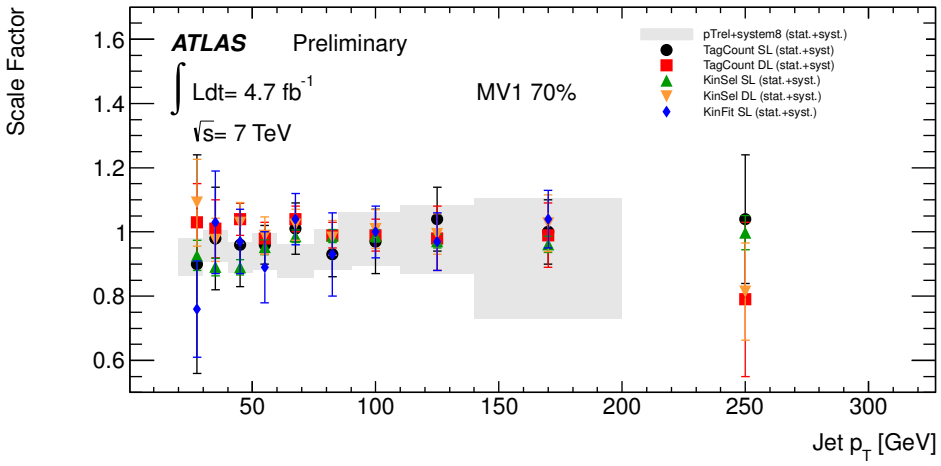

Figure 4.8: Comparison of all $t\bar{t}$-based scale factors with those from the combination of the system8 and p_T^{rel} calibration methods, which are based on dijet events [83].

For all methods, the jet energy scale, jet energy resolution and jet reconstruction efficiency are the dominant uncertainties [83]. The uncertainties caused by variations of ε_l and ε_c are smaller, but also significant. All methods, apart from the kinematic fit, strongly depend on simulation and thus uncertainties related to parton shower modelling, choice of generator, amount of initial and final state radiation are high and can lead to 10-15% relative uncertainty on the measured scale factor. Another significant uncertainty comes from factors that change the flavour composition of the analysed sample, such as the background description.

The b-tagging efficiency scale factors are close to unity for all values of jet p_T. The total uncertainties for the kinematic selection method in the single lepton channel are ranging from 5% to 15% when subdividing the data into bins of jet p_T. For other methods, the total uncertainties reach up to 30%. With the integrated luminosity of 4.7 fb^{-1} collected in 2011 at the centre-of-mass energy of $\sqrt{s}$ = 7 TeV the tag counting and kinematic selection methods are dominated by systematic uncertainties, while the measurement using the kinematic fit method is statistically limited. It is the first time that the $t\bar{t}$ calibration methods became competitive with methods based on dijet events.

CHAPTER 5

Measurement of R_b and $\sigma_{t\bar{t}}$

This chapter presents a measurement of $R_b = \mathcal{B}(t \to Wb)/\mathcal{B}(t \to Wq)$, the branching fraction of the top quark to a b quark, and the relative inclusive $t\bar{t}$ production cross section in pp collisions at $\sqrt{s} = 7$ TeV centre-of-mass energy, with a sample of dilepton $t\bar{t}$ events. Additionally, the measurement of R_b allows for a measurement of the $|V_{tb}|$ CKM matrix element.

The measurement method described in this chapter exploits the differences in the shape of the distribution of the number of b-tagged jets for $t\bar{t}$ events with different numbers of b quarks in the final state: $tt \to WWbb$, $tt \to WWqq$ and $tt \to WWqb$[1]. The presented method features the dilepton selection criteria, data-driven background estimation methods and simulated samples described in chapter 3, as well as the studies of b-tagging algorithms and calibration methods described in chapter 4.

5.1 Template fit

R_b and σ_{dilepton} are measured with a template fit using as template the distribution of the number of jets tagged with the MV1 b-tagging algorithm at the 85% average tagging efficiency working point[2].

The templates for the signal $t\bar{t}$ process are obtained from the Protos sample with $R_b = 0.5$, which are described in section 3.4.1. It contains 25% $tt \to WWbb$ events, 25% $tt \to WWqq$ and 50% $tt \to WWqb$, where q is a light quark, either a d- or s-quark. For each of these types of events a separate template is created. The Monte Carlo sample is divided into these three categories by checking the truth information before applying any selection criteria.

A separate template is built for the sum of all expected background processes: Z+jets, single top, diboson and events containing fake leptons, which are described in detail in section 3.3. The template for events with fake leptons, which is obtained directly from data using the matrix method, explained in section 3.3.2, is normalised to the total number of events predicted by the method. Similarly, the templates for $Z \to ee$ and $Z \to \mu\mu$ events in the ee and $\mu\mu$ channels, respectively, are normalised according to the data-driven estimation described in section 3.3.3. Other templates are derived from simulation and are normalised according to the production cross section of the processes and the total luminosity to keep relative fractions between background processes as predicted by the theory.

[1] To improve legibility, the particle and antiparticle notation is omitted.

[2] In this chapter, *b-tagged jets* always refer to jets being tagged with the MV1 b-tagging algorithm at the 85% average tagging efficiency working point.

The templates have four bins: 0, 1, 2 and 3 or more b-tagged jets. The number of events available in simulation to construct the Protos $t\bar{t}$ templates is shown in table 5.1. Figure 5.1 (left) shows the

template	$tt \to WWbb$	$tt \to WWqb$	$tt \to WWqq$
number of events	10144	21027	10922

Table 5.1: Number of selected events for the construction of the $tt \to WWbb$, $tt \to WWqb$ and $tt \to WWqq$ templates from the Protos sample.

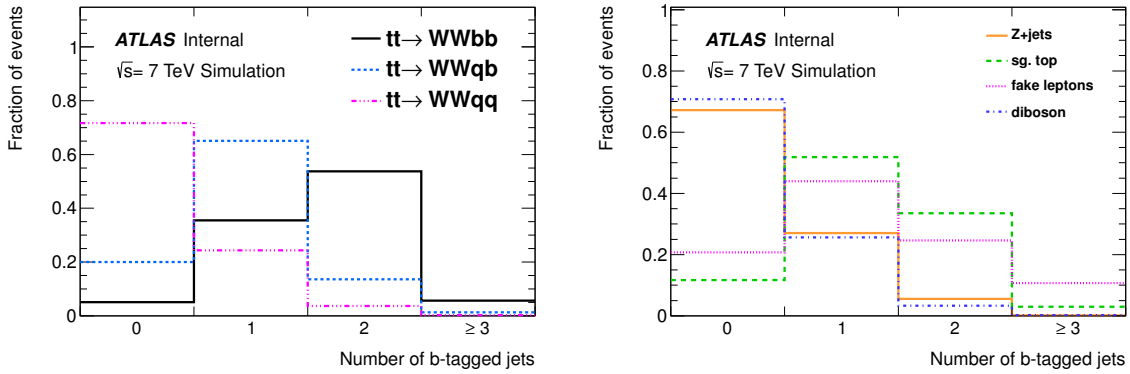

Figure 5.1: Number of b-tagged jets with MV1 at the 85% average efficiency working point for three signal categories: $tt \to WWbb$, $tt \to WWqb$ and $tt \to WWqq$ (left) and for the background processes (right). All distributions are normalised to unity.

shapes for all three categories of signal events and 5.1 (right) for background processes. Figure 5.2 illustrates a comparison between the sum of the background templates and the $tt \to WWbb$ template from the Protos sample with the data, showing that data and simulation agree within the uncertainties. The $tt \to WWbb$ template is normalised to the corresponding number of selected events from the Powheg+Pythia sample. $tt \to WWqb$ and $tt \to WWqq$ templates are not included.

The shape of the distribution of the number of b-tagged jets is compared between various Monte Carlo samples: MC@NLO+Herwig, Alpgen+Herwig, Powheg+Pythia and Protos+Pythia (only $tt \to WWbb$ events), which are described in detail in section 3.4.1. The comparison is presented in figure 5.3. The degree of agreement between the samples depends on the bin of the distribution, but overall the differences stay within ±10%.

The 85% average efficiency working point for the MV1 b-tagging algorithm is chosen based on a study showing that it has the highest discriminating power between the signal ($tt \to WWbb$) and background among all available working points (60%, 70%, 75% and 85%), and also an excellent discrimination between the two components $tt \to WWbb$ and $tt \to WWqb$. This study is shown in table 5.2, where the mean values of the distributions of the number of b-tagged jets are compared. Additionally, this working point is least sensitive to the choice of b-tagging scale factors, which is described in appendix D.

The fit is performed using a binned maximum likelihood method with the help of the *RooFit* interface [137], allowing the signal templates normalisation N_{bb}, N_{qb} and N_{qq} to vary. The normalisations of the signal templates can be expressed as functions of R_b, the production cross section σ_{dilepton}, the total

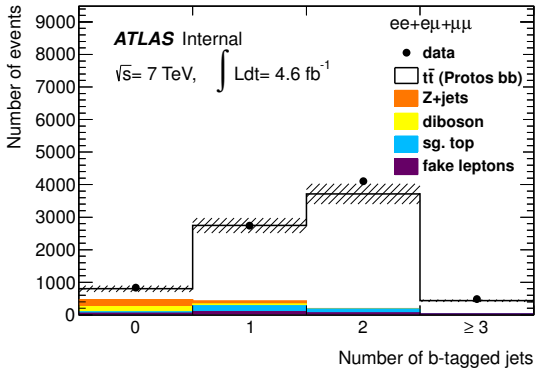

Figure 5.2: Number of b-tagged jets with MV1 at the 85% average efficiency working point. Data is compared to expectation from Monte Carlo simulation and a data-driven estimation of the contribution from fake leptons described in section 3.3.2. In case of Protos, only $tt \to WWbb$ events are considered here.

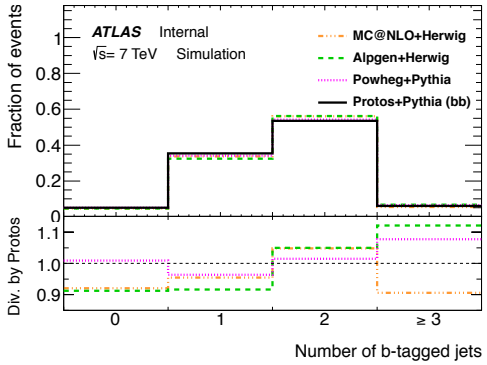

Figure 5.3: Number of b-tagged jets with MV1 at the 85% average efficiency working point for various $t\bar{t}$ samples: MC@NLO+Herwig, Alpgen+Herwig, Powheg+Pythia and Protos ($tt \to WWbb$ events only), which are described in section 3.4.1. All distributions are normalised to unity. The lower panel shows a comparison with Protos ($tt \to WWbb$), which is used as the baseline.

ε_b	$\overline{N}_{bb}$	$\overline{N}_{qb}$	$\overline{N}_{qq}$	$\overline{N}_{\text{bkg}}$	$\Delta(bb - \text{bkg})$	$\Delta(bb - qb)$
60%	1.48	1.00	0.52	0.91	0.57	0.48
70%	1.69	1.13	0.55	0.99	0.70	0.56
75%	1.81	1.20	0.59	1.06	0.75	0.61
85%	2.10	1.46	0.82	1.31	0.79	0.64

Table 5.2: Mean number of b-tagged jets for the $tt \to WWbb$, $tt \to WWqb$, $tt \to WWqq$ and background templates. The difference between $tt \to WWbb$ and background, and between $tt \to WWbb$ and $tt \to WWqb$ is shown in the last two columns.

integrated luminosity of collected data $\mathcal{L}$, and the selection efficiencies $\varepsilon_{bb}^{\text{selection}}$, $\varepsilon_{qb}^{\text{selection}}$ and $\varepsilon_{qq}^{\text{selection}}$:

$$\begin{aligned} N_{bb} &= \mathcal{L} \cdot \sigma_{\text{dilepton}} \cdot R_b^2 \cdot \varepsilon_{bb}^{\text{selection}} \\ N_{qb} &= \mathcal{L} \cdot \sigma_{\text{dilepton}} \cdot 2 \cdot R_b \cdot (1 - R_b) \cdot \varepsilon_{qb}^{\text{selection}} \\ N_{qq} &= \mathcal{L} \cdot \sigma_{\text{dilepton}} \cdot (1 - R_b)^2 \cdot \varepsilon_{qq}^{\text{selection}} \end{aligned} \tag{5.1}$$

The likelihood function L is expressed as a product of Poisson probability density functions for all bins $i = 1, .., 4$, for n_i observed events, given an expectation of $\mu_i(\sigma_{\text{dilepton}}, R_b)$:

$$L = \prod_{i=1}^{4} P(n_i^{obs}, \mu_i(\sigma_{\text{dilepton}}, R_b)), \tag{5.2}$$

where $\mu_i(\sigma_{\text{dilepton}}, R_b)$ is the sum of the normalisation of the $tt \to WWbb$, $tt \to WWqb$, $tt \to WWqq$ processes and the background events in i-th bin

$$\begin{aligned} \mu_i(\sigma_{\text{dilepton}}, R_b) &= N_{bb}^i + N_{qb}^i + N_{qq}^i + N_{\text{bkg}}^i \\ &= \mathcal{L} \cdot \sigma_{\text{dilepton}} \cdot [R_b^2 \cdot \varepsilon_{bb}^{\text{selection}} \cdot f_{bb}^i + 2 \cdot R_b \cdot (1 - R_b) \cdot \varepsilon_{qb}^{\text{selection}} \cdot f_{qb}^i \\ &\quad + (1 - R_b)^2 \cdot \varepsilon_{qq}^{\text{selection}} \cdot f_{qq}^i] + N_{\text{bkg}}^i. \end{aligned} \tag{5.3}$$

The $f_{bb,qb,qq}^i$ are the fractions of $tt \to WWbb$, $tt \to WWqb$ and $tt \to WWqq$ events in i-th bin of the corresponding template

$$f_k^i = \frac{b_k^i}{\sum_{i=1}^{4} b_k^i},$$

where b_k^i is the number of events in the i-th bin of the template $k = bb, qb, qq$. Table 5.3 shows selection

template	$tt \to WWbb$	$tt \to WWqb$	$tt \to WWqq$
efficiency	0.1322 ± 0.0012	0.1369 ± 0.0012	0.1417 ± 0.0013

Table 5.3: Measured selection efficiencies for $tt \to WWbb$, $tt \to WWqb$ and $tt \to WWqq$ events together with their statistical uncertainties.

efficiencies for $tt \to WWbb$, $tt \to WWqb$ and $tt \to WWqq$ events measured in the Protos sample. The difference is coming mostly from the difference in the p_{T} spectrum for b-jets and light jets, which is visible in figure 5.4. This causes events with b-jets to fail the jet p_{T} requirement more often than events with light jets.

A comparison of p_{T} distributions for b-jets for $t\bar{t}$ samples generated using different generators or parton showering models combinations: MC@NLO+Herwig, Alpgen+Herwig, Powheg+Pythia and Protos (only $tt \to WWbb$ events), is presented in figure 5.5 and it can be seen that they agree very well.

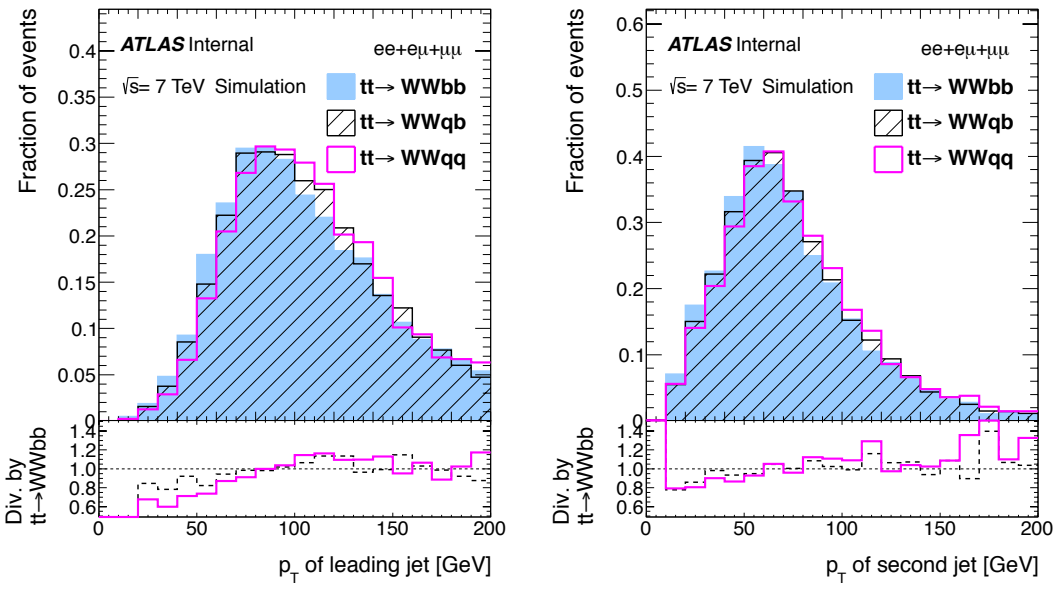

Figure 5.4: Distributions of p_{T} for the leading (left) and second (right) jet for $tt \to WWbb$, $tt \to WWqb$ and $tt \to WWqq$ events in the Protos + Pythia sample. The lower panel shows a comparison of the $tt \to WWqb$ and $tt \to WWqq$ distributions with $tt \to WWbb$, which is used as the baseline.

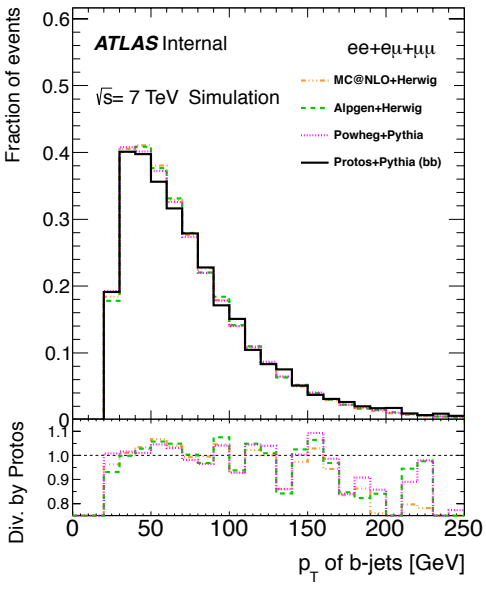

Figure 5.5: Distributions of p_{T} for b-jets in various $t\bar{t}$ samples: MC@NLO+Herwig, Alpgen+Herwig, Powheg+Pythia and Protos ($tt \to WWbb$ events only), which are described in section 3.4.1. The lower panel shows a comparison with Protos ($tt \to WWbb$), which is used as the baseline.

5.2 Validation of the fit strategy with pseudo-experiments

In order to test the quality of the fit, as well as to evaluate the impact of various sources of systematic uncertainties, multiple sets of *pseudo-experiments* are performed. Pseudo-experiments use pseudo-data, which is synthetic data that resembles *real* data. Pseudo-data is randomised, but follows input distribution shape and normalisation within the statistical uncertainty. This enables creation of multiple datasets and holding multiple pseudo-experiments. In this way it can be tested if effects observed in real data are true physical effects or statistical fluctuations.

First, pseudo-data is generated using the four templates described in section 5.1 obtained from Monte Carlo simulation with *default* settings, including all corrections such as b-tagging scale factors or jet energy scale. The value of R_b in the generated pseudo-data is set to 0.99830 which is obtained from $|V_{tb}|$ extracted from electroweak fits [16] and σ_{dilepton} is set to the value calculated in section 1.2.2, $\sigma_{\text{dilepton}} = 11.33$ pb. R_b and σ_{dilepton} are measured separately (i.e. when R_b is measured, σ_{dilepton} is kept constant). For each pseudo-dataset the number of generated signal and background events is determined according to Poisson distributions, with expectation given according to the input values of R_b, σ_{dilepton} and the luminosity of 4.6 fb^{-1}, corresponding to the amount of data used in this analysis. Next, the templates are fitted to the pseudo-data returning fitted values of R_b and σ_{dilepton}.

The generation of a pseudo-dataset and its fit is repeated 6000 times resulting in a smooth (Gaussian) distribution of fitted values of R_b and σ_{dilepton}. The resulting R_b (σ_{dilepton}) distribution is fit with a Gaussian function; the mean $\mu(R_b)$ ($\mu(\sigma_{\text{dilepton}})$) is the best estimate for the expected measured R_b (σ_{dilepton}) value, while the standard deviation $\sigma(R_b)$ ($\sigma(\sigma_{\text{dilepton}})$) is the best estimate for the expected statistical uncertainty on the measurement of $R_b(\sigma_{\text{dilepton}})$.

To estimate the size of the systematic uncertainties on the R_b (σ_{dilepton}) measurement, modified templates are obtained with varied factors that introduce the systematic uncertainty, such as the earlier mentioned b-tagging scale factors, for instance. The background normalisation and selection efficiency (described in section 5.1) are not free parameters in the fit, the impact of the variations is taken into account and they are recalculated for each of the variations. Results are presented at the end of this chapter, in section 5.4.6. Table 5.11 presents values of systematic uncertainties for R_b and table 5.12 for σ_{dilepton}.

A sample fit with $R_b = 0.99830$ and $\sigma_{\text{dilepton}} = 11.33$ pb and default settings is shown in figure 5.6. The result of the 6000 pseudo-experiments for R_b and σ_{dilepton} is shown in the figure 5.7. The bottom row

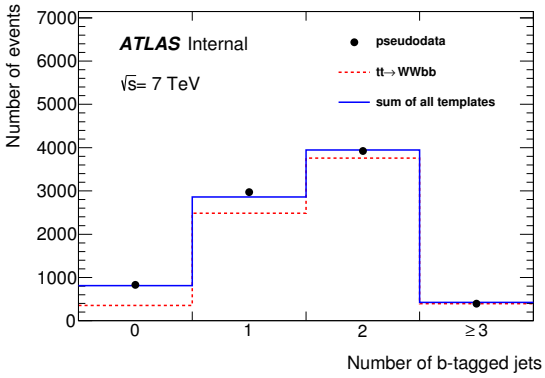

Figure 5.6: Result of one example pseudo-experiment with $R_b = 0.99830$ (free parameter) and $\sigma_{\text{dilepton}} = 11.33$ pb (fixed). The template for $tt \to WWbb$ is marked with a dashed line.

of figure 5.7 shows pull distributions for the measured values. Pulls, defined as distribution of the dif-

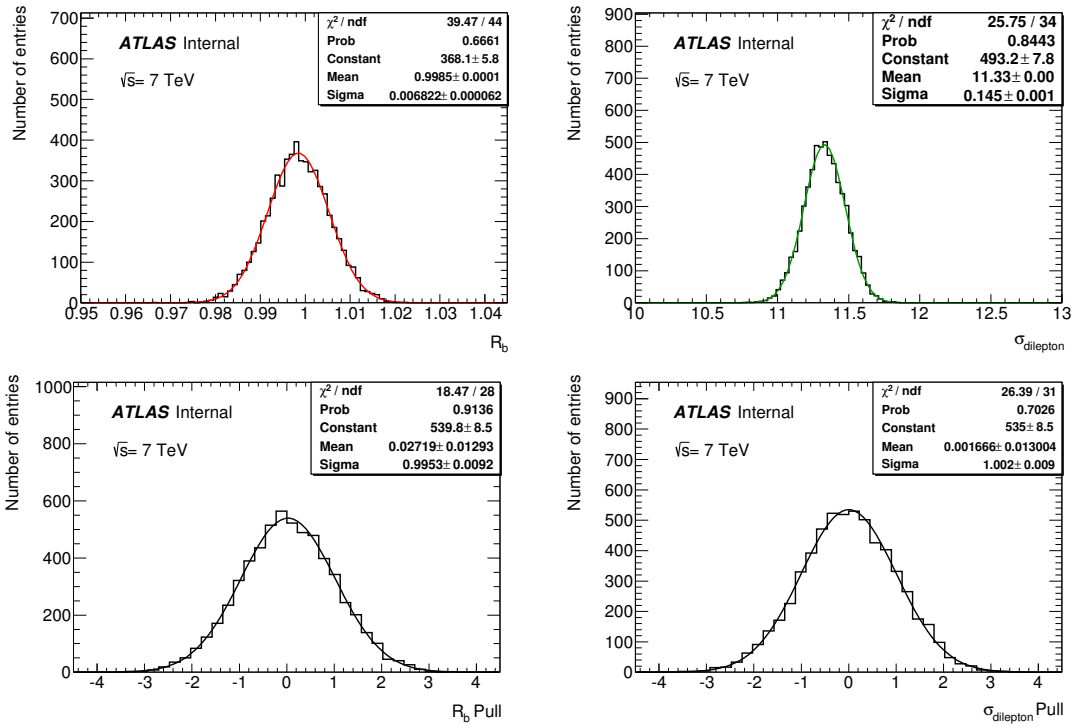

Figure 5.7: Result of 6000 pseudo-experiments for R_b (upper row left) and σ_{dilepton} (upper row right) and their pulls: (bottom row left) for R_b and (bottom row right) for σ_{dilepton}.

ference between the result x_i of each pseudo-experiment i and the mean x from all pseudo-experiments, divided by the standard deviation σ: $g_i = \frac{x_i - x}{\sigma}$, are a good test for fit biases. Ideally, the pull is centered at 0 (μ) and has a width (σ) of 1. Pulls presented in figure 5.7 fulfil these conditions within statistical uncertainties. Figure 5.8 is showing the impact of systematic uncertainties on the selection efficiency of $tt \to WWbb$, $tt \to WWqq$ and $tt \to WWqb$ events.

5.3 Fit linearity

The fit linearity is checked for both free parameters: R_b and σ_{dilepton}. The normalisation of the background template is kept constant. 6000 pseudo-experiments are performed for each value of R_b between 0.5 and 1.1 (with a step of 0.01). The same number of pseudo-experiments is performed for σ_{dilepton} between 5 and 15 (with a step of 0.1). Figure 5.9 shows the dependence between the generated and the fitted values. The y-axis shows the mean of the Gaussian distribution of fitted values in the 6000 pseudo-experiments and the error bars represent the width of the Gaussian. For both parameters, the relationship is linear within the statistical uncertainty, which means that the fitting method is not biased or skewed towards any particular range of R_b or σ_{dilepton}.

Figure 5.10 shows the relative difference between generated and fitted values: $\delta(R_b^{gen} - R_b^{fit})$ and $\delta(\sigma_{\text{dilepton}}^{gen} - \sigma_{\text{dilepton}}^{fit})$ with respect to the generated value expressed in %. The error bars are defined as uncertainties from figure 5.9 divided by the generated value of the parameter.

For all values of R_b and σ_{dilepton} pull distributions are checked and no anomalies are observed. Figures 5.11 and 5.12 present pull distributions for chosen values of R_b and σ_{dilepton}.

The possibility of a correlation between R_b and σ_{dilepton} is also checked – no dependence is observed

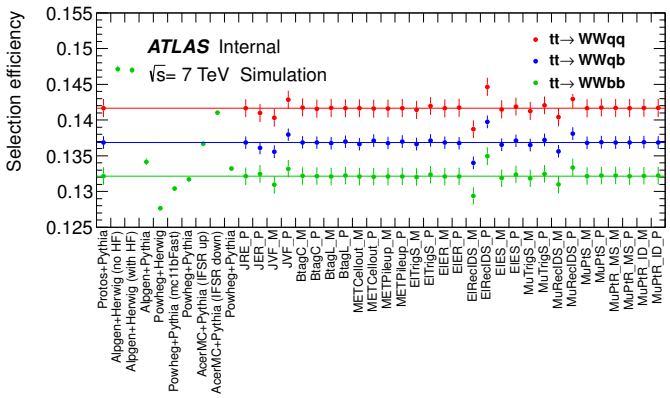

Figure 5.8: Selection efficiency for $tt \to WWbb$, $tt \to WWqq$ and $tt \to WWqb$ events for systematics variations and for different Monte Carlo $t\bar{t}$ simulation samples (entries only for $tt \to WWbb$, as they do not contain sufficient $tt \to WWqq$ and $tt \to WWqb$ events). The error bars show statistical uncertainties. The acronyms are explained in section 5.4.

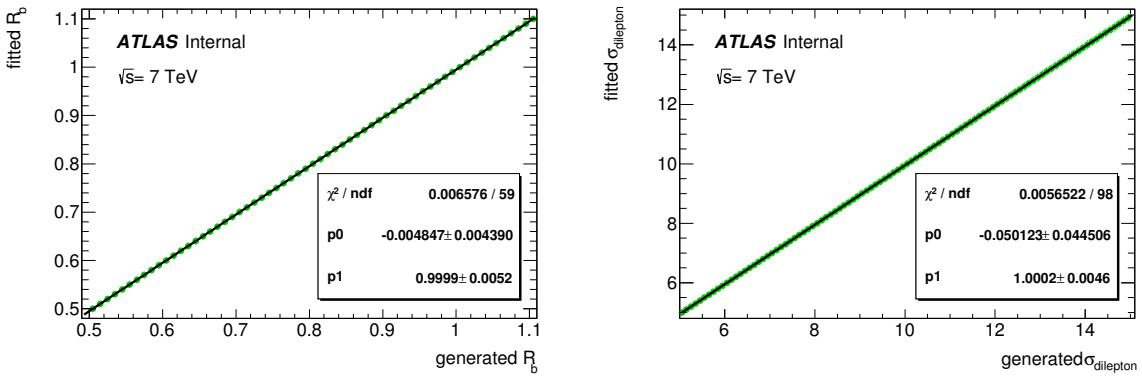

Figure 5.9: Dependence between generated and fitted values of R_b and σ_{dilepton}. For each generated value of R_b (σ_{dilepton}) a set of 6000 pseudo-experiments is performed.

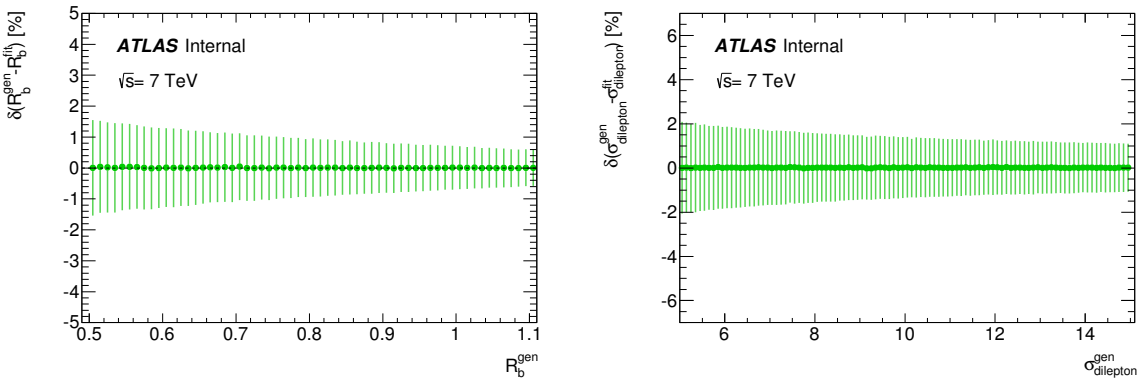

Figure 5.10: Difference between generated and fitted values of R_b and σ_{dilepton} as a function of the generated value. 6000 pseudo-experiments are performed for each generated point.

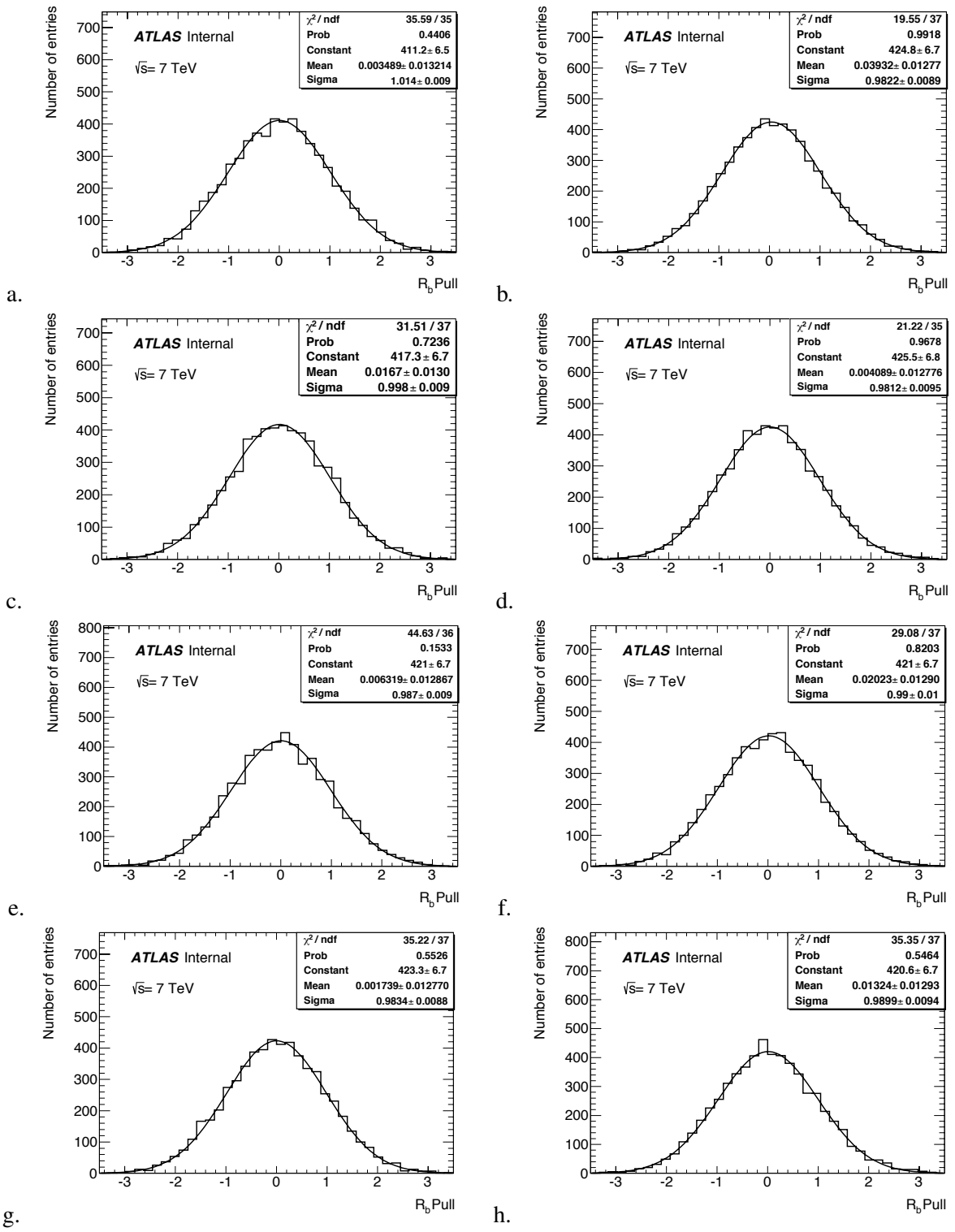

Figure 5.11: Pull distributions for $R_b = 0.5, 0.7, 0.8, 0.9, 0.95, 1.0, 1.05, 1.1$ (from (a) to (h)). For each of these values 6000 pseudo-experiments are performed.

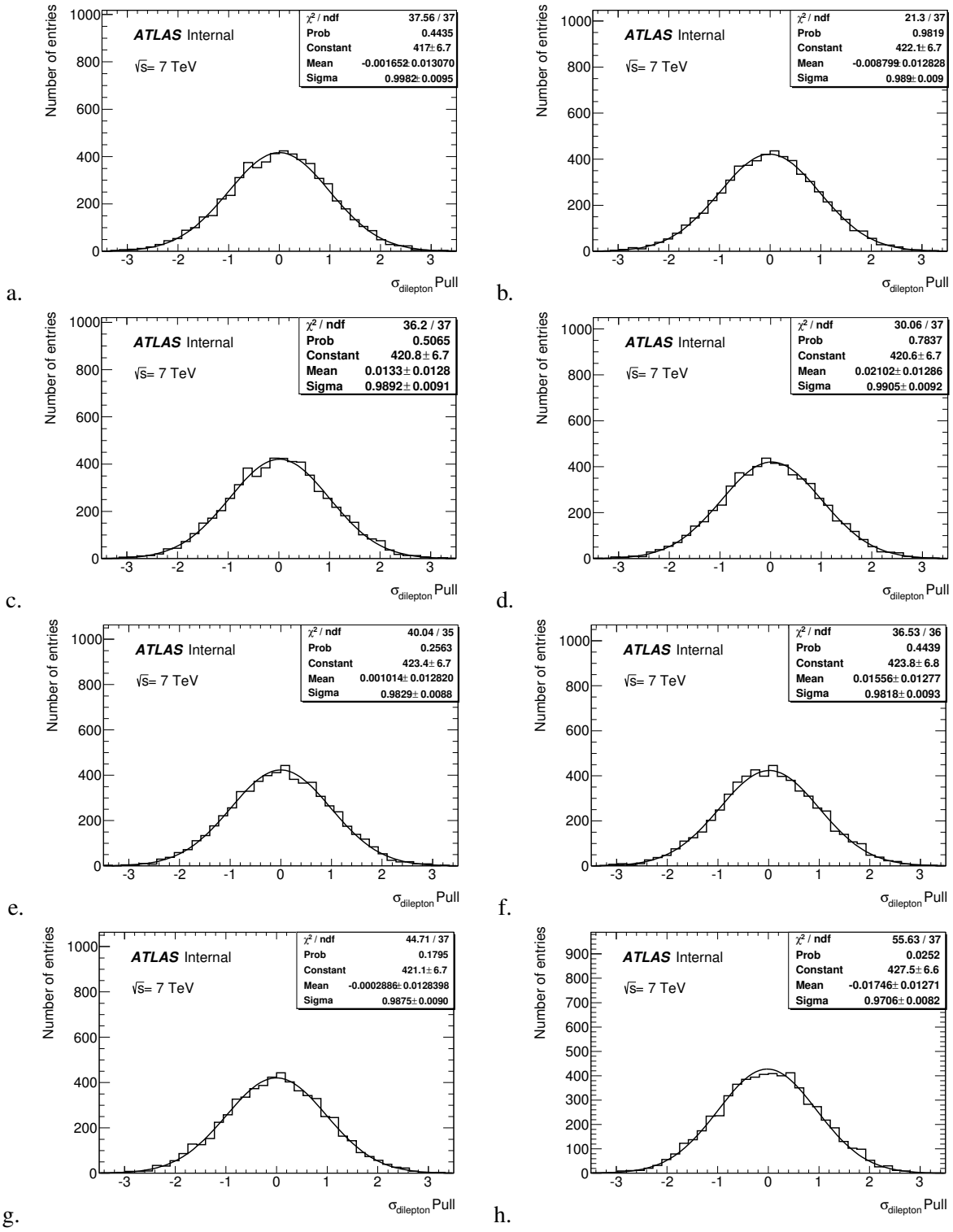

Figure 5.12: Pull distributions for $\sigma_{\text{dilepton}} = 5.0, 7.0, 9.0, 10.0, 11.0, 12.0, 13.0, 15.0$ pb (from (a) to (h)). For each of these values 6000 pseudo-experiments are performed.

which is illustrated in figure 5.13.

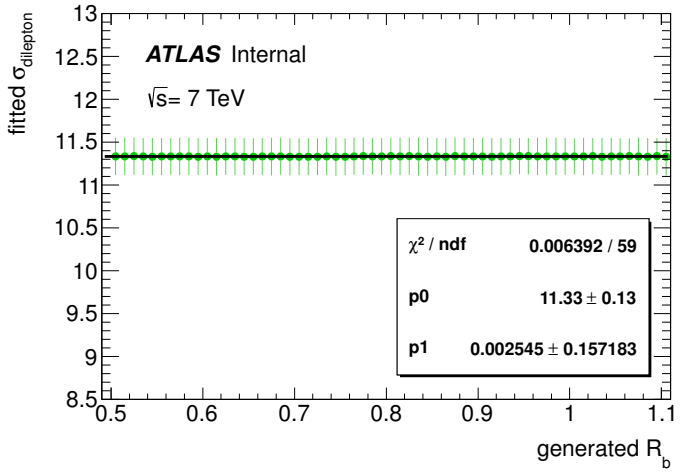

Figure 5.13: Fitted value of σ_{dilepton} as a function of generated R_b. Values of R_b from 0.5 to 1.1 with a step of 0.01 are generated and for each of them 6000 pseudo-experiments are performed.

5.4 Systematic uncertainties

5.4.1 Overview of sources of systematic uncertainties

A number of systematic effects could have an impact on the measurement of R_b and σ_{dilepton}. The following are considered and evaluated for this analysis. For systematic uncertainties that are evaluated by comparing two sets of Monte Carlo simulation, the whole available datasets are used.

- **Jet energy scale** - The jet energy scale (JES) uncertainty is estimated by scaling the energies of all considered jets up and down by $1\,\sigma$, the relative uncertainty on the jet energy. 21 nuisance parameters are varied separately, including the flavour composition of jets, the response to each jet flavour, b-jet JES, the effect of close-by jets, the uncertainty from in-situ calibrations performed in data and the impact of pile-up. The complete event selection and the reconstruction is then re-run with the scaled jets.

  In addition, $E_{\text{T}}^{\text{miss}}$ is re-evaluated, taking into account the scaled contributions of the jets in p_x and p_y. Each of the objects included in the $E_{\text{T}}^{\text{miss}}$ calculation has an uncertainty related to its energy scale and energy resolution. Therefore, the calculated energy scale and resolution uncertainty scale factors on the objects are propagated into $E_{\text{T}}^{\text{miss}}$. This is done by using $E_{\text{T}}^{\text{miss}}$ weights containing the information on whether or not the object was included in the $E_{\text{T}}^{\text{miss}}$ calculation.

  The quadrature sum of all contributions is considered as the total uncertainty.

- **Jet reconstruction efficiency** - The jet reconstruction efficiency (JRE) accounts for the difference between data and simulation in the reconstruction efficiency of calorimeter jets with respect to track jets, measured with a tag-and-probe method in QCD dijet events. It is evaluated by randomly dropping jets from events. The resulting difference with respect to the nominal case is symmetrised and quoted as systematic uncertainty on the JRE.

  The effect due to JRE systematic variation is propagated to $E_{\text{T}}^{\text{miss}}$ in the same way as for JES.

- **Jet energy resolution** (JER) - A smearing of the jet transverse momentum is applied to reflect the resolution uncertainty for the jet energy observed in data. The resulting difference is symmetrised and quoted as systematic uncertainty.

  The effect due to the JER systematic variation is propagated to $E_{\mathrm{T}}^{\mathrm{miss}}$.

- ***b*-tagging** - The performance of the MV1 algorithm is calibrated using data, in bins of jet p_{T} and η. Scale factors for the *b*-tagging efficiency of *b*-, *c*- and light flavour jets are provided separately, each with an uncertainty. To correct the *b*-tagging performance for the *b*-jets, scale factors from calibration methods using muon-enriched dijet samples, pTrel and system8, described in section 4.3.1, are applied. Those methods have the following sources of uncertainties: fake muons in *b*-jets, simulation tagging efficiency, size of the simulated sample, pTrel light template contamination, *b*-decay branching fractions, *b*-fragmentation function, modelling of the *b*-hadron direction, *b*-fraction constraint, modelling of *c*-production, *b*-fragmentation fraction, jet energy scale, spectrum of the muon momentum in the rest frame of the *b* hadron (p^*), semi-leptonic correction, muon p_{T} spectrum, *c*-light ratio, pile-up, pTrel cut variation, modelling of *b*-production and scale factor for inclusive *b*-jets. An eigenvector variation method is used, which is developed to reduce the number of variations (to 9, which is the number of bins used for the calibration for *b*-jets). It starts from the construction of a covariance matrix corresponding to each source of uncertainty, and then sums these covariance matrices to obtain the total covariance matrix. Being a symmetric, positive-definite matrix this can be considered as an eigenvalue problem. The eigenvectors that solve this problem can be seen as directions in which to carry out independent variations. The sizes of the variations are given by the square root of the corresponding eigenvalues. Terms related to the uncertainty from the jet energy resolution are treated separately, namely they are included in the variation of the jet energy resolution.

  Since in this analysis no large uncertainties from *c*- and light jets are expected, a simplified approach is used for them and only a total uncertainty on the values of scales factors is taken into account without dividing them into particular sources.

- **Missing transverse momentum** - Cell-out term[3] (METCellout), soft jets with p_T between 7 GeV and 20 GeV, and pile-up effects (METPileup) are taken into account in addition to the systematic uncertainties coming from jets, muon, and electrons that are propagated to $E_{\mathrm{T}}^{\mathrm{miss}}$ when those uncertainties are estimated. The cell-out term and soft jets are treated to be 100% correlated. The effect of pile-up on $E_{\mathrm{T}}^{\mathrm{miss}}$ is estimated to be 6.6% by a data/simulation ratio method for $Z \rightarrow \mu\mu$ events.

- **Lepton efficiencies** - In order to account for the electron and muon trigger (ElTrigS/MuTrigS), reconstruction and ID efficiencies (ElRecIDS/MuRecIDS), global and object-based scale factors and efficiencies are taken into account and a systematic uncertainty is assigned on an event basis (for global scale factors) or on an object basis, which are then combined into an overall electron (muon) scaling/efficiency uncertainty.

- **Lepton scales and resolution** (ElER, ElES, MuPtS, MuPtR) - The momentum scales and resolution in simulation differ from the ones observed in data for both electrons and muons. The momentum is smeared and a scaling is applied on object level to account for this discrepancy. A systematic uncertainty is assigned by smearing the momentum and by scaling it up and down by $1\,\sigma$.

[3] Calorimeter cells that measured a non-zero value, but are not associated with any reconstructed physics object.

Both systematic variations are applied to simulation and the effect has been propagated to $E_{\mathrm{T}}^{\mathrm{miss}}$. The event selection and reconstruction is then re-run for the different scales.

- **Fake leptons** - The fraction of selected events with at least one fake lepton (mainly single lepton $t\bar{t}$, W+jets and multi-jets) is estimated with a data-driven method described in section 3.3.2. The method carries 40% uncertainty on the normalisation in the ee and 50% and 30% in the $e\mu$ and $\mu\mu$ channels respectively.

- **Fake leptons shape** - The fake leptons event shape uncertainties are estimated by varying the loose-to-tight efficiencies of the fake leptons. The uncertainty on the efficiencies for the fake leptons is based on different definitions of loose (tight) lepton selections.

- **Z+jets** - In the ee and $\mu\mu$ channels the data-driven estimate provides a different normalisation for each source of systematic uncertainty considered in this analysis, which allows to take into account correlations between the Z+jets normalisation and other parameters. The uncertainty on this data-driven estimate is obtained by changing the control region as described in section 3.3.3. In order to quantify the uncertainty in the $e\mu$ channel, a Berends-Giele scaling uncertainty [138] of 35% is considered.

- **Other background processes** - In the case of the remaining background processes, which are estimated from simulation, theoretical values of uncertainties on the normalisation are applied: 35% for diboson, as for Z+jets, and 7% for Wt single top production [130].

- **Background flavour composition** - As this measurement is very sensitive to the presence of heavy flavour jets, it is crucial to account for possible mismodelling of additional radiation and check if varying the amount of background events with additional b-jets has an impact on the R_b and $\sigma_{\mathrm{dilepton}}$ measurements. In the Z+jets simulation sample the ratio of Zbb events with respect to other Z+jets events is varied by 50% [4]. In the case of diboson, the event weight is varied by 50% for events containing at least one b-jet. In the case of single top the same procedure is used, but for events containing at least 3 b-jet, as two b-jets might be coming directly from the single top production.

  The methods used for this study do not allow to precisely estimate if the b-jets originate from gluon splitting or some other source. Therefore, to account for the imperfection of the model used, a conservative approach is chosen and a large variation of 50% is applied. However, due to the fact that the background processes contribute only to 15% in this analysis, such large variations of the background flavour composition turns out to have no impact on the measurement of R_b and $\sigma_{\mathrm{dilepton}}$, as can be seen in tables 5.11 and 5.12.

  Additionally, since this study proves that the measurements of R_b and $\sigma_{\mathrm{dilepton}}$ are not sensitive to the variation of the flavour composition of the background template, it is concluded that the fact that the single top sample assumed $R_b = 1$ is not biasing the measurements either[5].

- **Generator** - To evaluate the uncertainty due to the choice of the $t\bar{t}$ generator the result of the fit obtained using the default $tt \to WWbb$, $tt \to WWqb$ and $tt \to WWqq$ templates from the

[4] The Z+jets samples contains the generator level information on the type of event: $Z + bb$, $Z + cc$ or Z boson decays with associated production of light jets only.

[5] As the expected value of R_b is close to 1, the correction on the single top template would be small and since single lepton events have a very small contribution in the total count of events used in this analysis, as can be seen in table 3.2, the effect on the R_b and $\sigma_{\mathrm{dilepton}}$ measurement would be negligible.

PROTOS sample[6] are compared with that obtained using the $tt \to WWbb$ template from POWHEG + PYTHIA, MC@NLO + HERWIG or ALPGEN + HERWIG (full simulation). Additionally, fit results using $tt \to WWbb$ templates from POWHEG + HERWIG and POWHEG + PYTHIA samples (fast simulation) are compared. A direct comparison of POWHEG + HERWIG with PROTOS is not possible, because the latter is not available in fast simulation. Values of R_b and σ_{dilepton} measured with these various $tt \to WWbb$ templates are presented in table 5.13 in section 5.4.6. The largest difference for both, the R_b and σ_{dilepton} measurements, is observed between the default PROTOS with the ALPGEN + HERWIG template and is considered as the value of the generator uncertainty.

- **Renormalisation/factorisation** - Additionally, two MC@NLO samples with varied renormalisation and factorisation scale are considered. The resulting uncertainty on the values of R_b and σ_{dilepton} is much smaller than the generator uncertainty and thus this uncertainty is not included in the total uncertainty.

- **Initial and final state radiation** - This uncertainty is potentially important and its evaluation is thus described in a dedicated section 5.4.2.

- **Parton distribution functions** - The $tt \to WWbb$ template from the MC@NLO generator is used to evaluate the impact of the choice of parton distribution functions (PDFs) to model the incoming partons to the hard scattering process. The systematic uncertainty is evaluated taking the largest difference between three models: CTEQ6.6(CT10) [96] best fit, MSTW2008nlo68cl [13] best fit, and the mean NNPDF20 [139] with the variation of 100 parameters.

- **Underlying events (UE)** - In order to take into account the modelling of the underlying events, $tt \to WWbb$ from two Monte Carlo datasets with different UE are compared. These two datasets are generated with POWHEG+PYTHIA. The difference, both in R_b and σ_{dilepton} measurements, is very small.

- **Colour reconnection (CR)** - A $tt \to WWbb$ template from a sample with and without CR is compared. These two datasets are generated with POWHEG+PYTHIA.

- **Associated heavy flavour production** - $tt \to WWbb$ templates from ALPGEN+HERWIG with and without additional heavy flavour jets are compared.

- **Pile-up** - The evaluation of this systematic uncertainty is described in a dedicated section 5.4.3.

- **Statistical uncertainty on the selection efficiency** - The measurement is repeated for selection efficiencies varied within the statistical uncertainty shown in table 5.3.

- **Statistically limited templates** - The templates are obtained with finite simulation samples. The statistical uncertainty on the templates is evaluated by performing 10000 pseudo-experiments where pseudo-data is generated with each bin of signal and background templates independently allowed to fluctuate within a Poisson distribution and its statistical uncertainties. The quadratic difference between $\mu(R_b)$ of the fits to these varied pseudo-data and that without template statistical fluctuation is considered to be the template statistical uncertainty. The impact on the R_b and σ_{dilepton} measurements is negligible.

Measured values of R_b and σ_{dilepton} for simulation samples used to evaluate some of the systematic effects are summarised in table 5.13 at the end of this section.

[6] All samples used for the evaluation of the generator and other simulation-related uncertainties are described in section 3.4.1.

For the evaluation of some of the systematic uncertainties, only varied $tt \to WWbb$ templates are available. A dedicated study is conducted to evaluate the effect of neglecting the variation of the smaller contributions from $tt \to WWqb$ and $tt \to WWqq$ using, as an example, the ISR/FSR uncertainty.

5.4.2 Initial/final state radiation

The systematic uncertainties related to signal modelling are evaluated by comparing the result of the fit when using $tt \to WWbb$ templates from the nominal Protos sample with that when using $tt \to WWbb$ templates from the varied sample (for instance the AcerMC with modified ISR/FSR parameters). In tables 5.11 and 5.12 these uncertainties are denoted as "Initial/final state radiation", "Generator", "Associated HF prod.", "Color reconnection" and "Underlying event". In all of these cases modified templates for $tt \to WWqb$ and $tt \to WWqq$ are not available and the effect of neglecting this is studied for ISR/FSR, the largest systematic uncertainty in the case of the R_b measurement, as an example.

In order to determine the systematic uncertainty stemming from the limited knowledge on the extent of initial and final state radiation (ISR/FSR), samples generated with AcerMC and showered and hadronised with Pythia are used. Two samples with varied amount of ISR/FSR are available: one sample corresponding to the maximum assumed amount of ISR/FSR, the other to the minimum. The PythiaP2011C tune [117] is used for the production of the samples, with modified values of the parameters responsible for the "up/down" variation of ISR/FSR. The possible maximal and minimal amount of radiation was determined from an auxiliary measurement to ATLAS data [140] and the respective values of the tunable parameters of Pythia were extracted. The parameters and their values are shown in table 5.4.

Sample	PARP(67)	PARP(64)	PARP(72)
Maximal ISR/FSR	1.40	0.90	0.37
Minimal ISR/FSR	0.60	3.50	0.11

Table 5.4: Pythia parameters controlling the amount of ISR/FSR and their values, as used in the production of the dedicated AcerMC samples.

AcerMC does not allow to decay a top quark to other final states than Wb. Therefore, the ISR/FSR variation was directly available only for the $tt \to WWbb$ template. In order to estimate the effect of the ISR/FSR variation on the other two templates, $tt \to WWqb$ and $tt \to WWqq$, each template was divided into additive categories. These categories are determined by the number of selected jets in an event and by the flavours of the matching quarks to these jets. If a given jet does not have a matching quark coming from a top quark decay, then the flavour of its matching quark is determined by the truth label of the jet[7]. A criterion of $\Delta R < 0.3$ is used for matching between the selected jets and the quarks from top quark decays. The number of categories for events with a given jet multiplicity is determined by the number of possible unique combinations of flavours of matching quarks. For example, the number of categories in the events with two jets is six, given the three possible flavours for matching quarks: b-, c- and light (q). These categories are "bb", "bc", "bq", "cc", "cq" and "qq". Accordingly, the number of categories in the events with three jets is ten. These are "bbb", "bbc", "bbq", "bcc", "bcq", "bqq", "ccc", "ccq", "cqq" and "qqq". Only categories determined up to four jets are used, while some of these four-jet categories are inclusive with respect to one or two flavours of matching quarks. For example, the "qqqq" category collected the events with four or more light jets (implies that all associated jets in this event were matched to light quarks). A dedicated study is performed to identify which categories are

[7] Only the flavour of the quark initiating a given jet is of interest but not its kinematic properties.

present in the selected events of the nominal Protos $t\bar{t}$ sample in order to reduce the number of categories to a reasonable amount, 25 in total. But not all of these categories have a significant contribution in the selected events. Table 5.5 presents only the categories with relative contributions exceeding 2% to at

Category	%		
	$tt \to WWbb$	$tt \to WWqb$	$tt \to WWqq$
bb	38.7	0.2	0.0
bbq	22.8	0.9	0.0
bbqq	11.1	0.8	0.2
bq	13.4	44.6	0.3
bqq	4.9	25.3	0.4
bqqq	2.0	12.5	0.5
qq	0.8	7.7	51.5
qqq	0.1	2.8	28.6
qqqq	0.1	1.0	13.9
bbb	2.3	0.1	0.0
cqqq	0.3	0.9	2.0
others	3.6	3.3	2.7

Table 5.5: Fractions of selected events in a given category for the three $t\bar{t}$ templates, as estimated from the nominal Protos sample. The "bbqq", "bqqq", "qqqq" and "cqqq" categories are inclusive with respect to the number of light jets. The "bbb" category is inclusive with respect to the number of b-jets. All other categories presented in this table are exclusive.

least one of the three templates. As it can be seen from the table, at most four categories significantly contribute to a given template. Figure 5.14 shows distributions of the number of b-tagged jets for the "bb" category of the $tt \to WWbb$ events. The nominal Protos and variation distributions, as obtained from the corresponding ISR/FSR variation samples, are presented together.

The ISR/FSR variation is expected to have a symmetric effect in each bin of the nominal distribution of a given category. The deviation from this expectation (see figure 5.14) are likely due to statistical fluctuations, the use of different generators and the use of full vs. fast simulation. In order to symmetrise the ISR/FSR distributions to the corresponding nominal distributions, a set of scale factors is determined for each category by equation 5.4,

$$\mathrm{SF}_i = \frac{2y_i^{\mathrm{nom}}}{y_i^{\mathrm{min}}} + y_i^{\mathrm{max}}, \tag{5.4}$$

where y_i^{nom}, y_i^{max} and y_i^{min} are respectively the nominal value and the higher and the lower values of the ISR/FSR distributions of the number of b-tagged jets in the i-th bin, where all distributions are normalised to unity. The scale factors, SF_i, are applied to the corresponding bins of the original ISR/FSR distributions (not normalised to unity). This leads to the symmetrisation of the ISR/FSR variation with respect to the nominal distribution.

The symmetrised ISR/FSR distributions (dashed red and blue histograms) of the "bb" category for the $tt \to WWbb$ template is shown in figure 5.14, together with the original ISR/FSR (solid red and blue histograms) and the nominal (solid black histogram) distributions. All distributions are normalised to the integrated luminosity in data. The approximate 4-times difference in normalisation of the nominal and the ISR/FSR distributions is due to the $R_b = 0.5$ parameter used in the generation of the nominal Protos sample. The normalisation of the ISR/FSR distributions is not necessarily preserved after the

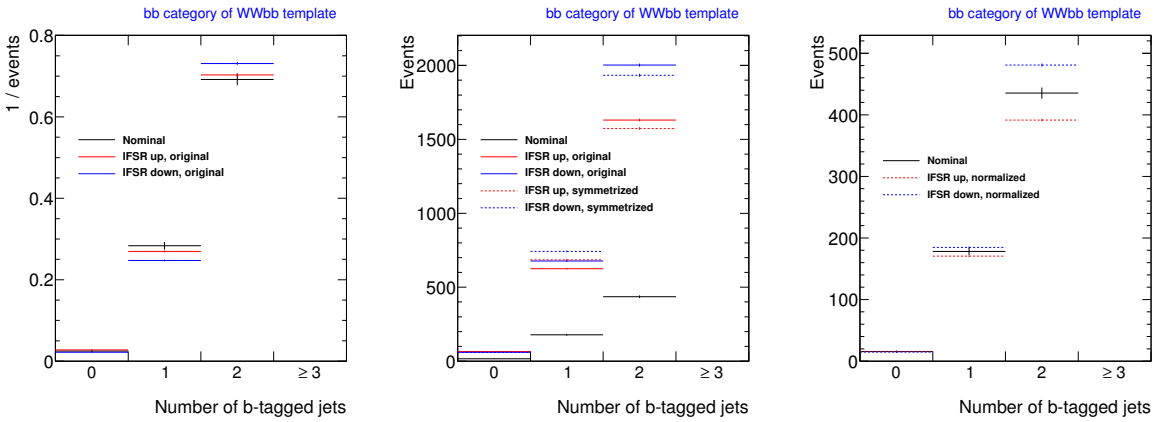

Figure 5.14: Distributions of number of b-tagged jets for the "bb" category of the selected $tt \to WWbb$ events, for the nominal Protos and ISR/FSR variations for the original (left), the symmetrised distributions (middle) and after normalisation (right). The solid black histograms correspond to the nominal distribution. The solid red and blue histograms stand for the original distributions of the ISR/FSR "up" and "down" variation respectively. The dashed red and blue histograms correspond to the modified distributions of the ISR/FSR "up" and "down" variation respectively.

symmetrisation procedure. For example, the solid red and the dashed red histograms in figure 5.14 might not correspond to the same number of events.

In the next step, the symmetrised distributions are normalised to the number of events in the corresponding nominal distributions. The normalisation factor is the ratio of the number of events in the nominal distribution over the averaged number of events in the symmetrised ISR/FSR "up" and "down" distributions. As an example, the resulting normalised ISR/FSR distributions for the "bb" category of the $tt \to WWbb$ template are shown in figure 5.14 together with the nominal distribution. The normalised distributions of ISR/FSR "up" ("down") variation of all categories are summed and then normalised to one in order to produce derived $tt \to WWbb$ ISR/FSR "up" ("down") templates. They are shown together with the nominal and the original ISR/FSR templates in figure 5.15.

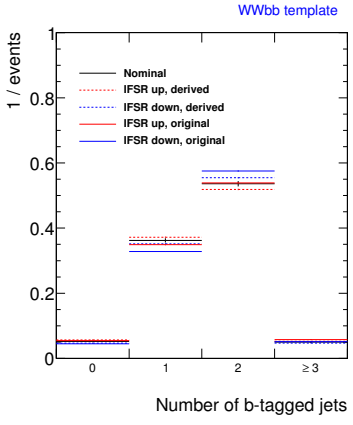

Figure 5.15: The nominal $tt \to WWbb$ template from Protos sample (solid black) and its original (solid red and blue) and derived (dashed red and blue) ISR/FSR "up" and "down" variation templates. All templates are normalised to unity.

The distribution of the number of b-tagged jets only depends on the event category and not on the type

of the template. This can be seen from the plots in figure 5.16. The same categories but corresponding

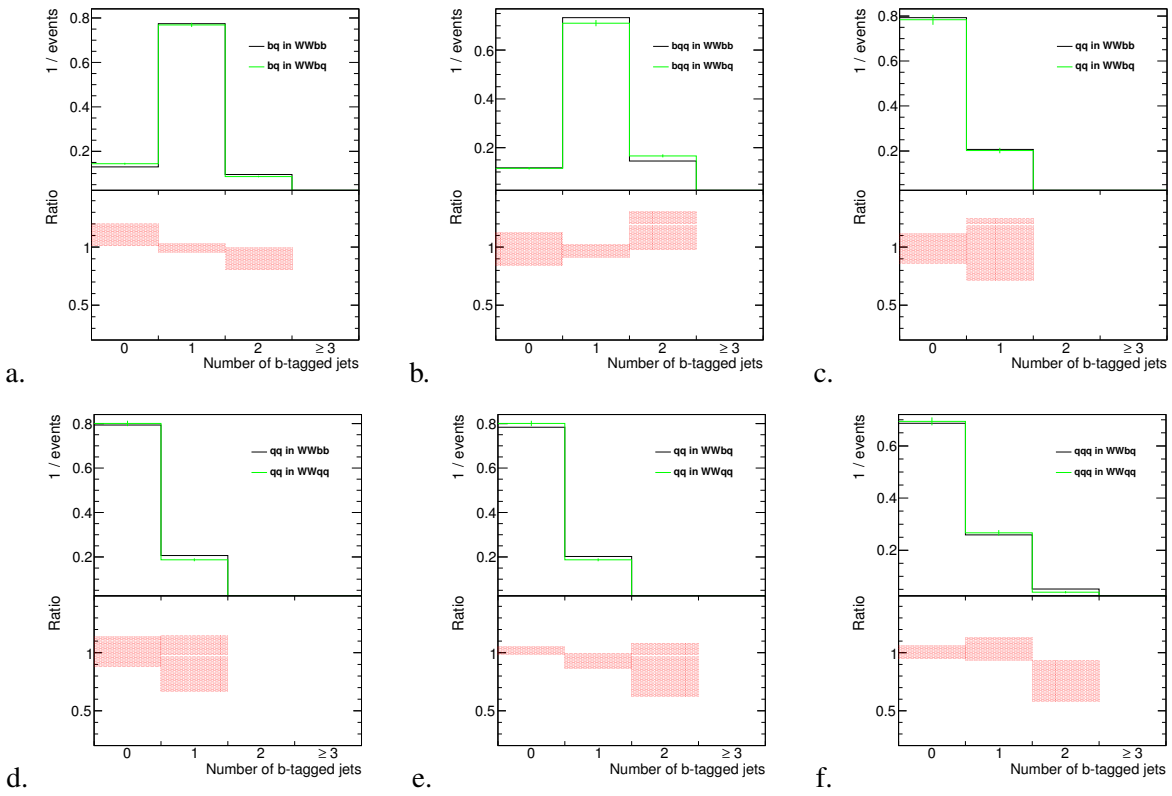

Figure 5.16: Distributions of number of b-tagged jets for the "bq" (a), "bqq" (b), "qq" (c-e) and "qqq" (f) categories compared for pairs of relevant templates $tt \to WWbb$ $tt \to WWqb$ and $tt \to WWqq$. The ratio bands show the statistical uncertainty and are centered at the ratio value.

to different templates are compared to each other. The categories, which contribute significantly in at least one of the three templates are chosen for comparison. All ratios are compatible with one within the statistical precision. Based on this finding, the ISR/FSR variations of the categories of the $tt \to WWbb$ template can be used to derive variations for the categories of the $tt \to WWqb$ and $tt \to WWqq$ templates.

The procedure of symmetrisation described before is used to derive similar symmetrised distributions for the categories of the other templates. The set of scale factors for each category is calculated with equation 5.4. Now, the normalised nominal distribution of a given category of the $tt \to WWbb$ template, from which the y_i^{nom} values are obtained, is replaced with the template under study, $tt \to WWqb$ or $tt \to WWqq$. Obviously, the corresponding distributions of the ISR/FSR variation, from which the y_i^{min} and y_i^{max} values are obtained, are taken from the $tt \to WWbb$ template. The scale factors, SF_i, are used to derive symmetrised distributions (similar to the distributions shown in figure 5.14) for all categories of the $tt \to WWqb$ and $tt \to WWqq$ templates. In the next step, the distributions are normalised to the number of events in the corresponding nominal distributions, as was explained above. Finally, the normalised distributions of all categories are summed to create the "up" and "down" ISR/FSR variation of the $tt \to WWqb$ and $tt \to WWqq$ templates. These derived templates are shown in figure 5.17 together with the corresponding nominal templates.

To estimate the effect of using the derived templates described above, three different sets of pseudo-

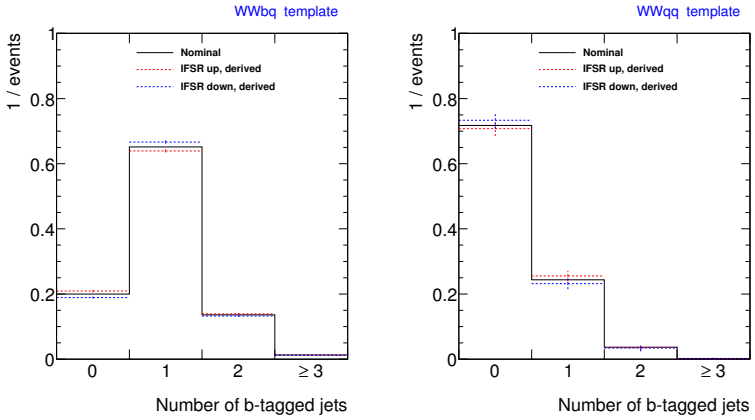

Figure 5.17: The $tt \to WWqb$ (left) and $tt \to WWqq$ (right) templates and their derived ISR/FSR "up" and "down" variations.

experiments are performed. Results obtained using the original ISR/FSR $tt \to WWbb$ template ($tt \to WWqb$ and $tt \to WWqq$ are taken from Protos), results obtained with only the $tt \to WWbb$ template derived, including the symmetrisation procedure ($tt \to WWqb$ and $tt \to WWqq$ are taken from Protos) and results where all derived templates $tt \to WWbb$, $tt \to WWqb$ and $tt \to WWqq$ are used, are compared and the resulting ISR/FSR uncertainty are shown in table 5.6.

Setting	ΔR_b	$\Delta\sigma_{\text{dilepton}}$
Varied sample ($tt \to WWbb$ only)	0.016	0.15 pb
Derived $tt \to WWbb$ template	0.018	0.16 pb
Derived $tt \to WWbb$, $tt \to WWqb$, $tt \to WWqq$	0.018	0.16 pb

Table 5.6: Uncertainty on R_b and σ_{dilepton} in different scenarios concerning the variation of the $tt \to WWbb$, $tt \to WWqb$ and $tt \to WWqq$ templates obtained from pseudo-experiments with $R_b = 0.99830$ and $\sigma_{\text{dilepton}} = 11.33$ pb.

No significant discrepancy is observed when comparing the results for R_b and σ_{dilepton} for the three different approaches.

5.4.3 Impact of pile-up

The high density of the proton beams at the LHC leads to multiple proton-proton interactions per bunch crossing (see section 2.2) and as a result, a pile-up of physics processes and multiple *primary*[8] vertices per event. This busy environment might have an impact on the quality of physics measurements. To recreate the pile-up conditions in the simulation, as previously mentioned in section 2.3, the events in simulation samples have a varying number of interactions (vertices) and the simulation samples are re-weighted such that the distribution of the average number of interactions $\langle\mu\rangle$ per luminosity block in the simulation matches the distribution in data, which is illustrated in figure 5.18 (left). The simulation and data distributions are not perfectly aligned, because the $\langle\mu\rangle$ re-weighting is applied before any of the selection criteria, but they agree within statistical uncertainty. Figure 5.18 (right) shows that re-

[8] In earlier chapters, primary vertex is defined as the vertex for which the associated tracks have the highest sum in squared transverse momenta. Here, primary vertex is understood as the position of the proton-proton interaction, as opposed to a secondary decay vertices.

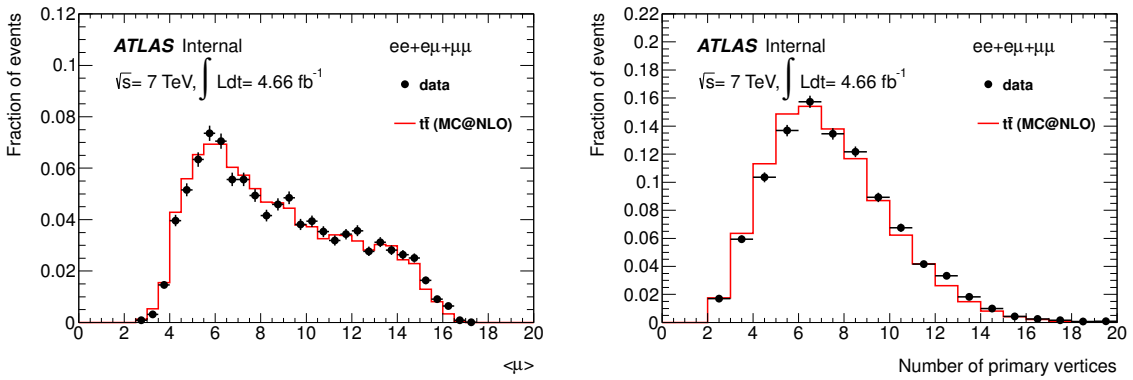

Figure 5.18: Distributions of the average number of interactions $\langle\mu\rangle$ and the number of primary vertices in data and simulation after re-weighting the simulation by $\langle\mu\rangle$ and applying all selection criteria from section 3.

weighting the simulation sample by $\langle\mu\rangle$ also aligns its distribution of number of primary vertices with data.

To verify the impact of pile-up on the measurement of R_b and σ_{dilepton}, the data is split into 26 sub-samples by $\langle\mu\rangle$ value (every sub-sample covered a 0.5 range from 3.5 to 16[9]) and a fit is performed separately for each sub-sample. For each of these measurements a distribution of the number of b-tagged jets in data, as well as the selection efficiencies for $tt \to WWbb$ $tt \to WWqb$ and $tt \to WWqq$ processes from simulation, are obtained. The templates for signal and background are not changed, i.e. they are obtained from the events from the entire $\langle\mu\rangle$ spectrum in simulation. The results are presented in figure 5.19. There is a small effect observed on the measured value of R_b and a linear dependence of σ_{dilepton} on $\langle\mu\rangle$.

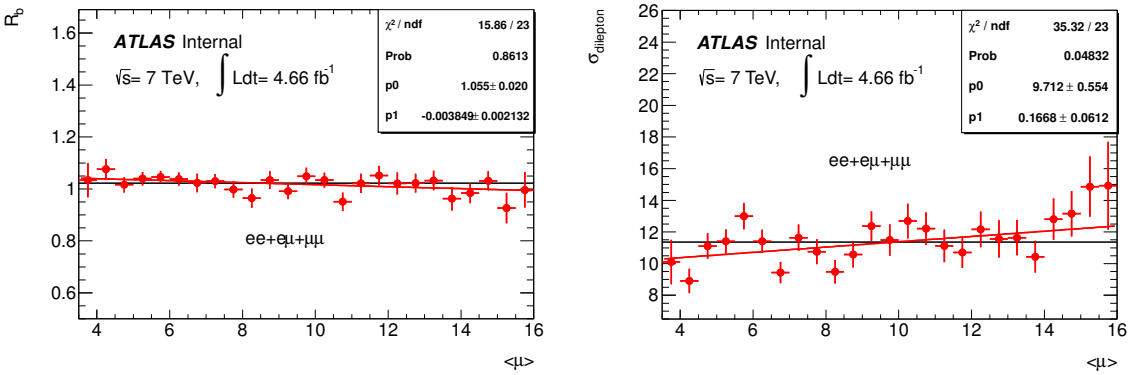

Figure 5.19: Measured values of R_b and σ_{dilepton} for average number of interactions $3.5 < \langle\mu\rangle < 16$. The error bars represent the sum of statistical uncertainties returned by the fit and the statistical uncertainty on the selection efficiency for the $tt \to WWbb$ process. The black line in the distribution of σ_{dilepton} shows the value measured with the entire dataset.

A similar test is repeated for the numbers of primary vertices: a series of measurements is performed for sub-samples of events with number of primary vertices between 2 and 16. The results are presented in figure 5.20. There is a linear dependence observed on the measured value of both R_b and σ_{dilepton}.

[9] There are not enough events with $\langle\mu\rangle < 3.5$ or $\langle\mu\rangle > 16$ to build templates for $\langle\mu\rangle$ outside of this range, as can be observed in figure 5.18 (left).

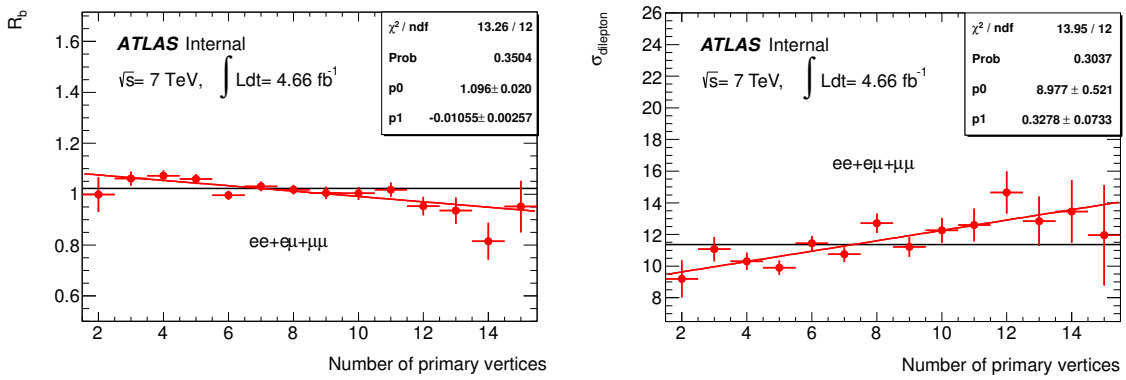

Figure 5.20: Measured values of R_b and σ_{dilepton} for events with number of primary vertices between 2 and 16. The error bars represent the sum of the statistical uncertainties returned by the fit and the statistical uncertainty on the selection efficiency for the $tt \to WWbb$ process. The black line shows the value measured with the entire dataset.

The impact of a possible mismodelling of pile-up in the simulation samples is evaluated by re-calculating the values of R_b and σ_{dilepton} using the found linear dependencies on the number of primary vertices and $\langle\mu\rangle$ and the distribution of those two variables for data and simulated samples shown in figure 5.18 in the following way

$$x = \frac{\sum_{i=1}^{n_{bins}} n_i \cdot (p_0 + p_1 \cdot y_i)}{\sum_{i=1}^{n_{bins}} n_i} \tag{5.5}$$

where x is either R_b or σ_{dilepton}, p_0 and p_1 are parameters describing the dependence of R_b and σ_{dilepton} on $\langle\mu\rangle$ or the number of primary vertices from fits in figures 5.19 and 5.20, which are summarised in table 5.7. n_i is the number of events and y_i is the central value in i-th bin of the respective distribution shown in figure 5.18.

	p_0	p_1
$\langle\mu\rangle$		
σ_{dilepton}	9.7	0.17
R_b	1.055	-0.004
number of primary vertices		
σ_{dilepton}	9.0	0.33
R_b	1.10	-0.01

Table 5.7: p_0 and p_1 parameters of linear functions fitted to the distributions of R_b and σ_{dilepton} in figures 5.19 and 5.20.

The resulting values of R_b and σ_{dilepton} measured in data and simulation are presented in table 5.8. The higher δ(data-sim.) is treated as the uncertainty resulting from the pile-up mismodelling in simulation.

As the sub-samples from data have a limited size, both measurements are repeated using generated pseudo-data to check if the dependencies described above are not an effect of statistical fluctuations. No dependence on $\langle\mu\rangle$ or number of primary vertices are observed for neither R_b nor σ_{dilepton}, which could indicate that pile-up does not impact these measurements, but more data would be needed for a definite conclusion. The results of the studies with pseudo-experiments are described in appendix E.

	data	simulation	δ(data-sim.)
		$\langle\mu\rangle$	
σ_{dilepton}	11.1797	11.154	0.0257
R_b	1.0211	1.0217	-0.0006
		number of primary vertices	
σ_{dilepton}	11.2854	11.2257	0.0597
R_b	1.0217	1.0236	-0.0019

Table 5.8: Values of R_b and σ_{dilepton} calculated with equation 5.5.

5.4.4 Dependence on the top quark mass

The dependence of the measurements on the top quark mass is checked with help of the dedicated simulation samples with top quark masses m_{top} of 165, 167.5, 170, 172.5, 175, 177.5 and 180 GeV, which are described in section 3.4. For each of these samples, a set of pseudo-experiments is conducted, in which a fit is performed with the $tt \to WWbb$ template obtained from the sample with varied top quark mass and the $tt \to WWqb$ and $tt \to WWqq$ templates from the Protos sample. Figure 5.21 shows the measured values of R_b and σ_{dilepton} as a function of m_{top}.

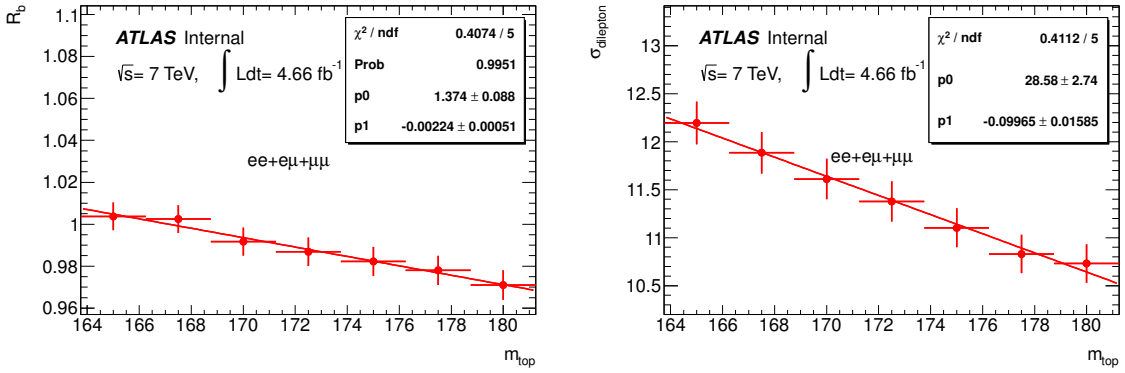

Figure 5.21: R_b and σ_{dilepton} as a function of top quark mass m_{top}.

For both R_b and σ_{dilepton}, a linear dependence on the top quark mass is observed. The parameters of the fitted linear functions from figure 5.21 are summarized in table 5.9. They allow to propagate the uncertainty on the top quark mass m_{top}, which according to reference [16] is 0.89 GeV, on the measurements of R_b and σ_{dilepton}. The resulting uncertainties are: $\delta_{R_b} = 0.002$ and $\delta_{\sigma_{\text{dilepton}}} = 0.09$ pb.

	p_0	p_1
σ_{dilepton}	28.6	-0.10
R_b	1.37	-0.002

Table 5.9: p_0 and p_1 parameters of the linear functions fitted to the distributions of R_b and σ_{dilepton} to account for the top quark mass dependence (see figures 5.21).

5.4.5 Dependence on the dilepton decay channel

A separate fit to data in each dilepton decay channel: ee, $\mu\mu$ and $e\mu$, is performed to investigate if there exists a dependence on the chosen decay mode. For this study, a distribution of number of b-tagged jets is obtained for each channel from data as well as separate $tt \to WWbb$, $tt \to WWqb$ and $tt \to WWqq$ templates and selection efficiencies from simulation. The results are presented in figure 5.22 and the

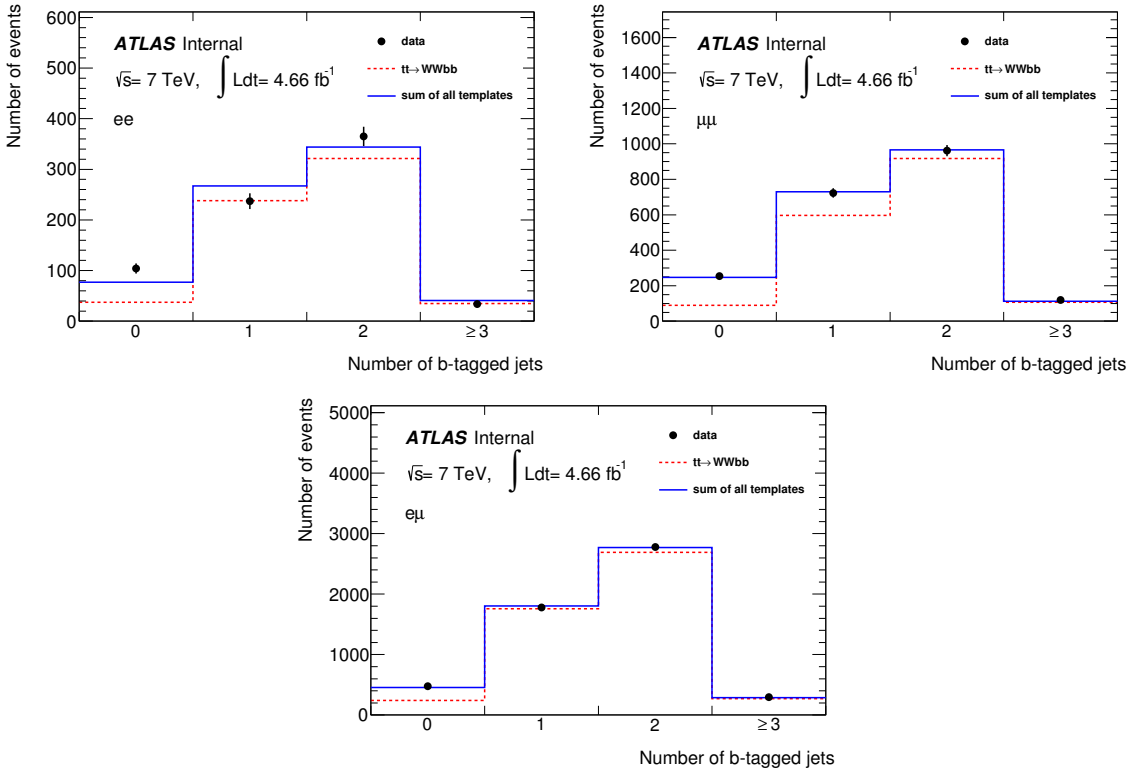

Figure 5.22: Fit to data, separated into ee, $\mu\mu$ and $e\mu$ channels. The extracted values of R_b and σ_{dilepton} are presented in table 5.10.

extracted R_b and σ_{dilepton} values together with the statistical uncertainty of the fit are listed in table 5.10.

	ee	$\mu\mu$	$e\mu$
σ_{dilepton}	10.58 ± 0.47	11.74 ± 0.30	11.32 ± 0.18
R_b	1.023 ± 0.028	0.992 ± 0.014	1.034 ± 0.008

Table 5.10: Values of R_b and σ_{dilepton} measured separately in ee, $\mu\mu$ and $e\mu$ channels in data.

Values of R_b and σ_{dilepton} measured in ee, $\mu\mu$ and $e\mu$ agree within statistical uncertainties with the combined measurements presented in section 5.5.

5.4.6 Evaluation of systematic uncertainties with pseudo-experiments

To estimate the size of the systematic uncertainties on the R_b measurement, modified templates are obtained with varied parameters that introduce the systematic uncertainty, such as the earlier mentioned

b-tagging scale factors, for instance. Although the background normalisation and selection efficiency (described in section 5.1) are kept constant in the fit, the influence of systematic variations on those quantities is taken into account. In appendix F the effect of the systematic uncertainties on the signal template shapes is shown.

In tables 5.11 and 5.12 the values of the systematic uncertainties on R_b and σ_{dilepton}, obtained from a series of pseudo-experiment, as described in section 5.2, are presented, assuming input values predicted by the standard model $R_b = 0.99830$ and $\sigma_{\text{dilepton}} = 11.33$ pb. Only the pile-up and top quark mass uncertainties are estimated directly from data as described in sections 5.4.3 and 5.4.4. Since uncertainties from electron and muon trigger efficiency, reconstruction efficiency, transverse momentum smearing and energy resolution for R_b are very small, they are joined for each of the lepton types. Moreover, a breakdown of the jet energy uncertainty into a variation of 21 nuisance parameters and a breakdown of the b-tagging uncertainty into contributions for 9 eigenvalues is provided in appendix G.

Fit results of pseudo-experiments for varied templates for the largest uncertainties are shown in appendix H. The R_b and σ_{dilepton} values measured for templates from various signal simulation samples are presented in table 5.13.

measured R_b	0.998		
Source	Var. Down	Var. Up	Averaged Var.
Initial/final state radiation	-0.018	0.018	0.018
Generator	-0.033	0.033	0.033
Associated HF prod.	-0.003	0.003	0.003
Colour reconnection	-0.001	0.001	0.001
Underlying event	-0.000	0.000	0.000
Parton distribution function	-0.001	0.001	0.001
Top quark mass	0.002	-0.002	0.002
Jet energy scale	-0.004	0.007	0.005
Jet reconstruction efficiency	0.000	-0.000	0.000
Jet energy resolution	0.004	-0.004	0.004
Jet vertex fraction	-0.000	0.000	0.000
b-tagging (b-jets)	-0.050	0.054	0.052
b-tagging (c-jets)	0.002	-0.002	0.002
b-tagging (light jets)	0.006	-0.007	0.007
$E_{\mathrm{T}}^{\mathrm{miss}}$	0.000	-0.000	0.000
e SF	-0.000	0.000	0.000
μ SF	-0.000	0.000	0.000
background flavour comp.	0.001	-0.001	0.001
Z+jets norm.	-0.003	0.003	0.003
Dib norm.	-0.003	0.003	0.003
Sg. top norm.	0.001	-0.001	0.001
Fake leptons shape	0.001	-0.001	0.001
Fake leptons norm.	0.002	-0.002	0.002
Pile-up	-0.002	0.002	0.002
Luminosity	-0.000	0.000	0.000
Sel. eff. stat.	-0.000	0.000	0.000
Total syst.	-0.064	0.067	0.065
Total stat.	-0.007	0.007	0.007
Total unc.	-0.064	0.067	0.066

Table 5.11: List of uncertainties on the measurement of R_b. The top quark mass and pile-up uncertainties are determined using fit to data as described in sections 5.4.3 and 5.4.4, the rest using pseudo-experiments with an R_b input value 0.99830. The total systematic uncertainty is the quadrature sum of all negative and positive contributions.

measured σ_{dilepton}	11.33 pb		
Source	Var. Down	Var. Up	Averaged Var.
Initial/final state radiation	-0.17	0.17	0.17
Generator	-1.05	1.05	1.05
Associated HF prod.	-0.04	0.04	0.04
Colour reconnection	-0.15	0.15	0.15
Underlying event	-0.01	0.01	0.01
Parton distribution functions	-0.12	0.12	0.12
Top quark mass	0.09	-0.09	0.09
Jet energy scale	-0.20	0.20	0.20
Jet reconstruction efficiency	0.00	-0.00	-0.00
Jet energy resolution	0.02	-0.02	-0.02
Jet vertex fraction	0.11	-0.09	0.10
b-tagging (b-jets)	-0.06	0.07	0.07
b-tagging (c-jets)	0.00	-0.00	0.00
b-tagging (light jets)	0.02	-0.01	0.01
$E_{\text{T}}^{\text{miss}}$	-0.01	0.01	0.01
e trigger	0.01	-0.02	0.01
e rec./id. efficiency	0.24	-0.23	0.24
e energy	0.02	-0.02	0.02
μ trigger	0.03	-0.03	0.03
μ rec./id.	0.10	-0.10	0.10
μ p_{T}	-0.01	0.00	0.00
background flavour composition	0.01	-0.01	0.01
Z+jets norm.	-0.01	0.02	0.01
Dib norm.	-0.01	0.02	0.01
Fake leptons norm. $e\mu$	0.01	-0.01	0.01
Pile-up	-0.06	0.06	0.06
Luminosity	-0.00	0.00	0.00
Sel. eff. stat.	-0.10	0.10	0.10
Total syst.	-1.14	1.15	1.15
Total stat.	-0.20	0.20	0.20
Total unc.	-1.16	1.17	1.16

Table 5.12: List of the uncertainties on the measurement of R_b. The top quark mass and pile-up uncertainties are determined using fit to data as described in sections 5.4.3 and 5.4.4, the rest using pseudo-experiments with a σ_{dilepton} input value 11.33 pb. The total systematic uncertainty is the quadrature sum of all negative and positive contributions.

Generator	Showering	Simulation type	Sel. efficiency	R_b	σ_{dilepton} [pb]
Protos	Pythia	mc11c full sim.	0.1322	0.9983	11.33
MC@NLO	Herwig	mc11c full sim.	0.1307	0.9779	11.44
MC@NLO (CT10)	Herwig	mc11c full sim.	0.1307	0.9779	11.44
MC@NLO (MSTW)	Herwig	mc11c full sim.	0.1287	0.9766	11.61
MC@NLO (NNPDF)	Herwig	mc11c full sim.	0.1280	0.9772	11.67
MC@NLO (ren/fac up)	Herwig	mc11c fast sim.	0.1348	0.9736	11.12
MC@NLO (ren/fac down)	Herwig	mc11c fast sim.	0.1355	0.9750	11.06
Alpgen (with HF)	Herwig	mc11c full sim.	0.1461	0.9621	10.32
Powheg	Herwig	mc11b fast sim.	0.1277	0.9778	11.72
Powheg	Pythia	mc11c full sim.	0.1317	0.9870	11.38
Powheg	Pythia	mc11b fast sim.	0.1304	0.9853	11.49
Powheg (117428)	Pythia	mc11c fast sim.	0.1332	0.9834	11.26
Powheg (no CR)	Pythia	mc11c fast sim.	0.1351	0.9826	11.11
Powheg (mpiHi)	Pythia	mc11c fast sim.	0.1331	0.9834	11.26
AcerMC (IFSR up)	Pythia	mc11c fast sim.	0.1367	0.9919	10.98
AcerMC (IFSR down)	Pythia	mc11c fast sim.	0.1410	0.9590	10.67
Powheg (m_{top} = 165 GeV)	Pythia	mc11c full sim.	0.1231	1.0040	12.20
Powheg (m_{top} = 167.5 GeV)	Pythia	mc11c full sim.	0.1263	1.0030	11.88
Powheg (m_{top} = 170 GeV)	Pythia	mc11c full sim.	0.1291	0.9918	11.61
Powheg (m_{top} = 175 GeV)	Pythia	mc11c full sim.	0.1350	0.9824	11.10
Powheg (m_{top} = 177.5 GeV)	Pythia	mc11c full sim.	0.1387	0.9781	10.83
Powheg (m_{top} = 180 GeV)	Pythia	mc11c full sim.	0.1401	0.9711	10.73

Table 5.13: Selection efficiencies and R_b and σ_{dilepton} values measured with various simulation samples. Protos, listed first, is the default sample used to build $tt \to WWbb$, $tt \to WWqb$ and $tt \to WWqq$ templates. Remaining samples, utilized to evaluate systematic uncertainties, are used only for the $tt \to WWbb$ template. For each sample, a series of pseudo-experiments is conducted, in which the templates (new $tt \to WWbb$, $tt \to WWqb$ and $tt \to WWqq$ from Protos and the background template) are fitted to pseudo-data generated from background template and the default $tt \to WWbb$, $tt \to WWqb$ and $tt \to WWqq$ templates with input values of $R_b = 0.99830$ and $\sigma_{\text{dilepton}} = 11.33$ pb.

5.5 Results

5.5.1 Fit to data

The fit is performed to the selected data. In total, 8127 events are selected from 4.6 fb^{-1} in the dilepton topologies ee, $e\mu$ and $\mu\mu$. The result is shown in figure 5.23. The value extracted for R_b is $R_b = 1.022 \pm 0.007\,(\text{stat.})$ and the cross section $\sigma_{\text{dilepton}} = 11.36 \pm 0.20\,(\text{stat.})$ pb.

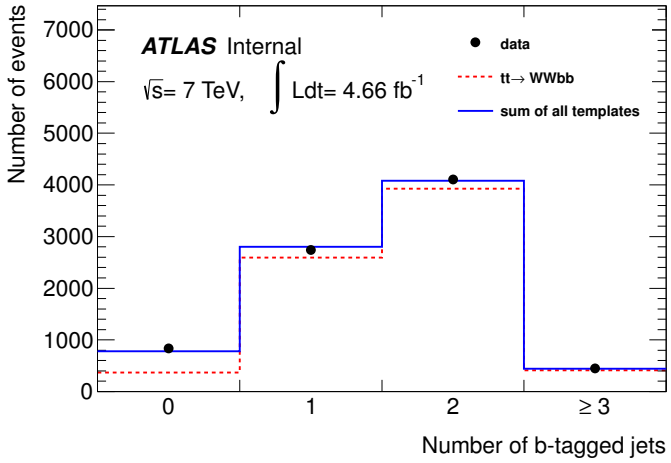

Figure 5.23: Fit to data. The measured value of R_b is 1.022 and σ_{dilepton} is 11.36 pb.

To estimate the systematic uncertainty in the values of R_b and σ_{dilepton} measured in data, pseudo-experiments as described in section 5.4.6 are repeated with the input values of $R_b = 1.022$ and the cross section $\sigma_{\text{dilepton}} = 11.36$ pb. However, the uncertainty originating from pile-up and top quark mass are estimated using the fit to data, as described in sections 5.4.3 and 5.4.4.

Table 5.14 provides the list of systematic uncertainties for R_b and σ_{dilepton}. Appendix G provides a breakdown of the b-tagging and JES uncertainties.

The uncertainties are also validated by performing a fit to data using templates with systematic variations and a very similar total uncertainty is measured. Detailed results can be found in appendix I.

Combining the fit to data with the study on systematics uncertainties presented in table 5.14 and the uncertainty on the dilepton branching fraction as calculated in section 1.2.2, the following results are obtained

$$R_b = 1.02 \pm 0.01\,(\text{stat.}) \pm 0.07\,(\text{syst.}),$$

and

$$\sigma_{t\bar{t}} = 178 \pm 3\,(\text{stat.}) \pm 19\,(\text{syst.})\ \text{pb}.$$

Additionally, following equation 1.19, $|V_{tb}| = \sqrt{R_b}$ and therefore

$$|V_{tb}| = 1.01 \pm 0.01\,(\text{stat.}) \pm 0.03\,(\text{syst.}).$$

5.5.2 Extraction of one-sided lower limits on R_b and $|V_{tb}|$

As outlined in section 1.2.3, R_b is directly linked to the CKM matrix element $|V_{tb}|$ and the presented measurement of R_b allows for setting limits on the values of both, R_b and $|V_{tb}|$. Since the measured value of R_b is larger than one, only a lower limit (at 95% C.L.) is extracted. The upper limit is determined

Variable	R_b	σ_{dilepton}
Measured Value	1.022	11.36 pb
Source	Average Unc.	Average Unc.
Initial/final state radiation	0.019	0.18
Generator	0.033	1.10
Associated HF prod.	0.003	0.04
Colour reconnection	0.001	0.16
Underlying event	0.000	0.01
Parton distribution function	0.001	0.12
Top quark mass	0.002	0.09
Jet energy scale	0.006	0.20
Jet reconstruction efficiency	0.000	0.00
Jet energy resolution	0.004	0.02
Jet vertex fraction	0.001	0.10
b-tagging (b-jets)	0.053	0.07
b-tagging (c-jets)	0.002	0.00
b-tagging (light jets)	0.006	0.01
$E_{\text{T}}^{\text{miss}}$	0.001	0.01
e trigger	0.000	0.01
e rec./id. efficiency	0.000	0.24
e energy	0.000	0.02
μ trigger	0.000	0.03
μ rec./id.	0.000	0.10
μ p_{T}	0.001	0.01
background flavour composition	0.001	0.01
Z+*jets* norm.	0.003	0.02
Dib norm.	0.003	0.02
Sg. top norm.	0.001	0.00
Fake leptons shape	0.000	0.00
Fake leptons norm.	0.002	0.01
Pile-up	0.002	0.06
Luminosity	0.000	0.03
Sel. eff. stat.	0.000	0.11
Total syst.	0.066	1.20
Total stat.	0.007	0.20
Total unc.	0.067	1.21

Table 5.14: List of the uncertainties on the measurement of R_b and σ_{dilepton}(evaluated separately). The top quark mass and pile-up uncertainties are determined using fit to data as described in sections 5.4.3 and 5.4.4, the rest using pseudo-experiments with using pseudo-experiments with $R_b = 1.022$ and $\sigma_{\text{dilepton}} = 11.36$ as input values. The total systematic uncertainty is the quadrature sum of all negative and positive contributions.

by the physics boundary of R_b to be 1. An implementation of the Feldman-Cousins method [141] in RooStats [142] is used to calculate the one-sided (lower) limit. RooFit [137] is used to construct likelihood functions. The likelihood function for the measured value of R_b is constructed using the result of pseudo-experiments presented in section 5.2. As it is found from these results, the fitted R_b value in the pseudo-experiments had a Gaussian distribution with the mean equal to the input value of R_b. An example distribution of the fitted R_b value in the pseudo-experiments performed at the input value of $R_b = 0.99830$ is shown in figure 5.7. The linearity test of the template fit results for varying input values of R_b shows that the width of the posterior Gaussian distribution of the fitted R_b value does not depend on the input R_b value and remains constant. Based on the aforementioned results, the likelihood function for the measured R_b is a Gaussian function with a constant σ parameter, $L_{R_b}(R_{b,\text{obs.}} \mid R_{b,\text{input}}) = G(R_{b,\text{obs.}} \mid \mu = R_{b,\text{input}}, \sigma^2 = \text{const})$. The constant value of the σ parameter is the statistical uncertainty of the measurement, as estimated from the fit of a Gaussian function to the posterior distribution of the fitted values of R_b obtained from the pseudo-experiments.

The systematic effects are not yet considered in the construction of the above likelihood function. The impact of each source of systematic uncertainty on the measurement is assumed to be orthogonal with respect to other sources. Therefore, the uncertainties of the measured R_b value due to a given source of systematic effects are added in quadrature to the statistical uncertainty. This means that two Gaussian widths are added to each other, to result into $G(\mu = R_{b,\text{input}}, \sigma^2_{\text{stat.}} + \sigma^2_{\text{syst.},i})$. Here, $\sigma_{\text{syst.},i}$ denotes the uncertainty due to the i-th source of systematic uncertainties. In this analysis a large number of systematic uncertainty sources is considered, all of which have a certain impact (physics expectation) on the measurement. Therefore, the assumption that each of these sources impacts the measurement according to a Gaussian can be released and the central limit theorem invoked, as the net effect is still Gaussian. Assuming that the total systematic uncertainty is symmetric, the likelihood function for the measured R_b is $L_{R_b}(R_{b,\text{obs.}} \mid R_{b,\text{input}}) = G(R_{b,\text{obs.}} \mid \mu = R_{b,\text{input}}, \sigma^2_{\text{stat.}} + \sigma^2_{\text{syst.}})$, where $\sigma^2_{\text{syst.}}$ is the total absolute systematic uncertainty squared, calculated as the quadrature sum of all systematic uncertainties. As it is explained earlier, the systematic effects of the measurement are estimated with the assumption of $R_b = 0.99830$, but the total systematic uncertainty does not depend on the assumed value of R_b if this latter is in its physics expected region. Thus, the sum of squared absolute uncertainties, $\sigma^2_{\text{stat.}} + \sigma^2_{\text{syst.}}$ is constant. The likelihood function is used to obtain the limits on R_b at 68.3% and 95% C.L. with the Feldman-Cousins method. The calculated limits as function of the measured R_b values are presented in figure 5.24 (left). The lower limit is found to be 0.88 at 95% C.L. given the measured R_b value and its uncertainty.

The likelihood function of the measured R_b parametrised as a function of $|V_{tb}|$ is obtained from the above likelihood function considering the relation between R_b and $|V_{tb}|$, $|V_{tb}| = \sqrt{R_b}$. After the simple transformation of the variables $L_{|V_{tb}|}(R_{b,\text{obs.}} \mid |V_{tb}|_{\text{input}}) = 2|V_{tb}|_{\text{input}} \times L_{R_b}(R_{b,\text{obs.}} \mid |V_{tb}|^2_{\text{input}})$. Using this likelihood function with the help of the Feldman-Cousins method the limits on the value of $|V_{tb}|$ can be calculated as function of the measured R_b. The resulting limit bands at 68.3% and 95% C.L. are shown in figure 5.24 (right). The extracted lower limit on the $|V_{tb}|$ is 0.94 at 95% C.L.

5.5.3 Summary and outlook

In this analysis, R_b, the ratio of the top quark branching fractions $R_b = \mathcal{B}(t \to Wb)/\mathcal{B}(t \to Wq)$[10] and the inclusive $t\bar{t}$ cross section $\sigma_{t\bar{t}}$ are measured using selected dilepton events. Data collected by ATLAS in 2011, corresponding to a total luminosity of 4.6 fb^{-1} of pp collisions is used. R_b and $\sigma_{t\bar{t}}$ are extracted with a template fit using as template the distribution of the number of jets tagged with the

[10] Here, q denotes b,s and d quarks.

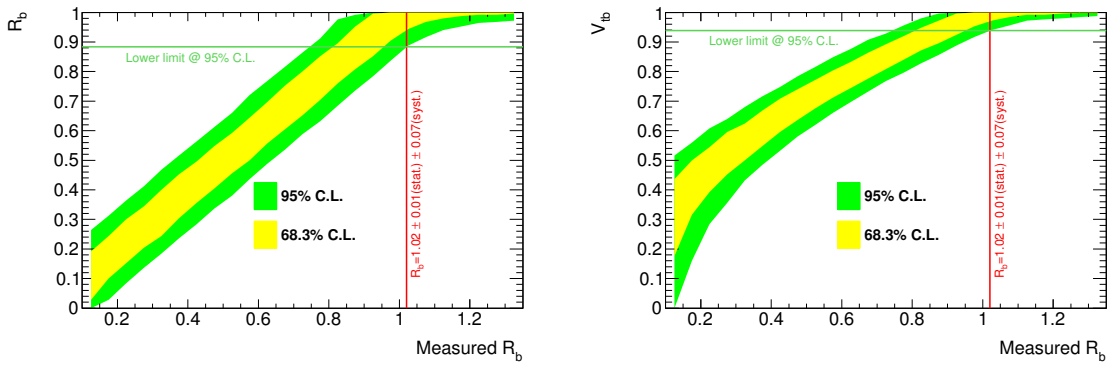

Figure 5.24: Limit bands for the true values of R_b and $|V_{tb}|$ at 68.3% (yellow) and 95% (green) C.L. as a function of the measured R_b value. The y-values of the green horizontal lines going through the crossing points of the green limit bands and the red vertical lines, which represent the R_b value measured in data, are the measured one-sided lower limits on the R_b and $|V_{tb}|$ at 95% C.L.

MV1 b-tagging algorithm.

The templates for the signal $t\bar{t}$ process are obtained from a Protos sample with $R_b = 0.5$ and thus contain $tt \to WWbb$, $tt \to WWqq$ and $tt \to WWqb$ events. A further template is built for the sum of all expected background processes: Z+jets, single top, diboson and events containing fake leptons, some of which are determined with data-driven techniques.

Several sources of systematic uncertainties affecting the shape of the templates have been considered. The total systematic uncertainty on the R_b measurement is ±0.068 and is dominated by the uncertainty on the b-tagging calibration and the modeling of additional QCD radiation and the $t\bar{t}$ decays. The total systematic uncertainty on $\sigma_{t\bar{t}}$ is ±19.2 pb and is dominated by the jet energy scale, luminosity, Monte Carlo modeling and lepton reconstruction and identification. Pseudo-experiments have been used to validate the fit, check its linearity and determine the statistical uncertainty of the measurement: 0.007 for R_b and 3.1 pb for $\sigma_{t\bar{t}}$.

The fit to data gave a result of

$$R_b = 1.02 \pm 0.01\,(\text{stat.}) \pm 0.07\,(\text{syst.}),$$

$$|V_{tb}| = 1.01 \pm 0.01\,(\text{stat.}) \pm 0.03\,(\text{syst.})$$

and

$$\sigma_{t\bar{t}} = 178 \pm 3\,(\text{stat.}) \pm 19\,(\text{syst.})\ \text{pb}$$

and is shown in figure 5.23. The obtained values of R_b and $|V_{tb}|$ are compatible with the expected standard model values of $R_b, |V_{tb}| \sim 1$.

The measured lower limits on R_b and $|V_{tb}|$ at 95% C.L. are

$$R_b > 0.88$$

and

$$|V_{tb}| > 0.94$$

The $|V_{tb}|$ value extracted from the R_b measurement presented in this thesis is in agreement with results discussed earlier in section 1.2.3: $|V_{tb}| = 1.02^{+0.06}_{-0.05}$ from combined measurements at Tevatron [14] , and

$|V_{tb}| = 1.020 \pm 0.040\,(\text{meas.}) \pm 0.020\,(\text{theo.})$ from combined measurements at the LHC [15]. It is also in agreement with the most recent measurement by the CMS Collaboration using single top quark t-channel production in pp collisions at $\sqrt{s} = 13$ TeV centre-of-mass energy, yielding $|V_{tb}| = 0.988 \pm 0.024$ [143], which set the lower limit on $|V_{tb}| > 0.97$ at 95% C.L.

A study documented in appendix J indicates that the uncertainty on the b-tagging calibration propagates linearly to the b-tagging uncertainty on the R_b and σ_{dilepton} measurement described in this work. As b-tagging accounts for almost 65% of the total systematic uncertainty[11] on the R_b measurement, this measurement would significantly benefit from the progress made in b-tagging calibration techniques since the time of this measurement.

The measured value of the inclusive $t\bar{t}$ cross section in pp collisions at $\sqrt{s} = 7$ TeV is also in agreement with earlier discussed results from ATLAS and CMS, $\sigma_{t\bar{t}} = 182.9 \pm 3.1\,(\text{stat.}) \pm 4.2\,(\text{syst.}) \pm 3.6\,(\text{lumi.}) \pm 3.3\,(\text{beam})$ pb [17] and $\sigma_{t\bar{t}} = 161.9 \pm 2.5\,(\text{stat.})\,^{+5.1}_{-5.0}\,(\text{syst.}) \pm 3.6\,(\text{lumi.})$ pb [18], see section 1.2.3.

A reduction of the uncertainty on the $\sigma_{t\bar{t}}$ could be possible, if more simulation samples with $R_b \neq 1$, enriched with $tt \to WWqb$ and $tt \to WWqq$ events, from various generators could be studied to better understand the origin of the large uncertainty due to choice of the generator.

[11] $\delta^2_{b\text{-tagging}}/\delta^2_{\text{totalsyst.}} = 0.64$ with values from table 5.14

Bibliography

[1] S Weinberg. The making of the standard model. *Eur. Phys. J.*, C34:5–13, 2004.

[2] G. 't Hooft. The making of the standard model. *Nature*, 448(7151):271–273, 2007.

[3] M. Tanabashi et al. (Particle Data Group). Review of particle physics. *Phys. Rev. D*, 98:030001, 2018.

[4] F. Halzen and A.D. Martin. *Quarks and leptons: an introductory course in modern particle physics*. Wiley, 1984.

[5] L. Alvarez-Gaume and M. A. Vazquez-Mozo. *An invitation to quantum field theory*. Springer-Verlag, Berlin Heidelberg, 2011.

[6] Y. Fukuda et al. Evidence for oscillation of atmospheric neutrinos. *Phys. Rev. Lett.*, 81:1562–1567, 1998.

[7] Q. R. Ahmad et al. Direct evidence for neutrino flavor transformation from neutral current interactions in the Sudbury Neutrino Observatory. *Phys. Rev. Lett.*, 89:011301, 2002.

[8] D0 Collaboration. Observation of the top quark. *Phys. Rev. Lett.*, 74:2632–2637, 1995.

[9] CDF Collaboration. Observation of top quark production in $\bar{p}p$ collisions. *Phys. Rev. Lett.*, 74:2626–2631, 1995.

[10] CMS Collaboration. First measurement of the cross section for top-quark pair production in proton-proton collisions at $\sqrt{s}$ = 7 TeV. *Phys. Lett.*, B695:424–443, 2011.

[11] ATLAS Collaboration. Measurement of the top quark-pair production cross section with ATLAS in pp collisions at $\sqrt{s}$ = 7 TeV. *Eur. Phys. J.*, C71:1577, 2011.

[12] I. C. Brock (ed.) and T. Schorner-Sadenius (ed.). *Physics at the Terascale*. Wiley, Weinheim, 2011.

[13] A. D. Martin, W. J. Stirling, R. S. Thorne, and G. Watt. Parton distributions for the LHC. *Eur. Phys. J.*, C63:189–285, 2009.

[14] M. Cristinziani. Top-quark production measurements. In *Proceedings, 27th International Symposium on Lepton Photon Interactions at High Energy (LP15): Ljubljana, Slovenia, August 17-22, 2015*. SISSA, 2016.

[15] LHC Top Physics Working Group. https://twiki.cern.ch/twiki/bin/view/LHCPhysics/LHCTopWGSummaryPlots.

[16] J. Behringer et al. (Particle Data Group). 2012 Review of Particle Physics. *Phys. Rev. D*, 86:010001, 2012.

[17] ATLAS Collaboration. Measurement of the $t\bar{t}$ production cross-section using $e\mu$ events with b-tagged jets in pp collisions at $\sqrt{s}$ = 7 and 8 TeV with the ATLAS detector. *Eur. Phys. J.*, C74(10):3109, 2014. [Addendum: Eur. Phys. J.C76,no.11,642(2016)].

[18] CMS Collaboration. Measurement of the $t\bar{t}$ production cross section in the dilepton channel in pp collisions at $\sqrt{s}$ = 7 TeV. *JHEP*, 1211:067, 2012.

[19] ATLAS and CMS Collaborations. Combination of ATLAS and CMS top quark pair cross section measurements in the $e\mu$ final state using proton-proton collisions at $\sqrt{s}$= 8 TeV. ATLAS-CONF-2014-054, 2014.

[20] ATLAS Collaboration. Measurement of the $t\bar{t}$ production cross-section using $e\mu$ events with b-tagged jets in pp collisions at $\sqrt{s}$ = 13 TeV with the ATLAS detector. *Phys. Lett.*, B761:136–157, 2016.

[21] CMS Collaboration. Measurement of the $t\bar{t}$ production cross section using events in the $e\mu$ final state in pp collisions at $\sqrt{s}$ = 13 TeV. *Eur. Phys. J.*, C77:172, 2017.

[22] D0 Collaboration. Precision Measurement of the ratio $\mathcal{B}(t \to Wb)/\mathcal{B}(t \to Wq)$ and extraction of V_{tb}. *Phys. Rev. Lett.*, 107:121802, 2011.

[23] ATLAS and CMS Collaborations. Combinations of single-top-quark production cross-section measurements and $|f_{\mathrm{LV}}V_{tb}|$ determinations at $\sqrt{s}$ = 7 and 8 TeV with the ATLAS and CMS experiments. *JHEP*, 2019(5):88, May 2019.

[24] CDF Collaboration. Measurement of $R = \mathcal{B}(t \to Wb)/\mathcal{B}(t \to Wq)$ in top–quark–pair decays using lepton+jets events and the full CDF Run II data set. *Phys. Rev.*, D87(11):111101, 2013.

[25] CMS Collaboration. First measurement of $\mathcal{B}(t \to Wb)/\mathcal{B}(t \to Wq)$ in the dilepton channel in pp collisions at $\sqrt{s}$ = 7 TeV. CMS-PAS-TOP-11-029, 2012.

[26] CMS Collaboration. Measurement of the ratio $\mathcal{B}(t \to Wb)/\mathcal{B}(t \to Wq)$. CMS-PAS-TOP-12-035, 2013.

[27] S. Alekhin, A. Djouadi, and S. Moch. The top quark and Higgs boson masses and the stability of the electroweak vacuum. *Phys. Lett.*, B716:214–219, 2012.

[28] M. Cristinziani and M. Mulders. Top-quark physics at the Large Hadron Collider. *J. Phys.*, G44(6):063001, 2017.

[29] The Tevatron Electroweak Working Group for the CDF and D0 Collaborations. Combination of CDF and D0 results on the mass of the top quark using up to 9.7 fb^{-1} at the Tevatron. FERMILAB-CONF-16-298-E, 2016.

[30] ATLAS Collaboration. Measurement of the top quark mass in the $t\bar{t} \to$ dilepton channel from $\sqrt{s}$ = 8 TeV ATLAS data. *Phys. Lett.*, B761:350–371, 2016.

[31] CMS Collaboration. Measurement of the top quark mass using proton-proton data at $\sqrt{s}$ = 7 and 8 TeV. *Phys. Rev.*, D93(7):072004, 2016.

[32] A. B. Meyer. Top Quark Properties. In *Proceedings, 27th International Symposium on Lepton Photon Interactions at High Energy (LP15): Ljubljana, Slovenia, August 17-22, 2015*, volume Lepton Photon 2015, page 028, 2016.

[33] ATLAS Collaboration. Top Quark Mass Summary Plots. Technical Report ATL-PHYS-PUB-2019-036, CERN, Geneva, Sep 2019.

[34] ATLAS Collaboration. Measurement of the mass difference between top and anti-top quarks in pp collisions at $\sqrt{s}$ = 7 TeV using the ATLAS detector. *Phys. Lett.*, B728:363–379, 2014.

[35] CMS Collaboration. Measurement of the mass difference between top and antitop quarks. *JHEP*, 06:109, 2012.

[36] S. J. Parke. Spin correlation effects in top quark pair production. In *Proceedings, 45th Rencontres de Moriond on QCD and High Energy Interactions: La Thuile, Italy, March 13-20, 2010*.

[37] D0 Collaboration. Measurement of spin correlation between top and antitop quarks produced in $p\bar{p}$ collisions at $\sqrt{s}$ = 1.96 TeV. *Phys. Lett.*, B757:199–206, 2016.

[38] ATLAS Collaboration. Measurements of spin correlation in top-antitop quark events from proton-proton collisions at $\sqrt{s}$ = 7 TeV using the ATLAS detector. ATLAS-CONF-2013-101, 2013.

[39] CMS Collaboration. Measurement of spin correlations in $t\bar{t}$ production. CMS-PAS-TOP-12-004, 2012.

[40] ATLAS Collaboration. Measurements of top-quark pair spin correlations in the $e\mu$ channel at $\sqrt{s}$ = 13 TeV using pp collisions in the ATLAS detector. arXiv:1903.07570 (Accepted for publication by EPJC), 2019.

[41] M. Czakon, P. Fiedler, and A. Mitov. Resolving the Tevatron top quark forward-backward asymmetry puzzle: fully differential Next-to-Next-to-Leading-Order calculation. *Phys. Rev. Lett.*, 115(5):052001, 2015.

[42] W. Bernreuther and Z. Si. Top quark and leptonic charge asymmetries for the Tevatron and LHC. *Phys. Rev.*, D86:034026, 2012.

[43] CDF and D0 Collaborations. Forward-backward asymmetries in top-antitop quark production at the Tevatron. FERMILAB-CONF-16-386-PPD, 2016.

[44] U. Husemann. Top-quark physics: status and prospects. *Prog. Part. Nucl. Phys.*, 95:48–97, 2017.

[45] ATLAS Collaboration. Observation of top-quark pair production in association with a photon and measurement of the $t\bar{t}\gamma$ production cross section in pp collisions at $\sqrt{s}$ = 7 TeV using the ATLAS detector. *Phys. Rev.*, D91(7):072007, 2015.

[46] ATLAS Collaboration. Measurement of the $t\bar{t}W$ and $t\bar{t}Z$ production cross sections in pp collisions at $\sqrt{s}$ = 8 TeV with the ATLAS detector. *JHEP*, 11:172, 2015.

[47] CMS Collaboration. Observation of top quark pairs produced in association with a vector boson in pp collisions at $\sqrt{s}$ = 8 TeV. *JHEP*, 01:096, 2016.

[48] CMS Collaboration. Observation of $t\bar{t}H$ Production. *Phys. Rev. Lett.*, 120:231801, 2018.

[49] ATLAS Collaboration. Observation of Higgs boson production in association with a top quark pair at the LHC with the ATLAS detector. *Phys. Lett. B*, 784:173 – 191, 2018.

[50] D. de Florian et al. Handbook of LHC Higgs Cross Sections: 4. Deciphering the Nature of the Higgs Sector. 2016.

[51] R. Raitio and W. W. Wada. Higgs-boson production at large transverse momentum in quantum chromodynamics. *Phys. Rev. D*, 19:941–944, 1979.

[52] Z. Kunszt. Associated production of heavy Higgs boson with top quarks. *Nucl. Phys. B*, 247(2):339 – 359, 1984.

[53] W. Beenakker, S. Dittmaier, M. Kraemer, B. Pluemper, M. Spira, and P.M. Zerwas. Higgs Radiation Off Top Quarks at the Tevatron and the LHC. *Phys. Rev. Lett.*, 87:201805, 2001.

[54] W. Beenakker, S. Dittmaier, M. Kraemer, B. Pluemper, M. Spira, and P.M. Zerwas. NLO QCD corrections to $t\bar{t}H$ production in hadron collisions. *Nucl. Phys. B*, 653(1):151 – 203, 2003.

[55] S. Dawson, L. H. Orr, L. Reina, and D. Wackeroth. Next-to-leading order QCD corrections to $pp \to t\bar{t}H$ at the CERN Large Hadron Collider. *Phys. Rev. D*, 67:071503, 2003.

[56] S. Dawson, C. Jackson, L. H. Orr, L. Reina, and D. Wackeroth. Associated Higgs boson production with top quarks at the CERN Large Hadron Collider: NLO QCD corrections. *Phys. Rev. D*, 68:034022, 2003.

[57] Y. Zhang, W.-G. Ma, R.-Y. Zhang, Ch. Chen, and L. Guo. QCD NLO and EW NLO corrections to $t\bar{t}H$ production with top quark decays at hadron collider. *Phys. Lett. B*, 738:1 – 5, 2014.

[58] S. Frixione, V. Hirschi, D. Pagani, H. S. Shao, and M. Zaro. Weak corrections to Higgs hadroproduction in association with a top-quark pair. *JHEP*, 09:065, 2014.

[59] S. Frixione, V. Hirschi, D. Pagani, H. S. Shao, and M. Zaro. Electroweak and QCD corrections to top-pair hadroproduction in association with heavy bosons. *JHEP*, 06:184, 2015.

[60] ATLAS Collaboration. Search for top quark decays $t \to qH$, with $H \to \gamma\gamma$, in $\sqrt{s} = 13$ TeV pp collisions using the ATLAS detector. *JHEP*, 10:129, 2017.

[61] CMS Collaboration. Search for the flavor-changing neutral current interactions of the top quark and the Higgs boson which decays into a pair of b quarks at $\sqrt{s} = 13$ TeV. *JHEP*, 06:102, 2018.

[62] J. A. Aguilar-Saavedra. Top flavor-changing neutral interactions: Theoretical expectations and experimental detection. *Acta Phys. Polon.*, B35:2695–2710, 2004.

[63] O. S. Bruening, P. Collier, P. Lebrun, S. Myers, R. Ostojic, J. Poole, and P. Proudlock. LHC Design Report. https://cds.cern.ch/record/782076, 2004.

[64] F. Marcastel. CERN's Accelerator Complex. OPEN-PHO-CHART-2013-001, 2013. General Photo.

[65] M. Benedikt, P. Collier, V. Mertens, J. Poole, and K. Schindl. LHC Design Report. https://cds.cern.ch/record/823808, 2004.

[66] http://press.cern/press-releases/2008/10/cern-releases-analysis-lhc-incident.

[67] ATLAS Collaboration. The ATLAS Experiment at the CERN Large Hadron Collider. *JINST*, 3:S08003, 2008.

[68] J. Pequenao and P. Schaffner. An computer generated image representing how ATLAS detects particles. CERN-EX-1301009, 2013.

[69] J. Pequenao. Computer generated image of the whole ATLAS detector. CERN-GE-0803012, 2008.

[70] S. Agostinelli et al. GEANT4: A Simulation toolkit. *NIM*, A506:250–303, 2003.

[71] J. Allison et al. GEANT4 developments and applications. *IEEE Trans. Nucl. Sci.*, 53:270, 2006.

[72] ATLAS Collaboration. The ATLAS Simulation Infrastructure. *Eur.Phys.J.*, C70:823–874, 2010.

[73] T. Sjostrand, S. Mrenna, and P. Skands. PYTHIA Generator version 6.418. *JHEP*, 05:026, 2006.

[74] http://wlcg-public.web.cern.ch.

[75] https://root.cern.ch/about-root.

[76] W.J. Stirling. private communication, 2012.

[77] S. D. Drell and T.-M. Yan. Massive lepton-pair production in hadron-hadron collisions at high energies. *Phys. Rev. Lett.*, 25:316–320, 1970.

[78] ATLAS Collaboration. Electron performance measurements with the ATLAS detector using the 2010 LHC proton-proton collision data. *Eur. Phys.J.*, C72:1909, 2012.

[79] ATLAS Collaboration. Measurement of the $W \to \ell\nu$ and $Z/\gamma^\star \to \ell\ell$ production cross sections in proton-proton collisions at $\sqrt{s} = 7$ TeV with the ATLAS detector. *JHEP*, 1012:060, 2010.

[80] M. Cacciari, G.P. Salam and G. Soyez. The Anti-k(t) jet clustering algorithm. *JHEP*, 04:63, 2008.

[81] ATLAS Collaboration. Jet energy measurement and its systematic uncertainty in proton–proton collisions at $\sqrt{s} = 7$ TeV with the ATLAS detector. *Eur. Phys. J. C*, 75(1):17, 2015.

[82] ATLAS Collaboration. Performance of the missing transverse energy reconstruction and calibration in proton-proton collisions at a center-of-mass energy of 7 TeV with the ATLAS detector. ATLAS-CONF-2010-057, 2010.

[83] ATLAS Collaboration. Measuring the b-tag efficiency in a top-pair sample with 4.7 fb^{-1} of data from the ATLAS detector. ATLAS-CONF-2012-097, 2012.

[84] ATLAS Collaboration. Improved luminosity determination in pp collisions at $\sqrt{s} = 7$ TeV using the ATLAS detector at the LHC. ATLAS-DAPR-2011-01-002, 2012.

[85] ATLAS Collaboration. Measuring the b-tag efficiency in a top-pair sample with 5 fb^{-1} of data from the ATLAS detector. ATL-COM-PHYS-2012-128, 2012.

[86] ATLAS Collaboration. Measurement of the charge asymmetry in top quark pair production in pp collisions at $\sqrt{s}$ = 7 TeV using the ATLAS detector. *Eur. Phys. J.*, C72:2039, 2012.

[87] Ch.-H. Kom and W. Stirling. Charge asymmetry in W+jets production at the LHC. *Eur. Phys. J. C*, 69:67–73, 2010.

[88] ATLAS Collaboration. Measurement of the t-channel single top-quark production cross section in pp collisions at $\sqrt{s}$ = 7 TeV with the ATLAS detector. *Phys. Lett.*, B717:330–350, 2012.

[89] ATLAS Collaboration. Object selection and calibration, background estimations and MC samples for the Summer 2012 Top Quark analyses with 2011 data. ATL-COM-PHYS-2012-499, 2012.

[90] ATLAS Collaboration. Mis-identified lepton backgrounds to top quark pair production for Moriond 2011 analysis. ATL-COM-PHYS-2011-144, 2011.

[91] ATLAS Collaboration. The measurement of $t\bar{t}$ cross section in the dilepton decay channel with cut-and-count methods at $\sqrt{s}$ = 7 TeVwith 35 pb^{-1}. ATL-PHYS-INT-2011-046, 2011.

[92] ATLAS Collaboration. Improved electron reconstruction in ATLAS using the gaussian sum filter-based model for bremsstrahlung. ATLAS-CONF-2012-047, 2012.

[93] S. Frixione and B. R. Webber. Matching NLO QCD computations and parton shower simulations. *JHEP*, 0206:029, 2002.

[94] S. Frixione, E. Laenen, P. Motylinski, and B.R. Webber. Single-top production in MC@NLO. *JHEP*, 0603:092, 2006.

[95] S. Frixione, P. Nason, and B.R. Webber. Matching NLO QCD and parton showers in heavy flavor production. *JHEP*, 0308:007, 2003.

[96] H. Lai, M. Guzzi, J. Huston, Li Z., Nadolsky P. M., et al. New parton distributions for collider physics. *Phys.Rev.*, D82:074024, 2010.

[97] G. Corcella et al. HERWIG 6.5: an event generator for Hadron Emission Reactions With Interfering Gluons (including supersymmetric processes). *JHEP*, 1:10, 2001.

[98] J.A. Aguilar-Saavedra. Single top quark production at LHC with anomalous Wtb couplings. *Nucl. Phys. B*, 804:160, 2008.

[99] J.A. Aguilar-Saavedra. PROgram for TOp Simulations, User Manual v1.2. https://svnweb.cern.ch/trac/atlasoff/browser/Generators/Protos_i/trunk/doc/protos_12.pdf.

[100] ATLAS Collaboration. ATLAS tunes of PYTHIA 6 and Pythia 8 for MC11. ATL-PHYS-PUB-2011-009, 2011.

[101] J. Pumplin et al. New generation of parton distributions with uncertainties from global QCD analysis. *JHEP*, 07:012, 2002.

[102] M. Cacciari, M. Czakon, M. Mangano, A. Mitov, and P. Nason. Top-pair production at hadron colliders with next-to-next-to-leading logarithmic soft-gluon resummation. *Phys.Lett.*, B710:612–622, 2012.

[103] P. Baernreuther, M. Czakon, and A. Mitov. Percent level precision physics at the Tevatron: first genuine NNLO QCD corrections to $q\bar{q} \to t\bar{t} + X$. *Phys.Rev.Lett.*, 109:132001, 2012.

[104] M. Czakon and A. Mitov. NNLO corrections to top-pair production at hadron colliders: the all-fermionic scattering channels. *JHEP*, 1212:054, 2012.

[105] M. Czakon and A. Mitov. NNLO corrections to top pair production at hadron colliders: the quark-gluon reaction. *JHEP*, 1301:080, 2013.

[106] M. Czakon, P. Fiedler, and A. Mitov. Total Top-Quark Pair-Production Cross Section at Hadron Colliders Through $O(\alpha_S^4)$. *Phys. Rev. Lett.*, 110:252004, 2013.

[107] M. Czakon and A. Mitov. Top++: a program for the calculation of the top-pair cross-section at hadron colliders. *Comput. Phys. Commun.*, 185:2930, 2014.

[108] M. Botje, J. Butterworth, A. Cooper-Sarkar, A. de Roeck, J. Feltesse, et al. The PDF4LHC Working Group interim recommendations. arxiv:1101.0538, 2011.

[109] A.D. Martin, W.J. Stirling, R.S. Thorne, and G. Watt. Uncertainties on $\alpha(S)$ in global PDF analyses and implications for predicted hadronic cross sections. *Eur.Phys.J.*, C64:653–680, 2009.

[110] J. Gao, M. Guzzi, J. Huston, H. Lai, Z. Li, et al. The CT10 NNLO global analysis of QCD. *Phys. Rev.*, D89(3):033009, 2014.

[111] R. D. Ball, V. Bertone, S. Carrazza, Ch. S. Deans, L. Del Debbio, et al. Parton distributions with LHC data. *Nucl.Phys.*, B867:244–289, 2013.

[112] M. Aliev et al. HATHOR: HAdronic Top and Heavy quarks cross section calculatoR. *Comput. Phys. Commun.*, 182:1034–1046, 2011.

[113] P. Nason. A New method for combining NLO QCD with shower Monte Carlo algorithms. *JHEP*, 11:040, 2004.

[114] M. L. Mangano, M. Moretti, F. Piccinini, R. Pittau, and A. D. Polosa. ALPGEN, a generator for hard multiparton processes in hadronic collisions. *JHEP*, 07:001, 2003.

[115] B. P. Kersevan and E. Richter-Was. The Monte Carlo event generator AcerMC version 2.0 with interfaces to PYTHIA 6.2 and HERWIG 6.5. *Comput. Phys. Commun.*, 184:919–985, 2013.

[116] H.L. Lai et al. (CTEQ Collaboration). Global QCD analysis of parton structure of the nucleon: CTEQ5 parton distributions. *Eur. Phys. J.*, C12:375–392, 2000.

[117] P. Skands. Tuning Monte Carlo Generators: The Perugia Tunes. *Phys. Rev.*, D82:074018, 2010.

[118] ATLAS Collaboration. Monte Carlo samples used for top physics. ATL-PHYS-INT-2010-132, 2010.

[119] J. Alwall et al. Comparative study of various algorithms for the merging of parton showers and matrix elements in hadronic collisions. *Eur. Phys. J.*, C53:473–500, 2008.

[120] J. M. Campbell and R. K. Ellis. An update on vector boson pair production at hadron colliders. *Phys. Rev.*, D60:113006, 1999.

[121] G. Corcella, I.G. Knowles, G. Marchesini, S. Moretti, K. Odagiri, et al. HERWIG 6: An Event generator for hadron emission reactions with interfering gluons (including supersymmetric processes). *JHEP*, 0101:010, 2001.

[122] J. M. Butterworth, J. R. Forshaw, and M. H. Seymour. Multiparton interactions in photoproduction at HERA. *Z. Phys.*, C72:637–646, 1996.

[123] J. M. Butterworth and J. R. Forshaw. Photoproduction of multi-jet events at HERA: A Monte Carlo simulation. *J. Phys.*, G19:1657–1663, 1993.

[124] ATLAS Collaboration. Performance of b-jet identification in the ATLAS experiment. *JINST*, 11(04):P04008, 2016.

[125] A. Leyko for the ATLAS Collaboration. Measurement of the b-jet tagging efficiency using top quark pair events with ATLAS data. *PoS*, ICHEP2012:521, 2013.

[126] ATLAS Collaboration. Secondary vertex finding for jet flavour identification with the ATLAS detector. ATL-PHYS-PUB-2017-011, 2017.

[127] ATLAS Collaboration. Object selection and calibration, background estimations and MC samples for the Winter 2012 Top Quark analyses with 2011 data. ATL-COM-PHYS-2012-224, 2012.

[128] ATLAS Collaboration. Measurement of the t-channel single top-quark production cross section in 0.70 fb^{-1} of pp collisions at $\sqrt{s}$ = 7 TeV collected with the ATLAS detector. ATLAS-CONF-2011-101, 2011.

[129] S. Moch and P. Uwer. Heavy-quark pair production at two loops in QCD. *Nucl.Phys.Proc.Suppl.*, 183:75–80, 2008.

[130] N. Kidonakis. Two-loop soft anomalous dimensions for single top quark associated production with a W^- or H^-. *Phys. Rev. D*, 82:054018, 2010.

[131] N. Kidonakis. Next-to-next-to-leading-order collinear and soft gluon corrections for t-channel single top quark production. *Phys. Rev. D*, 83:091503, 2011.

[132] N. Kidonakis. Next-to-next-to-leading logarithm resummation for s-channel single top quark production. *Phys. Rev. D*, 81:054028, 2010.

[133] J. M. Campbell, R. K. Ellis, and C. Williams. Vector boson pair production at the LHC. *JHEP*, 1107:018, 2011.

[134] ATLAS Collaboration. Probing the measurement of jet energies with the ATLAS detector using Z+jet events from proton-proton collisions at $\sqrt{s}$ = 7 TeV. ATLAS-CONF-2012-053, 2012.

[135] ATLAS Collaboration. Expected Performance of the ATLAS Experiment - Detector, Trigger and Physics. *JINST*, 3:S08003, 2008.

[136] ATLAS Collaboration. Measurement of the charge asymmetry in dileptonic decay of top quark pairs in pp collisions at $\sqrt{s}$ = 7 TeV using the ATLAS detector. ATLAS-CONF-2012-057, 2012.

[137] http://roofit.sourceforge.net.

[138] ATLAS Collaboration. Estimation of the W+jets background for top quark re-discovery in the single lepton+jets channel. Technical Report ATL-COM-PHYS-2010-834, CERN, Geneva, 2010. Supporting document.

[139] R. D. Ball et al. A first unbiased global NLO determination of parton distributions and their uncertainties. *Nucl. Phys.*, B838:136–206, 2010.

[140] ATLAS Collaboration. Monte Carlo generator comparisons to ATLAS measurements constraining QCD radiation in top anti-top final states. *ATL-PHYS-PUB-2013-005*, 2013.

[141] G. J. Feldman and R. D. Cousins. Unified approach to the classical statistical analysis of small signals. *Phys. Rev. D*, 57:3873–3889, 1998.

[142] https://roostatsworkbook.readthedocs.io.

[143] CMS Collaboration. Measurement of CKM matrix elements in single top quark t-channel production in proton-proton collisions at $\sqrt{s}$ = 13 TeV. *Phys. Lett. B*, 808:135609, Sep 2020.

APPENDIX A

Kinematic distributions in dilepton channel

In all distributions of kinematic variables the shape from the Protos sample (using only $tt \rightarrow WWbb$ events) is normalised to the corresponding number of selected events from Powheg+Pythia .

A.1 Signal region

Following figures present distributions in the signal region described by the criteria listed in section 3.2.2. Figure A.1 presents the the $|\eta|$ distributions for the jets in the signal region. Figure A.2 shows the transverse momentum and figure A.3 the $|\eta|$ distributions for the leptons in the signal region.

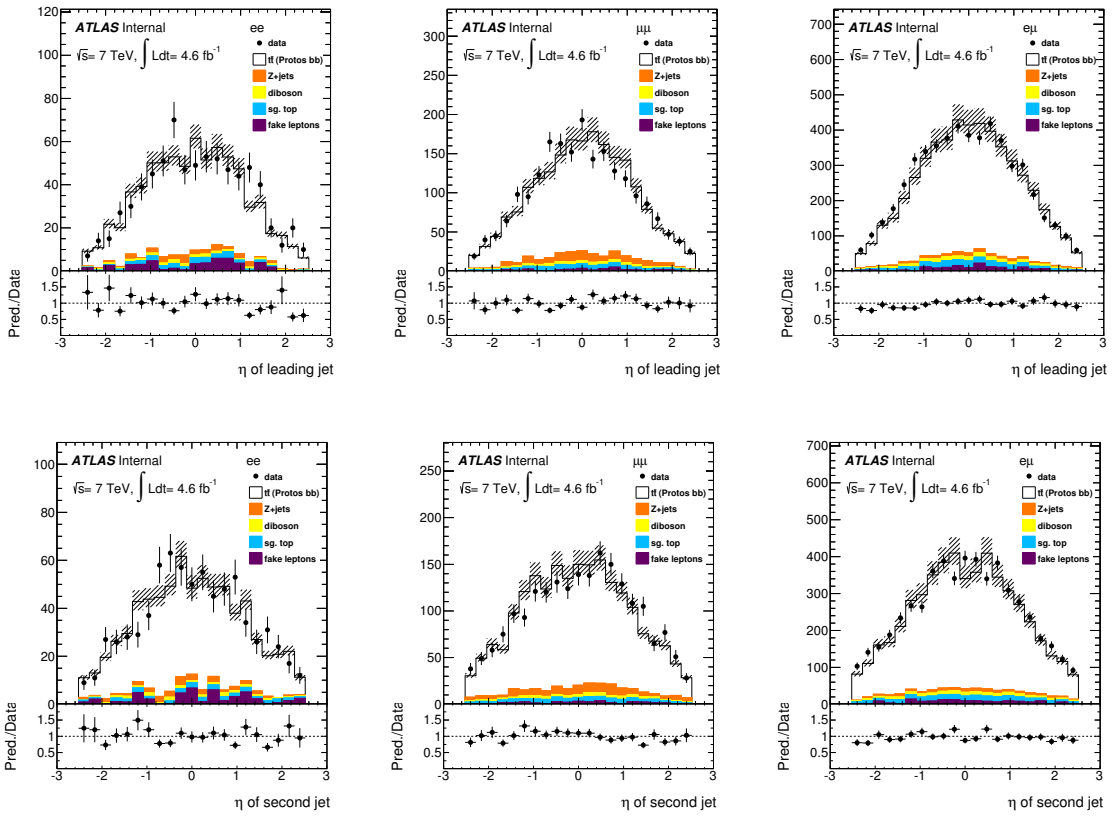

Figure A.1: Distribution of the η of the leading (upper row) and second (lower row) jet in ee (left), $\mu\mu$ (middle) and $e\mu$ channel (right). All event selection criteria are applied. The error band represents the sum of theoretical uncertainties on the cross sections ($t\bar{t}$, single top, diboson and Z+jets production in $e\mu$ channel) and uncertainties on the estimation directly from data (fakes, $Z \to ee$ and $Z \to \mu\mu$).

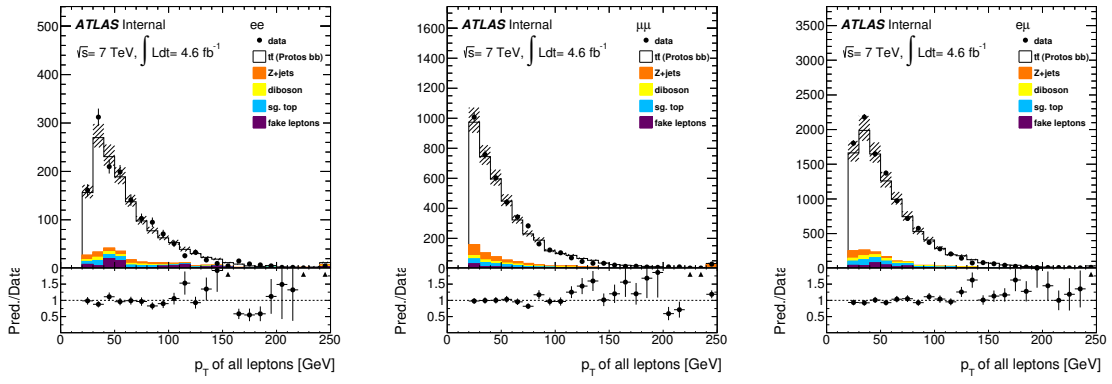

Figure A.2: Distribution of the p_{T} of all leptons in ee (left), $\mu\mu$ (middle) and $e\mu$ channel (right). All event selection criteria are applied. The error band represents the sum of theoretical uncertainties on the cross sections ($t\bar{t}$, single top, diboson and Z+jets production in $e\mu$ channel) and uncertainties on the estimation directly from data (fakes, $Z \to ee$ and $Z \to \mu\mu$). The last bin is inclusive.

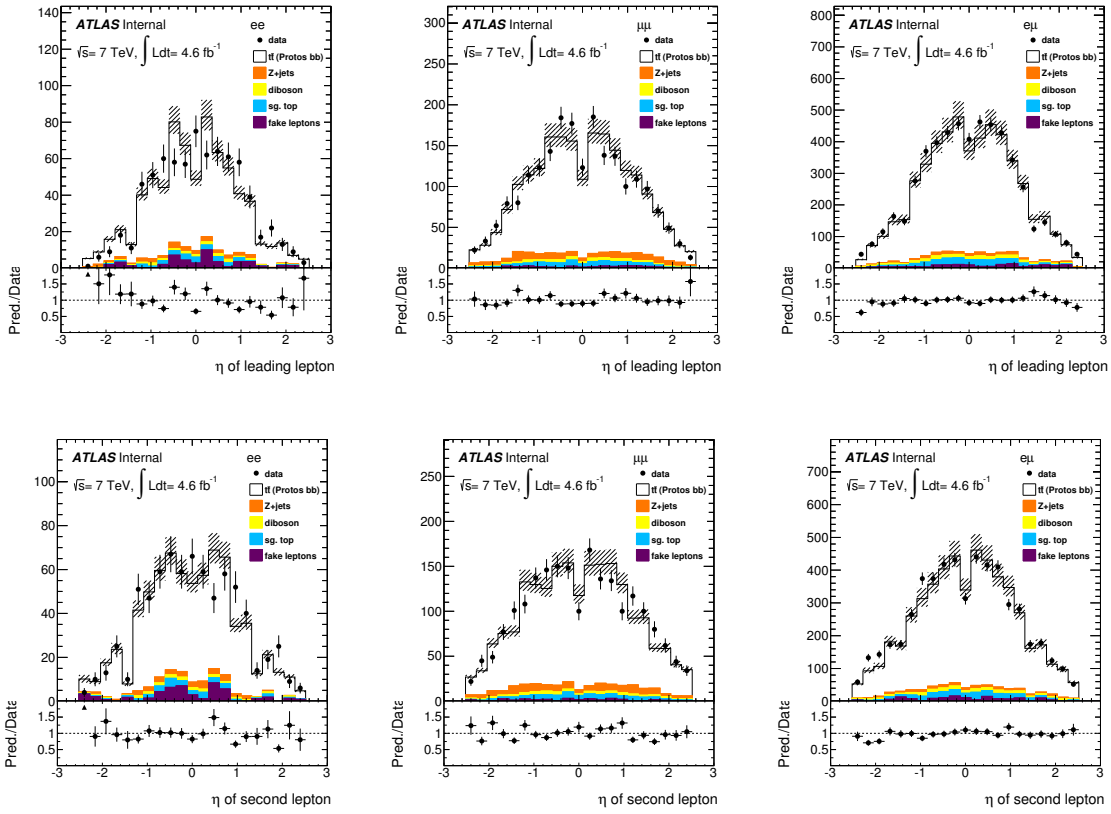

Figure A.3: Distribution of the η of leading (upper row) and second (lower row) lepton in ee (left), $\mu\mu$ (middle) and $e\mu$ channel (right). All event selection criteria are applied. The error band represents the sum of theoretical uncertainties on the cross sections ($t\bar{t}$, single top, diboson and Z+jets production in $e\mu$ channel) and uncertainties on the estimation directly from data (fakes, $Z \to ee$ and $Z \to \mu\mu$).

A.2 Control region

Following figures show distributions in a control region with $E_{\mathrm{T}}^{\mathrm{miss}} < 60$ GeV or $|m_{ll} - 91\ \mathrm{GeV}| < 10$ GeV dominated by background processes. It is different than the control region chosen for estimation of the Z+jets background described in section 3.3.3 in order to include more contributions from other background processes and not only Z+jets .

Figure A.4 shows the transverse momentum and figure A.5 the $|\eta|$ distributions for the leptons in the control region.

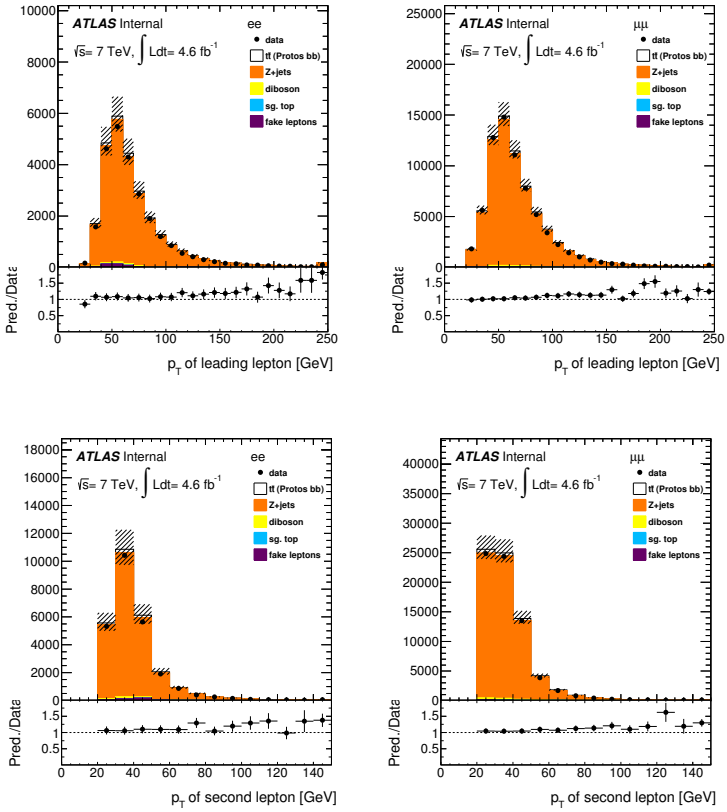

Figure A.4: Distribution of the p_{T} of leading (upper row) and second (lower row) lepton in ee (left) and $\mu\mu$ (right) in the control region with $E_{\mathrm{T}}^{\mathrm{miss}} < 60$ GeV or $|m_{ll} - 91\ \mathrm{GeV}| < 10$ GeV. All other standard event selection criteria are applied. The error band represents the sum of theoretical uncertainties on the cross sections (Z+jets, $t\bar{t}$, single top, diboson) and uncertainties on the estimation directly from data (fakes). The last bin is inclusive.

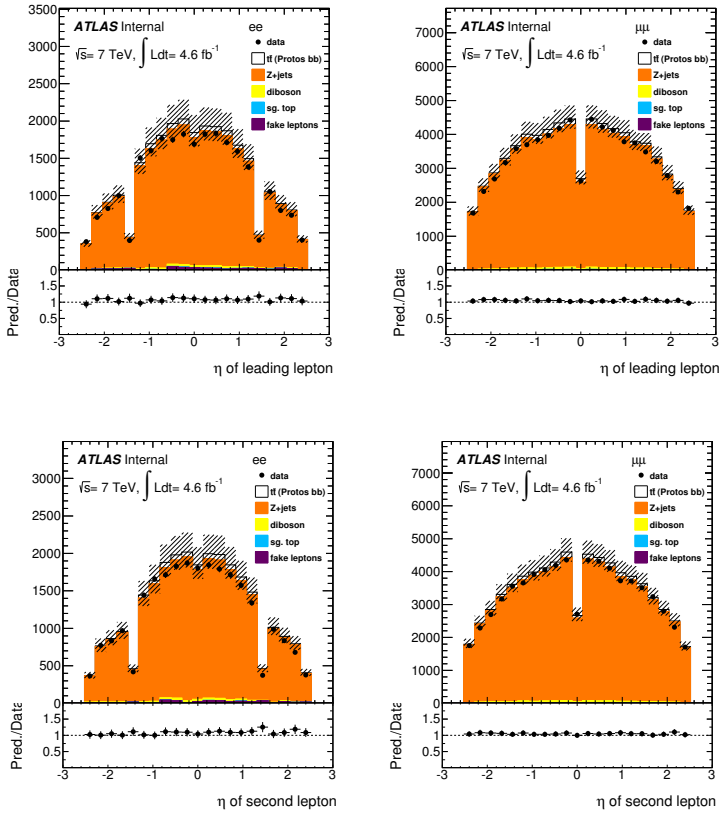

Figure A.5: Distribution of the η of leading (upper row) and second (lower row) lepton in ee (left) and $\mu\mu$ (right) in the control region with $E_{\mathrm{T}}^{\mathrm{miss}} < 60$ GeV or $|m_{ll} - 91\ \mathrm{GeV}| < 10$ GeV. All other standard event selection criteria are applied. The error band represents the sum of theoretical uncertainties on the cross sections (Z+jets, $t\bar{t}$, single top, diboson) and uncertainties on the estimation directly from data (fakes). The last bin is inclusive.

APPENDIX **B**

List of Monte Carlo samples

ID	Description	Generator	σ [pb]	k-factor	N_{events}	$\mathcal{L}$ [fb^{-1}]
107650	$Z(\rightarrow ee)$ + 0p	ALPGEN+HERWIG	668.3	1.25	6618284	7.92
107651	$Z(\rightarrow ee)$ + 1p	ALPGEN+HERWIG	134.4	1.25	1334897	7.95
107652	$Z(\rightarrow ee)$ + 2p	ALPGEN+HERWIG	40.5	1.25	809999	15.98
107653	$Z(\rightarrow ee)$ + 3p	ALPGEN+HERWIG	11.2	1.25	220000	15.77
107654	$Z(\rightarrow ee)$ + 4p	ALPGEN+HERWIG	2.9	1.25	60000	16.67
107655	$Z(\rightarrow ee)$ + 5p	ALPGEN+HERWIG	0.8	1.25	20000	19.28
107660	$Z(\rightarrow \mu\mu)$ + 0p	ALPGEN+HERWIG	668.7	1.25	6615230	7.91
107661	$Z(\rightarrow \mu\mu)$ + 1p	ALPGEN+HERWIG	134.1	1.25	1334296	7.96
107662	$Z(\rightarrow \mu\mu)$ + 2p	ALPGEN+HERWIG	40.3	1.25	404947	8.03
107663	$Z(\rightarrow \mu\mu)$ + 3p	ALPGEN+HERWIG	11.2	1.25	110000	7.86
107664	$Z(\rightarrow \mu\mu)$ + 4p	ALPGEN+HERWIG	2.8	1.25	30000	8.73
107665	$Z(\rightarrow \mu\mu)$ + 5p	ALPGEN+HERWIG	0.8	1.25	10000	10.39
107670	$Z(\rightarrow \tau\tau)$ + 0p	ALPGEN+HERWIG	668.4	1.25	10613179	12.70
107671	$Z(\rightarrow \tau\tau)$ + 1p	ALPGEN+HERWIG	134.8	1.25	3334137	19.79
107672	$Z(\rightarrow \tau\tau)$ + 2p	ALPGEN+HERWIG	40.4	1.25	1004847	19.92
107673	$Z(\rightarrow \tau\tau)$ + 3p	ALPGEN+HERWIG	11.3	1.25	509847	36.26
107674	$Z(\rightarrow \tau\tau)$ + 4p	ALPGEN+HERWIG	2.8	1.25	144999	41.58
107675	$Z(\rightarrow \tau\tau)$ + 5p	ALPGEN+HERWIG	0.8	1.25	45000	46.75

Table B.1: Z+jets samples with phase space cuts $40 < m_{ll} < 2000$ GeV. Configuration tags: e835 s1299 s1300 r3043 r2993.

ID	Description	Generator	σ [pb]	k-factor	N_{events}	$\mathcal{L}$ [fb^{-1}]
109300	$Z(\to ee) + bb$ + 0p	ALPGEN+HERWIG	6.57	1.25	150000	18.26
109301	$Z(\to ee) + bb$ + 1p	ALPGEN+HERWIG	2.48	1.25	100000	32.26
109302	$Z(\to ee) + bb$ + 2p	ALPGEN+HERWIG	0.89	1.25	40000	35.95
109303	$Z(\to ee) + bb$ + 3p	ALPGEN+HERWIG	0.39	1.25	10000	20.51
109305	$Z(\to \mu\mu) + bb$ + 0p	ALPGEN+HERWIG	6.56	1.25	149950	18.29
109306	$Z(\to \mu\mu) + bb$ + 1p	ALPGEN+HERWIG	2.47	1.25	100000	32.39
109307	$Z(\to \mu\mu) + bb$ + 2p	ALPGEN+HERWIG	0.89	1.25	40000	35.95
109308	$Z(\to \mu\mu) + bb$ + 3p	ALPGEN+HERWIG	0.39	1.25	9999	20.51
109310	$Z(\to \tau\tau) + bb$ + 0p	ALPGEN+HERWIG	6.57	1.25	150000	18.26
109311	$Z(\to \tau\tau) + bb$ + 1p	ALPGEN+HERWIG	2.49	1.25	99999	32.13
109312	$Z(\to \tau\tau) + bb$ + 2p	ALPGEN+HERWIG	0.89	1.25	40000	35.95
109313	$Z(\to \tau\tau) + bb$ + 3p	ALPGEN+HERWIG	0.39	1.25	9000	18.46

Table B.2: $Z + bb$+jets samples. Configuration tags: e835 s1310 s1300 r3043 r2993.

ID	Description	Generator	σ [pb]	k-factor	N_{events}	$\mathcal{L}$ [fb^{-1}]	Configuration tag
116250	$Z(\rightarrow ee)$ + 0p	ALPGEN+HERWIG	3055.2	1.25	994949	0.26	e959 s1310 s1300 r3043 r2993
116251	$Z(\rightarrow ee)$ + 1p	ALPGEN+HERWIG	84.9	1.25	299998	2.83	e959 s1310 s1300 r3043 r2993
116252	$Z(\rightarrow ee)$ + 2p	ALPGEN+HERWIG	41.4	1.25	999946	19.32	e944 s1310 s1300 r3043 r2993
116253	$Z(\rightarrow ee)$ + 3p	ALPGEN+HERWIG	8.4	1.25	149998	14.32	e944 s1310 s1300 r3043 r2993
116254	$Z(\rightarrow ee)$ + 4p	ALPGEN+HERWIG	1.9	1.25	40000	17.30	e944 s1310 s1300 r3043 r2993
116255	$Z(\rightarrow ee)$ + 5p	ALPGEN+HERWIG	0.5	1.25	10000	17.39	e944 s1310 s1300 r3043 r2993
116260	$Z(\rightarrow \mu\mu)$ + 0p	ALPGEN+HERWIG	3054.9	1.25	999849	0.26	e959 s1310 s1300 r3043 r2993
116261	$Z(\rightarrow \mu\mu)$ + 1p	ALPGEN+HERWIG	84.9	1.25	300000	2.83	e959 s1310 s1300 r3043 r2993
116262	$Z(\rightarrow \mu\mu)$ + 2p	ALPGEN+HERWIG	41.5	1.25	999995	19.30	e944 s1310 s1300 r3043 r2993
116263	$Z(\rightarrow \mu\mu)$ + 3p	ALPGEN+HERWIG	8.4	1.25	150000	14.32	e944 s1310 s1300 r3043 r2993
116264	$Z(\rightarrow \mu\mu)$ + 4p	ALPGEN+HERWIG	1.9	1.25	39999	17.30	e944 s1310 s1300 r3043 r2993
116265	$Z(\rightarrow \mu\mu)$ + 5p	ALPGEN+HERWIG	0.5	1.25	10000	17.39	e944 s1310 s1300 r3043 r2993
116270	$Z(\rightarrow \tau\tau)$ + 0p	ALPGEN+HERWIG	3055.1	1.25	999649	0.26	e959 s1310 s1300 r3043 r2993
116271	$Z(\rightarrow \tau\tau)$ + 1p	ALPGEN+HERWIG	84.9	1.25	299999	2.83	e959 s1310 s1300 r3043 r2993
116272	$Z(\rightarrow \tau\tau)$ + 2p	ALPGEN+HERWIG	41.5	1.25	498899	9.62	e959 s1310 s1300 r3043 r2993
116273	$Z(\rightarrow \tau\tau)$ + 3p	ALPGEN+HERWIG	8.4	1.25	150000	14.35	e959 s1310 s1300 r3043 r2993
116274	$Z(\rightarrow \tau\tau)$ + 4p	ALPGEN+HERWIG	1.9	1.25	39999	17.30	e959 s1310 s1300 r3043 r2993
116275	$Z(\rightarrow \tau\tau)$ + 5p	ALPGEN+HERWIG	0.5	1.25	10000	17.39	e959 s1310 s1300 r3043 r2993

Table B.3: Z+jets samples with phase space cuts 10 GeV $< m_{ll} <$ 40 GeV.

ID	Description	Generator	σ [pb]	k-factor	N_{events}	$\mathcal{L}$ [fb^{-1}]	Configuration tags
107100	WW, both $W \to l\nu$ + 0p	ALPGEN+HERWIG	2.10	1.26	19999	75.76	e835 s1372 s1370 r3043 r2993
107101	WW, both $W \to l\nu$ + 1p	ALPGEN+HERWIG	1.00	1.26	100000	79.67	e835 s1372 s1370 r3043 r2993
107102	WW, both $W \to l\nu$ + 2p	ALPGEN+HERWIG	0.45	1.26	59999	104.7	e835 s1372 s1370 r3043 r2993
107103	WW, both $W \to l\nu$ + 3p	ALPGEN+HERWIG	0.18	1.26	40000	180.6	e835 s1372 s1370 r3043 r2993
107104	WZ, $W \to$ inclusive, $Z \to ll$ + 0p	ALPGEN+HERWIG	0.67	1.28	59900	69.66	e995 s1372 s1370 r3043 r2993
107105	WZ, $W \to$ inclusive, $Z \to ll$ + 1p	ALPGEN+HERWIG	0.41	1.28	40000	75.52	e995 s1372 s1370 r3043 r2993
107106	WZ, $W \to$ inclusive, $Z \to ll$ + 2p	ALPGEN+HERWIG	0.22	1.28	20000	69.47	e995 s1372 s1370 r3043 r2993
107107	WZ, $W \to$ inclusive, $Z \to ll$ + 3p	ALPGEN+HERWIG	0.10	1.28	20000	164.5	e995 s1372 s1370 r3043 r2993
107108	ZZ, $Z \to$ inclusive, $Z \to ll$ + 0p	ALPGEN+HERWIG	0.51	1.30	40000	60.50	e995 s1372 s1370 r3043 r2993
107109	ZZ, $Z \to$ inclusive, $Z \to ll$ + 1p	ALPGEN+HERWIG	0.23	1.30	20000	65.69	e995 s1372 s1370 r3043 r2993
107110	ZZ, $Z \to$ inclusive, $Z \to ll$ + 2p	ALPGEN+HERWIG	0.09	1.30	20000	173.64	e995 s1372 s1370 r3043 r2993
107111	ZZ, $Z \to$ inclusive, $Z \to ll$ + 3p	ALPGEN+HERWIG	0.03	1.30	10000	245.0	e995 s1372 s1370 r3043 r2993

Table B.4: Diboson samples.

APPENDIX C

Kinematic selection results

This appendix presents results of the *b*-tagging calibration with the kinematic selection method described in section 4.3.2 for all working points listed in section 4.3.

For the MV1 algorithm, the 70% efficiency working point results are presented separately for the *e*+jets and μ+jets channels, including tables with a detailed list of uncertainties, to demonstrate that no significant differences exist. Additionally, combined results are presented for the 60%, 75% and 85% working points. The combined results for the 70% working point were already discussed in section 4.3.2. For the other *b*-tagging algorithms only results for the combined channels are presented.

C.1 Results for the MV1 algorithm

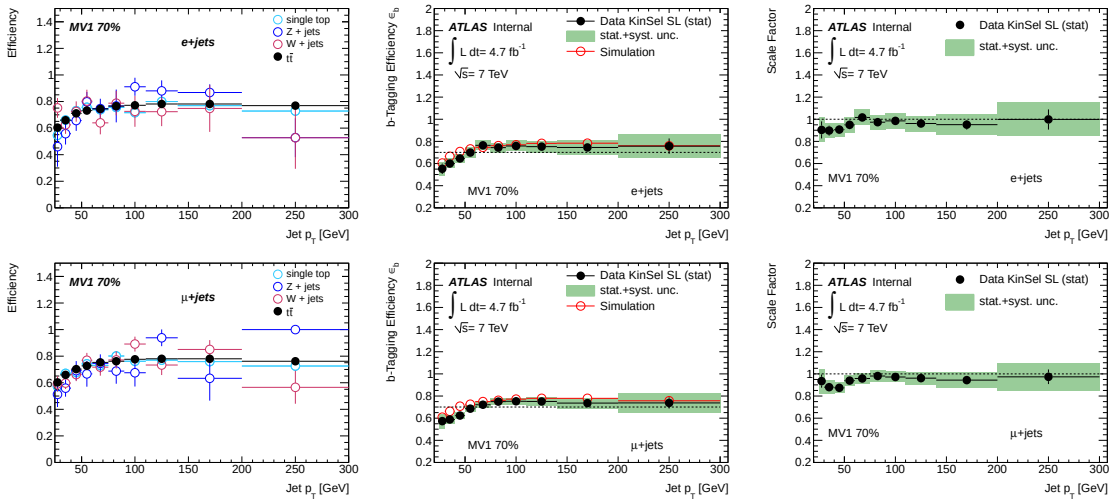

Figure C.1: Electron (top) and muon (bottom) channel results are shown separately. True *b*-tagging efficiency for different Monte Carlo samples (left), *b*-tagging efficiency estimated from data compared with simulation (middle) and resulting scale factors (right) together with statistical and systematic uncertainties for the MV1 tagger at the working point corresponding to 70% efficiency [85].

$p_{\mathrm{T}}^{\mathrm{min}}$[GeV/$c$]	25-30	30-40	40-50	50-60	60-75	75-90	90-110	110-140	140-200	200-300
IFSR	±5.4	±3.4	±2.8	±3.2	±4.0	±4.1	±3.6	±3.7	±5.1	±7.9
Gen.	±0.3	±0.8	±0.6	±0.2	±0.7	±0.0	±0.4	±1.6	±1.5	±3.7
Diboson	±0.0	±0.0	±0.0	±0.0	±0.0	±0.0	±0.0	±0.0	±0.0	±0.0
Single top	±0.0	±0.0	±0.0	±0.0	±0.0	±0.0	±0.0	±0.0	±0.1	±0.1
Z+jets	±0.1	±0.3	±0.3	±0.3	±0.4	±0.3	±0.5	±0.5	±0.4	±0.7
$t\bar{t}$	±0.7	±0.8	±0.7	±0.8	±1.0	±0.9	±0.9	±0.9	±1.2	±1.4
$W + jets$	±1.1	±1.4	±0.7	±0.6	±0.8	±0.7	±0.5	±0.5	±0.9	±1.3
Mulitjet	±2.0	±1.2	±1.7	±1.9	±2.2	±1.6	±1.3	±1.4	±1.6	±1.9
ε_{fake}	±0.1	±1.9	±2.6	±4.1	±3.0	±3.4	±4.3	±4.0	±5.6	±5.3
JES	±4.1	±2.9	±2.2	±0.4	±0.4	±0.2	±0.5	±1.3	±1.9	±3.1
JER	±5.2	±1.1	±0.7	±1.6	±0.2	±0.9	±0.5	±0.1	±0.9	±0.5
JRE	±0.1	±0.2	±0.1	±0.1	±0.1	±0.0	±0.0	±0.0	±0.1	±0.3
JVF	±0.1	±0.6	±0.1	±0.1	±0.4	±0.3	±0.1	±0.0	±0.0	±1.3
W+HF SF	±0.2	±0.1	±0.1	±0.1	±0.1	±0.1	±0.2	±0.2	±0.4	±0.5
ε_c	±0.2	±0.1	±0.1	±0.2	±0.1	±0.1	±0.2	±0.2	±0.3	±0.3
ε_l	±0.1	±0.1	±0.2	±0.3	±0.2	±0.3	±0.4	±0.4	±0.7	±0.9
$E_{\mathrm{T}}^{\mathrm{miss}}$ cellout	±0.1	±0.0	±0.0	±0.0	±0.1	±0.0	±0.0	±0.2	±0.1	±0.3
$E_{\mathrm{T}}^{\mathrm{miss}}$ pileup	±0.1	±0.0	±0.0	±0.0	±0.0	±0.0	±0.0	±0.1	±0.0	±0.1
e trig.	±0.0	±0.0	±0.0	±0.0	±0.0	±0.0	±0.0	±0.0	±0.0	±0.0
e smear.	±0.1	±0.0	±0.0	±0.0	±0.0	±0.0	±0.0	±0.0	±0.0	±0.0
e recID	±0.1	±0.1	±0.1	±0.1	±0.1	±0.1	±0.1	±0.1	±0.1	±0.1
MC e-en.sc.	±0.0	±0.0	±0.0	±0.0	±0.0	±0.0	±0.0	±0.0	±0.2	±0.1
μ trig.	±0.0	±0.0	±0.0	±0.0	±0.0	±0.0	±0.0	±0.0	±0.0	±0.0
μ smear.	±0.0	±0.0	±0.0	±0.0	±0.0	±0.0	±0.0	±0.0	±0.0	±0.0
μ recID	±0.0	±0.0	±0.0	±0.0	±0.0	±0.0	±0.0	±0.0	±0.0	±0.0
Lumi	±0.1	±0.2	±0.0	±0.1	±0.1	±0.1	±0.1	±0.1	±0.1	±0.1
Stat.	±8.4	±5.0	±4.4	±4.2	±3.2	±3.4	±3.3	±3.6	±4.4	±8.7
Total Syst.	±8.9	±5.5	±5.2	±6.3	±5.9	±5.9	±6.0	±6.3	±8.5	±11.9
Total	±12.3	±7.4	±6.8	±7.5	±6.8	±6.8	±6.9	±7.3	±9.6	±14.8

Table C.1: Kinematic selection: single lepton (e+jets channel). Relative uncertainties for MV1 at the working point corresponding to 70% tagging efficiency.

$p_{\mathrm{T}}^{\mathrm{min}}$[GeV/$c$]	25-30	30-40	40-50	50-60	60-75	75-90	90-110	110-140	140-200	200-300
IFSR	±3.6	±3.1	±2.5	±2.9	±3.3	±3.9	±3.6	±4.2	±5.2	±8.1
Gen.	±1.0	±0.9	±0.4	±0.2	±0.1	±0.2	±0.8	±1.0	±2.2	±4.2
Fragm.	±0.5	±1.5	±2.1	±0.4	±2.2	±1.0	±0.8	±0.4	±0.7	±2.4
Diboson	±0.0	±0.0	±0.0	±0.0	±0.0	±0.0	±0.0	±0.0	±0.0	±0.0
Single top	±0.0	±0.0	±0.0	±0.0	±0.1	±0.1	±0.1	±0.1	±0.1	±0.2
Z+jets	±0.1	±0.0	±0.0	±0.1	±0.1	±0.1	±0.1	±0.2	±0.3	±0.4
$t\bar{t}$	±1.1	±0.9	±0.8	±0.7	±0.8	±0.9	±0.9	±1.1	±1.3	±1.4
W + $jets$	±2.2	±1.5	±1.2	±0.9	±0.9	±0.8	±0.8	±0.9	±1.1	±1.4
Mulitjet	±0.9	±0.8	±0.8	±0.7	±0.7	±0.7	±1.0	±0.9	±1.0	±0.8
ε_{fake}	±2.2	±1.0	±0.3	±0.1	±0.0	±0.0	±0.1	±0.0	±0.1	±0.3
JES	±6.7	±3.5	±2.2	±1.6	±1.1	±0.3	±0.6	±1.0	±0.6	±2.3
JER	±5.0	±1.0	±0.3	±1.3	±0.6	±0.7	±0.7	±0.9	±0.3	±1.4
JRE	±0.1	±0.1	±0.0	±0.0	±0.1	±0.1	±0.0	±0.0	±0.1	±0.2
JVF	±0.3	±0.1	±0.1	±0.0	±0.0	±0.1	±0.0	±0.0	±0.1	±0.0
W+HF SF	±0.3	±0.3	±0.3	±0.2	±0.4	±0.4	±0.5	±0.7	±0.8	±1.2
ε_c	±0.9	±0.6	±0.5	±0.4	±0.5	±0.5	±0.5	±0.6	±0.7	±1.0
ε_l	±0.6	±0.5	±0.6	±0.6	±0.9	±1.0	±1.2	±1.5	±1.8	±2.7
$E_{\mathrm{T}}^{\mathrm{miss}}$ cellout	±0.1	±0.0	±0.0	±0.0	±0.0	±0.1	±0.1	±0.0	±0.1	±0.1
$E_{\mathrm{T}}^{\mathrm{miss}}$ pileup	±0.1	±0.0	±0.0	±0.0	±0.0	±0.1	±0.0	±0.0	±0.0	±0.0
e trig.	±0.0	±0.0	±0.0	±0.0	±0.0	±0.0	±0.0	±0.0	±0.0	±0.0
e smear.	±0.0	±0.0	±0.0	±0.0	±0.0	±0.0	±0.0	±0.0	±0.0	±0.0
e recID	±0.0	±0.0	±0.0	±0.0	±0.0	±0.0	±0.0	±0.0	±0.0	±0.0
MC e-en.sc.	±0.0	±0.0	±0.0	±0.0	±0.0	±0.0	±0.0	±0.0	±0.0	±0.1
μ trig.	±0.1	±0.1	±0.0	±0.0	±0.1	±0.0	±0.1	±0.0	±0.1	±0.1
μ smear.	±0.0	±0.0	±0.0	±0.0	±0.0	±0.0	±0.0	±0.0	±0.0	±0.0
μ recID	±0.0	±0.0	±0.0	±0.0	±0.0	±0.0	±0.0	±0.0	±0.0	±0.0
Lumi	±0.3	±0.2	±0.1	±0.1	±0.0	±0.0	±0.0	±0.0	±0.0	±0.1
Stat.	±6.3	±3.8	±3.3	±3.0	±2.4	±2.4	±2.4	±2.6	±3.2	±6.4
Total Syst.	±9.9	±5.6	±4.4	±4.0	±4.5	±4.5	±4.5	±5.3	±6.6	±10.7
Total	±11.7	±6.8	±5.5	±5.0	±5.1	±5.1	±5.1	±5.9	±7.3	±12.5

Table C.2: Kinematic selection: single lepton (μ+jets channel). Relative uncertainties for MV1 at the working point corresponding to 70% tagging efficiency.

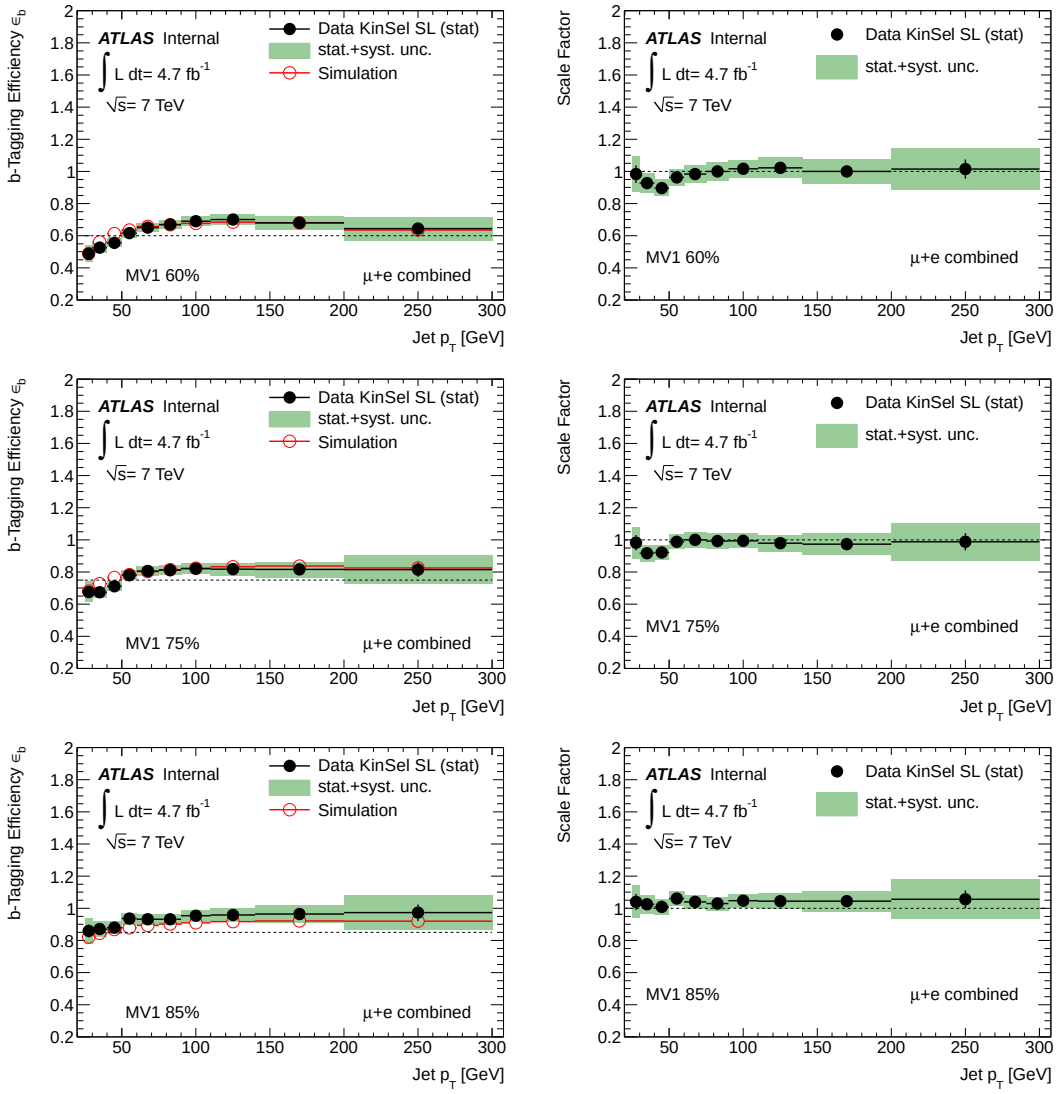

Figure C.2: *b*-tagging efficiency estimated from data compared with true efficiency (left) and resulting scale factors (right) together with statistical (bars) and systematic (band) uncertainties for the MV1 tagger at the working points corresponding to 60%, 75% and 85% *b*-tagging efficiency measured with the kinematic selection method in the single lepton channel [85]. The 70% working point is presented in figure 4.7.

C.2 Results for the SV0 algorithm

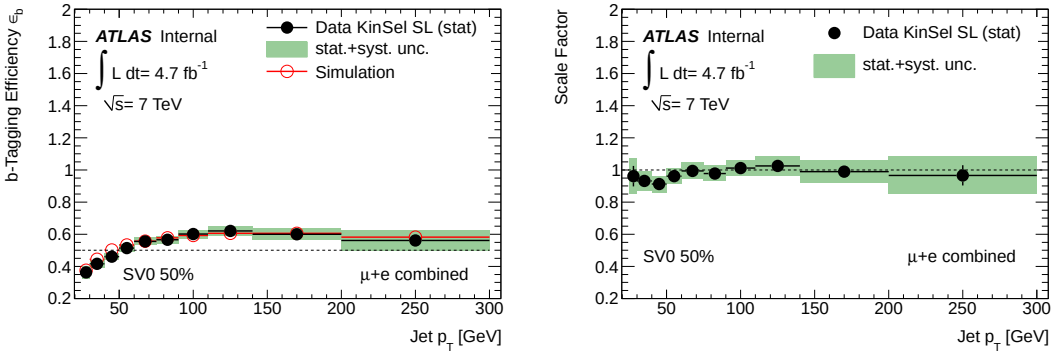

Figure C.3: *b*-tagging efficiency estimated from data compared with true efficiency (left) and resulting scale factors (right) together with statistical (bars) and systematic (band) uncertainties for the SV0 tagger at the working point corresponding to 50% efficiency measured with the kinematic selection method in the single lepton channel [85].

C.3 Results for the IP3D+SV1 algorithm

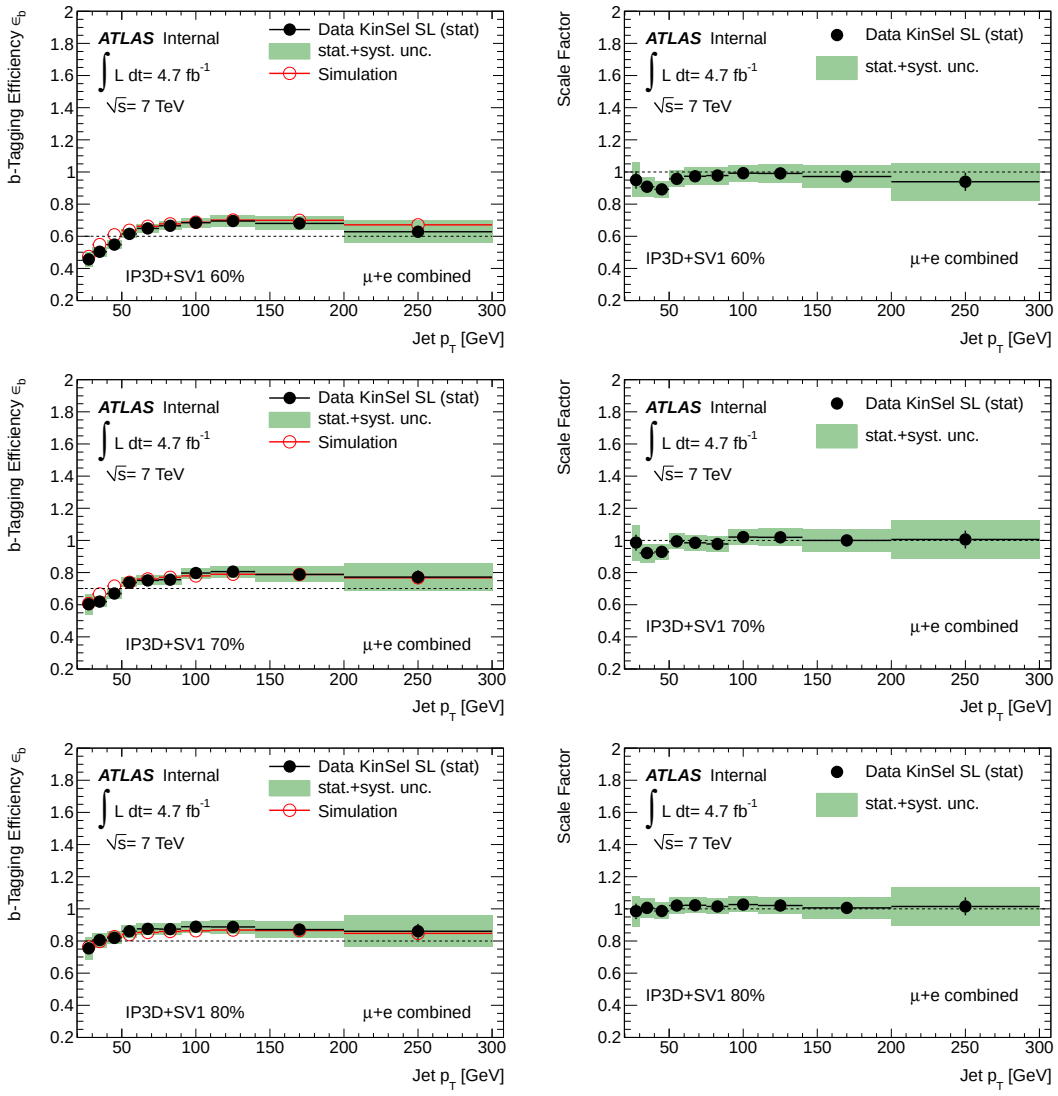

Figure C.4: *b*-tagging efficiency estimated from data compared with true efficiency (left) and resulting scale factors (right) together with statistical (bars) and systematic (band) uncertainties for the IP3D+SV1 tagger at the working points corresponding to 60%, 70% and 80% efficiency measured with the kinematic selection method in the single lepton channel [85].

C.4 Results for the IP3D+JetFitter algorithm

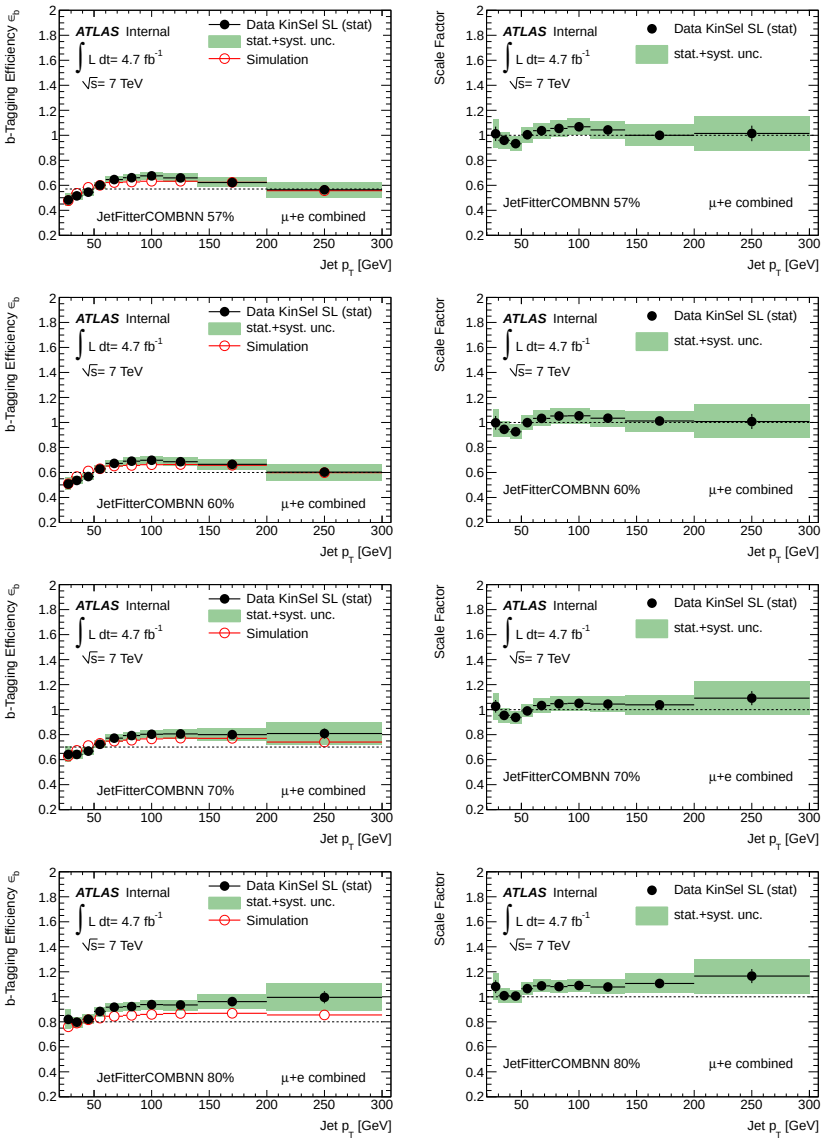

Figure C.5: *b*-tagging efficiency estimated from data compared with true efficiency (left) and resulting scale factors (right) together with statistical (bars) and systematic (band) uncertainties for the JetFitter+IP3D[1] tagger at the working points corresponding to 57%, 60%, 70% and 80% efficiency measured with the kinematic selection method in the single lepton channel [85].

[1] At the time of creation of these plots, the IP3D+JetFitter algorithm was called *JetFitterCombNN*

APPENDIX D

Performance of b-tagging in Z+jets control region

As there were various b-tagging calibration methods available and the b-tagging calibration was one of the major sources of uncertainty in the measurement of R_b, the sensitivity of the template to the choice of the method was evaluated. The impact of the b-tagging scale factors on the distribution of the number of b-tagged jets was studied in a control region for all available MV1 algorithm working points: 60%, 70%, 75% and 85%. Compared were scale factors obtained from methods using jets with muons (combination of pTrel and system8) and the scale factors from the kinematic fit method using $t\bar{t}$ events from the single lepton channel. The control region, dominated by Z+jets events, was created by changing the m_{ll} and $E_{\mathrm{T}}^{\mathrm{miss}}$ criteria of the dilepton selection described in section 3.2.2:

- $|m_{ll} - 91\ \mathrm{GeV}| < 10\ \mathrm{GeV}$
- $E_{\mathrm{T}}^{\mathrm{miss}} < 30\ \mathrm{GeV}$

All other requirements of the dilepton selection were followed. The control region was orthogonal to the signal region to avoid bias when choosing the best performing b-tagging working point.

Tables D.1 – D.8 show the number of events selected and the composition of Z+jets events for all available MV1 working points, for ee and $\mu\mu$ separately and for their sum. Figures D.1 – D.3 present the comparison between data and simulation with different b-tagging scale factors applied or without applying them. Finally, figure D.4 shows the ratio of the results obtained with different b-tagging scale factors with respect to no scale factors applied. It is clearly visible that the 85% working point was the most robust and insensitive to the choice of the b-tagging calibration method. Additionally, for the 85% working point, the b-tagging uncertainty had the smallest impact on the shape of the template.

	ee	$\mu\mu$	sum
Zqq	6584.2	17284.9	23869.1
Zcc	1332.9	3577.2	4910.1
Zbb	621.2	1643.7	2265.0
Diboson	155.4	371.4	526.8
Fakes	60.5	7.5	68.0
$t\bar{t}$	33.9	83.9	117.8
Single top	0.8	2.7	3.6
Sum	8789.0	22971.4	31760.4
Observed	7984	21197	29181

Table D.1: Numbers of events and composition in the Z+jets control region for MV1 algorithm at the 60% average tagging efficiency working point.

	0−tag	1-tag	2-tag	≥ 3-tags
ee channel				
Zqq	0.82	0.10	0.02	–
Zcc	0.14	0.36	0.10	–
Zbb	0.04	0.54	0.88	–
$\mu\mu$ channel				
Zqq	0.81	0.10	0.03	0.00
Zcc	0.15	0.35	0.08	0.23
Zbb	0.04	0.54	0.89	0.77
ee+$\mu\mu$ channels combined				
Zqq	0.81	0.10	0.03	0.00
Zcc	0.15	0.35	0.09	0.23
Zbb	0.04	0.54	0.88	0.77

Table D.2: Composition of the Z+jets events for different number of b-tagged jets in an event for MV1 algorithm at the 60% average tagging efficiency working point.

	ee	$\mu\mu$	sum
Zqq	6590.2	17294.0	23884.3
Zcc	1334.4	3581.6	4916.0
Zbb	624.0	1646.2	2270.3
Diboson	155.5	371.8	527.4
Fakes	60.5	7.5	68.0
$t\bar{t}$	34.2	84.4	118.6
Single top	0.8	2.7	3.5
Σ	8799.8	22988.2	31788.0
Observed	7984.0	21197.0	29181.0

Table D.3: Numbers of events and composition in the Z+jets control region for MV1 algorithm at the 70% average tagging efficiency working point.

	0−tag	1−tag	2−tag	≥ 3−tags
ee channel				
Zqq	0.83	0.24	0.05	0.00
Zcc	0.14	0.36	0.16	0.00
Zbb	0.03	0.40	0.79	1.00
$\mu\mu$ channel				
Zqq	0.82	0.23	0.04	0.00
Zcc	0.14	0.36	0.14	0.11
Zbb	0.04	0.41	0.81	0.89
ee+$\mu\mu$ channels combined				
Zqq	0.83	0.23	0.05	0.00
Zcc	0.14	0.36	0.15	0.08
Zbb	0.03	0.41	0.80	0.92

Table D.4: Composition of the Z+jets events for different number of *b*-tagged jets in an event for MV1 algorithm at the 70% average tagging efficiency working point.

	ee	$\mu\mu$	sum
Zqq	6595.7	17293.8	23889.5
Zcc	1338.0	3578.5	4916.5
Zbb	626.5	1650.0	2276.5
Diboson	155.7	371.7	527.4
Fakes	60.5	7.5	68.0
$t\bar{t}$	34.4	84.9	119.3
Single top	0.8	2.7	3.5
Σ	8811.5	22989.2	31800.7
Observed	7984.0	21197.0	29181.0

Table D.5: Numbers of events and composition in the *Z*+jets control region for MV1 algorithm at the 75% average tagging efficiency working point.

	0−tag	1−tag	2−tag	≥ 3−tags
ee channel				
Zqq	0.84	0.35	0.08	0.00
Zcc	0.13	0.34	0.23	0.00
Zbb	0.03	0.32	0.68	1.00
$\mu\mu$ channel				
Zqq	0.83	0.32	0.06	0.00
Zcc	0.13	0.34	0.19	0.07
Zbb	0.03	0.33	0.75	0.93
ee+$\mu\mu$ channels combined				
Zqq	0.83	0.33	0.07	0.00
Zcc	0.13	0.34	0.21	0.05
Zbb	0.03	0.33	0.73	0.95

Table D.6: Composition of the Z+jets events for different number of *b*-tagged jets in an event for MV1 algorithm at the 75% average tagging efficiency working point.

	ee	$\mu\mu$	sum
Zqq	6589.3	17293.9	23883.2
Zcc	1337.7	3582.1	4919.7
Zbb	629.7	1654.0	2283.7
Diboson	155.3	371.8	527.1
Fakes	60.5	7.5	68.0
$t\bar{t}$	34.3	85.7	119.9
Single top	0.8	2.7	3.6
Σ	8807.6	22997.6	31805.2
Observed	7984.0	21196.0	29180.0

Table D.7: Numbers of events and composition in the Z+jets control region for MV1 algorithm at the 85% average tagging efficiency working point.

	0−tag	1−tag	2−tag	≥ 3−tags
ee channel				
Zqq	0.85	0.60	0.32	0.04
Zcc	0.12	0.24	0.29	0.28
Zbb	0.03	0.15	0.39	0.68
$\mu\mu$ channel				
Zqq	0.85	0.60	0.34	0.10
Zcc	0.12	0.25	0.26	0.25
Zbb	0.03	0.15	0.40	0.65
ee+$\mu\mu$ channels combined				
Zqq	0.85	0.60	0.33	0.08
Zcc	0.12	0.25	0.27	0.26
Zbb	0.03	0.15	0.40	0.66

Table D.8: Composition of the Z+jets events for different number of b-tagged jets in an event for MV1 algorithm at the 85% average tagging efficiency working point.

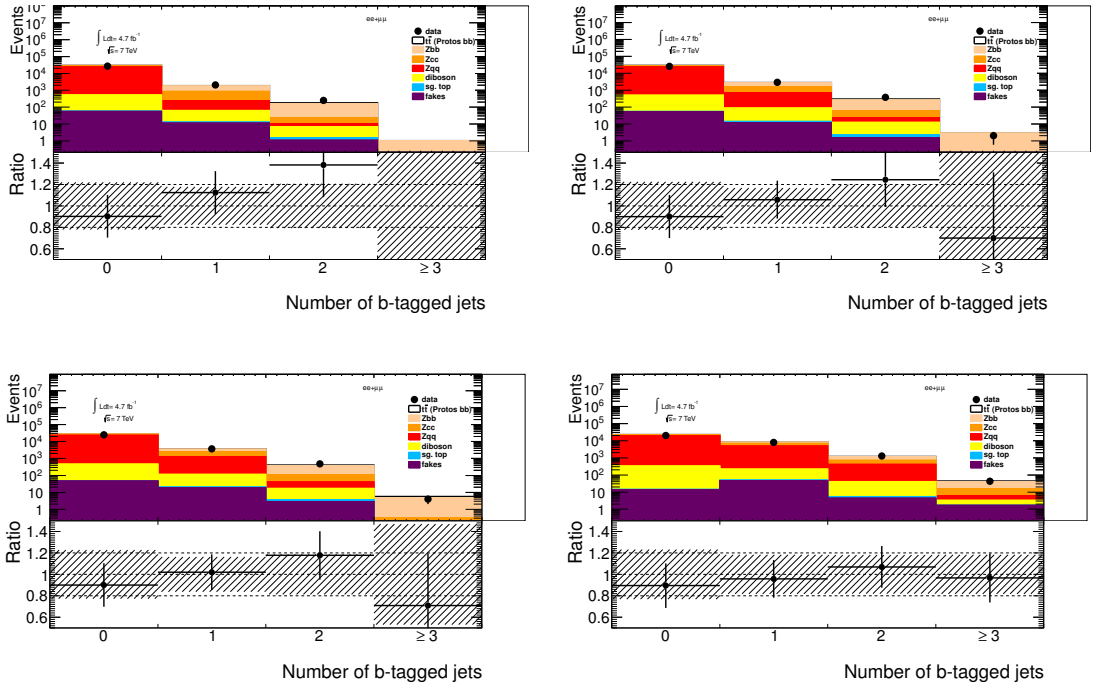

Figure D.1: Comparison of templates of physics processes simulation and data in Z+jets control region (ee+$\mu\mu$ channels combined). pTrel+system8 b-tagging scale factors had been applied to simulation. Distributions show number of tagged jets with MV1 algorithm at the (a) 60%, (b) 70%, (c) 75%, (d) 85% average tagging efficiency working point. The bottom panel shows data to simulation ratio, the shaded area shows the uncertainty associated with the b-tagging scale factors and the flavour composition of jets in the Z+jets events.

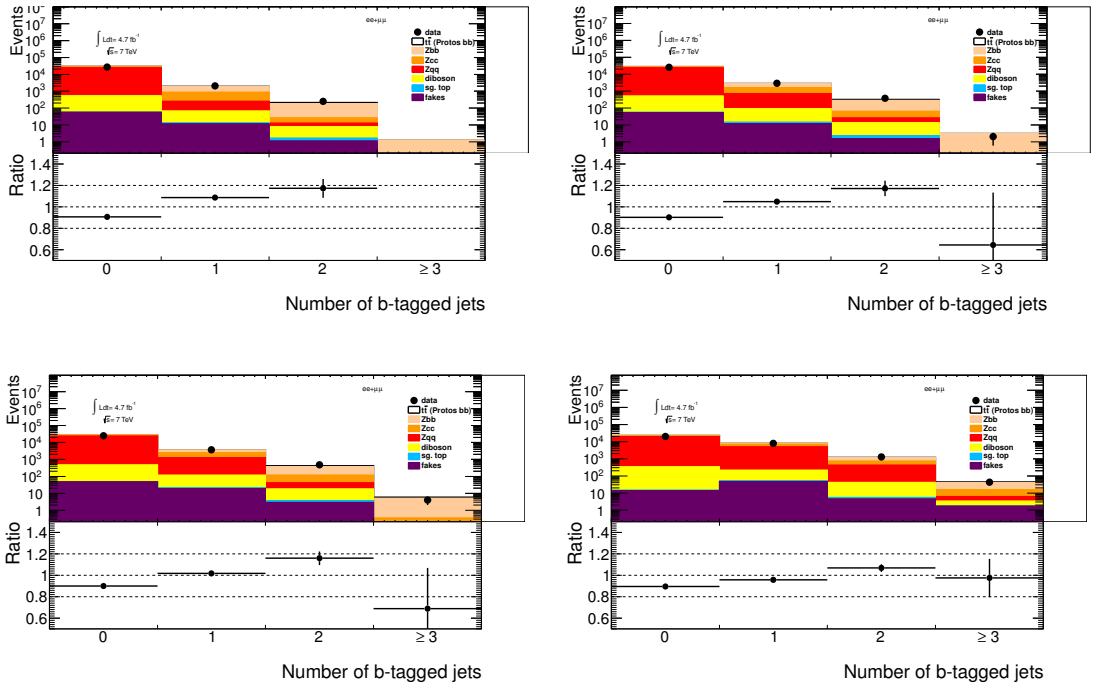

Figure D.2: Comparison of templates of physics processes simulation and data in Z+jets control region (ee+$\mu\mu$ channels combined). $t\bar{t}$ kinematic fit b-tagging scale factors had been applied to simulation. Distributions show number of tagged jets with MV1 algorithm at the (a) 60%, (b) 70%, (c) 75%, (d) 85% average tagging efficiency working point. The bottom panel shows data to simulation ratio.

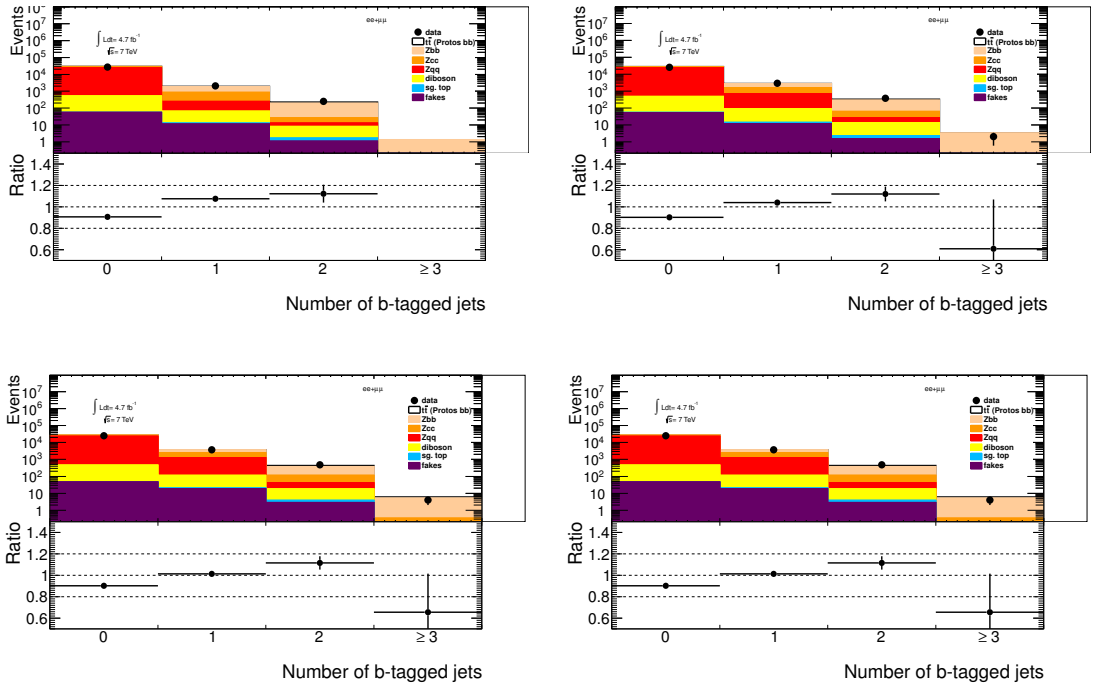

Figure D.3: Comparison of templates of physics processes simulation and data in Z+jets control region (ee+$\mu\mu$ channels combined). No scale factors had been applied to simulation. Distributions show number of tagged jets with MV1 algorithm at the (a) 60%, (b) 70%, (c) 75%, (d) 85% average tagging efficiency working point. The bottom panel shows data to simulation ratio.

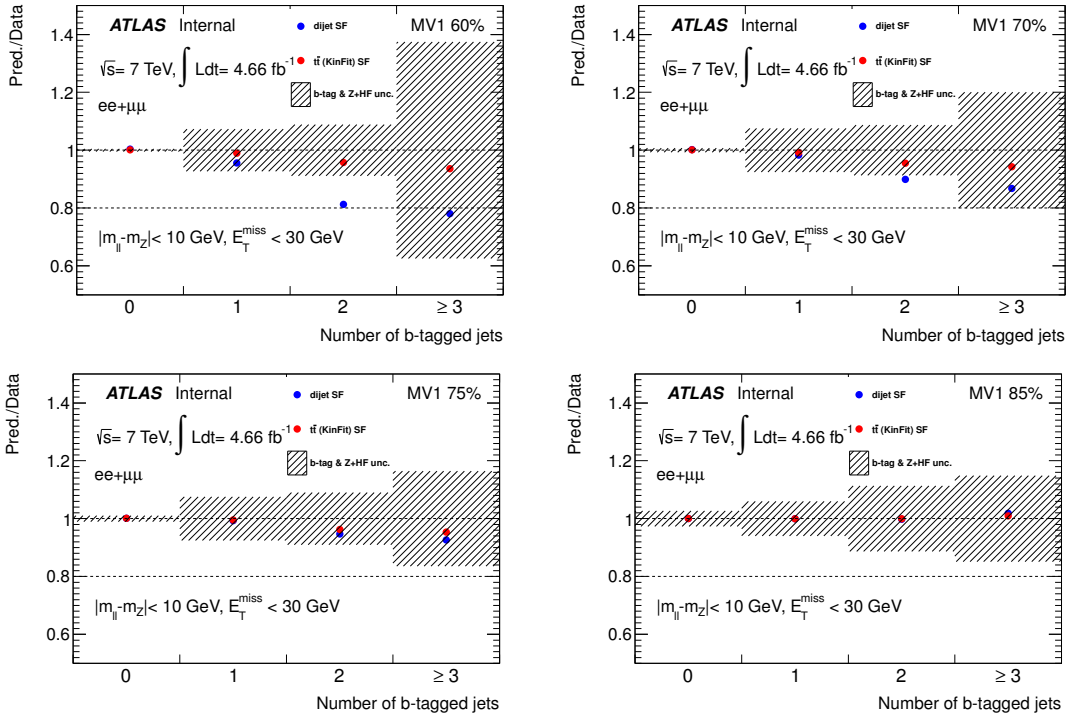

Figure D.4: Ratio of templates with pTrel+system8 scale factors and $t\bar{t}$ scale factors with respect to results with no *b*-tagging scale factors applied (ee+$\mu\mu$ channels combined). The shaded area represents the uncertainty associated with the pTrel+system8 *b*-tagging scale factors and the flavour composition of jets in the Z+jets events. Distributions show ratios for the number of tagged jets with MV1 algorithm at the (a) 60%, (b) 70%, (c) 75%, (d) 85% average tagging efficiency working point. The bottom panel shows data to simulation ratio.

APPENDIX E

Impact of pile-up studied with pseudo-experiments

In addition to the evaluation of the dependence of R_b and σ_{dilepton} on pile-up using data described in section 5.4.3, the measurement was repeated using pseudo-experiments. A series of 3000 pseudo-experiments was performed for each of the 26 sub-samples with the average number of interactions $3.5 < \langle\mu\rangle < 16$ (step of 0.5), as well as for each of the 14 sub-samples with number of primary vertices between 0 and 14 (step of 1). The pseudo-data was generated separately for each value of $\langle\mu\rangle$ and number of primary vertices. The templates for signal and background used for the fit were obtained from the events from the entire $\langle\mu\rangle$ (number of primary vertices) spectrum. Figure E.1 shows the measured values of R_b and σ_{dilepton} as a function of $\langle\mu\rangle$ and figure E.2 as a function of the number of primary vertices. There was no dependence observed for neither R_b nor σ_{dilepton}, which could indicated that the effect observed in section 5.4.3 was driven by statistical effects. Table E.1 shows the size of datasets used for the evaluation in section 5.4.3.

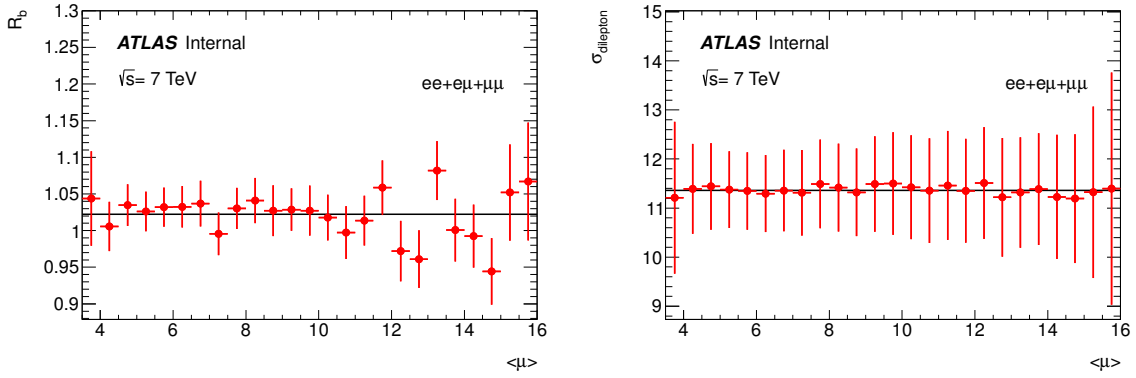

Figure E.1: Values of R_b and σ_{dilepton} measured for average number of interactions $3.5 < \langle\mu\rangle < 16$ in pseudo-experiments. The error bars represent the sum of statistical uncertainties returned by the fit and the statistical uncertainty on the selection efficiency for $tt \to WWbb$ process. The black line in the σ_{dilepton} plot shows the value measured with data and used as input for the generated data in pseudo-experiments.

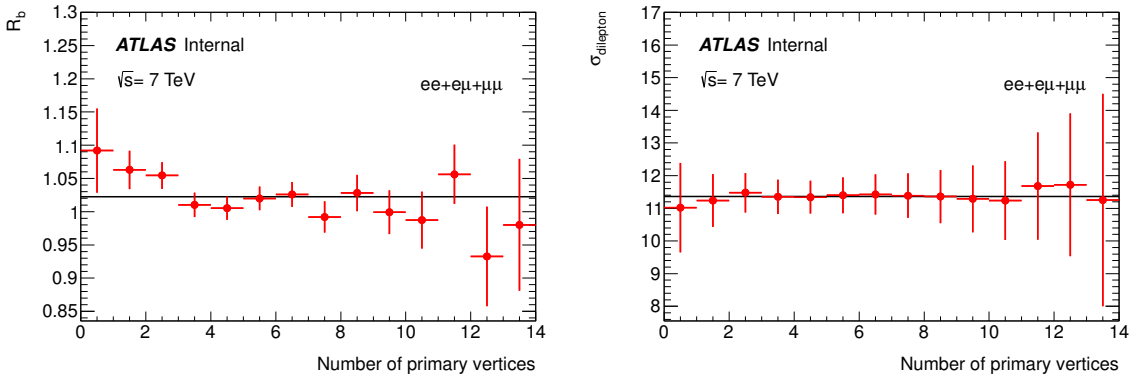

Figure E.2: Values of R_b and σ_{dilepton} measured for events with number of primary vertices between 0 and 14 in pseudo-experiments. The error bars represent the sum of statistical uncertainties returned by the fit and the statistical uncertainty on the selection efficiency for $tt \to WWbb$ process. The black line in the σ_{dilepton} plot shows the value measured with data and used as input for the generated data in pseudo-experiments.

Npv.	events in data	R_b	unc. from fit	unc. from sel. eff.	tot. stat. unc.
2	137	0.998	0.069	0.000	0.069
3	481	1.061	0.027	0.003	0.027
4	837	1.072	0.021	0.003	0.021
5	1106	1.060	0.020	0.002	0.020
6	1272	0.995	0.018	0.000	0.018
7	1087	1.030	0.019	0.001	0.019
8	982	1.018	0.018	0.001	0.018
9	723	1.005	0.024	0.000	0.024
10	548	1.003	0.026	0.000	0.026
11	339	1.017	0.029	0.001	0.029
12	270	0.953	0.036	0.003	0.036
13	147	0.935	0.051	0.005	0.051
14	81	0.815	0.071	0.011	0.072
15	35	0.951	0.101	0.008	0.101
16	20	0.905	0.134	0.023	0.136

Table E.1: Overview of the datasets used for the evaluation of the dependence of R_b on the number of primary vertices together with the size, the measured value of R_b, and the uncertainties.

APPENDIX F

Shape variations of templates

The effect of the systematic uncertainties on the template shapes is shown in the plots in this section.

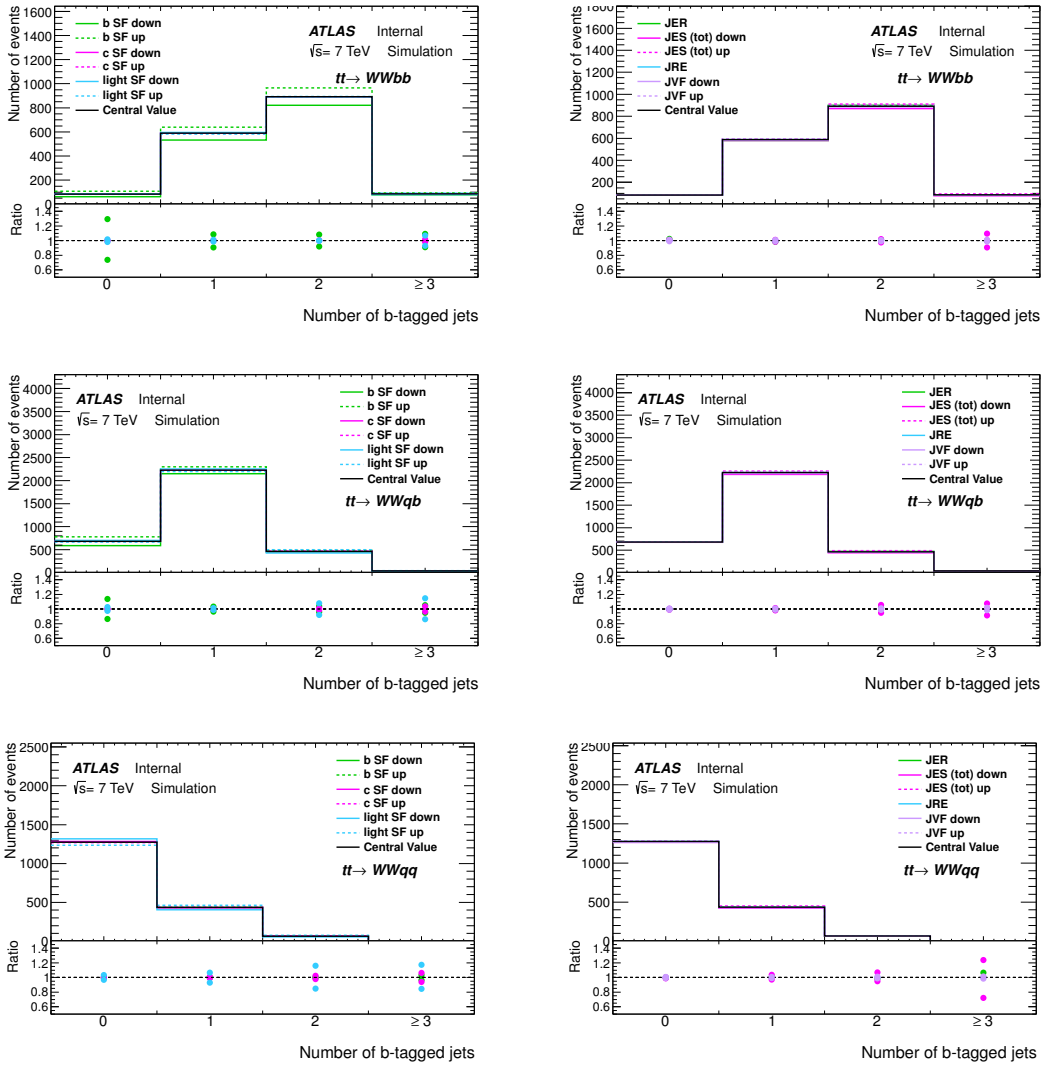

Figure F.1: Signal templates shape change due to the variation of *b*-tagging (left) and jet-related (right) systematic uncertainties for $tt \to WWbb$ (top), $tt \to WWqb$ (center) and $tt \to WWqq$ (bottom) templates. The bottom panel shows ratio of the varied template to the nominal Protos template with default settings.

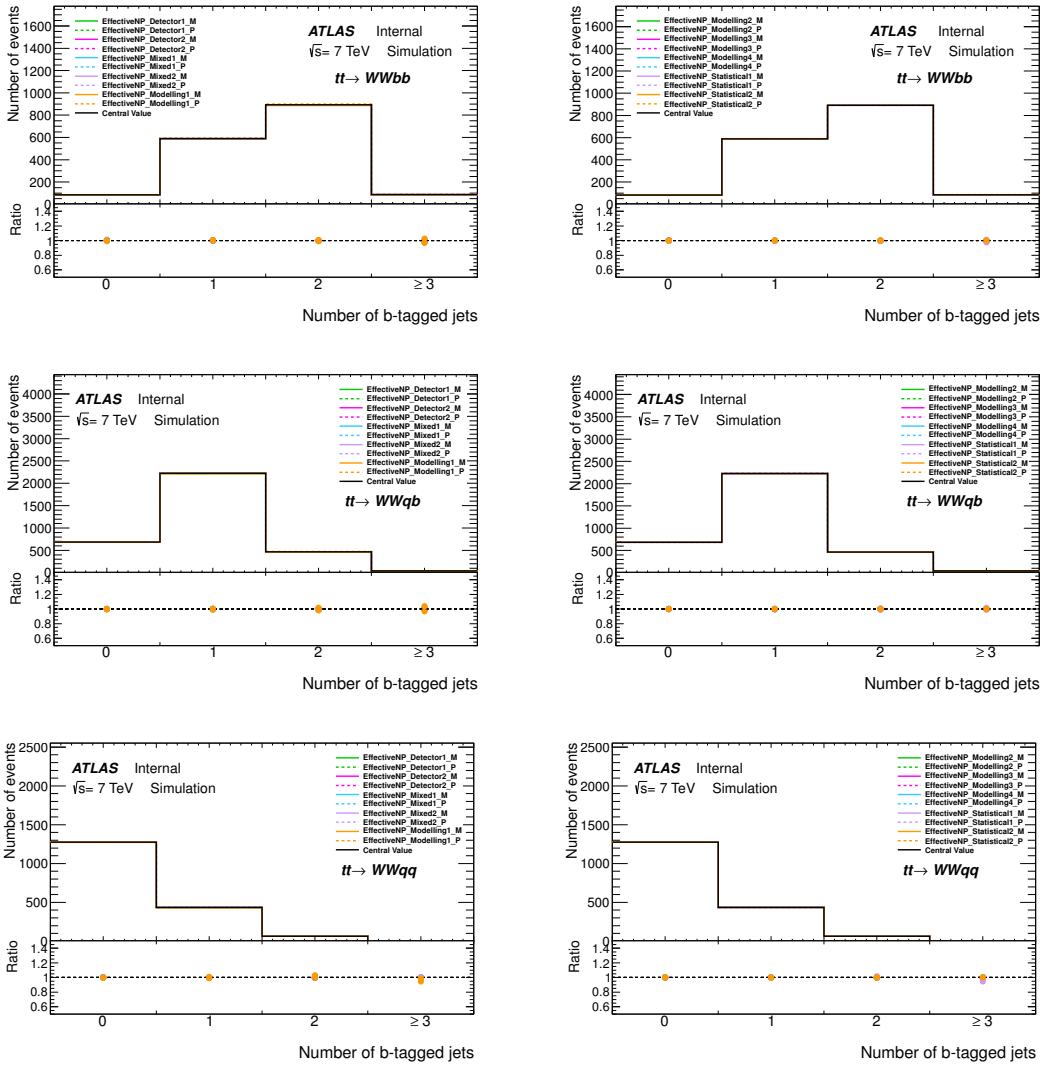

Figure F.2: Signal templates shape change due to variation of JES nuisance parameters (part I – left and part II – right))for $tt \to WWbb$ (top), $tt \to WWqb$ (center) and $tt \to WWqq$ (bottom) templates. The bottom panel shows ratio of the varied template to the nominal Protos template with default settings.

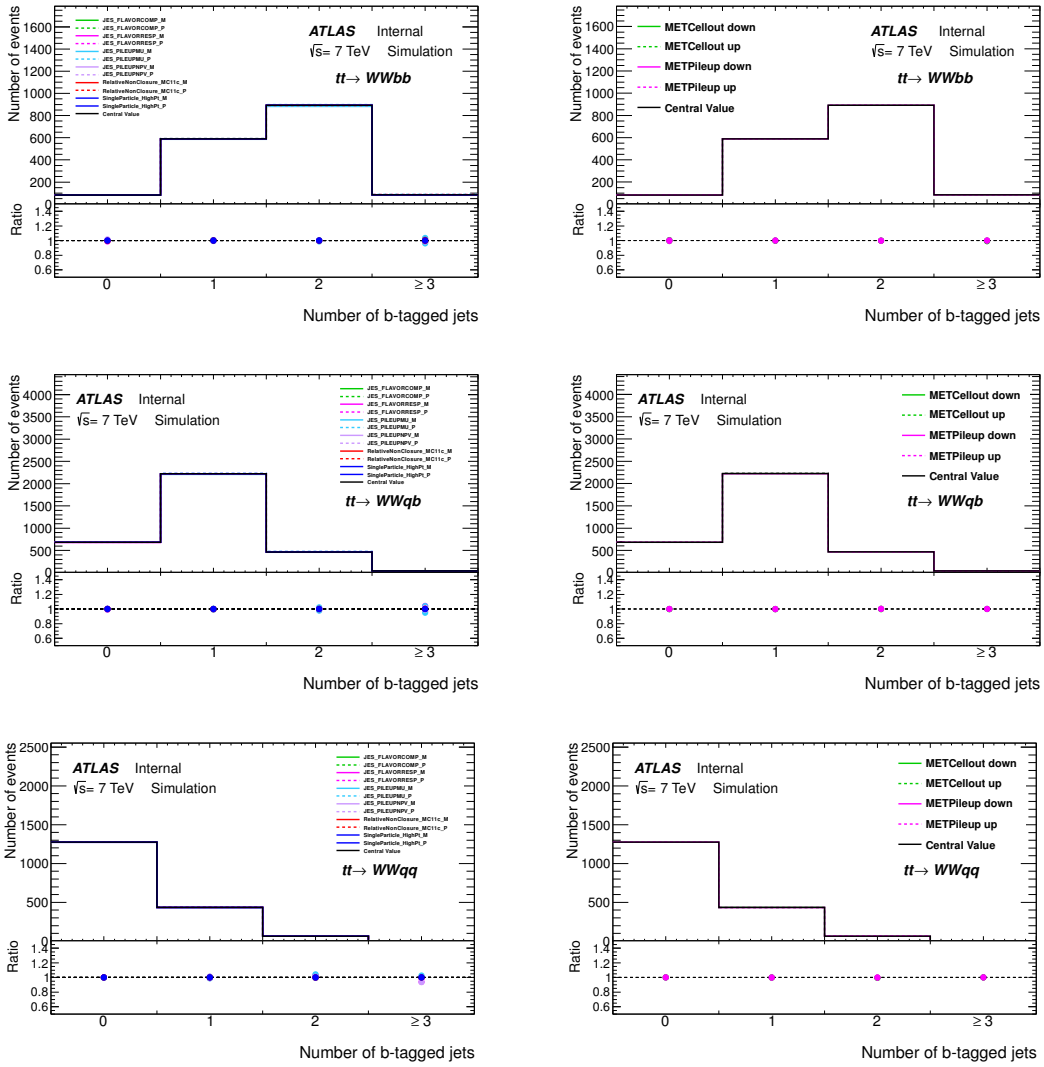

Figure F.3: Signal templates shape change due to variation of JES nuisance parameters (part III – left) and $E_{\mathrm{T}}^{\mathrm{miss}}$ systematic uncertainties for $tt \to WWbb$ (top), $tt \to WWqb$ (center) and $tt \to WWqq$ (bottom) templates. The bottom panel shows ratio of the varied template to the nominal Protos template with default settings.

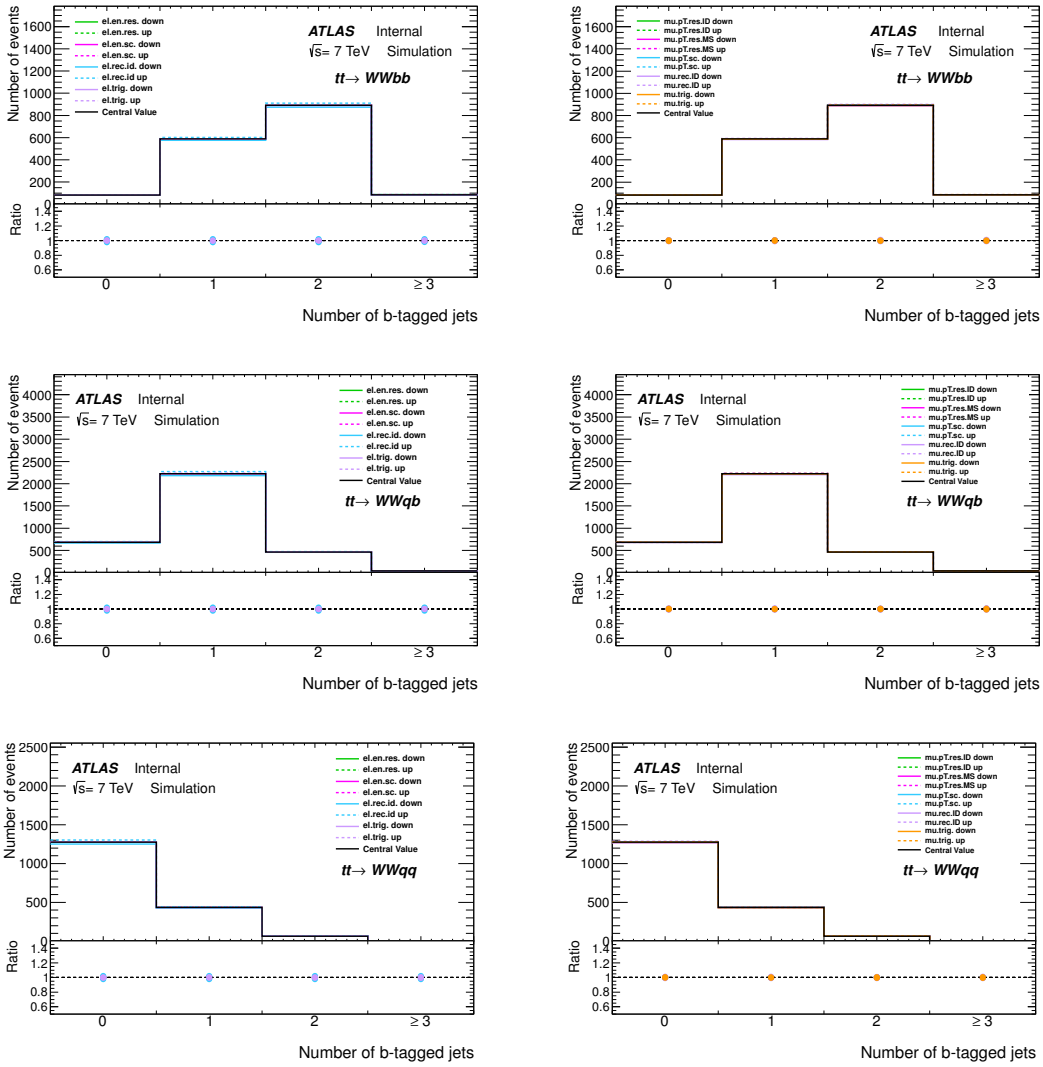

Figure F.4: Signal templates shape change due to variation of lepton related systematic uncertainties (electron – left and muon – right) for $tt \rightarrow WWbb$ (top), $tt \rightarrow WWqb$ (center) and $tt \rightarrow WWqq$ (bottom) templates. The bottom panel shows ratio of the varied template to the nominal Protos template with default settings.

APPENDIX G

Breakdown of b-tagging and JES uncertainties

Both b-tagging and JES uncertainties were obtained by evaluating multiple factors. Since both b-tagging and JES had significant contributions to the the total uncertainty of both R_b and σ_{dilepton} measurements, this section presents breakdown of b-tagging and JES systematic uncertainties.

The b-tagging and JEs uncertainies were evaluated both for the values predicted by the standard model and the values measured in data and no significant different was observed.

G.1 $R_b = 0.998$ and $\sigma_{\text{dilepton}} = 11.33$ pb

In section 5.4.6 systematic uncertainties were evaluated using pseudo-experiments with values predicted by standard model, $R_b = 0.99830$ and $\sigma_{\text{dilepton}} = 11.33$ pb, as input values. Tables G.1 – G.4 show breakdown of b-tagging and JES uncertainties presened in section 5.4.6.

G.2 $R_b = 1.022$ and $\sigma_{\text{dilepton}} = 11.36$ pb

In section 5.5.1 systematic uncertainties were evaluated using pseudo-experiments with $R_b = 1.022$ and the cross-section $\sigma_{\text{dilepton}} = 11.362$ pb which were measured in data, as input values.

Tables G.5 – G.6 show breakdown of b-tagging and JES uncertainties presened in section 5.5.1.

Source	Var. Down	Var. Up	Averaged Var.
JES (tot NP)	-0.004	0.007	0.005
Eff. NP Det. 1	0.001	-0.001	0.001
Eff. NP Det. 2	0.000	-0.000	0.000
Eff. NP Mix. 1	-0.000	0.000	0.000
Eff. NP Mix. 2	0.000	-0.000	0.000
Eff. NP Mod. 1	0.002	-0.001	0.001
Eff. NP Mod. 2	0.000	-0.000	0.000
Eff. NP Mod. 3	-0.000	0.001	0.000
Eff. NP Mod. 4	0.000	-0.000	0.000
Eff. NP Stat. 1	0.001	-0.001	0.001
Eff. NP Stat. 2	0.000	-0.000	0.000
Eff. NP Stat. 3	0.000	-0.000	0.000
Eta Intercalib. Mod.	0.001	-0.000	0.001
Eta Intercalib. Tot. Stat.	-0.000	0.000	0.000
JES b-jets	0.004	-0.003	0.003
JES closeby	0.002	-0.001	0.002
JES flav. comp.	-0.000	0.002	0.001
JES flav. resp.	-0.001	0.002	0.001
JES pileup	0.003	-0.001	0.002
JES pileup-npv	-0.001	0.001	0.001
Rel. NonClosure MC11c	-0.001	0.001	0.001
Sing. Part. HighPt	-0.000	-0.000	0.000

Table G.1: Breakdown of JES systematic uncertainty on the measurement of R_b with pseudo-experiments with the R_b input value 0.99830. The sum of all these variations (tot. NP) is obtained by adding in quadrature positive and negative contributions.

Source	Var. Down	Var. Up	Averaged Var.
BtagB	-0.050	0.054	0.052
BtagB EV 1	0.001	-0.001	0.001
BtagB EV 2	-0.001	0.001	0.001
BtagB EV 3	-0.001	0.001	0.001
BtagB EV 4	-0.001	0.001	0.001
BtagB EV 5	0.000	-0.000	0.000
BtagB EV 6	-0.001	0.001	0.001
BtagB EV 7	0.008	-0.009	0.009
BtagB EV 8	-0.033	0.035	0.034
BtagB EV 9	0.040	-0.037	0.038

Table G.2: Breakdown of b-tagging systematic uncertainty for b-jets on pseudo-experiments with the R_b input value 0.99830. The sum of all these variations is obtained by adding in quadrature positive and negative contributions.

Source	Var. Down	Var. Up	Averaged Var.
JES (tot NP)	-0.20	0.20	0.20
Eff. NP Det. 1	0.05	-0.06	0.05
Eff. NP Det. 2	0.00	-0.01	0.00
Eff. NP Mix. 1	0.00	-0.01	0.00
Eff. NP Mix. 2	0.01	-0.02	0.02
Eff. NP Mod. 1	0.07	-0.09	0.08
Eff. NP Mod. 2	0.00	-0.00	0.00
Eff. NP Mod. 3	-0.01	0.00	0.01
Eff. NP Mod. 4	0.00	-0.01	0.01
Eff. NP Stat. 1	0.03	-0.04	0.04
Eff. NP Stat. 2	0.00	-0.00	0.00
Eff. NP Stat. 3	0.01	-0.02	0.01
Eta Intercalib. Mod.	0.07	-0.05	0.06
Eta Intercalib. Tot. Stat.	0.02	-0.03	0.02
JES b-jets	0.09	-0.09	0.09
JES closeby	0.06	-0.06	0.06
JES flav. comp.	0.00	-0.01	0.01
JES flav. resp.	0.02	-0.02	0.02
JES pileup	0.11	-0.10	0.11
JES pileup-npv	-0.01	0.01	0.01
Rel. NonClosure MC11c	0.01	-0.00	0.01
Sing. Part. HighPt	0.00	0.00	0.00

Table G.3: Breakdown of JES systematic uncertainty on the measurement of σ_{dilepton} with pseudo-experiments with the σ_{dilepton} input value 11.33 pb. The sum of all these variations (tot. NP) is obtained by adding in quadrature positive and negative contributions.

Source	Var. Down	Var. Up	Averaged Var.
BtagB	-0.06	0.07	0.07
BtagB EV 1	0.00	-0.00	0.00
BtagB EV 2	-0.00	0.01	0.00
BtagB EV 3	-0.00	0.00	0.00
BtagB EV 4	0.00	-0.00	0.00
BtagB EV 5	-0.00	0.00	0.00
BtagB EV 6	-0.00	0.00	0.00
BtagB EV 7	-0.00	0.01	0.01
BtagB EV 8	-0.00	0.01	0.00
BtagB EV 9	0.07	-0.06	0.07

Table G.4: Breakdown of b-tagging systematic uncertainty for b-jets on the σ_{dilepton} measurement on pseudo-experiments with the σ_{dilepton} input value 11.33 pb. The sum of all these variations is obtained by adding in quadrature positive and negative contributions.

Variable	R_b	σ_{dilepton}
Source	Average Unc.	Average Unc.
JES (tot NP)	0.006	0.20
Eff. NP Det. 1	0.001	0.05
Eff. NP Det. 2	0.000	0.00
Eff. NP Mix. 1	0.000	0.00
Eff. NP Mix. 2	0.001	0.02
Eff. NP Mod. 1	0.001	0.08
Eff. NP Mod. 2	0.001	0.01
Eff. NP Mod. 3	0.001	0.01
Eff. NP Mod. 4	0.000	0.00
Eff. NP Stat. 1	0.001	0.04
Eff. NP Stat. 2	0.000	0.00
Eff. NP Stat. 3	0.000	0.02
Eta Intercalib. Mod.	0.001	0.06
Eta Intercalib. Tot. Stat.	0.001	0.02
JES b-jets	0.003	0.09
JES closeby	0.001	0.06
JES flav. comp.	0.001	0.01
JES flav. resp.	0.001	0.02
JES pile-up	0.002	0.11
JES pile-up-npv	0.001	0.01
Rel. NonClosure MC11c	0.001	0.01
Sing. Part. HighPt	0.000	0.00

Table G.5: Breakdown of JES systematic uncertainty on the measurement of R_b and σ_{dilepton} determined using pseudo-experiments with $R_b = 1.022$ and $\sigma_{\text{dilepton}} = 11.36$. The sum of all these variations (tot. NP) was obtained by adding in quadrature positive and negative contributions.

Variable	R_b	σ_{dilepton}
Source	Average Unc.	Average Unc.
BtagB	0.053	0.07
BtagB EV 1	0.001	0.00
BtagB EV 2	0.001	0.00
BtagB EV 3	0.001	0.00
BtagB EV 4	0.001	0.00
BtagB EV 5	0.000	0.00
BtagB EV 6	0.001	0.00
BtagB EV 7	0.009	0.01
BtagB EV 8	0.036	0.01
BtagB EV 9	0.038	0.06

Table G.6: Breakdown of b-tagging systematic uncertainty for b-jets on pseudo-experiments with the $R_b = 1.022$ and $\sigma_{\text{dilepton}} = 11.36$. The sum of all these variations was obtained by adding in quadrature positive and negative contributions.

APPENDIX H

Pseudo-experiments results for selected systematic uncertainty variations

Figures H.1, H.2 and H.3 show results of the series of pseudo-experiments conducted to evaluate the systematic uncertainty related to b-tagging and for templates from different simulation samples: initial/final state radiation (all signal templates varied as described in section 5.4.2) and for the fits with $tt \rightarrow WWbb$ templates from MC@NLO+Herwig and Alpgen+ Herwig samples. MC@NLO+Herwig and Alpgen+ Herwig simulation samples were used to evaluate the uncertainty coming from choice of simulation generator.

Each figure includes an example fit to pseudo-data, a distribution of measured values of R_b and a distribution of measured values of σ_{dilepton}. R_b and σ_{dilepton} were fitted separately and the pseudo-data was generated with $R_b = 0.99830$ and $\sigma_{\text{dilepton}} = 11.33$ pb as input values.

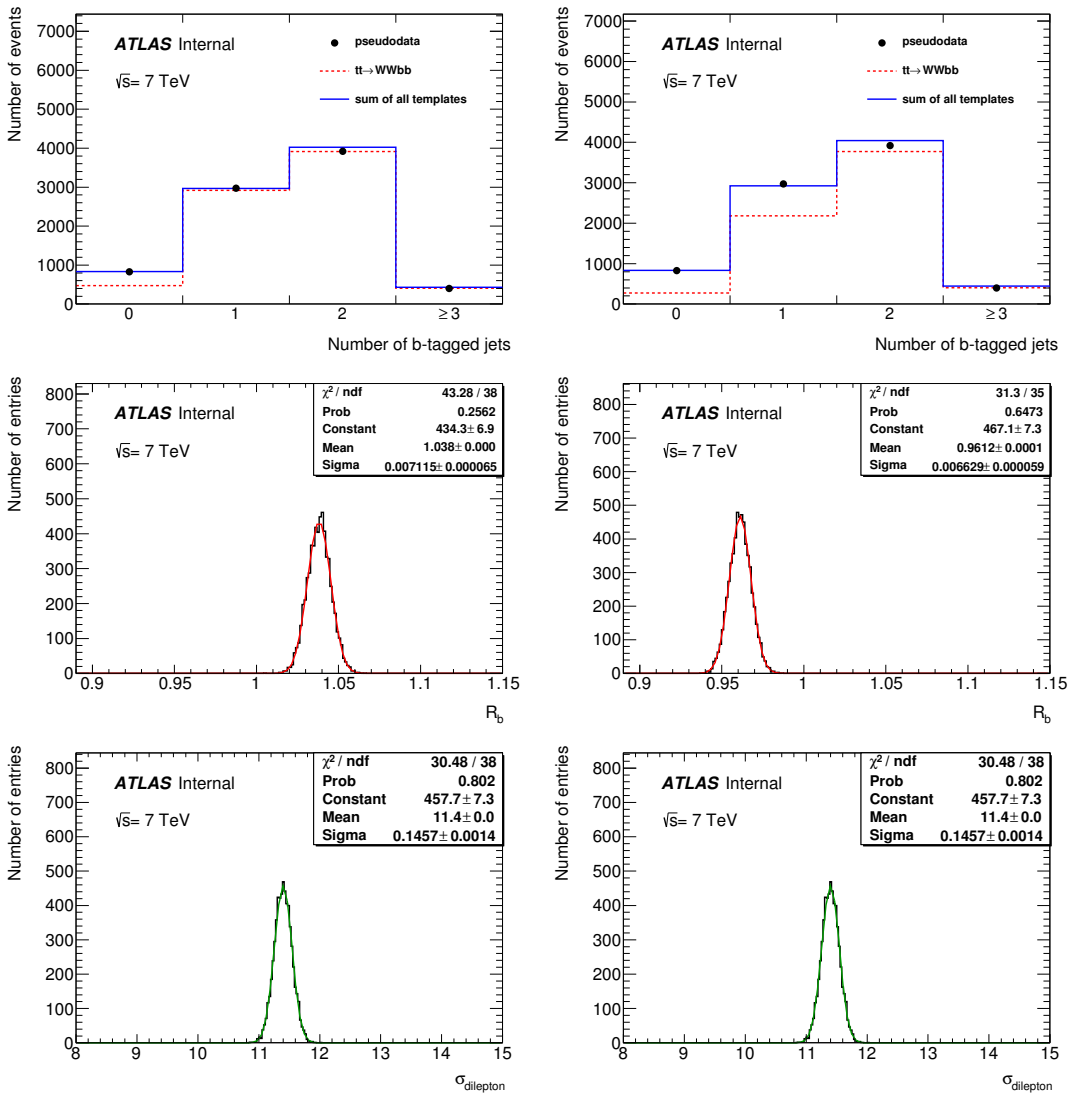

Figure H.1: Results for pseudo-experiments using templates with b-tagging 9^{th} eigenvalue variation – *Btag EV 9* – down (left) and up (right). Btag EV 9 introduced the largest uncertainty from all 9 b-tagging eigenvalues, see appendix G. The top row shows an example fit in one of the pseudo-experiments, middle row shows distribution of measured values of R_b in the series of pseudo-experiments and the bottom rows shows the distribution of measured values of σ_{dilepton}.

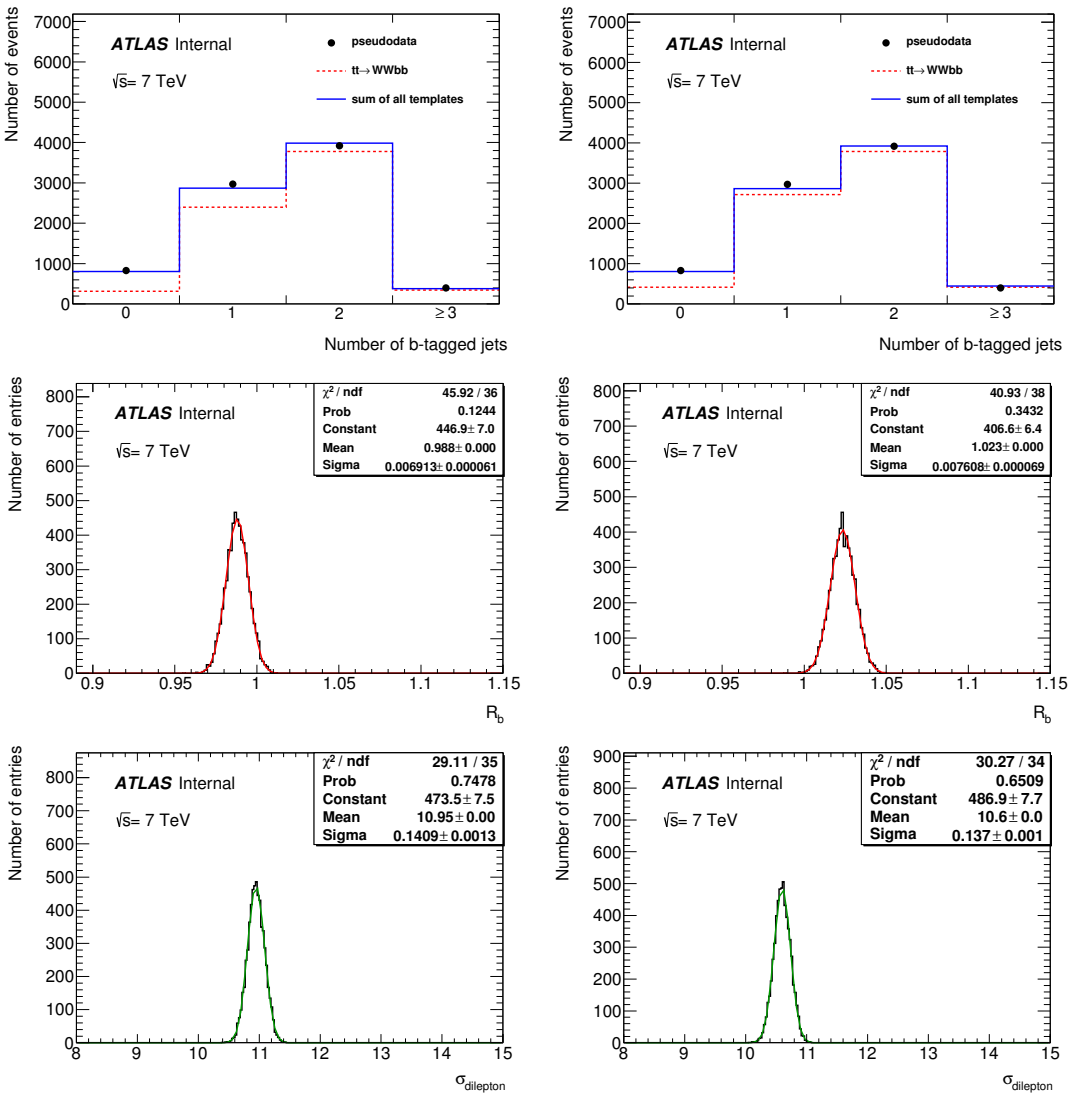

Figure H.2: Results for pseudo-experiments using templates with minimal (left) and maximal (right) ISR/FSR. The top row shows an example fit in one of the pseudo-experiments, middle row shows distribution of measured values of R_b in the series of pseudo-experiments and the bottom rows shows the distribution of measured values of σ_{dilepton}.

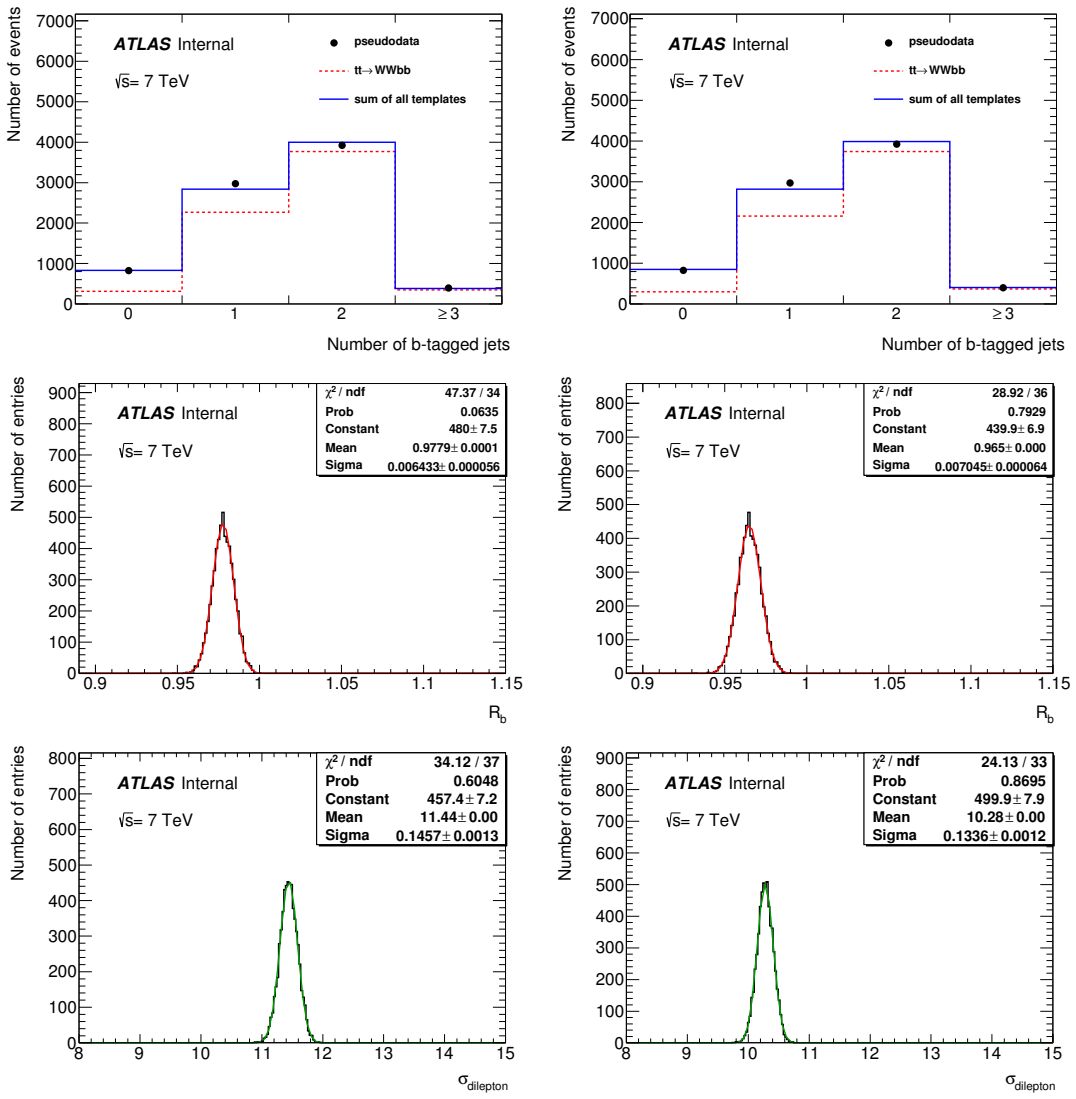

Figure H.3: Results for pseudo-experiments using templates from MC@NLO+Herwig (left) and Alpgen+Herwig sample (right), which are compared in order to evaluate the uncertainty coming from choice of simulation generator. The top row shows an example fit in one of the pseudo-experiments, middle row shows distribution of measured values of R_b in the series of pseudo-experiments and the bottom rows shows the distribution of measured values of σ_{dilepton}.

APPENDIX I

Estimation of systematic uncertainties in data

The fit to data was performed using templates with systematic variations described in section 5.4 and the resulting uncertainties are presented in tables I.1 – I.3 for R_b and I.4 – I.6 for σ_{dilepton}. The pile-up and top quark mass uncertainties were estimated as described in section 5.4.3.

Total uncertainties obtained with fit to data are comparable to those obtained with pseudo-experiments and presented in section 5.5.1.

measured R_b	1.02		
Source	Var. Down	Var. Up	Averaged Var.
Initial/final state radiation	-0.019	0.019	0.019
Generator	-0.036	0.036	0.036
Associated HF prod.	-0.003	0.003	0.003
Colour reconnection	-0.000	0.000	0.000
Underlying event	-0.000	0.000	0.000
Parton distribution function	-0.001	0.001	0.001
Top quark mass	0.002	-0.002	0.002
Jet energy scale	-0.006	0.009	0.008
Jet reconstruction efficiency	0.000	-0.000	-0.000
Jet energy resolution	0.003	-0.003	-0.003
Jet vertex fraction	-0.000	0.001	0.001
b-tagging (b-jets)	-0.051	0.055	0.053
b-tagging (c-jets)	0.002	-0.001	0.002
b-tagging (light jets)	0.006	-0.006	0.006
$E_{\mathrm{T}}^{\mathrm{miss}}$	0.001	-0.001	0.001
e SF	-0.001	0.002	0.001
μ SF	-0.002	0.002	0.002
background flavour comp.	0.001	-0.001	0.001
Z+jets norm.	-0.009	0.009	0.009
Dib. norm.	-0.010	0.009	0.009
Sg. top norm.	-0.001	0.001	0.001
Fake leptons shape	0.001	-0.001	0.001
Fake leptons norm.	-0.004	0.004	0.004
Pile-up	-0.002	0.002	0.002
Luminosity	-0.002	0.002	0.002
Sel. eff. stat.	-0.000	0.000	0.000
Total syst.	-0.068	0.071	0.069
Total stat.	-0.007	0.007	0.007
Total unc.	-0.068	0.071	0.070

Table I.1: Full list of uncertainties on the measurement of R_b. The top mass and pile-up uncertainties are determined as described in sections 5.4.3 and 5.4.4, the rest is determined with a fit to data. The total systematic uncertainty is a quadrature sum of all negative and positive contributions.

Source	Var. Down	Var. Up	Averaged Var.
JES (tot NP)	-0.006	0.009	0.008
Eff. NP Det. 1	-0.001	0.001	0.001
Eff. NP Det. 2	-0.001	0.001	0.001
Eff. NP Mix. 1	-0.001	0.001	0.001
Eff. NP Mix. 2	-0.001	0.001	0.001
Eff. NP Mod. 1	0.001	-0.001	0.001
Eff. NP Mod. 2	0.001	-0.001	0.001
Eff. NP Mod. 3	-0.001	0.001	0.001
Eff. NP Mod. 4	-0.001	0.001	0.001
Eff. NP Stat. 1	0.001	-0.001	0.001
Eff. NP Stat. 2	0.001	-0.001	0.001
Eff. NP Stat. 3	-0.001	0.001	0.001
Eta Intercalib. Mod.	-0.001	0.001	0.001
Eta Intercalib. Tot. Stat.	-0.001	0.001	0.001
JES b-jets	0.004	-0.002	0.003
JES closeby	0.001	-0.001	0.001
JES flav. comp.	-0.003	0.005	0.004
JES flav. resp.	-0.002	0.004	0.003
JES pileup	0.001	-0.001	0.001
JES pileup-npv	-0.002	0.002	0.002
Rel. NonClosure MC11c	-0.002	0.002	0.002
Sing. Part. HighPt	0.000	0.000	0.000

Table I.2: Breakdown of JES systematic uncertainty on the measurement of R_b with data. The sum of all these variations (tot. NP) is obtained by adding in quadrature positive and negative contributions.

Source	Var. Down	Var. Up	Averaged Var.
BtagB	-0.051	0.055	0.053
BtagB EV 1	0.002	-0.001	0.001
BtagB EV 2	-0.000	0.001	0.001
BtagB EV 3	-0.001	0.002	0.001
BtagB EV 4	-0.001	0.002	0.001
BtagB EV 5	0.001	-0.001	0.001
BtagB EV 6	-0.001	0.002	0.001
BtagB EV 7	0.009	-0.008	0.009
BtagB EV 8	-0.033	0.036	0.034
BtagB EV 9	0.041	-0.037	0.039

Table I.3: Breakdown of b-tagging systematic uncertainty for b-jets on R_b measured with fit to data. The sum of all these variations is obtained by adding in quadrature positive and negative contributions.

measured $\sigma_{t\bar{t}}$	11.36 pb		
Source	Var. Down	Var. Up	Averaged Var.
Initial/final state radiation	-0.18	0.18	0.18
Generator	-1.12	1.12	1.12
Associated HF prod.	-0.02	0.02	0.02
Colour reconnection	-0.16	0.16	0.16
Underlying event	-0.01	0.01	0.01
Parton distribution function	-0.07	0.07	0.07
Top quark mass	0.09	-0.09	0.09
Jet energy scale	-0.28	0.26	0.27
Jet reconstruction efficiency	-0.00	0.00	0.00
Jet energy resolution	0.04	-0.04	-0.04
Jet vertex fraction	0.11	-0.10	0.11
b-tagging (b-jets)	-0.07	0.07	0.07
b-tagging (c-jets)	0.01	-0.01	0.01
b-tagging (light jets)	0.01	-0.02	0.01
$E_{\mathrm{T}}^{\mathrm{miss}}$	-0.00	0.01	0.00
e trigger	0.01	-0.02	0.02
e energy resolution	0.02	-0.03	0.02
e rec./id. efficiency	0.26	-0.26	0.26
μ trigger	0.02	-0.03	0.03
μ rec./id. efficiency	0.11	-0.12	0.11
μ p_{T}	0.02	-0.02	0.02
background flavour comp.	0.01	-0.01	0.01
Z+jets norm.	0.10	-0.10	0.10
Dib. norm.	0.11	-0.10	0.10
Sg. top norm.	0.04	-0.04	0.04
Fake leptons norm. $e\mu$	0.11	-0.11	0.11
Pile-up	-0.06	0.06	0.06
Luminosity	0.03	-0.03	0.03
Sel. eff. stat.	-0.11	0.11	0.11
Total syst.	-1.25	1.24	1.24
Total stat.	-0.14	0.14	0.14
Total unc.	-1.25	1.25	1.25

Table I.4: Full list of uncertainties on the measurement of $\sigma_{\mathrm{dilepton}}$. The top mass and pile-up uncertainties are determined as described in sections 5.4.3 and 5.4.4, the rest is determined with a fit to data. The total systematic uncertainty is a quadrature sum of all negative and positive contributions.

Source	Var. Down	Var. Up	Averaged Var.
JES (tot NP)	-0.28	0.26	0.27
Eff. NP Det. 1	0.06	-0.08	0.07
Eff. NP Det. 2	0.01	-0.01	0.01
Eff. NP Mix. 1	0.02	-0.02	0.02
Eff. NP Mix. 2	0.01	-0.03	0.02
Eff. NP Mod. 1	0.09	-0.12	0.10
Eff. NP Mod. 2	0.01	-0.01	0.01
Eff. NP Mod. 3	-0.02	0.02	0.02
Eff. NP Mod. 4	0.01	-0.01	0.01
Eff. NP Stat. 1	0.04	-0.06	0.05
Eff. NP Stat. 2	0.01	-0.01	0.01
Eff. NP Stat. 3	0.01	-0.03	0.02
Eta Intercalib. Mod.	0.09	-0.08	0.08
Eta Intercalib. Tot. Stat.	0.02	-0.04	0.03
JES b-jets	0.09	-0.10	0.10
JES closeby	0.07	-0.08	0.07
JES flav. comp.	0.05	-0.06	0.06
JES flav. resp.	0.04	-0.06	0.05
JES pileup	0.14	-0.13	0.14
JES pileup-npv	-0.02	0.02	0.02
Rel. NonClosure MC11c	0.06	-0.06	0.06
Sing. Part. HighPt	-0.01	-0.01	0.01

Table I.5: Breakdown of JES systematic uncertainty on the measurement of σ_{dilepton} with data. The sum of all these variations (tot. NP) is obtained by adding in quadrature positive and negative contributions.

Source	Var. Down	Var. Up	Averaged Var.
BtagB	-0.07	0.07	0.07
BtagB EV 1	0.01	-0.01	0.01
BtagB EV 2	-0.01	0.01	0.01
BtagB EV 3	-0.01	0.01	0.01
BtagB EV 4	0.01	-0.01	0.01
BtagB EV 5	-0.01	0.01	0.01
BtagB EV 6	-0.01	0.01	0.01
BtagB EV 7	-0.01	0.01	0.01
BtagB EV 8	-0.01	0.00	0.01
BtagB EV 9	0.06	-0.07	0.07

Table I.6: Breakdown of b-tagging systematic uncertainty for b-jets on R_b measured with fit to data. The sum of all these variations is obtained by adding in quadrature positive and negative contributions.

APPENDIX J

Influence of the initial uncertainty on the *b*-tagging scale factors on the measurements

The uncertainty on the *b*-tagging together with the uncertainty from the Monte Carlo generator choice had the highest impact on the total uncertainty in the measurement of R_b and σ_{dilepton} as presented in tables 5.11 and 5.12. A study was conducted to estimate the dependence between the initial uncertainty on the *b*-tagging scale factors and the uncertainty on R_b (σ_{dilepton}) arising from *b*-tagging.

The *b*-tagging scale factors were provided in 2D bins of p_{T} and η for each jet flavour and depending on the information whether the jet was tagged by the chosen tagging algorithm. An eigenvector method was used to vary the *b*-tagging scale factors within their uncertainties, as described in section 5.4. The design, the largest variation is carried by the last two factors: BtagB EV 8 and BtagB EV 9, as can be seen for example in table G.6 in appendix G. However, it is not possible to determine which sources of uncertainty[1] contribute to those two factors. Moreover, for different bins, different effects might be the dominant sources of uncertainty.

Therefore, in this study, a simplified scenario was considered, where regardless of the original source of the uncertainty, the uncertainty on the *b*-tagging scale factor (for both tagged and not tagged *b*-jets) associated with BtagB EV 8 and BtagB EV 9 was half the default size. New $tt \to WWbb$, $tt \to WWqb$ and $tt \to WWqq$ templates had been created, as well as new selection efficiencies for those three signal processes were calculated. The changes of the selection efficiency for BtagB EV 9 with respect to the central value used in the main analysis are summarised in table J.1. The variation on the selection efficiency after decreasing the BtagB EV 9 variation on the *b*-tagging scale factors by 50% was lower by 50 – 60% depending on the type of the process, comparing with the default size of the BtagB EV 9 variation.

Figure J.1 shows the $tt \to WWbb$ variation templates created with the default and decreased BtagB EV 9 "up" uncertainty applied. For comparison, also the central value template is presented. For these modified selection efficiencies and templates a series of pseudo-experiments was performed like in the case of the default values of the uncertainties. The resulting final *b*-tagging uncertainties are presented in table J.2 for σ_{dilepton}. New values of uncertainties calculated in this study are 50% – 60% lower than the previous values depending on default variations. When using the new values to calculate the total uncertainty originating from *b*-tagging of *b*-jets, the total uncertainty decreases from 0.052 to 0.028 for R_b and from 0.07 pb to 0.03 pb for σ_{dilepton}, so respectively by 46% and 57%.

[1] All sources of uncertainties on the *b*-tagging scale factors are listed in section 5.4

Variation	$tt \to WWbb$	$tt \to WWqb$	$tt \to WWqq$
BtagB EV 9 down (default)	−0.32%	−0.08%	0.02%
BtagB EV 9 up (default)	0.35%	0.08%	−0.02%
BtagB EV 9 down (half size)	−0.15%	−0.03%	0.01%
BtagB EV 9 up (half size)	0.16%	0.03%	−0.01%

Table J.1: Difference in per cent between the selection efficiency for BtagB EV 9 variations and the the selection efficiency used in the default analysis.

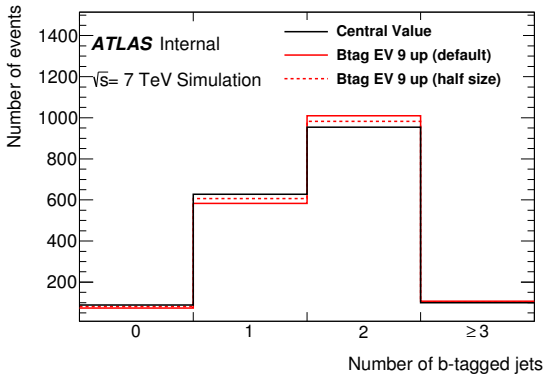

Figure J.1: $tt \to WWbb$ templates created with the default and decreased by 50% BtagB EV 9 "up" uncertainty compared with the central value template used in the analysis.

Source	Var. Down	Var. Up	Averaged Var.
BtagB EV 8 (default)	−0.033	0.035	0.034
BtagB EV 9 (default)	0.040	−0.037	0.038
BtagB EV 8 (half size)	−0.017	0.018	0.017
BtagB EV 9 (half size)	0.020	−0.019	0.020

Table J.2: Comparison of uncertainty on the σ_{dilepton} originating from BtagB EV 8 and BtagB EV 9 with the default size of variation and variation decreased by 50%. These uncertainties were obtained from a series of pseudo-experiments with input value $R_b = 0.99830$.

for R_b and table J.3

Source	Var. Down	Var. Up	Averaged Var.
BtagB EV 8 (default)	−0.00	0.01	0.00
BtagB EV 9 (default)	0.07	−0.06	0.07
BtagB EV 8 (half size)	−0.00	0.00	0.00
BtagB EV 9 (half size)	0.03	−0.03	0.03

Table J.3: Comparison of uncertainty on the σ_{dilepton} originating from BtagB EV 8 and BtagB EV 9 with the default size of variation and variation decreased by 50%. These uncertainties were obtained from a series of pseudo-experiments with input value $\sigma_{\text{dilepton}} = 11.33$ pb.

Acknowledgements

Growing up in an academic family getting a PhD myself one day seemed like the most natural education path. I admired natural science, but I felt I could not fill my father's and grandfather's shoes and become a successful mechanical engineer (my father's lab was too noisy and full of grease!) or follow my grandmother's footsteps in biophysics (due to my poor memory, organic chemistry was my biggest nightmare in high school!). During the summer after high school my mom brought me a collection of popular science books that were on sale in the university library shop. One of them presented an overview of the most exciting topics in modern research and not surprisingly had a chapter on the particle physics experiments at CERN. It sparked my fascination with particle physics, but at that time I did not dare to dream about ever working at CERN.

I thank my parents, Malgorzata and Jacek, for supporting my intellectual development and letting me pursue my passion in fields in which women are still a minority. Thank you for bringing me up to be curious, independent and persistent. Although those quantities have often got me in trouble I consider them to be my biggest strengths and I would not be able to finish my PhD without them. I also want to express my gratitude to my grandmothers, Stenia and Wanda, for being loving, supportive and inspiring. I wish Wanda could be here to see me bringing this thesis to the finish line.

In 2008, three summers after I read that book, I met Bilge Demirköz who was touring German research facilities after the Lindau Nobel Laureate Meeting. At that time I have already applied to the CERN summer programme twice, got rejected both times and was losing hope to ever get a chance to work at CERN. Seeing my passion and despair, Bilge invited me for a two week training at ATLAS. I worked with Daniel Dobos on developing the GUI to control the Diamond Beam Monitor[1]. Bilge and Daniel, thank you so much for giving me this opportunity. I was in the centre of action right before the LHC was switched on for the first time and I will never forget that special atmosphere. It was definitely a turning point in my life.

I returned to CERN in March 2009 as a Technical Student at ISOLDE experiment and in January 2010 I joined Markus Cristinziani's group at the University of Bonn as a PhD student. The timing could not be better – the LHC was about to re-start after the accident. Markus, thank you for selecting me for your group. It was an honor and pleasure to be your student.

I also want to thank other members of the group: Duc Bao Ta, Kirika Uchida, Gia Khoriauli, Gizo Nanava, Vadim Kostyukhin and Tatevik Poghosyan. You were my supervisors, mentors and became my friends. Duc, thank you for teaching me pretty much everything in my first year. Kirika, thank you for guiding me through the b-tagging calibration. Gia, thank you for your help with the ISR/FSR template evaluation and calculation of limits on R_b and $|V_{tb}|$.

Thank you, Professor Norbert Wermes for mentoring and fostering an atmosphere encouraging scientific collaboration.

[1] When I came back in summer 2012 to do shifts in the ATLAS Control Room, the GUI I built was still in use.

Members of Professor Wermes' group: Jana Kraus, Cecile Lapoire, Serena Psoroulas, Elisabeth Schopf, Jan Therhaag, Dennis Hellmich, Marc Lehmacher, Klemens Müller, Stephan Hageböck and Götz Gaycken – thank you for countless pieces of advice, helping to fix my computer and/or code, discussing physics problems over a glass of wine, reviewing and proof reading pieces of this thesis. Not less important, thank you for skiing trips, rock climbing and all the fun we had together at CERN, as well as helping me move and being there when I needed you.

I thank the *b*-tagging community. The conveners: Sara Strandberg, Christian Weiser and Gordon Watts – for guidance and feedback and excellent *b*-tagging workshops. Christian Jung, for explaining to me the muon-based calibration methods and preparing me for the Moriond conference. Lukas Heinrich, Dominik Duda and Rob Calkins – for the incredible year we spent working on the *b*-tagging calibration with $t\bar{t}$ events.

Finishing a PhD while working full time is very challenging. I would not be able to finish this thesis without the understanding and flexibility of my employers: Deloitte A.G. in Switzerland and Deloitte Consulting LLP in USA. Partners and Managing Directors: Sven Probst, Sinja Christiani, Mark Carter, Beat Burtscher and Brandon Cox – thank you for your patience and understanding. Counselors: Mervi Kech and James Ray – for helping me to manage my workload and enabling me to achieve both my professional and personal goals. To all my colleagues and project teams over the years – thank you for your support and encouragement.

I want to thank my friends Ola, Marta, Alana, Bo, Viktoria, Thomas, Gosia, my roommates in Bonn, Zurich and Boston and many more for expressing their support in many different ways during this process. I am extremely grateful for your faith in me and helping me find motivation. Last but not least, Jesse – thank you for giving me love, balance and a peace of mind, so that I felt empowered to finish this thesis.